Trajectory and aerodynamic analyses of air launched fire-extinguishing projectiles

Hugo Filipe Leça Pereira da Rocha

Dissertação para obtenção do Grau de Mestre em
Engenharia Aeronáutica
Mestrado Integrado

Orientador: Prof. Doutor Pedro Vieira Gamboa

junho de 2020

Dedication

To my uncle Carlos “Cabeça Pensadora” Leça and my aunt Generosa Andrade.

Acknowledgements

As I reach the closure of this life chapter, there are many people who I owe my deepest and sincerest gratitude, for the direct or indirect help they provided me along this phase, especially in this last milestone.

To my advisor Professor Pedro Gamboa, my deepest appreciation, for the insurmountable patience, for the given suggestions and help, and for his dedication in teaching.

To Professor Francisco Brójo for his readiness and assistance in the utilization of the Computational Cluster.

To Doctor Véronique deBriey, from Brussels' Royal Military Academy's Department of Mechanics, for her aid in the validations of the trajectory and CFD models.

To João Monteiro and Paulo Antunes, from *SpaceWay*, for their suggestions and for the opportunity to work in this excitingly interesting project.

To my family, specially to my parents and siblings, Andreia, Paulo, and Sofia, for their unconditional support in all my endeavors.

To all my friends and colleagues, particularly Ricardo, 倩妮, Diogo, and Diana Rodrigues, for their motivation and their enormous and constant emotional support.

To all others who, in some way or another, helped me overcome the various obstacles which led me to the point I am at today.

Resumo

Os incêndios florestais são uma fonte devastadora de custos humanos e ambientais, e os meios disponíveis para combater as suas fases iniciais poderão ser melhoradas. Com o auxílio de sistemas de aeronaves não-tripuladas e de FEB (bolas extintoras), os incêndios florestais poderão ser extintos nas suas fases iniciais, mantendo vidas humanas livres de risco. Considerando o uso de uma aeronave não tripulada de asa fixa para lançar o projétil-extintor, lançar a bola extintora tal como é não aparenta ser a melhor opção, sendo alguns dos problemas relacionados com o seu lançamento a dificuldade em prever a sua trajetória e um possível mau desempenho no impacto, com a possibilidade da bola rolar para longe do seu alvo. Assim, três configurações para o projétil extintor que tem a FEB como base foram estudados, todos eles utilizando empenagens como forma de estabilização. As configurações diferem em termos da cauda acoplada à FEB: uma delas é um tubo, outra um cone tangencial, e outra um perfil NACA simétrico girado em torno do seu eixo. Os coeficientes aerodinâmicos estáticos foram obtidos através de CFD (dinâmica de fluidos computacional), enquanto que os dinâmicos foram obtidos por expressões analíticas. Implementando um modelo de trajetória 6-DOF (6 graus de liberdade) 17 trajetórias foram estudadas para cada uma das configurações. Outras análises foram realizadas, como a relevância na trajetória da turbulência do vento, a consideração de uma quarta configuração com o dobro da área das empenagens, e a determinação da importância dos coeficientes dinâmicos, testando vários valores para alguns dos coeficientes. Em relação às configurações do projétil testadas, os resultados CFD sugerem que a configuração com o tubo possui um comportamento transiente nas velocidades testadas, e que o cone tangencial é uma forma bastante eficaz de tornar a esfera mais aerodinâmica, nesta gama de velocidades não havendo uma diferença considerável entre esta configuração e a configuração com a cauda NACA. Os resultados das trajetórias destacam a importância da consideração da velocidade e orientação do vento médio, a importância de obter uma estimativa apropriada para a turbulência do vento, e a relevância dos coeficientes dinâmicos para a caracterização aerodinâmica completa do projétil, concretamente em relação à estabilização e atitude. Entre as configurações testadas, o melhor candidato é a configuração com cauda em cone, pela sua simplicidade de construção e desempenho nas trajetórias.

Palavras-chave

Bola;extintora;UAS;incêndios;trajetória;balística;6-DOF;CFD;aerodinâmica

Abstract

Wildfires are a devastating source of human and environmental loss, and the available means to combat them in their early stages can be improved. With the aid of Unmanned Aerial Systems and FEB (Fire-extinguishing balls), wildfires' early stages might be suppressed while keeping human lives safe and firefighters risk-free. Considering the use of a fixed wing Unmanned Aircraft Vehicle to launch the fire-extinguishing projectile, launching the FEB as it is, without any modification, does not seem to be the best available option, with problems ranging from difficulty in predicting its trajectory to the possible bad impact performance, with the possibility of the FEB rolling away from the target as it lands. Therefore, three other configurations for the projectile with FEB as its basis were studied, all of them utilizing fins for the means of stability. These configurations differed in terms of tail design attached to the FEB: one is a tube, the other a tangential cone, and the other a symmetrical NACA airfoil revolved around its axis. Their aerodynamic static coefficients were obtained through CFD (computational fluid dynamics), while the dynamic ones were obtained through analytical expressions. Using an implemented 6-DOF (degrees of freedom) model, 17 trajectories were studied for each of these configurations. Other analyses were carried out, as the consideration of the influence of wind turbulence, consideration of a fourth configuration with double the area of the fins, and asserting the importance of the consideration of the dynamic coefficients while testing different values for some of these coefficients. Regarding the FEB-projectile configurations, CFD results suggest that the tube configuration has a transient behavior in the tested speeds, and that the tangential cone is a very suitable way of streamlining the FEB in these range of speeds, with no considerable difference to the NACA tail configuration. Trajectory results highlight the importance of considering the mean wind speed and direction, the importance of obtaining an appropriate estimate of the wind turbulence, and the importance of the dynamic coefficients for the full aerodynamic characterization of the projectile, concretely for its stability and attitude results. Ultimately, between the tested configurations, the best candidate is the cone tail configuration, for its simplicity in construction and performance in the trajectories.

Keywords

Fire-extinguishing;ball;UAS;wildfires;trajectory;ballistics;6-DOF;CFD;aerodynamics

Content

List of Figures

List of Tables

List of Acronyms

CFD	Computational Fluid Dynamics
CG	Center of gravity
DOF	Degrees of freedom
FEB	Fire-extinguishing ball/balls
UAS	Unmanned aerial systems
UAV	Unmanned aerial vehicle

List of Symbols, Constants and Variables

a_t	Slope of the $C_L(\alpha)$ curve of the tail
C_D	Drag coefficient
C_L	Lift coefficient
C_M	Pitching/overturning moment coefficient
C_{M_q}	Pitch damping moment coefficient proportional to q
$C_{M_{\dot{\alpha}}}$	Pitch damping moment coefficient proportional to $\dot{\alpha}$
C_{N_r}	Yaw damping moment coefficient proportional to r
$C_{N_{\dot{\beta}}}$	Yaw damping moment coefficient proportional to $\dot{\beta}$
C_X	Axial force coefficient
C_Y	Side force coefficient
C_{Y_r}	Yaw damping force coefficient proportional to r
$C_{Y_{\dot{\beta}}}$	Yaw damping force coefficient proportional to beta dot
C_Z	Normal force coefficient
C_{Z_q}	Pitch damping force coefficient proportional to q
$C_{Z_{\dot{\alpha}}}$	Pitch damping force coefficient proportional to alpha dot
d	Diameter of the projectile
D	Drag force
$E_{M.H.}$	Percent error in maximum height of flight, in trajectory model validation
E_R	Percent error in range of flight, in trajectory model validation
$E_{T_{flight}}$	Percent error in time of flight, in trajectory model validation
g	Gravitational acceleration
h_{launch}	Launching height
I_x, I_y, I_z	Moments of inertia
I_{xy},I_{yx},I_{yz},I_{zy}, I_{xz}, I_{zx}	Products of inertia
l	Length of the projectile
L	Lift force
l_t	Distance between the projectile's CG and the tail aerodynamic center
m	Mass of the projectile
$M.H.$	Maximum height of flight, in trajectory model validation
$M.V.$	Muzzle velocity
$MW_{direction}$	Mean wind direction
$MW_{velocity}$	Mean wind velocity
$Oxyz$	Projectile-fixed reference coordinate system
$Ox_a y_a z_a$	Air-trajectory reference coordinate system
$Ox_g y_g z_g$	Earth-fixed reference coordinate system
p	Rolling velocity
PDF	Pitch damping force
PDM	Pitch damping moment
PM	Pitching/overturning moment
q	Pitching velocity
$Q.E.$	Quadrant elevation
Q_∞	Dynamic pressure

r	Yawing velocity
R	Range of flight, in trajectory model validation
Re	Reynolds number
S	Reference area (projectile's frontal area)
S_{tail}	Reference area of the horizontal tail (area projected on the xz plane)
t	Time variable during trajectory
T_{flight}	Time of flight, in trajectory model validation
u	Projectile velocity in x axis
u_{WT}	Wind turbulence velocity in x axis
v	Projectile velocity in y axis
V	Total projectile air velocity
V_H	Horizontal tail volume coefficient
V_{launch}	Launching velocity
v_{WT}	Wind turbulence velocity in y axis
w	Projectile velocity in z axis
W	Weight force
w_{WT}	Wind turbulence velocity in z axis
x_{cg}	Position of the projectile's center of gravity, measured from the most forward point
YDF	Yaw damping force
YDM	Yaw damping moment
YM	Yawing moment
α	Angle of attack
$\dot{\alpha}$	Rate of change of angle of attack
β	Sideslip/yaw angle
$\dot{\beta}$	Rate of change of angle of sideslip
$\Delta C_{L_{tail}}$	Change in tail lift coefficient
ΔC_M	Change in moment coefficient
$\Delta\alpha_t$	Change in tail alpha
θ	Pitch angle
ρ	Density of the airflow
ϕ	Bank angle
ψ	Yaw angle

1. Introduction

1.1. Motivation

During the last decade, Portugal has seen an increase in wildfires occurrences, as well as in their severity. The current climate change scenario is an important factor, which will worsen the situation as average temperatures rise and atmospheric precipitation decreases, leading to more prolonged dry seasons [1]-[6], all while the unpredictability of occurrence of forest fires is at an all-time high [7]. Many other factors put Portugal at very high risk of wildfires, such as rural areas being overwhelmed with secondary housings, which increases the Urban-Wildlife Interface [8]; a rural exodus by younger people which leave the countryside with an advanced age population incapable of properly cleaning their plots from highly flammable dried vegetation [9]; the still prevailing use of slash-and-burn agriculture in rural areas [10]; and problems regarding the planning and managing of the country's forest, like the planting of highly flammable arboreal species such as *Pinus pinaster* and *Eucalyptus globalus* [9], [11].

In 2017, Portugal was marked by having an increase of 428% in burnt area, comparing to the annual average until that date, with a burnt area of more than 4,420 km^2, distinguishing it as the year with most burnt area since 2007 [12]. The forest fire in Pedrogão Grande stands out from the other occurrences that year. It killed 66 people, the deadliest forest fire since 1966 [13], affected more than 1,000 structures, mainly houses, and caused an estimated economical loss of 500 million euros [14]. In 2018, Monchique's mountain burned for more than a week straight, in a forest fire that injured 49 and consumed 27,000 hectares [15]. Other countries have also been affected by similar scenarios. In 2018, the state of California in the U.S.A. suffered both its deadliest forest fire, with 85 dead [16], and the biggest in terms of burnt area, with a single forest fire burning more than 459,000 hectares [17]. The 2019/2020 bushfires in Australia ravaged more than 18 million hectares of land, destroyed more than 2,000 homes, killed 34 people and about one billion animals [18], while releasing an estimate of 306 million tons of carbon dioxide [19], and costing more than 4.4 billion Australian dollars [20].

Therefore, because of their economic, social, and environmental cost, the search for efficient wildfire firefighting is essential. Furthermore, by focusing efforts on forest fires prevention and a quick and efficient attack on its origin, the costs associated with firefighting could be reduced drastically, especially since putting out a fire in its initial stages, with a small hotspot, is easier than fighting a fully developed forest fire [21].

The current advanced and reliable technological state of Unmanned Aircraft Systems makes their use possible and desirable in various activities related to firefighting, such as surveillance, prevention, and even direct firefighting or any other difficult or dangerous action. In fact, these various applications have been increasing throughout the last decade, guided by feasibility studies and surveys [22], [23] and aided by developments on the systems' branching disciplines, like, for example, fire detection [23]-[28] and cooperative control [29]. Moreover, a study predicts that in 2020 the market value of firefighting UAS (unmanned aerial systems) will be 881 million dollars, in the United States alone [30]. The use of UAS in firefighting allows a reduction of necessary human resources and decreasing the risk of injury or even death. They can also act on circumstances when resorting to conventional firefighting means is difficult or even impossible, such as fires on terrains of difficult access, on top of buildings, in oil rigs, or in inadequate meteorological or visibility conditions that prevent the use of the currently available firefighting aerial resources [22], [29], [31]-[33].

Indeed, the current scientific and technological advancement permits the creation of a totally automatized system of detection and immediate response to forest fires, with a ready and efficient response that would prevent the still beginning fire to spread. In this sense, *SpaceWay* proposed the concept of suppressing the very first stages of a forest fire by launching a projectile from an UAV (Unmanned Aerial Vehicle), which upon impact with the ground or near impact would explode and release a fire suppressant or retardant chemical. It is also proposed for a fire-extinguishing ball to be the projectile design basis. This UAS would act as an initial attack, mobilized immediately after the detection and actuating precisely on the area where the fire is starting, before it spreads to the fuel surrounding it, preventing therefore a full-blown forest fire.

1.2. Objectives

The main objective of this dissertation is to evaluate the aerodynamics and trajectory performance of possible configurations for a fire-extinguishing projectile which uses a fire-extinguishing ball as a design basis.

1.3. Dissertation structure

Firstly, a study on the state of the art on the various topics addressed in the dissertation is presented. Secondly, the forces and moments relevant for the trajectory model are defined, followed by the formulation of the model itself and by the explanation of the wind model. After this, the methodology to obtain the projectile aerodynamic characterization is defined. This is followed by the mission and projectile requirements, preliminary design choices, and the presentation of the proposed configurations that are studied. After this, the analyses and their respective results are presented. This encompasses not only the analyses and results of the configurations' aerodynamics but also the validation of the various implemented methodologies. Finally, the conclusions are addressed, and the future work is disclosed.

2. State of the Art

This chapter presents a brief history and current state of the art of the various topics addressed in the present dissertation. Firstly, the field of Ballistics is briefly reviewed, followed by a discussion on some of the various models used to predict projectile's motion. Secondly, the different means of obtaining the projectile characteristics are briefly evaluated. Subsequently, firefighting utilizing projectiles is covered, and, lastly, the used initial methods while tacking a wildfire are discussed.

2.1. Ballistics and trajectory models

Ballistics can be divided into three sub-fields: Internal Ballistics, Exterior Ballistics, and Terminal Ballistics.

The first, often also called Interior Ballistics, deals with the means of propulsion that generate the thrust necessary for the motion of projectiles. In firearms, these studies are focused on the phenomena inside the chamber and the gun barrel, as well as its affecting variables, such as the properties of the ignition charge or the geometry of the barrel. In other words, Internal Ballistics discusses the interaction between the launching/propelling device and the projectile itself.

The second field, also referred to as External Ballistics, relates to the movement of the projectile along its atmospheric trajectory, including the forces, moments, and other variables that affect it, such as air properties or the projectile geometry. One of the major interests in Exterior Ballistics studies is projectile's dynamics and stability along its trajectory.

The last one, Terminal Ballistics, focuses on studying the target impact of the projectile, such as all the effects that occur on impact, and its goal performance, that is, the effectiveness of the desired effect, be its effectiveness in destroying a target or its precision on the impact target [34]-[38].

Some also append a subfield called Transition Ballistics, which is the study of the projectile motion and behavior after it leaves the barrel but while it is still under the influence of gases from the propellent, and it is usually applied when studying guns [37], [38]. The scope of this dissertation is only on the study of the Exterior Ballistics.

Exterior Ballistics trajectory prediction models emerged from Rigid Body Dynamics. In Rigid Body Dynamics, the bodies are considered undeformable, and their dynamics are described by the application of either Newton's second law or Lagrangian mechanics, and by the laws of kinematics. The projectile's geometry, aerodynamics, used means of stabilization, and some transient aerodynamic effects, for example, all have great effect on the way a projectile behaves in its aerodynamic flight, but the different set of forces and moments a symmetric projectile is subjected to throughout its trajectory differ mostly due to its stabilization method. In order to understand some of the main differences between Exterior ballistics models, it is necessary to define before-hand these different set of forces. For fin-stabilized projectiles, the main forces and moments acting on them during flight are drag, lift, and overturning moment. Spin-stabilized projectiles experience the same forces as fin-stabilized ones, with the addition of the Magnus force and Magnus moment. Both sets can also be complemented with damping forces and damping moments, related to the transitional effects of the projectile rotation around its axes, and, obviously, both consider gravitational force. Some other disregarded forces and moments are the Magnus cross force, Magnus cross moment and buoyancy. Coriolis effects might also be taken into account, depending on the trajectory distance [1], [35], [39], [40]. The forces applied to the projectile are explained more in-depth in Section 3.1.

Niccolò Fontana (1499/1500-1557) was a remarkable Renaissance mathematician, and in his work titled Nova Scientia he presented his study on projectile motion, being the first ballistician to ever remark the presence of a curvature in a projectile's path [41], [42]. His efforts propelled Galileo Galilei's work on ballistics, which include the first analytic projectile trajectory solution and the discovery that projectiles' path under the exclusive influence of gravity are parabolic [43]. In turn, Robert L. McCoy distinguishes Isaac Newton as one of the most influential modern founders of Exterior Ballistics, since the field's theoretical foundation lays on Newton's laws of motion and classical mechanics. Many were the scientists that contributed to the advance of Exterior Ballistics, and its modern state has evolved largely in the pursuit of better and faster accuracy in the calculation and prediction of a projectile's trajectory, which is considered the classical Exterior Ballistics problem [35]. In this sense, several models have been developed through the ages, according to the knowledge, technology, and advancements available at those times.

Galileo's work was based on an In-Vacuo Model. In this model, the projectile is considered a point particle (also named point-mass), i.e., the three-dimensional projectile is reduced to a single point, in which all its mass is concentrated. This means the effect of the projectile's geometry is not considered, and the only force that the projectile is subjected to is gravity. This simplistic model only has two variables determining the projectile's trajectory, namely the launching velocity and launching angle, and the result is always a parabolic path, as Galileo stated in his work [1], [38].

The models in the studies of Galileo and Niccolò were essentially very early Point-Mass Models. In this type of model, as the name implies, the projectile is considered a point-mass, permitting only three translational degrees of freedom and the total yaw of the projectile is considered small enough that lift and Magnus force are neglected, and thus only aerodynamic drag and gravity are considered [35], [44]. Sometimes the Coriolis acceleration is also taken into account [45]. In 1753 Euler presented the first general solution to the Point-Mass trajectory [46]. Later, the model was refined by accounting for the Coriolis effect, as well as crosswind [1].

Point-mass models can be linearized, permitting an approximate analytical solution or their comprising nonlinear equations can be solved numerically. One example of a linearized point-mass model is the flat-fire point-mass model, which is valid for angles of launch and fall less than 5.7 degrees, considering no crosswind and with a drag coefficient that is an elementary function of the Mach number. In fact, a flat-fire trajectory with constant drag coefficient is a good approximation for a plethora of subsonic trajectories for a great number of projectiles and is considered a good approximation in free-flight ballistics [35], [38].

At the beginning of the twentieth century, R. H. Fowler, E. G. Gallop, C. H. Lock, and H. W. Richmond published The Aerodynamics of a Spinning Shell [47], in which the basis of the 6-DOF (degrees of freedom) Model are made explicit. In this model, which was completed and refined by other scientists, the projectile is considered a rigid body, and its motion comprises three rotational and three translational degrees of freedom. It is the most accurate model to date, adequately describing most physics along the projectile's trajectory, as well as its complete movement [35], [36], [38], [48]. However, the model had a quite enormous disadvantage at the time of its advent: there was no practical way to obtain solutions for the equations. It was not until mid-20th century, when computers with an adequate size and memory size appeared, that it was possible to integrate numerically the model's equations of motion in a reasonable time and with a considerable degree of accuracy [35], [38]. This type of models requires the most input data and, therefore, might be more susceptible to errors arising from poor input parameters and initial state errors [35], [44].

Due to the early computational limitations that prevented the implementation of the 6-DOF Model, ballisticians' interest at that time revolved in modifying the simpler Point-Mass Model, in order to attain good trajectory prediction results with decent processing times. Moreover, the Point-Mass Model did not account for all observed phenomena - concretely, the swerve due to yaw or the yaw's effect on drag and lift, especially in longer projectiles. Furthermore, the model did not present the support to the stability of the projectiles. Considering this, Robert F. Lieske and Mary L. Reiter proposed the Modified Point-Mass Model in 1966 [48], [49]. In this model, the angle of attack is approximated by its average (yaw of repose) and it corresponds to the fourth degree of freedom, the first three being the translational ones. This means the yaw, pitching moment, and transient movement of the projectile are not considered [1], [35], [36], [38], [50]. As in the Point-Mass Model, only the essential forces and moments are considered, while assuming the pitching and yawing motion are small enough throughout the projectile trajectory [36]. The model has been standardized by NATO and was used to develop fire tables [48]. Since the model is given by an implicitly defined differential equation, Baranowski, Gadomski, Majewski and Szymonik presented a reformulated model, termed Ballistic M-model, that is modeled by a solvable explicit system which still has reasonable complexity [51].

Another relevant advancement on trajectory models is the Projectile Linear Theory, which stemmed from the 6-DOF model and was first developed by the same authors [43]. It comprises of a series of simplifications that result in a set of simplified and solvable differential equations, while still retaining good accuracy and providing understanding of the projectile's flight dynamics [52]. Projectile Linear Theory was refined by several ballisticians, some referred in [38], [43], and it has been used for stability analysis, aerodynamic coefficient estimation and rapid trajectory prediction [43], [53]. Eventually a great number of scientists contributed with specific advancements, customizing it to comply with, for example, asymmetric mass properties, fluid payloads, and aerodynamic configurations [53], as well as moving internal parts, dual-spin projectiles, lateral force impulses [52], and ascending and descending flight. References for these works can be found in [43], [53].

2.2. Projectile aerodynamics

As has been explained, different trajectory models, which have different precision and time-efficiency, require different data input and theoretical or mathematical considerations, while their different usage might depend on the developing stage of the projectile or even the importance or type of the projectile itself. The aerodynamic characteristics necessary for the implementation of an Exterior Ballistics model cannot be obtained through a general method, therefore, depending on the available information, available resources, and the problem itself, different techniques are employed [54].

To predict a projectile configuration trajectory utilizing a 6-DOF model, usually four sets of techniques are used to obtain the necessary aerodynamics: CFD (computational fluid dynamics) simulations, wind tunnel testing, flight testing, or using some aerodynamic coefficient prediction software package. It is important to notice that the correct estimation of the projectile aerodynamic behavior is especially important in new configurations, in order to correctly assess its trajectory prior to flight tests, therefore reducing development costs [40], [55], [56].

Wind tunnel testing gives considerable accurate results, allowing in-depth studies of certain parameters. It is considered, however, a time expensive method since the extensive and meticulous study of all design options require considerable costs. Other obstacles to wind tunnel testing are the difficulty in identifying the source of a certain design problem, and the fact that most wind-tunnels do not allow for full-scale Reynolds simulation which can lead to significant errors [57]. Moreover, this method is not available for a great number of ballisticians, and some effects must be taken into account and considered when studying and analyzing the results, like aerodynamic interferences on the model or disturbances in the air flow (such as turbulent fluctuations or soundwaves), therefore requiring additional knowledge, work, and time expense, as well as correct maintenance and instrument calibration [40], [56], [58], [59].

Flight testing has the most accurate results of all these techniques, but it is also considered expensive and time consuming, especially if many tests are required [40], [56]. One type of free-flight testing, called spark photography testing, involves using spark shadowgraphs taken at determined flight points of the tested projectile trajectory. Even though considered the “gold standard” of projectile dynamic coefficient estimation, these tests are the most expensive and exclusive ones, requiring access to a spark range facility and proper measuring instruments [40].

Another way of obtaining a projectile’s aerodynamic coefficients is using CFD. In CFD simulations, the fluid flow is modeled by equations, which are then numerically solved for a specific configuration. These equations are based on the Navier-Stokes equations, which fully describe the flow, and different sets of equations have different levels of simplification, since it is not feasible to fully solve the Navier-Stokes equations by use of Direct Numerical Simulation in a time-adequate manner [60]. Recent advances in computing and CFD technologies allow for less costly design developments and deeper insight into the aerodynamic phenomena. Moreover, presently it is possible to correctly predict projectile dynamics during its flight based only on CFD simulations, with the principal advantage being the ease of changing almost any definition of the simulation [40], [55]-[57], [61], [62]. The major problem with CFD is that it requires substantial knowledge and experience on the subject to correctly setup the calculations. The choice of the correct turbulence model for the case in study, as well as its boundary resolution, and the implementation of a good grid which can correctly predict the important aspects of the flow are three of the major considerations for a good CFD implementation [57], [62].

Nowadays, CFD and computational technologies are at a point where the coupling of RBD (rigid body dynamics) and CFD has become a recurrent way of studying projectile's dynamics. This way, at every time step of the trajectory simulation, the RBD equations of motion are integrated, while the aerodynamic forces and moments are calculated through CFD programs. Granted that RBD and CFD coupling is more common than ever, it is still considered a time and computational expensive analysis, and is not considered a practical method for typical flight dynamic analysis, where the study of different parameters and a substantial amount of simulation runs is sometimes needed [40], [55]. CFD/RBD coupling has been used for studying, for example, multibody projectile aerodynamics, store separation problems and time-accurate numerical aerodynamic prediction. References for these works can be found in [55].

Another way to predict a projectile's aerodynamic coefficients is to use existing software packages that estimate those based on a set of geometric properties. Some of these programs involve a database of catalogued dynamic coefficients of many different projectiles, obtained from wind tunnels or free-flight tests. Some examples of this types of programs are *Digital DATCOM*, *Missile DATCOM*, *AP98*, and *PRODAS*. Other programs resort to simpler numerical methods to compute the flow around a configuration, needing only basic geometric definition. These programs are especially useful in the conceptual design of projectiles, providing fast estimates of the coefficients needed. However, the estimates' accuracy is largely affected by the configuration of the projectile in study, since newer and different configurations may have aerodynamics which are not correctly reproduced by the projectile databased used, or the configuration might be too complex to accurately predict the flow behavior around it, requiring more sophisticated CFD approaches . Moreover, although some programs like *OpenRocket*, *Aerolab* and *Tornado* are free and open to public, most are either military or governmental property or are paid for, which makes them inaccessible to several groups of ballisticians [40], [56], [63].

2.3. Firefighting projectiles

Since the definition of a projectile is "a body projected by external force and continuing in motion by its own inertia" [64], this section would not be complete without a reference to projectiles thrown by hand. The first fire extinguishing device was invented by Ambrose Godfrey in 1723 [65], and since the device could be thrown into the fire, it is only fair to award him as the inventor of the first firefighting projectile. Despite this, the popularity and use of hand thrown firefighting devices had its peak later, in the late Victorian Era, using globes containing carbon tetrachloride [66], [67]. As for modern firefighting projectile concepts, the earliest found in this research dates to 1903, a patent filed by Roderick Chisholm which relates to bullets loaded with fire-extinguishing fluid, as well as the concept for the gun [68]. However, earlier concepts of firefighting guns do exist, since the patent mentions improvements to the existing ones at that time, although they could not be found.

Regarding projectiles or concepts similar to the one developed in this dissertation i.e., air launched, the earliest found in the research dates back to 1939, when Ronald Roberts filed a patent where he details a projectile able to distribute fluids and granular materials for applications in fire extinguishing, fire prevention, or even seeding and fertilizing. It differed from the firefighting bombs existing at that time by releasing its contents when reaching a predetermined altitude, obtaining a wider area of effect than projectiles whose method of payload release depended on ground impact. Moreover, the projectile would be inexpensive, and the release would not resort to any type of explosive charge [69].

Multiple firefighting concepts, projectiles and their respective delivery systems have been patented or studied since then, for example [34], [68]-[89]. The developed projectiles usually differ in ways the fire-extinguishing or suppressant payload is delivered, or the way the projectile is deployed, most of them requiring a “firearm-like” device to launch it.

In Portugal there is a project being developed since 2005 called FIREND. This firefighting projectile concept was presented in 2005 by Lieutenant-Colonel Marquês Sousa, Pedro Vilaça da Silva, and Francisco Lima [34]. Since then, several changes have been made, like shell design and detonation method, accompanied by several Internal and Exterior Ballistics studies. One of the several important and relevant advancements in this project is the choice of Polylactide (PLA) for the outer shell material. PLA was chosen in order to reduce the environmental impact of the projectile, since this polymer is fabricated from renewable biomass and it is compostable [89]. Some other projects, like [73], [76], and [78], also had the consideration of biodegradable materials composing the shell, or even a biodegradable firefighting payload.

Interestingly, even though several studies and projects of firefighting projectiles have been developed throughout the years, there could not be found much information on currently running companies dedicated to manufacturing them, especially projectiles launched by aircraft. NPO Bazalt, now a part of Rostec, was a Russian weapons manufacturing company and in 2004 they developed the ASP – 500, a fire-extinguishing bomb which could act on 1000 m2 [90]. The other commercial product found was the KFEB, from the company Killburn. The bomb detonates when it reaches a certain altitude, dispersing a fire-fighting agent that also acts as a fertilizer [91]. This research, however, did not find records of use of these devices.

The project which encompasses this dissertation plans to use a fire-extinguishing ball (FEB). There are two main manufacturers of this kind of fire extinguishing device, Elide Fire [92] and AFO [93]. The one this project intends to use is the AFO Ball, which is the base part of all projectile configurations studied in this dissertation. It comprises of a polystyrene shell, which encloses a dry fire extinguishing agent, Mono Ammonium Phosphate. The outer case encompasses a fuse, which after a few seconds detonates a charge present on the center of the ball, blasting the case and spreading the fire extinguishing powder.

As for projects and researches much similar to this one, that is, using FEB, some studies were made quite recently. One very important study is the one by Aydin et.al [88], in which the effectiveness of FEB to combat wildfires is assessed. The conducted trials were all successful and the FEB was able to extinguish the fire source, which showed potential for the use of FEB in this sense. Other studies assess the use of UAS in conjunction with FEB, for example, with a detection-response method [94], or swarm robotics [95]. Another interesting study [96] analyzed three different UAV configurations to launch/release a FEB. However, no study was found on the trajectory of the FEB after release.

2.4. Initial attack in firefighting

In firefighting, the initial attack is the set of “actions taken by the first resources to arrive at a wildfire to protect lives and property and prevent further extension of the fire” [97]. The first approach to a wildfire, once its detection occurs, depends upon its size and means of access. Regarding fires in their early phase, in Portugal the used procedures are two: first intervention helicopters and airplanes, or the GNR’s intervention group GIPS.

Regarding aerial firefighting, the type of aircraft that respond to fires in their first stages and small fires are termed First Intervention Means. They are deployed from their respective heliports or airstrips, immediately after the fire alert [21].

GIPS itself has two means of approaching this type of fires, subdividing their Intervention to Forest Firefighting group in heli-transported and land-transported. The first intervention method is based on the transportation of a crew of five to eight military by light or medium helicopter, equipped with sapper tools, in order to conduct direct attack once they land. The second intervention method consists of deploying a crew of four firefighters, transported in a Light Firefighting Vehicle. Besides the 500 liters of water the vehicle carries, the crew is also provided with sapper tools for direct and indirect combat. Usually this crew is deployed to assist the heli-transported crew [98].

The above-mentioned approaches are somewhat common throughout the world, with little differences between them. Some countries have other means to deal with fires in their early phase. For example, Russia, Canada, and the U.S.A. employ Smokejumpers, which are highly trained firefighters who parachute into wildfires, in order to perform an initial attack. By parachuting, Smokejumpers can access difficult terrains, as well as remote inaccessible areas [99], [100].

The methods made explicit above carry clear disadvantages. Regarding aircrafts, one of the disadvantages is the dependence on environmental conditions. They cannot operate at night and the accuracy of water or chemical delivery is harshly affected by the wind. Moreover, if their initial attack fails, a considerably wide time window between the first attack and the next provides enough time for the fire to spread and increase in size, making it even more difficult to control and extinguish [101]. As for GIPS and Smokejumpers, one of the evident disadvantages is the risk of harm (or even death) the firefighters endure, especially if the containment of the fire in its early phase is not achievable and a sudden need for more and different resources emerges.

Even though the possibility of improvement on initial attack firefighting methods is tangible, the advancements, products, and proposals found in this research mostly focus on combating medium to large fires. Bazalt’s ASP-500 could be used as an initial attack independently of the fire size, either suppressing it or increasing the effectiveness of subsequently discharged water or chemicals [91]. André Moreau referred to the possibility of using his device as a mean of initial attack on fires in their first phases, although that opportunity is highly reliable on the performance of the aircraft carrying the projectile [88]. Another concept identified in this research, one created by Shiro Ishida, was developed with the objective of initial attack firefighting. This invention relates to a fire-extinguishing rocket shell launched from a rocket launcher mounted on a fire truck, developed to perform initial attack firefighting on fires in their early phase, emerging on mountains. Since mountains are of difficult access, this invention would extinguish the fire, or at least delay or prevent the spreading of the hotspot, while requiring few human resources [76].

3. Exterior ballistics trajectory model

In this chapter, a description of the projectile trajectory model is made explicit. Firstly, the forces the projectiles are subjected to during their simulated aerodynamic flight are explained. Next, the motion equations that encompass the model are presented, followed by the explanation of the wind turbulence model that was used.

3.1. Forces and moments

The different forces a projectile undergoes during its aerodynamic flight depend mostly on the projectile's method of stabilization, while some forces are common to any type of projectile. McCoy [35] presents a detailed overview of the complete force-moment system of projectiles, which is followed to some degree in this chapter. Since the proposed projectile configurations employ a fin-stabilization method, only the forces and moments relevant to the trajectory prediction of this type of projectiles are presented. This set of forces is firstly addressed in Chapter 2, Section 2.1, and are completed and fully explained in the present section.

Naturally, the projectile is always under the influence of gravity throughout the trajectory. This force depends on certain factors. For example, location on Earth, topography, elevation, and even differences in the density of the crust and mantle affect the acceleration due to gravity, g, along the surface of the Earth [102]. Since in this dissertation the projectile is only submitted to small trajectories, with a small variance of atmospheric altitude, a constant value of g can be assumed. Therefore, value of the gravity force can be obtained through

$$W = mg \tag{1}$$

in which m is the projectile mass.

Drag is the force common to any object subjected to a fluid flow past its surface and is the component of the resultant aerodynamic force in the velocity direction. It corresponds to the momentum transferred from the moving body to the surrounding fluid and can be divided in four types: skin-friction drag, pressure drag, induced drag, and wave drag. Friction drag has a viscous nature, resulting from the molecular resistance fluid particles exhibit against displacement in relation to each other, giving arise to a tangential force, namely friction drag. Pressure drag, on the other hand, has an inviscid nature, resulting from the distribution of the forces normal to the body surface. The net difference in the distribution of normal forces arises from the alteration of the pressure field because of the object, its boundary layer, and its wake, but a part of it can also be caused by boundary layer separation and by recirculating flow in the aft part of the body. In bluff bodies, drag is mostly constituted by pressure drag, while in streamlined bodies the major contributor to this force is friction drag [103]. Induced drag constitutes most of the drag due to lift, and results from trailing vortices generated in wing tips. Wave drag appears in supersonic flow, and since the present work relates to low velocities, there is no need for it to be addressed in this dissertation [59], [104]. The magnitude of the drag force is calculated by the equation

$$D = \frac{1}{2}\rho V^2 S C_D = Q_\infty \, S C_D \tag{2}$$

where ρ is the airflow density, V is the total projectile air velocity, S is the reference area, in this work the frontal area, C_D is the drag coefficient, and Q_∞ is the dynamic pressure.

Lift is the force normal to the trajectory, the component of the resultant aerodynamic force perpendicular to the projectile velocity. The physics behind aerodynamic lift production are somewhat complex, and is not explained here, although extensive information regarding this phenomenon can be found in [104] and [105]. In projectiles, lift is usually null at zero angle of attack and increases with the increment of this angle. This force is also generated by the fins of fin-stabilized projectiles and is responsible for their stabilizing overturning moment, explained in the next paragraph [39]. The magnitude of the lift force is obtained by

$$L = Q_\infty S C_L \tag{3}$$

where C_L is the lift coefficient.

The overturning moment, also called pitching moment or static moment, relates heavily to the stability of projectiles. If the projectile's angle of attack, α, is positive, a positive overturning moment is generated, which in turn increases the angle of attack even more. In order to stabilize non-spinning projectiles, fins are attached to their tails, which create the lift force necessary to result in a negative pitching moment, which acts to decrease the angle of attack. The overturning moment magnitude is obtained by the following equation:

$$M = Q_\infty S d C_M \tag{4}$$

in which d is the projectile's diameter and C_M is the overturning moment coefficient.

Analogously to the pitching moment, a yawing moment can be defined. In some works, especially when working with spin-stabilized projectiles, the pitching moment is defined as a function of the total angle of attack, which takes into the consideration the sideslip (or yaw) angle β. In this work though, the pitching and yawing moment are considered individually, since the cases of study do not have simultaneously high α and β. This is not uncommon in works with fin-stabilized projectiles, as in, for example, [56]. A non-zero angle of yaw generates a positive moment that would act to increase this angle absolute value. In this sense, the tail fins must generate a stabilizing yawing moment that counteracts the first one, so the angle value is reduced. The value of this moment can be calculated by equation (5).

$$N = Q_\infty S d C_N \tag{5}$$

where C_N denotes the yawing moment coefficient.

The pitch damping force acts on the same plane as the pitching velocity q and can be divided in two components: one proportional to q and one proportional to the rate of change of the angle of attack $\dot{\alpha}$. However, $\dot{\alpha}$ can be approximated by q, which allows for the definition of the pitch damping force as

$$PDF = Q_{\infty}S\left(\frac{qd}{V}\right)\left(C_{z_q} + C_{z_{\dot{\alpha}}}\right) \tag{6}$$

In (6) C_{z_q} is the pitch damping force coefficient proportional to q and $C_{z_{\dot{\alpha}}}$ is the pitch damping force coefficient proportional to $\dot{\alpha}$.

The yaw damping force can be defined analogously to the previous force. Similarly, to the yawing moment, sometimes the pitch damping force is defined as the total pitch damping force, considering the total transverse angular velocity q_t, which considers the yawing velocity r. In this work however, the yaw damping force is considered proportional to r and to the rate of change of the angle of sideslip $\dot{\beta}$ by approximating them both as the same value, analogously to the pitch damping force. The yaw damping force equation is therefore defined as

$$YDF = Q_{\infty}S\left(\frac{rd}{V}\right)\left(C_{Y_r} + C_{Y_{\dot{\beta}}}\right) \tag{7}$$

where C_{y_r} is the yaw damping force coefficient proportional to r and $C_{y_{\dot{\beta}}}$ is the yaw damping force coefficient proportional to $\dot{\beta}$.

The pitch damping moment is defined very similarly as the pitch damping force. Two distinct contributions to it can be made, one from q and another from $\dot{\alpha}$. The pitch damping moment is crucial for the dynamic stability of the projectile: if positive, it increases the pitching angular velocity, and is therefore considered destabilizing. Therefore, it must be negative, in order to have a stabilizing effect. The moment is calculated by equation (8).

$$PDM = Q_{\infty}Sd\left(\frac{qd}{V}\right)\left(C_{M_q} + C_{M_{\dot{\alpha}}}\right) \tag{8}$$

with C_{M_q} as the pitch damping moment coefficient proportional to q and $C_{M_{\dot{\alpha}}}$ the pitch damping moment coefficient proportional to $\dot{\alpha}$.

The yaw damping moment is defined in the same manner as the pitch damping moment, similarly to the yaw damping force. A negative value is necessary to retain dynamic stability, acting to decrease the yawing angular velocity. Its respective mathematical definition is as follows:

$$YDM = Q_{\infty}Sd\left(\frac{rd}{V}\right)\left(C_{N_r} + C_{N_{\dot{\beta}}}\right) \tag{9}$$

Here, C_{N_r} is the yaw damping moment coefficient proportional to r and $C_{N_{\dot{\beta}}}$ is the yaw damping moment coefficient proportional to $\dot{\beta}$.

The Coriolis effect (or force) represents the apparent deflection by the projectile as it travels along the rotating Earth. In trajectories with a significant distance, i.e. with ranges above 20km, approximately, the rotation of the Earth, approximately 15 degrees per hour, must be taken into account, otherwise the projectile will land deviated from its target. Since the studied trajectories have a small range, the Coriolis effect is small enough to not be considered [1],[106], [107].

3.2. Equations of motion

Before explaining the mathematical model of the projectile trajectory, it is necessary to define a set of coordinate systems. These are $Oxyz$, the projectile-fixed reference coordinate system; $Ox_ay_az_a$, the air-trajectory reference coordinate system; and $Ox_gy_gz_g$, the Earth-fixed reference coordinate system.

The projectile-fixed system $Oxyz$ relates to the Earth-fixed reference system $Ox_gy_gz_g$ by means of the Euler angles (ϕ, θ, ψ, which are the roll, pitch, and yaw angles, respectively), by the following equation, using a transformation matrix:

$$\begin{bmatrix} x_g \\ y_g \\ z_g \end{bmatrix} = \begin{bmatrix} \cos\theta\cos\psi & \sin\phi\sin\theta\cos\psi - \cos\phi\sin\psi & \cos\phi\sin\theta\cos\psi + \sin\phi\sin\psi \\ \cos\theta\sin\psi & \sin\phi\sin\theta\sin\psi + \cos\phi\cos\psi & \cos\phi\sin\theta\sin\psi + \sin\phi\cos\psi \\ -\sin\theta & \sin\phi\cos\theta & \cos\phi\cos\theta \end{bmatrix} \begin{bmatrix} x \\ y \\ b \end{bmatrix} \tag{10}$$

The projectile-fixed system $Oxyz$ and the air-trajectory system $Ox_ay_az_a$ are related by the angle of attack α and the sideslip angle β as follows:

$$\begin{bmatrix} x_a \\ y_a \\ z_a \end{bmatrix} = \begin{bmatrix} \cos\alpha\cos\beta & \sin\beta & \sin\alpha\cos\beta \\ -\cos\alpha\sin\beta & \cos\beta & -\sin\alpha\sin\beta \\ -\sin\alpha & 0 & \cos\alpha \end{bmatrix} \begin{bmatrix} x \\ y \\ b \end{bmatrix} \tag{11}$$

The relation between the projectile-fixed system and the Earth-fixed one defined in (10) can be visually represented by Figure 1.

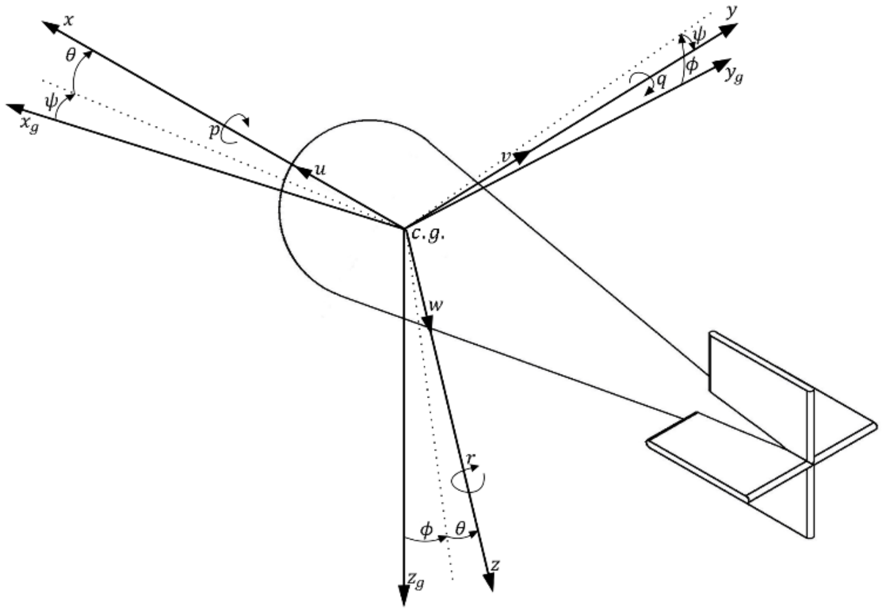

Figure 1 Geometry between $Oxyz$ and $Ox_gy_gz_g$

On the other hand, the relationship in (11) can be visually represented by Figure 2.

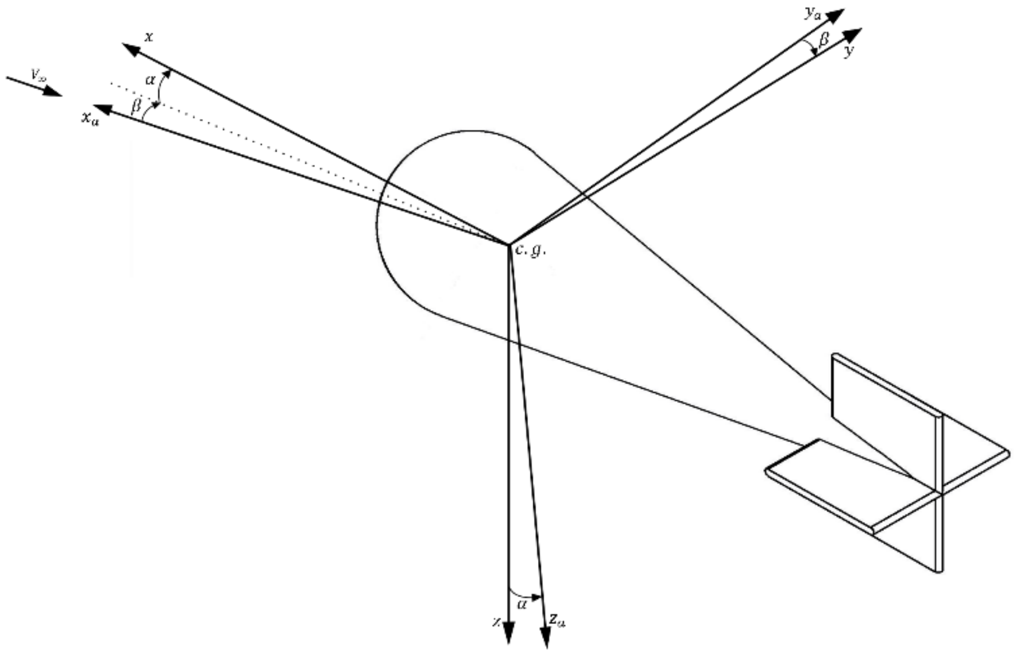

Figure 2 Geometry between $Ox_by_bz_b$ *and* $Ox_ay_az_a$

In order to construct this 6-DOF model, a number of assumptions have been made:

1. The projectile is considered a rigid body, with a constant mass, moment of inertia, and position of center of mass;
2. The projectile has two planes of symmetry, xy and xz, and the stabilizing surfaces are all equal, fixed, arranged symmetrically in a cross. This means the products of inertia I_{xy}, I_{yx}, I_{yz}, I_{zy}, I_{xz} and I_{zx} are equal to zero and that $I_y = I_z$;
3. The Earth is considered flat and non-rotating, with a constant gravity acceleration, and the azimuth angle during the trajectory remains constant.

Newton's second law of motion states "The sum of all external forces and moments acting on a body must equal the time rate of change of its momentum and angular momentum respectively". This is expressed mathematically by:

$$\sum \vec{F} = \frac{d(m\vec{V})}{dt} \tag{12}$$

$$\sum \vec{M} = \frac{d(\vec{H})}{dt} = \frac{d(I\vec{\omega})}{dt} \tag{13}$$

where $\vec{V} = [u \quad v \quad w]^T$, I is the inertia tensor and $\vec{\omega} = [p \quad q \quad r]^T$. Moreover, $\vec{F}$ and $\vec{M}$ can be defined by their components in the projectile-fixed coordinate system, i.e. $\vec{F} = [X \quad Y \quad Z]^T$ and $\vec{M} = [L \quad M \quad N]^T$. Equation (12) can be rewritten as

$$\frac{d(m\vec{V})}{dt} = \frac{\partial(m\vec{V})}{\partial t} + \vec{\omega} \times \left(m\vec{V}\right) \tag{14}$$

Since mass is assumed constant, (14) yields:

$$\frac{\partial(m\vec{V})}{\partial t} + \vec{\omega} \times \left(m\vec{V}\right) = m\left(\frac{\partial\vec{V}}{\partial t} + \vec{\omega} \times \vec{V}\right) \tag{15}$$

In turn, (15) results in

$$\begin{bmatrix} X \\ Y \\ Z \end{bmatrix} = \begin{bmatrix} m(\dot{u} + qw - rv) \\ m(\dot{v} + ru - pw) \\ m(\dot{w} + pv - qu) \end{bmatrix} \tag{16}$$

An analogous analysis can be made to (13). That equation can be written as follows:

$$\frac{d(\vec{H})}{dt} = \frac{\partial\vec{H}}{\partial t} + \vec{\omega} \times \vec{H} \tag{17}$$

Since the moments and products of inertia are considered constant, the partial derivative with respect to time in equation (17) can be rewritten as

$$\frac{\partial\vec{H}}{\partial t} = \frac{\partial(I\vec{\omega})}{\partial t} = I\frac{\partial\vec{\omega}}{\partial t} \tag{18}$$

The inertia tensor I is defined as

$$I = \begin{bmatrix} I_x & -I_{xy} & -I_{xz} \\ -I_{yx} & I_y & -I_{yz} \\ -I_{zx} & -I_{zy} & I_z \end{bmatrix} \tag{19}$$

Using (19), equation (18) can be transformed, obtaining the following system:

$$\begin{bmatrix} L \\ M \\ N \end{bmatrix} = \begin{bmatrix} I_x\dot{p} - I_{yz}(q^2 - r^2) - I_{zx}(\dot{r} + pq) - I_{xy}(\dot{q} - rp) - \left(I_y - I_z\right)qr \\ I_y\dot{q} - I_{zx}(r^2 - p^2) - I_{xy}(\dot{p} + qr) - I_{yz}(\dot{r} - pq) - (I_z - I_x)rp \\ I_z\dot{r} - I_{xy}(p^2 - q^2) - I_{yz}(\dot{q} + rp) - I_{zx}(\dot{p} - qr) - \left(I_x - I_y\right)pq \end{bmatrix} \tag{20}$$

Additionally, the rates of change of the Euler angles have a direct relationship with the angular velocities of the projectile, like so:

$$\begin{bmatrix} \dot{\phi} \\ \dot{\theta} \\ \dot{\psi} \end{bmatrix} = \begin{bmatrix} 1 & \sin\phi\tan\theta & \cos\phi\tan\theta \\ 0 & \cos\phi & -\sin\phi \\ 0 & \sin\phi\,/\cos\theta & \cos\phi\,/\cos\theta \end{bmatrix} \begin{bmatrix} p \\ q \\ r \end{bmatrix} = \begin{bmatrix} p + (r\cos\phi + q\sin\phi)\tan\theta \\ q\cos\phi - r\sin\phi \\ \frac{1}{\cos\theta}(r\cos\phi + q\sin\phi) \end{bmatrix} \tag{21}$$

Finally, it is necessary to define the position with respect to inertial axes, i.e., the Earth-referenced coordinate system, in order to fully describe the projectile's trajectory. In this sense, the projectile velocity is converted to a position rate in the inertial coordinate system, using the transformation matrix in (10), which returns

$$\begin{bmatrix} \dot{x}_g \\ \dot{y}_g \\ \dot{z}_g \end{bmatrix} = \begin{bmatrix} u\cos\theta\cos\psi + v(\sin\phi\sin\theta\cos\psi - \cos\phi\sin\psi) + w(\cos\phi\sin\theta\cos\psi + \sin\phi\sin\psi) \\ u\cos\theta\sin\psi + v(\sin\phi\sin\theta\sin\psi + \cos\phi\cos\psi) + w(\cos\phi\sin\theta\sin\psi + \sin\phi\cos\psi) \\ -u\sin\theta + v\sin\phi\cos\theta + w\cos\phi\cos\theta \end{bmatrix} \tag{22}$$

Equations (16), (20), (21) and (22) can describe the 6-DOF trajectory of any projectile. They will now be arranged, based on the assumptions made explicit earlier, as well as the moments and forces acting on the projectile, that have been established in Section 3.1, and considerations based on the present project.

Starting from (16), $[X \quad Y \quad Z]^T$ can be substituted by the considered forces on the projectile. These are drag, lift and gravity, as well as the damping forces, defined in the previous section. In this model, lift and drag are substituted by axial, normal and side forces, in order to work with the projectile-fixed coordinate system instead of the air-trajectory one. This is done by the following equations:

$$\begin{bmatrix} C_X \\ C_Y \\ C_Z \end{bmatrix} = \begin{bmatrix} C_D \cos\alpha - C_L \sin\alpha \\ C_D \sin\beta + C_L \cos\beta \\ C_D \sin\alpha + C_L \cos\alpha \end{bmatrix} \tag{23}$$

Accordingly, these forces are calculated as follows:

$$\begin{bmatrix} F_X \\ F_Y \\ F_Z \end{bmatrix} = \begin{bmatrix} Q_\infty S C_X \\ Q_\infty S\left(C_Y + \left(C_{Y_r} + C_{Y_{\dot\beta}}\right)\frac{rd}{V}\right) \\ Q_\infty S\left(C_Z + \left(C_{Z_q} + C_{Z_{\dot\alpha}}\right)\frac{qd}{V}\right) \end{bmatrix} \tag{24}$$

The gravity force can be decomposed in its components in the body frame:

$$\begin{bmatrix} W_X \\ W_Y \\ W_Z \end{bmatrix} = mg \begin{bmatrix} -\sin\theta \\ \sin\phi\cos\theta \\ \cos\phi\cos\theta \end{bmatrix} \tag{25}$$

Consequently, by (24) and (25), equation (16) can be arranged to obtain

$$\begin{bmatrix} \dot u \\ \dot v \\ \dot w \end{bmatrix} = \begin{bmatrix} \frac{-mg\sin\theta + Q_\infty S C_X}{m} + rv - qw \\ \frac{mg\sin\phi\cos\theta + Q_\infty S\left(C_Y + \left(C_{Y_r} + C_{Y_{\dot\beta}}\right)\frac{rd}{V}\right)}{m} + pw - ru \\ \frac{mg\cos\phi\cos\theta + Q_\infty S\left(C_Z + \left(C_{Z_q} + C_{Z_{\dot\alpha}}\right)\frac{qd}{V}\right)}{m} + qu - pv \end{bmatrix} \tag{26}$$

After this, (20) will be simplified. By the assumptions made in the beginning, all products of inertia are zero and $I_y = I_z$. Inputting the considered moments that act on the projectile, (20) yields:

$$\begin{bmatrix} 0 \\ Q_\infty S d\left(C_M + \left(C_{M_q} + C_{M_{\dot\alpha}}\right)\frac{qd}{V}\right) \\ Q_\infty S d\left(C_N + \left(C_{N_r} + C_{N_{\dot\beta}}\right)\frac{rd}{V}\right) \end{bmatrix} = \begin{bmatrix} I_x \dot p \\ I_y \dot q - (I_z - I_x) rp \\ I_z \dot r - (I_x - I_y) pq \end{bmatrix} \tag{27}$$

(27) can then be arranged to obtain

$$\begin{bmatrix} \dot p \\ \dot q \\ \dot r \end{bmatrix} = \begin{bmatrix} 0 \\ \frac{1}{I_y}\left(Q_\infty S d\left(C_M + \left(C_{M_q} + C_{M_{\dot\alpha}}\right)\frac{qd}{V}\right) + (I_z - I_x) rp\right) \\ \frac{1}{I_z}\left(Q_\infty S d\left(C_N + \left(C_{N_r} + C_{N_{\dot\beta}}\right)\frac{rd}{V}\right) + (I_x - I_y) pq\right) \end{bmatrix} \tag{28}$$

The developed model can be implemented as it is, but a final set of simplifications can be made. Since the projectile is fin-stabilized and no rotation caused by the wind is considered, p can be initially set to zero. Both these considerations are substantiated in Chapter 5 and Section 3.3, respectively. Additionally, as no moment acts on the roll axis, $\dot{p}$ is always zero, and therefore it can be assumed that p is also always zero. Consequently, ϕ is zero throughout the flight. Therefore, (21), (22), (26), and (28) can be rewritten, obtaining the defining equations of the implemented 6-DOF mathematical model:

$$\begin{bmatrix} \dot{\phi} \\ \dot{\theta} \\ \dot{\psi} \end{bmatrix} = \begin{bmatrix} r \tan\theta \\ q \\ \frac{r}{\cos\theta} \end{bmatrix} \tag{29}$$

$$\begin{bmatrix} \dot{x}_g \\ \dot{y}_g \\ \dot{z}_g \end{bmatrix} = \begin{bmatrix} u\cos\theta\cos\psi - v\sin\psi + w\sin\theta\cos\psi \\ u\cos\theta\sin\psi + v\cos\psi + w\sin\theta\sin\psi \\ -u\sin\theta + w\cos\theta \end{bmatrix} \tag{30}$$

$$\begin{bmatrix} \dot{u} \\ \dot{v} \\ \dot{w} \end{bmatrix} = \begin{bmatrix} \frac{-mg\sin\theta + Q_\infty S C_X}{m} + rv - qw \\ \frac{mg\sin\phi\cos\theta + Q_\infty S\left(C_Y + \left(C_{Y_r} + C_{Y_{\dot{\beta}}}\right)\frac{rd}{V}\right)}{m} - ru \\ \frac{mg\cos\phi\cos\theta + Q_\infty S\left(C_Z + \left(C_{Z_q} + C_{Z_{\dot{\alpha}}}\right)\frac{qd}{V}\right)}{m} + qu \end{bmatrix} \tag{31}$$

$$\begin{bmatrix} \dot{p} \\ \dot{q} \\ \dot{r} \end{bmatrix} = \begin{bmatrix} 0 \\ \frac{1}{I_y} Q_\infty S d\left(C_M + \left(C_{M_q} + C_{M_{\dot{\alpha}}}\right)\frac{qd}{V}\right) \\ \frac{1}{I_z} Q_\infty S d\left(C_N + \left(C_{N_r} + C_{N_{\dot{\beta}}}\right)\frac{rd}{V}\right) \end{bmatrix} \tag{32}$$

3.3. Numerical solutions to the equations of motion

In order to solve the aforementioned differential equations, the numerical integration method Runge-Kutta of 4th order is used, since this family of iterative methods offers efficient results, in terms of accuracy and computational time, and is considered a good method to implement for exterior ballistic studies [35]. The 4th order Runge-Kutta method is an extension of Euler's forward method, using a weighted average of four points, in order to increase its accuracy. The method can be expressed as:

$$\dot{y} = f(t, y) \tag{33}$$

$$y_{n+1} = y_n + \frac{1}{6}h(k_1 + 2k_2 + 2k_3 + k_4) \tag{34}$$

$$k_1 = f(t_n, y_n) \tag{35}$$

$$k_2 = f\left(t_n + \frac{1}{2}h, y_n + \frac{1}{2}hk_1\right) \tag{36}$$

$$k_3 = f\left(t_n + \frac{1}{2}h, y_n + \frac{1}{2}hk_2\right) \tag{37}$$

$$k_4 = f(t_n + h, y_n + hk_3) \tag{38}$$

Besides its accuracy, the method is well-suited for its ability to self-start, since y_{n+1} is obtained only through y_n, when integrating forward in time. In this model, the total accumulated error is the order of $O(h^4)$ and the local truncation one is in the order of $O(h^5)$ [50].

3.4. Wind

In order to understand the influence of various parameters on the projectile's trajectory and consequently on its precision, the influence of wind is considered.

Wind is described in [108] as "a continuous vector random process that varies in three space dimensions and also in time" and, according to [109], it can be divided in two parts: the large-scale horizontal winds, with a certain direction and mean magnitude, and the localized turbulence. This wind turbulence has inherent stochastic behavior, which is caused by pressure instabilities and variations of temperature, which change in space and time [109]. Thus, a mathematical model which encompasses all known atmospheric phenomena and characteristics would be very complex. Therefore, a few simplifications and assumptions are made about the statistical properties of the turbulence [54], [108], [109]: these properties are stationary and independent of time, so "time variations are statistically equivalent to distance variations in traversing the turbulence field" ; and these properties are horizontally homogeneous. Comparing the characteristic dimensions of wind gusts and the dimension of the projectiles in study, a uniform effect in the objects can be assumed, and no rotations caused by them is considered. Thus, only the translational speed variations are taken into consideration, which in turn affect the angle of attack and sideslip of the projectile [54].

Throughout the years, several methods to simulate the stochastic nature of atmospheric turbulence have been developed, such as the Shinozuka method [110], the von Kárman Continuous model [111], and the Dryden Continuous model [112], the last two being the most commonly used [109].

The horizontal mean wind speed and direction can be obtained through weather databases or weather forecasts. MATLAB's Simulink [113] is used to obtain the wind turbulence, by using the Dryden Continuous Wind Model for a series of speeds, and the values are interpolated for the current projectile speed. In this model, as well as some others, a band-limited white noise signal is passed through a forming filter derived from the turbulence spectra representation. The model's defining expressions can be found in detail in [114], along with their respective original references, which are military handbooks.

With this, a slight modification is needed in the trajectory model, in order to account for the mean wind and wind turbulence. Considering that the obtained wind turbulence velocity components are in the projectile body-fixed system [108], equations (29) and (30) are now substituted by the equations (39) and (40), respectively:

$$\begin{bmatrix} \dot{x_g} \\ \dot{y_g} \\ \dot{z_g} \end{bmatrix} = \begin{bmatrix} (u + u_{WT}) \cos\theta \cos\psi - (v + v_{WT}) \sin\psi + (w + w_{WT}) \sin\theta \cos\psi - MW_{velocity} \times \cos\ MW_{direction} \\ (u + u_{WT}) \cos\theta \sin\psi + (v + v_{WT}) \cos\psi + (w + w_{WT}) \sin\psi \sin\psi - MW_{velocity} \times \sin\ MW_{direction} \\ -(u + u_{WT}) \sin\theta + (w + w_{WT}) \cos\theta \end{bmatrix} \tag{39}$$

$$\begin{bmatrix} \dot{u} \\ \dot{v} \\ \dot{w} \end{bmatrix} = \begin{bmatrix} \frac{-mg\sin\theta + Q_\infty S C_X}{m} + r(v + v_{WT}) - q(w + w_{WT}) \\ \frac{mg\sin\phi\cos\theta + Q_\infty S\left(C_Y + \left(C_{Y_r} + C_{Y_{\dot{\beta}}}\right)\frac{rd}{V}\right)}{m} - r(u + u_{WT}) \\ \frac{mg\cos\phi\cos\theta + Q_\infty S\left(C_Z + \left(C_{z_q} + C_{z_{\dot{\alpha}}}\right)\frac{qd}{V}\right)}{m} + q(u + u_{WT}) \end{bmatrix} \tag{40}$$

where the subscript TW is related to the wind turbulence, $MW_{velocity}$ is the mean wind velocity, and $MW_{direction}$ is the mean wind direction.

4. Projectile aerodynamic coefficients

In this dissertation, the static aerodynamic coefficients are obtained through CFD analyses and the dynamic derivative coefficients are estimated using the analytical methods present in [115]. These methods were chosen taking into consideration the available resources, including time available, and the current early stage of the project.

The axial force coefficient C_X and the normal force coefficient C_Z are calculated based on the drag coefficient C_D and lift coefficient $\mathrm{C_L}$ as shown in , which is obtained with the software *ANSYS Fluent* [116], along with the pitching moment coefficient C_M. Since the projectile has both xy and xz as planes of symmetry, the existence of aerodynamic symmetry between these planes can be considered. Therefore, the side force C_Y derivative with respect to the angle of sideslip β is considered equal to the C_Z derivative with respect to the angle of attack α, and the yawing moment C_N derivative with respect to β is considered equal to the C_M derivative with respect to α. It is important to refer, again, that this definition is not unheard of (for example, [56], takes this approach), and it is valid for the cases in study since there is not a considerable β in the launching cases of study. If that would be the case, C_X, C_Y, C_Z and the moment derivatives would have to be considered as a function of both α and β. The same approach is used for the dynamic derivatives, so $\left(C_{Y_r} + C_{Y_{\dot{\beta}}}\right)$ is considered equal to $\left(C_{Z_q} + C_{Z_{\dot{\alpha}}}\right)$ and $\left(C_{N_r} + C_{N_{\dot{\beta}}}\right)$ is considered equal to $\left(C_{M_q} + C_{M_{\dot{\alpha}}}\right)$.

The next sections describe the methods used to obtain the mentioned coefficients.

4.1. Static aerodynamic coefficients – CFD methodology

The work carried out utilizes the CFD software package *ANSYS Fluent*. The used method works by solving the governing integral equations of conservation of momentum, mass, energy, turbulence, and other fluid variables using a finite volume discretization process to solve the Reynolds-averaged Navier-Stokes equations [117].

Before the numerical analysis itself, some tasks must be carried out. Firstly, the geometry of the object in study is defined, as well the surrounding fluid domain. Secondly, the domain is discretized in thousands of discrete control volumes called cells, which is done using a preprocessor included in Fluent called Gambit. This process is called meshing, and the quality of the mesh produced is critical for accurate results [57], [62]. The boundary conditions are defined, the method for Pressure-Velocity Coupling is chosen, and the turbulence model is defined, which is needed to simulate the small scale and high frequency fluctuations of a turbulent flow [118].

In this dissertation, the geometry definition is accomplished using the computer aided design software *CATIA*, from the company Dassault Systèmes [119]. The domain is radially extended 10 projectile lengths in front of the body and 20 projectile lengths downstream of the body. The fluid domain has a finer mesh subdivision, in order to more accurately resolve the wake behind the projectile and to guarantee the correct orientation of the streamlines in front of the projectile. This subdivision is radially extended 1,5 body lengths in front of the projectile and 3 lengths aft of the body. An unstructured mainly tetrahedral mesh is used, since it is appropriate for different complex configurations, allowing for a consistent meshing methodology.

A velocity inlet boundary condition was considered for the upstream boundary and a pressure outlet for the downstream boundary. Both were set with the atmospheric conditions at sea level, according to the International Standard Atmosphere [120]. Regarding the projectile wall, an adiabatic no slip boundary was defined. No compressibility effects were taken into consideration, since the Mach number during CFD simulations is around 0.04. Figure 3 presents the representation of the CFD domain, and Figure 4 presents the CFD mesh.

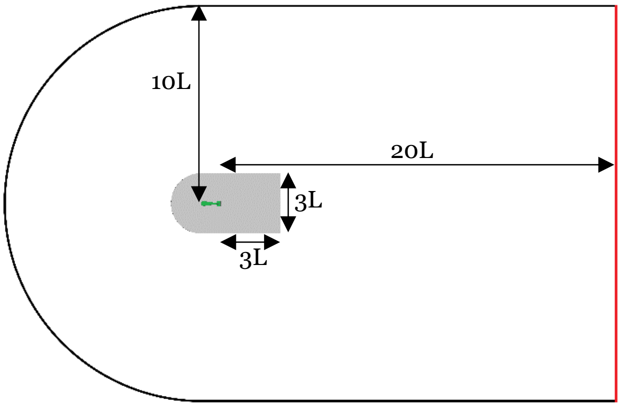

Figure 3 CFD Domain. The projectile's adiabatic no slip wall is in green, the pressure outlet in red, and the velocity inlet in black. The area in grey is the finer subdivision of the mesh. The dimensions are all in relation to the projectile's length, L.

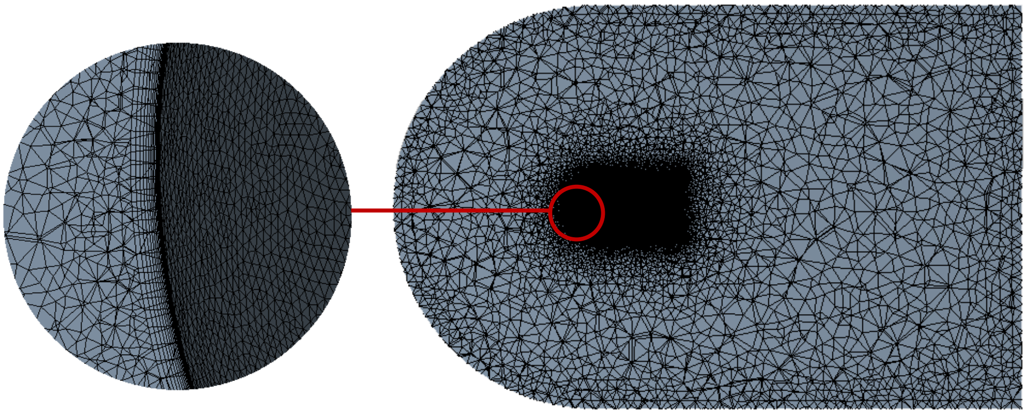

Figure 4 CFD mesh. The unstructured mesh can be observed throughout the domain, and the detail portrays the correct definition of the projectile shape and the Inflation layers in the Boundary layer region.

The model used is the k-ω SST [124], which is a two-equation eddy-viscosity model. This model was chosen for its large use in aeronautics, and because it is considered a good model for flows withstanding separation, which might be a relevant aspect in some of the flow around the proposed configurations, analyzed in the following chapter [121], [122]. The model blends the k-ε behavior in the free-stream with the k-ω formulation in the near-wall region, eliminating the sensitivity problems associated with the sensitivity of the ω-equation to the inlet free stream turbulence properties. Since the model solves the flow up to the viscous sub-layer every mesh is ensured to have a $y^+ \leq 1$ in order to properly resolve the boundary layer, while keeping the minimum orthogonal quality above 0.01 ensures better results [60], [62], [122]-[124]. As for the coupling between the pressure and velocity fields, the Coupled scheme was selected.

The resulting aerodynamic static coefficients will be linearly interpolated during the trajectory prediction.

4.2. Dynamic aerodynamic coefficients

Etkin [115] presents a quite accurate way to calculate the dynamic derivative coefficients based on analytical expressions, which is the method used in this work to do so. The dynamic coefficients that are obtained can be divided into two groups, q derivatives and $\dot{\alpha}$ derivatives. The first ones arise from the aerodynamic effects on the tail when the projectile rotates around its y axis, while the angle of attack remains zero. The latter ones emerge from the delayed adjustment of the pressure distribution on the tail after a quick change in angle of attack.

It is relevant to mention that some authors commonly estimate the pitch moment damping coefficient sum $\left(C_{M_q} + C_{M_{\dot{\alpha}}}\right)$ instead of the individual coefficients. A great number of methods can be used to estimate the pitch damping coefficient sum, either by use of CFD methodologies, slender-body theory or modifications to it, or other simpler methods. The CFD methodologies use unsteady flow techniques, such as the time accurate planar pitching technique [125]-[127]. [125-129] enumerate some of these methods and outline some works about this subject.

Etkin defines $C_{z_{\dot{\alpha}}}$ and $C_{M_{\dot{\alpha}}}$ based on the lag of the downwash present on the tail, which is primarily caused by the trailing vortices of a wing. Since the projectile does not have wing, $C_{z_{\dot{\alpha}}}$ and $C_{M_{\dot{\alpha}}}$ are considered both zero. However, the values for the coefficients are not really zero even if the projectile does not have wings, and this consideration might give rise to some prediction errors in relation to the stability and attitude of the configurations. It is still considered a suitable approximation for this primary stage of the project, and it is in line with many other works that only consider the q derivatives [130].

A positive q acts to increase the angle of attack on the tail by $\frac{ql_t}{V}$ radians, where l_t is the distance between the projectile's center of gravity and the tail aerodynamic center. The location of the aerodynamic center is obtained through the open-source software *XFLR5* [131], while the center of gravity is obtained through *CATIA*. The change in the tail lift coefficient is therefore

$$\Delta C_{L_{tail}} = a_t \Delta\alpha_t = a_t \frac{ql_t}{V} \tag{41}$$

where a_t is the slope of the curve $C_L(\alpha)$ of the tail, which is also be obtained through *XFLR5*. The change in the total lift coefficient of the projectile can be obtained by

$$\Delta C_L = \frac{S_{tail}}{S} \Delta C_{L_{tail}} = \frac{S_{tail}}{S} a_t \frac{ql_t}{V} \tag{42}$$

In (42), S_{tail} is the reference area of the horizontal tail, projected on the xz plane, while S is the reference area, which in this work is the projectile frontal area. From (39), it can be obtained

$$\frac{\partial C_L}{\partial q} = a_t \frac{S_{tail} l_t}{SV} \tag{43}$$

Finally, C_{z_q} can be obtained:

$$C_{z_q} = -\frac{2V}{d}\frac{\partial C_L}{\partial q} = -\frac{2V}{d} a_t \frac{S_{tail} l_t}{SV} = -2a_t V_H \tag{44}$$

in which d is the diameter of the frontal area, and V_H is defined as the horizontal tail volume coefficient, which is $\frac{S_{tail} l_t}{Sd}$.

As for C_{M_q}, the increment ΔC_M caused by $\Delta C_{L_{tail}}$ can be calculated by

$$\Delta C_M = -\mathrm{V_H} \Delta C_{L_{tail}} \tag{45}$$

and so, analogously to (44), C_{M_q} can be obtained by the following:

$$\frac{\partial \Delta C_M}{\partial q} = -a_t V_H \frac{l_t}{V} \tag{46}$$

$$C_{M_q} = -\frac{2V}{d}\frac{\partial \Delta C_M}{\partial q} = -2a_t \frac{l_t}{d} V_H \tag{47}$$

5. Projectile design

In this chapter the concepts supporting the design and development choices of the projectile are presented. Firstly, the requirements for the projectile and mission are laid out. Secondly, the preliminary design choices are presented. Finally, the configurations proposed to be studied in this dissertation are presented.

5.1. Projectile and mission requirements

Before analyzing all the design choices, as well as their theorical and practical justifications, it is important to define the projectile and mission requirements. The trajectory cases are defined in Section 6.7, which can give some further insight to the choices made in the projectile design phase.

One of the requirements of the projectile is that during the phase of transportation of the mission the additional drag must be low. Since the implementation of this mission should not require modifications to the UAV that will transport the projectile, it will most likely be transported outside the UAV. Therefore, to guarantee a low impact on the UAV's performance - e.g. high increase in energy consumption or considerable reduction in the maximum velocity - either the projectile will need a low drag configuration, or a configuration able to be covered by a drag reduction fairing.

Another evident requirement is the precision of the projectile. This objective is fundamental to all projectile missions, but with the inherent emergency of a firefighting mission and the functioning of the fire extinguishing component of the projectile, this objective becomes even more critical. The importance of precision is evidenced in the way the FEB works: a great offset from the fire source prevents the fuse from being ignited and, therefore, does not spread the fire-extinguishing agent, and the objective is not met.

A further requirement is to obtain a quick Minimum Viable Product. The project is a proposition from *SpaceWay*, and the company requires a viable product as quickly as possible, facing the emergent situation of increased wildfires. Thus, some decisions were made having this in consideration.

5.1.1. Stability

It is crucial for every projectile configuration to have good characteristics of both static and dynamic stability. Static stability is related to the pitching and yawing moments, while the dynamic stability is related to the pitch damping and yaw damping moments. As stated in Chapter 3.1, in order to achieve static stability, a positive angle of attack must correlate to a negative pitch moment (and analogously, a positive angle of yaw must correlate to a negative yaw moment). It is also important that in the trajectory the projectiles do not face high angles of attack since high angles of attack in bodies of revolution can give rise to asymmetrical vortices with irregular shedding, which result in irregular, difficult to predict side forces[132], [133]. Regarding dynamic stability, a positive angle of attack needs to be corresponded by a negative pitch damping moment, and a positive angle of yaw to a negative yaw damping moment. Dynamic stability is also important to guarantee that a continuously oscillatory motion is not present, and the angle of attack always reduces to zero, in a damped manner [35], [134].

5.2. Preliminary design choices

There are various ways to control a projectile, and their respective use depends on several factors, the most important ones being the distance the projectile needs to cover, the type of target or mission, and the means of launch [135]. Different stability control systems involve different costs of production and time, as well as different research and study requirements. In this project, the projectiles may not be retrievable, and therefore the use of an active control system would increase the general cost of the projectile production. Therefore, the choice was to implement an unguided projectile configuration. In this type of configuration, stability is achieved by two ways: imposed rotation around the symmetry axis of the projectile, or by using tail fins [1]. The tail fins were chosen since the method of launching would be simpler, at first analysis.

This irretrievability also influences the choice of materials for the tail and fins, which consequently gravitate towards low price and environmentally safe. Some good contenders, depending on the configuration geometry, are some type of biodegradable wood derivative -like cardboard or paper-, bamboo hardwood or other cheap wood, and cork.

5.2.1. Projectile length

Various geometrical dimensions of the configurations were chosen before defining the possible projectile configurations. The first aspect to be determined was the length of the projectile. The length/diameter ratio l/d, also called fineness ratio, was set at 4, by comparing its value from some fin-stabilized free-flight projectiles [136], [137].

5.2.2. Fins dimensions and airfoil

The area of the fins was chosen similarly to the projectile length, taking into account the value for some projectiles [136], [137]. When nondimensionalized by d^2, the value of the total area chosen for the fins was 0.4. This area does not take into consideration the tail, so the area exposed to the airflow is slightly different for each projectile. With the area defined, the chord and span for the fins was to be determined. The span was set at the value of the FEB radius (which is the projectile's maximum radius, as presented in the next section), $\frac{1}{2}d$, 0.055 m. Therefore, from the area value and this value, it comes that the fin span would be $\frac{4}{5}d$, 0.088 m.

For the fin airfoil, the most important consideration was that it should be a developable surface, that is, it can be constructed by "bending a planar surface, without requiring extensional deformations" [138]. This is important to maintain a simple construction and also allows the use of paper or cardboard for their materials, which are both cheap, recyclable, and somewhat biodegradable. Influenced by the fins in the non-lethal 12-gauge fin-stabilized projectile studied by [134], the designed airfoil shape is presented in Figure5. The respective x/c and y/c coordinates are presented in Annex 1.

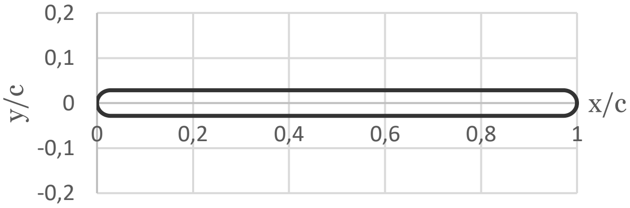

Figure 5 Nondimensionalized airfoil shape for the fins

5.3. Proposed configurations

The four possible configurations for the projectile are presented in this section. The first proposed configuration is a sphere, as in considering no modification to the fire-extinguishing ball. The other three configurations use fins as a stabilizing method, differing on the aft body: one being a tubular boom, the other a tangential cone to the sphere, and the last one made by revolving a symmetrical NACA airfoil. It is relevant to mention that the research made in this work did not find studies regarding the flow around bodies like the 2nd, 3rd and 4th configurations. Therefore, their aerodynamic characteristics are evaluated by CFD analysis, which can be a valuable addition to the State of Art in flow around bodies of revolution. The three-view drawings of Configuration 2, Configuration 3, and Configuration 4 are presented in Annex 2, Annex 3 and Annex 4, respectively.

5.3.1. Configuration 1 – Sphere

The simplest implementation of the projectile would be to not make any modification to the FEB, and simply launching it as it is. The exterior ballistics performance of this configuration will be evaluated resorting to the various studies carried out throughout the years, done by a great number of authors, consisting of CFD analysis, wind-tunnel testing and even free-flight testing. Some of these studies, and references containing these studies are [59], [118], [139]-[147]. The analysis of these studies, and the conclusion which follows it is laid out in the next chapter, although some possible problems are possible to predict, like the influence of the Magnus effect on the trajectory, asymmetric flow separation on the sphere or a bad landing performance.

Figure 6 AFO fire-extinguishing ball.

5.3.2. Configuration 2 – Sphere, tubular boom, and fins

One of the other possible configurations according to the requirements and preliminary design choices is to attach a tubular boom to the aft part of the sphere, with the fins located at the other end of it.

This way the possible problems with landing performance and the Magnus effect from the 1st configuration can be minimized or even eliminated. A considerable amount of pressure drag is predicted, originating from the large wake behind the sphere. Comparing to just the sphere, however, the boom located in the rearward may act in the same way a sting can cause air tunnel results to obtain a reduction in drag, by incrementing the shape's fineness ratio [59]. Either way, if necessary, a fairing can accommodate this configuration in the transport phase, reducing the possible considerable drag.

The implementation of this configuration can be simple, since it only uses developable surfaces. Again, this indicates they can be constructed out of paper or cardboard while retaining simplicity in its fabrication.

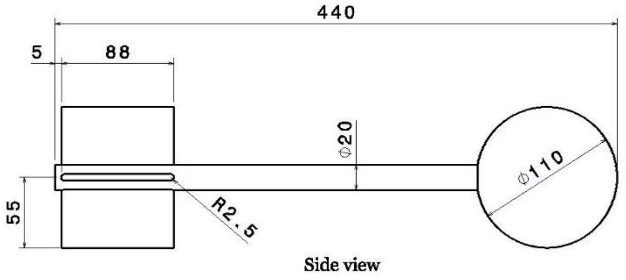

Figure 7 Configuration 2 side view, dimensions in mm

5.3.3. Configuration 3 – Sphere, tangential cone, and fins

This configuration is a really simple way to streamline the fire-extinguishing sphere, considerably reducing the separation that occurs in the aft part of the sphere. The lengthened afterbody maintains the flow attached to the surface for longer, reducing the pressure drag, while probably increasing the skin friction drag [59]. This might be good for the transportation-phase and can even mitigate the need for a fairing.

Its construction is still be simple, since the tail can be made with just developable surfaces, as the previous configuration, and so its manufacturing might be achieved with paper or cardboard, as stated before.

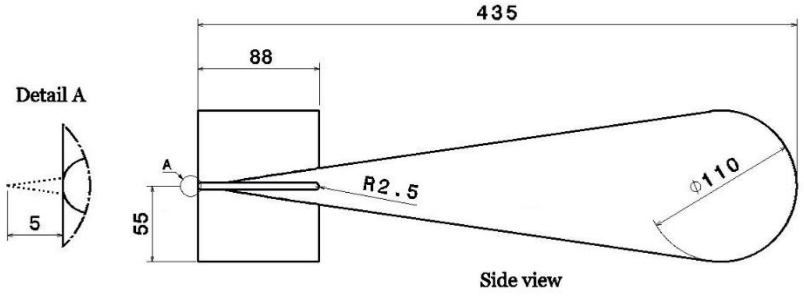

Figure 8 Configuration 3 side view, dimensions in mm

It is important to notice that the actual full length of this configuration 435 mm since the last 5 mm of the cone are cut (as can be seen in detail A of the drawing), so the actual l/d of this configuration is, approximately, 3.954 and not 4. This has two justifications: firstly, this would be hard to construct in certain materials, because of the sharp vertex, and the replicability of the configuration is of great importance; secondly, this very small section is of complex representation in the CFD mesh, and it might have created calculations problems. This is not considered a problem in the comparison of the configurations, but it is appropriate to refer.

5.3.4. Configuration 4 – Sphere, NACA tail, and fins

A streamlined afterbody with an intrinsically curved surface is also proposed to be studied. For this work, it was decided to rotate a symmetrical NACA 0020 airfoil around its chord line, and cutting the leading edge at the maximum thickness, accommodating the sphere in front. The idea behind this configuration design is basically the same as in the sphere-cone configuration, i.e., a reduction in pressure drag by the lengthening the afterbody, but it would be interesting to understand if significant difference between these two configurations arise at the tested Reynolds number.

The construction of this configuration might be more complex, and probably difficult to guarantee its construction in biodegradable materials, because of the double curvature of the tail. Some possible materials for the tail could be cork, wood, or even PLA, allowing for the use of 3D printing technology.

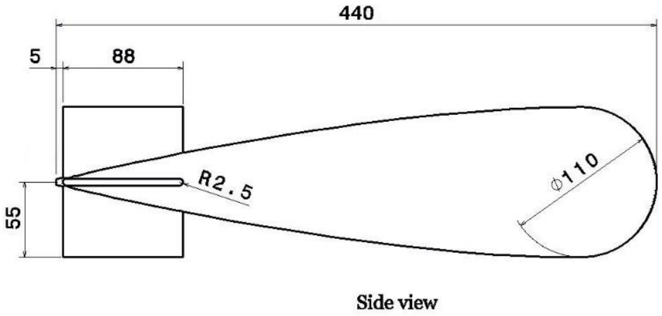

Figure 9 Configuration 4 side view, dimensions in mm

6. Results and discussion

In this chapter, the various results for this dissertation are presented. Firstly, the theoretical analysis for configuration 1 is carried out. After this, some experimental validation to the methods applied are carried out, including a trajectory model validation, a CFD methodology validation, and a grid independence study. Subsequently, the aerodynamic results for configurations 2, 3, and 4 are given, followed by their dynamic coefficients results. Finally, the results for the trajectories are worked out and discussed.

6.1. Analysis of configuration 1

As mentioned in Subsection 5.3.1, the analysis of this configuration is done in a theoretical sense. Since the flow around spheres is a widely studied phenomenon, many papers and studies can be used to analyze the possible performance of launching the FEB by itself.

The flow around the sphere, the resulting wake, and their characteristics are somewhat complex and very unstable [147]. For the case in study, there is no interest in characterizing the flow at very low Reynolds numbers, since it would translate, in this case, to very small speeds. In fact, as it is appointed in Section 6.6, the launching velocity of the simulations is between 10 m/s and 20 m/s, which, considering air properties at sea level and the FEB diameter as the reference length, corresponds to a Reynolds number range between 0.75×10^5 and 1.5×10^5.

Thus, according to Achenbach [144], starting from Reynolds numbers in the order of 10^4 it is possible to divide the flow regime around a sphere in four characteristic regimes. A first one, denominated subcritical regime, in which there is an almost independency between the drag coefficient and Reynolds number, thus the drag coefficient in this regime is considered constant. This value can vary from author to author or in between studies, but it is generally considered to be 0.5 [118]. The second phase is called critical regime, and it is characterized by a brisk decrease on the drag coefficient. This phenomenon, also called drag crisis, was first recognized by Eiffel and Prandtl [59], and it is due to boundary layer transition from laminar to turbulent. Since a turbulent boundary layer has more kinetic energy than a laminar one, it endures the positive pressure gradient along the rearward surface of the sphere more effectively. This makes it remain attached further rearward, narrowing the wake and reducing the pressure drag [35], [59], and consequently the drag coefficient reaches a minimum of 0.08 at the critical Reynolds number $Re=3.8\times 10^5$ [144], [145]. After this, the supercritical regime is entered, where an increase in Re number is met with an increase in C_D, while the point of flow separation remains constant. By further increasing the Re number, the transcritical regime is reached, and here C_D also increases with Re number, while the transition point shifts upstream [144], [145].

As explained, the flow around a sphere is unstable and difficult to predict, while also being affected by the inherent unpredictability of the boundary layer transition, as this phenomenon is affected by a great number of flow and body characteristics [59]. Furthermore, other aspects impact the correct prediction of the real trajectory of a falling sphere. One, for example, is surface imperfections, which cause unpredictability of the boundary layer transition, and can cause an erratic behavior on the boundary layer [146]. In fact, spheres without a smooth surface (by patching, for example) can twist and "corkscrew" when falling [147]. This might present a problem in the present case, since the used fire-extinguishing sphere has a fuse which "sticks out", preventing an almost perfect roundness. Another consideration to the unpredictability of the sphere path is the fluctuating lateral forces caused by vortex shedding, especially in the subcritical regime [145]. Furthermore, one more physical phenomenon that can highly impact the correct estimation of the sphere trajectory is the Magnus effect. If rotation on the FEB arises while launching, a deflection in the direction of the rotation results, caused by the Magnus force [148]. Both these facts can add a layer of complexity to the prediction of the aerodynamic coefficients of the flow around the sphere, or to the model used. Figure 10 presents typical experimental results for the drag coefficient of the sphere in the critical regime.

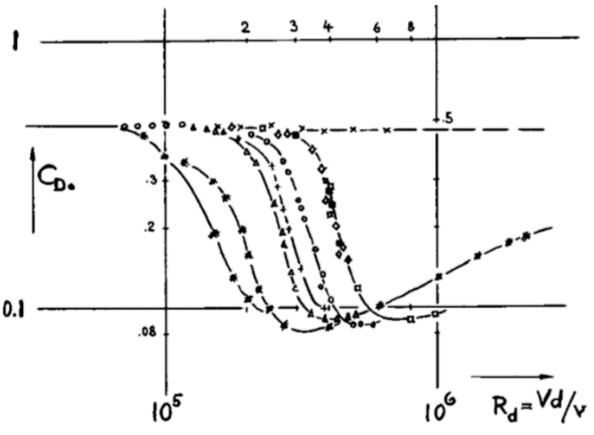

Figure 10 Experimental results for the drag coefficient of spheres in the critical regime [59].

The referred difficulty in predicting the necessary aerodynamics is shown here. Moreover, as referred in the beginning of this section, the Reynolds number at launch ranges between 0.75×10^5 and 1.5×10^5. This means the velocity of the FEB throughout the trajectory would be mostly in this critical regime.

One remark can be made about the landing quality. There is a possibility of the sphere rolling away from the target when landing, nullifying completely the value of the launch. This is especially relevant since the UAV that will be used to carry the projectile will probably be a fixed wing one, and, therefore, the launching phase will have a considerable translational speed.

Taking all previous aspects into account, launching just the FEB is not considered a good option. Therefore, this configuration is not considered a viable option, and will not be further discussed.

6.2. Trajectory model validation

In order to correctly implement the trajectory prediction model, it is fundamental to carry out a validation procedure. This is done by implementing the various needed physical properties of an already tested projectile and comparing the model's results with the results of the projectile in the previous tests.

In this work, the model validation was done by implementing the properties of a 120mm mortar, since it is also a fin stabilized projectile. Validation cases from reference [35] were carried out, using the properties and results for the mortar present in the same reference.

In the validation process, the aerodynamic coefficients were obtained by linear interpolation, and the step-size used in the numerical integration method, the Runge-Kutta 4th order method, was 10^{-5} seconds. The validation cases and their launch variables are shown in Table 1, where $M.V.$ is the launching muzzle velocity in meters per second, $Q.E.$ is the quadrant elevation in degrees, q_1 is the initial pitch rate in radians per second and Ψ_1 is the respective first maximum yaw in degrees.

Table 1 Validation cases variables

Case	$M.V.$ (m/s)	$Q.E.$ (degrees)	q_1 (rad/s)	Ψ_1 (degrees)
1	102	45	0.913	8
2	102	65	0.913	8
3	102	85	0.913	8
4	318	45	1.795	3
5	318	65	1.795	3
6	318	85	1.795	3

The trajectory model results for the six cases are shown in Table 2, along with the results of reference [35]. T_{flight} is the flight time in seconds, R is the range in meters, $M.H.$ is the maximum height in meters. It is seen that the percent error in time of flight, range and maximum height is below 1% for almost all values in relation to [35]. Therefore, it can be concluded the accuracy of the model is suited for this first stage in the project, allowing for the comparison between the projectile configurations, as well as studying the effects of other factors on the resulting trajectory.

Table 2 Resuls for the trajectory model validation

Case	$T_{flight[35]}$(s)	T_{flight}(s)	$E_{T_{flight}}$(%)	$R_{[35]}$(m)	R(m)	E_R(%)	M.H.$_{[35]}$(m)	M.H.(m)	$E_{M.H.}$(%)
1	14.6	14.6	0.00	1010	1001	0.89	260	260	0.00
2	18.6	18.6	0.00	770	759	1.43	420	424	0.95
3	20.5	20.5	0.00	165	163	1.21	510	510	0.00
4	41.4	41.3	0.24	7315	7298	0.23	2100	2098	0.10
5	52.6	52.5	0.19	5570	5561	0.16	3380	3375	0.15
6	57.7	57.6	0.17	1275	1272	0.24	4040	4065	0.62

6.3. CFD methodology validation and grid independence study

To ensure a correct CFD methodology is used, it is imperative to validate it, by comparing the aerodynamic results of the used method with available results. In this dissertation, this validation was carried out by comparing the results of a Non-Lethal 12-Gauge Fin-Stabilized projectile, with the ones present in [149], facilitated by the author. This projectile and test case were chosen for the similar flow characteristics, which are low speed and uncompressible flow, and since it also employed fin-stabilization.

Thus, all the elements of the methodology laid out in Section 4.2 were applied. The global sizing method was set to Fine, the finest mesh subsection was created with a Body of Influence, with 1.25 mm of element size, the projectile wall was meshed with a Face Sizing method, with an element size of 0.2 mm, and an Inflation method of 18 layers was applied to the projectile wall, with a first layer height of 0.004 mm, to guarantee a $y^+ \leq 1$. These definitions allowed for the correct representation of the projectile and its details. The mesh was improved in order to maintain the minimum orthogonal quality above 0.01. The standard coefficients for the k-ω SST model were used. The results for the 12-Gauge projectile are presented in Figures 11 and 12.

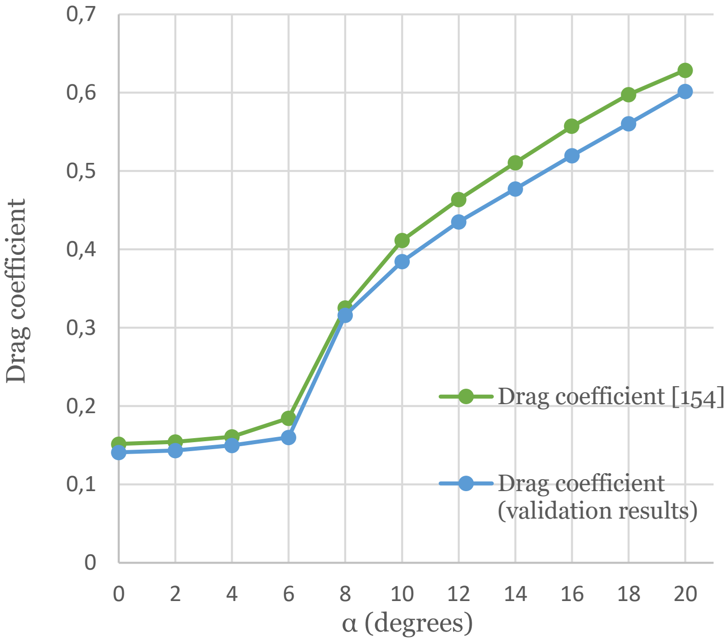

Figure 11 CFD Validation results for drag coefficient.

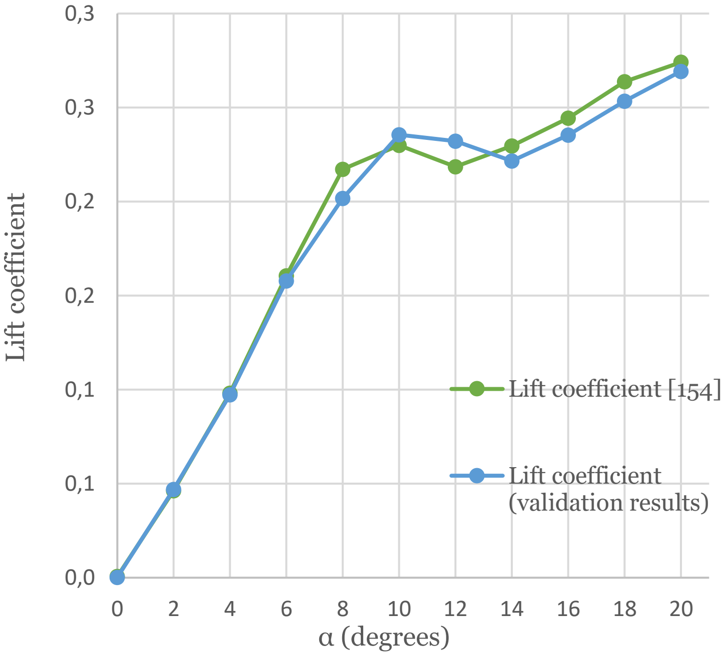

Figure 12 CFD Validation results for lift coefficient.

A maximum difference of 13.2 % for the drag coefficient for α=6° and 7.1 % for the lift coefficient for α=8° are observed in these results, while the other results for drag are below 7.2 % and below 6.3 % for lift. Moreover, the drag coefficient and lift coefficient curves are correctly predicted, which indicates a correct prediction of the aerodynamic effects around the body, such as stall. Therefore, the CFD model is considered correctly validated. The numerical results are presented in Annex 5. It is important to refer that the maximum percent difference for the lift coefficient is actually 69%, at 0 degrees of angle of attack, but the difference in the value is just 0.004, not being therefore a considerable difference in the coefficient value.

Another relevant aspect to study in CFD methodologies is grid independence. Grid independence studies are used to have an estimate of the number of elements used is necessary to obtain an accurate result while taking in consideration the time of calculation. In this dissertation, the grid independence study was carried out using the 2nd Configuration, by varying the density of the mesh in its finer subsection, by varying the Element Size in the Body of Influence meshing method. The results are presented in Figure 13, and the values for the results can be found in Annex 6.

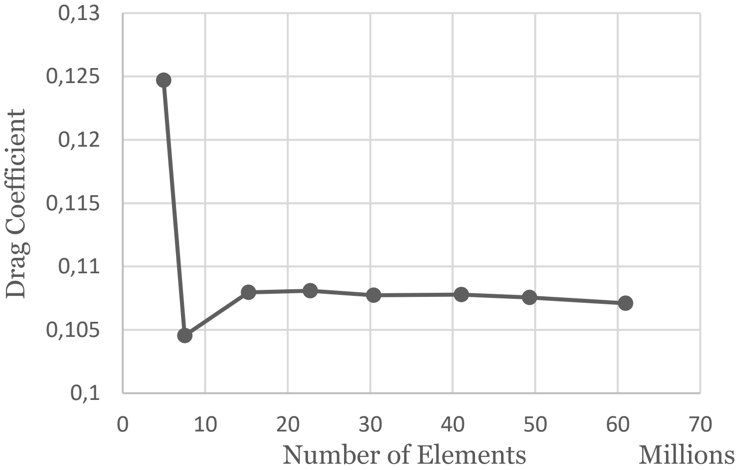

Figure 13 Results for grid independence study.

The difference between 30 million elements and 61 million is approximately 0.58%, and since after 30 million elements the simulation time cost gets quite large, 30 million elements is considered a good value for the number of elements in the mesh. Therefore, all CFD simulations are run with meshes with an element number around this value.

6.4. Inertial properties

In this section the inertial properties for Configuration 2, 3, and 4 are presented. The inertial properties of these configurations were obtained through *CATIA*. The FEB was considered a solid sphere, with its mass uniformly distributed. Since the mass of the FEB is 0.470 kg, and its diameter is 0.11 m, the resulting density is 674 kg/m^3. The tail components were considered made of cardboard with a density of 700 kg/m^3 (value obtained from [150]) and 1 mm of thickness. The inertial properties of the configurations are presented in Table 3.

Table 3 Inertial properties of Configurations 2,3, and 4.

	x_{cg} (m)	m (kg)	I_x (kg.m^2)	$I_y = I_z$ (kg.m^2)	l (m)	d (m)	S (m^2)
Configuration 2	0.0794	0.5120	0.0006	0.004273	0.440	0.110	0.0095
Configuration 3	0.0832	0.5426	0.000663	0.004489	0.440	0.110	0.0095
Configuration 4	0.0952	0.6004	0.000797	0.005945	0.440	0.110	0.0095

x_{cg} is the position of the center of gravity, measured from the most forward point, in front of the FEB. It is important to mention that even though cardboard could not be used for the construction of configuration 4, the material is considered in theory, in order to properly compare the results with the other configurations.

6.5. Static aerodynamic coefficients results

The CFD aerodynamic results were obtained for angles of attack ranging from 0º to 14º, every 2º, for a velocity of 15 m/s (the average launching velocity), which, considering the reference length 0.11 m, an air density of 1.225 kg/m3, and a dynamic viscosity of 1.7894×10^{-5} kg/(m.s), corresponds to a Reynolds number of around 113,000. Aerodynamic symmetry was considered, as explained before, in order to obtain the results from -14º to -2º. The CFD methodology laid out in Section 4.2 was applied. The global sizing method was set to Fine, and the finest mesh subsection was defined using a Body of Influence method, with an element size of 11 mm. A Face Sizing method was used to mesh the projectile wall, with an element size of 0.9 mm, and an Inflation method was applied to the projectile wall, with 20 layers and a first layer height of 0.015 mm, guaranteeing a $y^+\leq 1$. As for the turbulence model and other definitions, the ones defined in Section 4.2 were used. Figures 14, 15, and 16 present the results for the tested configurations:

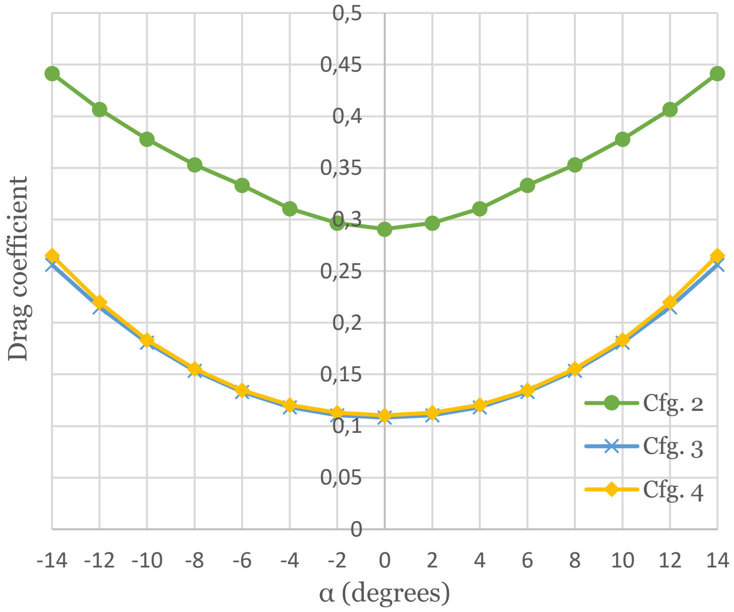

Figure 14 CFD results for the drag coefficient, for Configurations 2, 3, and 4.

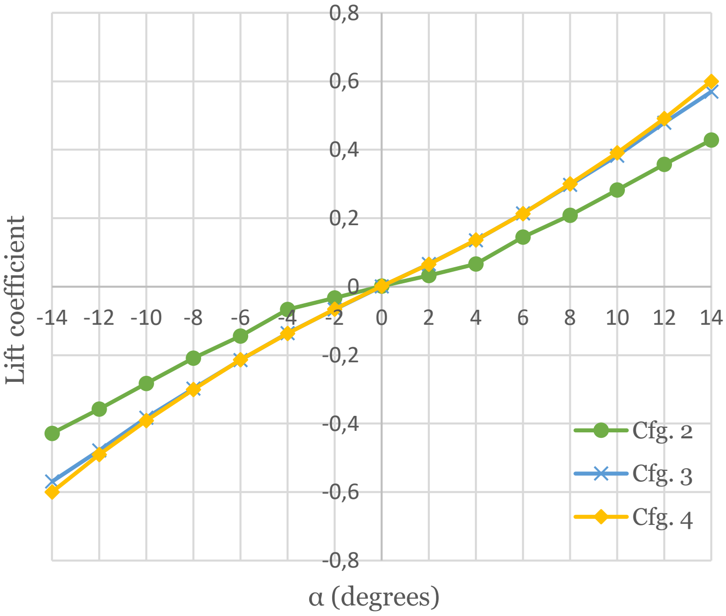

Figure 15 CFD results for the lift coefficient, for Configurations 2, 3, and 4.

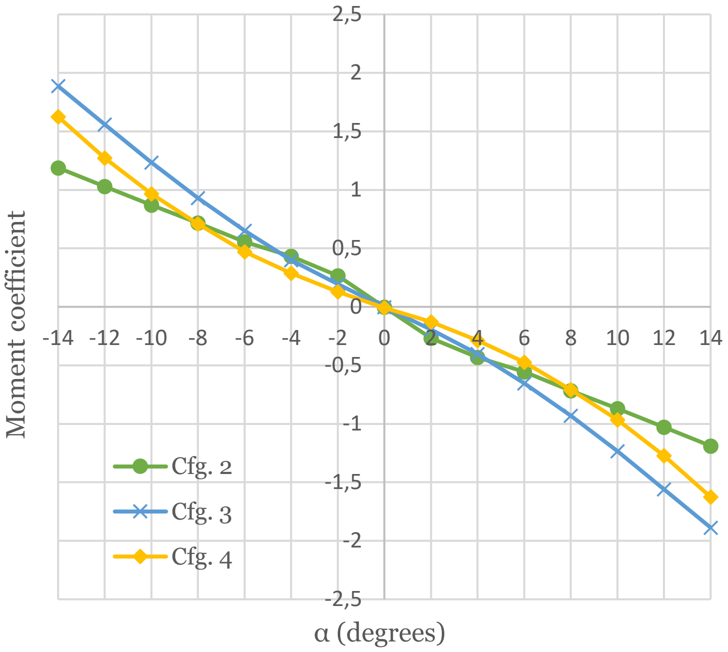

Figure 16 CFD results for the moment coefficient around the C.G., for Configurations 2, 3, and 4.

Firstly, from Figure 16, it can be noted that all configurations are statically stable since the moment coefficient with respect to α curves have a negative slope, as it was expected for this kind of fin stabilized configurations, as explained before. It can also be observed that in terms of C_D and C_L the results for the 3rd and 4th configurations are very similar, and the difference between them in the moment coefficient arises from the different center of gravity position. As for Configuration 2, a much greater amount of drag coefficient, more than 2 times of the other configurations, can be observed. This is due to the larger pressure drag arising from the wake behind the FEB, in the areas where the tail is not connected, which are areas of detached flow. This can be observed in Figures 17 and 18.

As for the other configurations, for this range of α, the flow seems to be mostly attached to the body, especially in the lower values of α. This is mostly because of their streamlined bodies which do not have any geometric discontinuities. This can be seen in Figures 19-22.

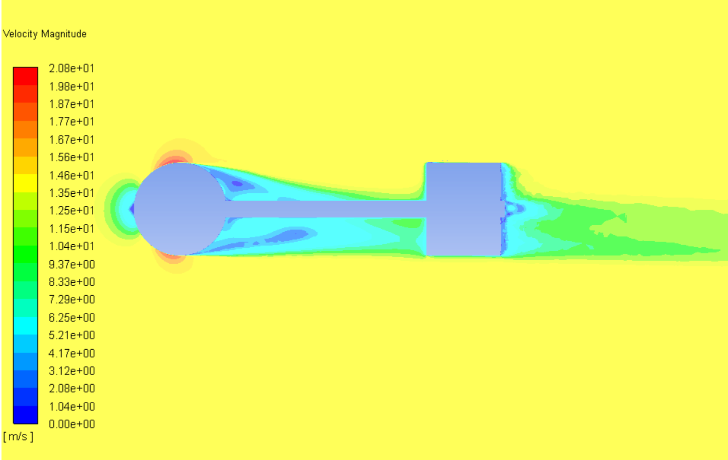

Figure 17 Velocity profile in the plane xy of Configuration 2, at 15 m/s and 0º of angle of attack.

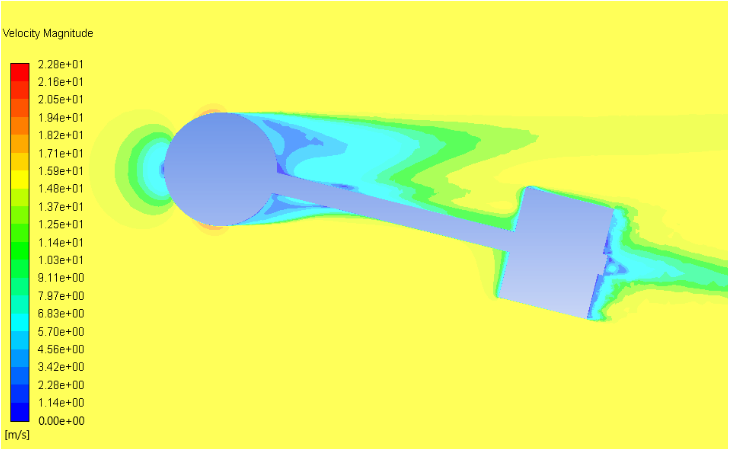

Figure 18 Velocity profile in the plane xy of Configuration 2, at 15 m/s and 14º of angle of attack.

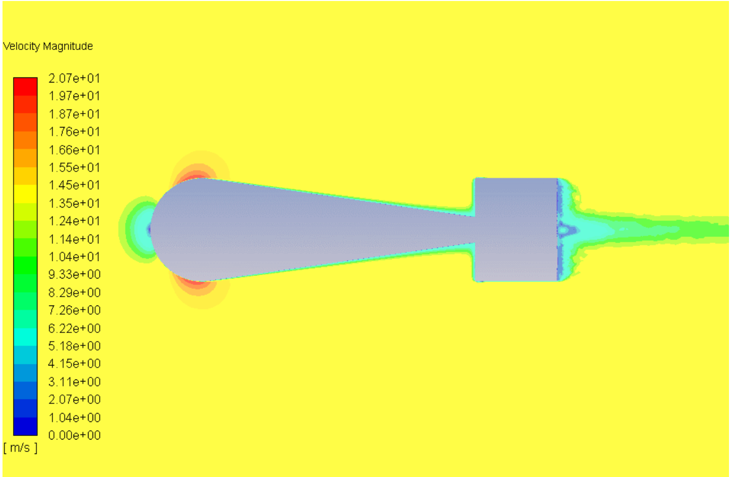

Figure 19 Velocity profile in the plane xy of Configuration 3, at 15 m/s and 0º of angle of attack.

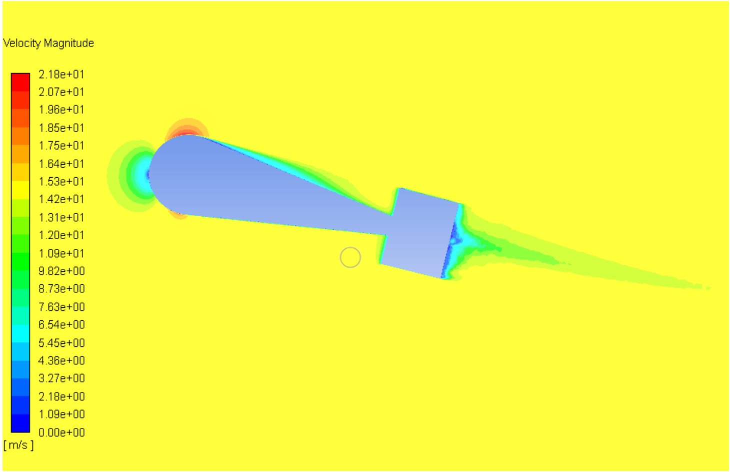

Figure 20 Velocity profile in the plane xy of Configuration 3, at 15 m/s and 14º of angle of attack.

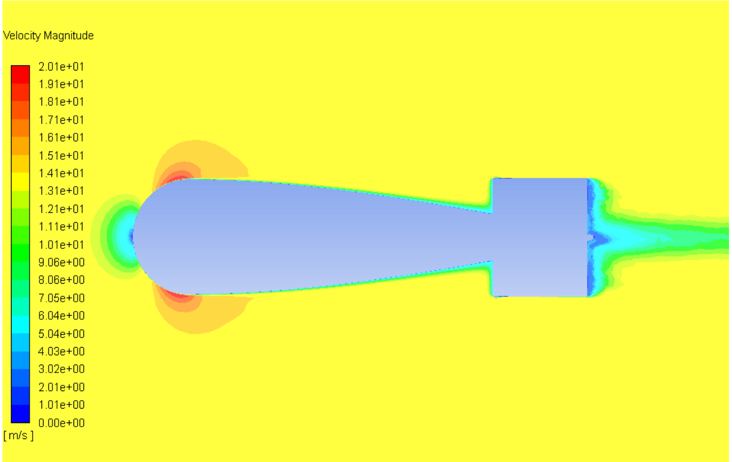

Figure 21 Velocity profile in the plane xy of Configuration 4, at 15 m/s and 0º of angle of attack.

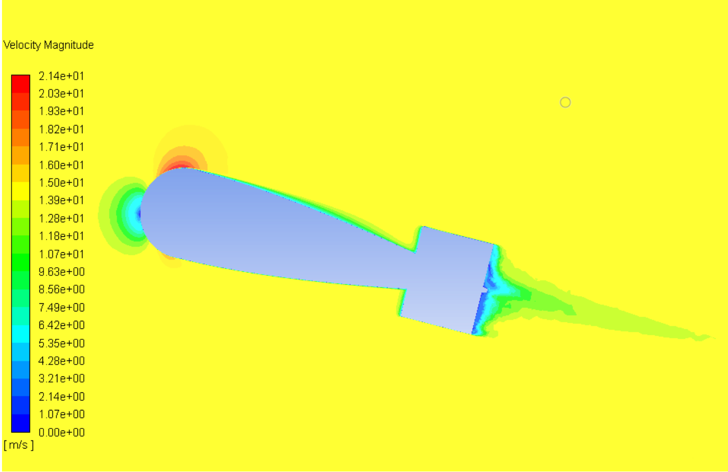

Figure 22 Velocity profile in the plane xy of Configuration 4, at 15 m/s and 14º of angle of attack.

As for the fins, it seems that a certain amount of detachment is always present, at least at the trailing edge, and a considerable amount at the upper surface as α reaches its higher values of the range. This is observable in Figures 23 and 24. All these assessments could be better evaluated by analyzing the axial wall shear stress and the pressure coefficient, but it is not considered a relevant analysis for this work.

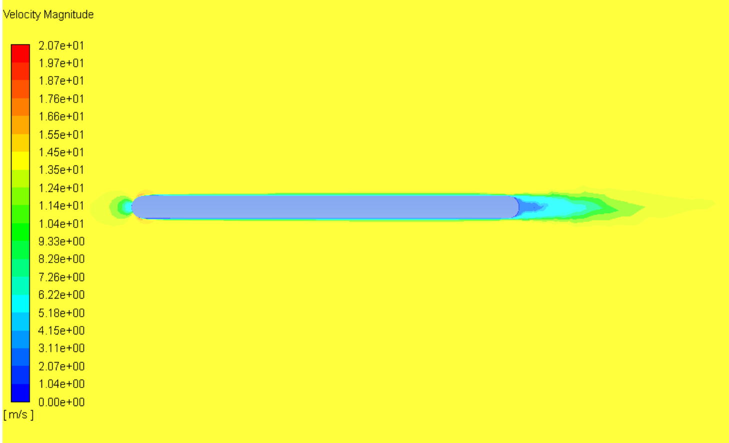

Figure 23 Velocity profile in the plane xy of the fins, at 15 m/s and 0º of angle of attack

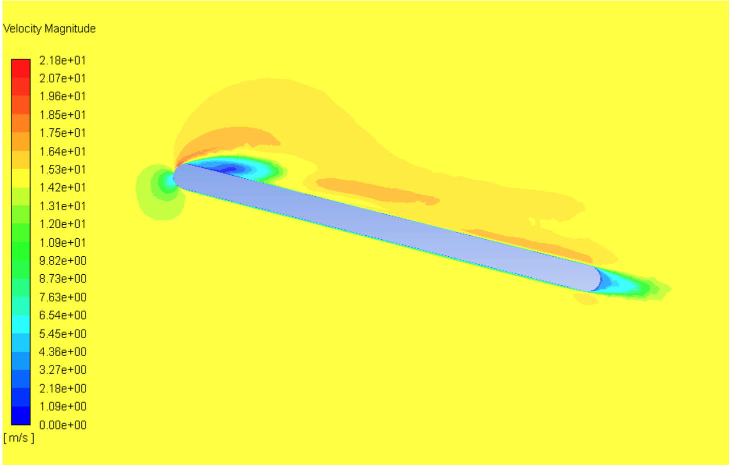

Figure 24 Velocity profile in the plane xy of the fins, at 15 m/s and 14º of angle of attack

As for the adequacy of the applied CFD methodology, it was very efficient to obtain the results for the cone and NACA tail configurations. On the other hand, Configuration 2 was noted to have a transient behavior, indicated by its results having oscillatory patterns. This might have two origins: the first, is most likely due to the flow detachment that occurs in the sphere, having a wake with characteristics similar to the ones referred to in Section 6.1; the second origin might be the flow around the tubular boom, which can have a similar behavior to the one around the sphere, in some flow regimes, and can be a contributor for the transient behavior. The drag coefficient was the easiest value to obtain in this configuration, while the lift and moment coefficients were difficult to predict. Therefore, for Configuration 2, the static aerodynamic results which were considered were the ones with minimum residual values, while for the other configurations the converged values were considered, which also coincided with the lowest residual values. Also, double precision was used for the calculations, which had a notable positive impact on the precision of the results, and also accelerated the convergence of the results. Another limitation regarding the CFD results for Configuration 2 was that different runs of the CFD calculations gave slightly different results, sometimes with more than 15% difference. The problems regarding Configuration 2 results could be solved using an Unsteady Reynolds Averaged Navier-Stokes method, which was not oused due to time constraints for the present work.

Even though some limitations arise with this methodology, the results still allow for an early comparison between the projectile configurations, while giving important insight into the configurations' aerodynamic behavior, which can affect the predictability of the configurations' trajectory.

6.6. Dynamic aerodynamic coefficients results

As explained in Section 4.3, to obtain the dynamic coefficients of the fins, it is necessary to determine l_t and a_t, which was done using *XFLR5*. As stated in Section 4.3, l_t is the distance between the projectile center of gravity and the fins' aerodynamic center, and a_t is the slope of the $C_L(\alpha)$ curve. Figure 25 presents the $C_L(\alpha)$ curve, and from the linear regression curve, the slope of the $C_L(\alpha)$ curve can be determined as a_t=1.758 rad^{-1}.

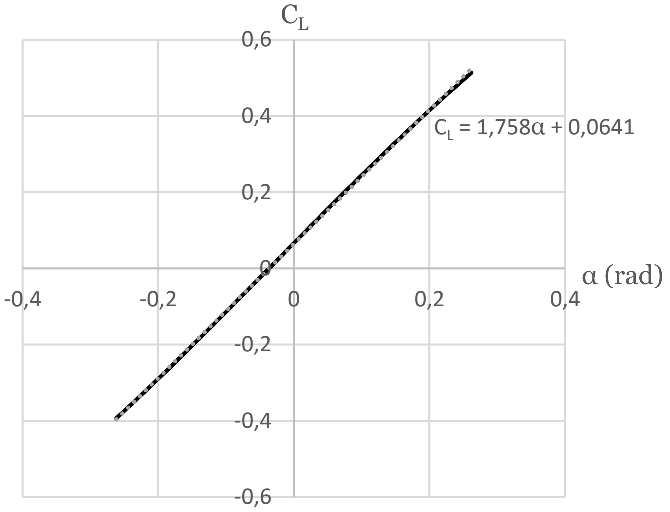

Figure 25 $C_L(\alpha)$ curve for the fin assembly, with a linear trend curve

From the linear regression curve, the slope of the $C_L(\alpha)$ curve can be determined as a_t=1.758 rad^{-1}.

In order to obtain the aerodynamic center, an iterative method was used, by plotting the $C_M(\alpha)$ curve in various locations, until the point in which the slope is 0, i.e., the C_M is constant, is found. That point is the aerodynamic center. With this approach, it was found that the aerodynamic center is located at, approximately, 18.18 % of the chord, at 0.016 m from the leading edge. Therefore, with the center of gravity of the different configurations specified in the previous section, the l_t for the different configurations can be obtained, as shown in Table 4.

Table 4 l_t for Configurations 2,3, and 4.

	Configuration 2	Configuration 3	Configuration 4
l_t	0.2836 m	0.2798 m	0.2678 m

The resulting dynamic coefficients for these configurations are, obtained through (41) and (44), while $C_{Y_r} = -C_{Z_q}$ and $C_{N_r} = C_{M_q}$, as explained in Chapter 4. The results for the coefficients are summarized in Table 5.

Table 5 Dynamic coefficients for Configuration 2, 3, and 4.

	Configuration 2	Configuration 3	Configuration 4
C_{Z_q}	-9.2334	-9.1097	-8.7190
C_{M_q}	-23.8054	-23.1718	-21.2268
C_{Y_r}	9.2334	9.1097	8.7190
C_{N_r}	-23.8054	-23.1718	-21.2268

6.7. Trajectory results

A total of 17 trajectory cases for each projectile have been chosen, with the variables being height of launch h_{launch}, velocity of launch V_{launch}, mean wind speed $MW_{velocity}$, and mean wind direction

$MW_{direction}$. These were divided in two groups: Group 1, which evaluates the different results for different launching heights and different launch velocities while considering inexistent mean wind speed; and Group 2, which assesses the influence of the mean wind on the trajectory and projectile's behavior, varying its speed and direction for two launching velocities while maintaining the height of launch. Tables 6 and 7 present the cases for Group 1 and Group 2, respectively:

Table 6 Group 1 launching cases, with h_{launch} and V_{launch} as variables and no $MW_{velocity}$ considered.

	Case 1.1	Case 1.2	Case 1.3	Case 1.4	Case 1.5	Case 1.6	Case 1.7	Case 1.8	Case 1.9
h_{launch} (m)	30	30	30	50	50	50	100	100	100
V_{launch} (m/s)	10	15	20	10	15	20	10	15	20

Table 7 Group 2 launching cases, with $MW_{velocity}$, $MW_{direction}$ and V_{launch} as variables and a constant h_{launch}.

	Case 2.1	Case 2.2	Case 2.3	Case 2.4	Case 2.5	Case 2.6	Case 2.7	Case 2.8
$MW_{velocity}$ (m/s)	2.5	2.5	2.5	2.5	5	5	5	5
$MW_{direction}$ (º)	0	90	0	90	0	90	0	90
h_{launch} (m)	100	100	100 m	100	100	100	100	100
V_{launch} (m/s)	10	10	20	20	10	10	20	20

All individual results are presented throughout Annexes 11, 12, and 13, for Configuration 2, 3, and 4, respectively. Here, only some of the results are presented or referred to, in order to compare the configurations' performance, without cluttering the following pages with very similar result images, or results that do not allow for important and relevant analysis.

Firstly, some of the results for the angle of attack as a function of time of the trajectory are presented for some trajectory cases in Group 1, in Figures 26-30.

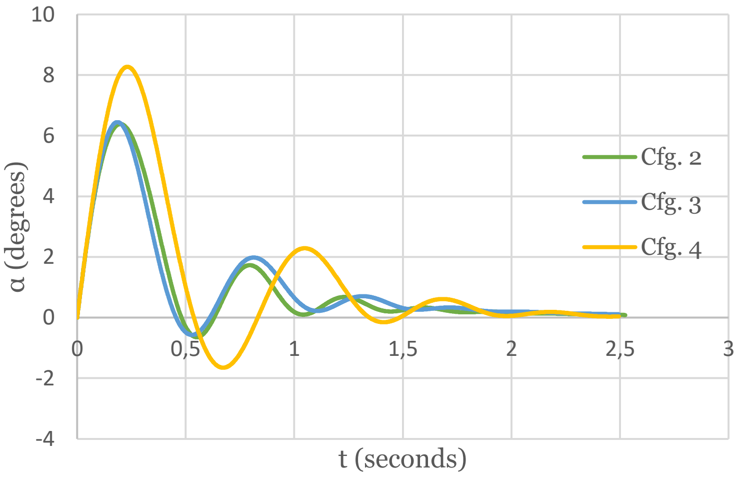

Figure 26 α(t) results for Configurations 2, 3, and 4, from the trajectory case 1.1.

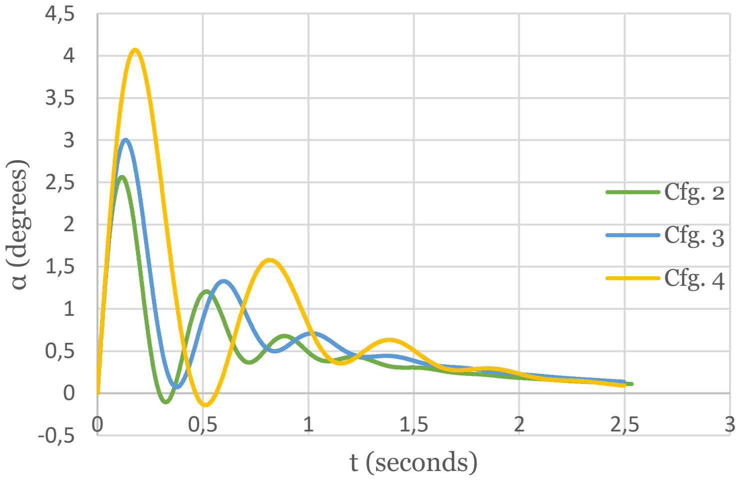

Figure 27 α(t) results for Configurations 2, 3, and 4, from the trajectory case 1.2.

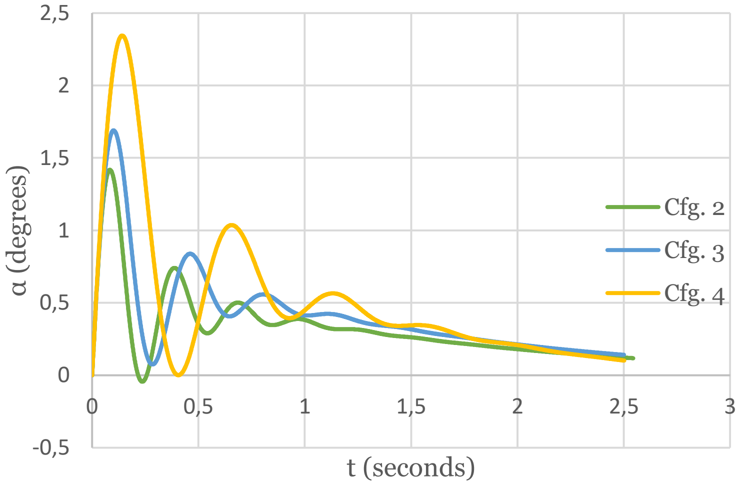

Figure 28 α(t) results for Configurations 2, 3, and 4, from the trajectory case 1.3.

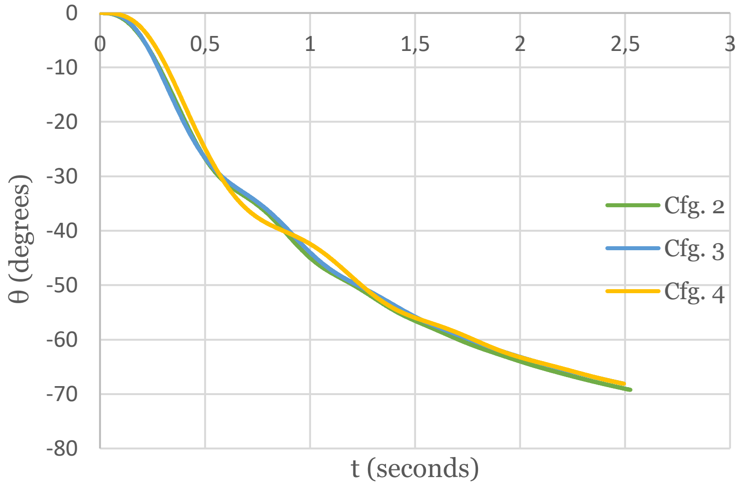

Figure 29 θ(t) results for Configurations 2, 3, and 4, from trajectory case 1.1.

Looking at these results, some observations can be made. From Figures 25-27, it can be confirmed that all configurations have positive dynamic and static stability, which, considering the results for the previously obtained coefficients, was already expected and referred. All configurations have a dynamically damped behavior, decreasing the oscillation amplitude of the angle of attack and pitch angle throughout the trajectory, and eventually asymptotically approaching 0 degrees and 90 degrees, respectively. It can also be observed that the 2nd and 3rd configurations seem to have a slightly better dynamically stable behavior than the NACA tail configuration, since they dampen the oscillations quicker than the other configuration, which is a result from slightly higher absolute values for the dynamic coefficients and l_t, and a lower value of I_y and I_z, which seem to be more adequate for these trajectory cases. It can also be observed that, in relation to the launching variables, the factor that influences the maximum angle of attack in the trajectory is the launching velocity, and a higher launching velocity reduces the maximum angle of attack the projectile endures during flight.

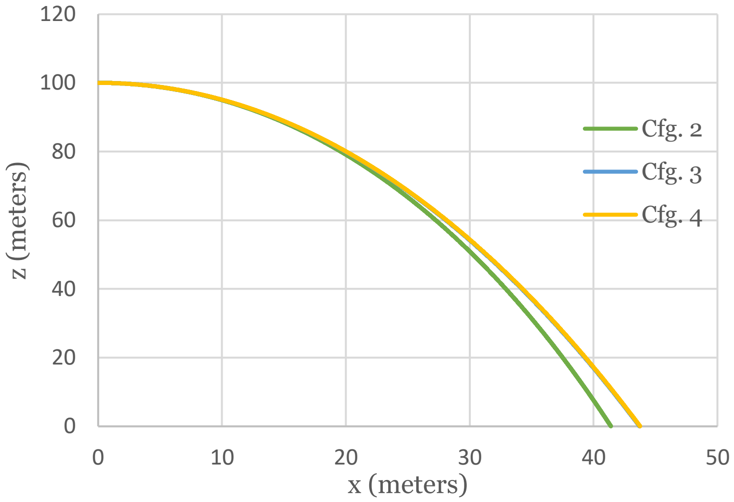

Figure 30 z(x) for Configurations 2, 3, and 4, from trajectory case 1.7.

Among the three tested configurations, the trajectory cases in Group 1 allow to draw the conclusion that, in terms of impact velocity and location, configurations 3 and 4 are very similar. Even the final θ in all cases are extremely close, differing 0.1 degrees at most. The impact θ can be relevant, because if the angle between the projectile and ground during landing is low then the projectile might slide. Considering that α is small on impact (which can be confirmed by Figures 26-28), this angle of impact is practically equal to θ. The impact θ is affected by two launching variables: launching height and launching speed. A slower launching speed and a higher launching height correlate to a higher θ on impact.

Some results for the Group 2 trajectories are now presented in Figures 31 and 32.

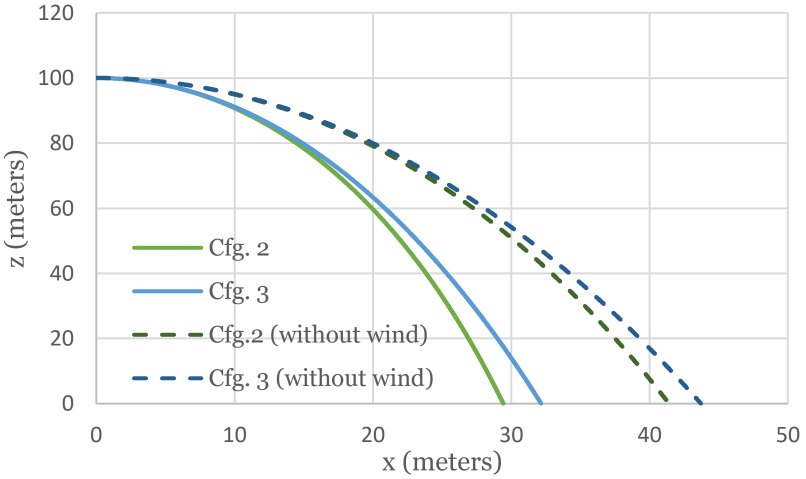

Figure 31 z(x) results for Configurations 2 and 3, from Case 2.1 (solid lines) and Case 1.7 (dashed lines).

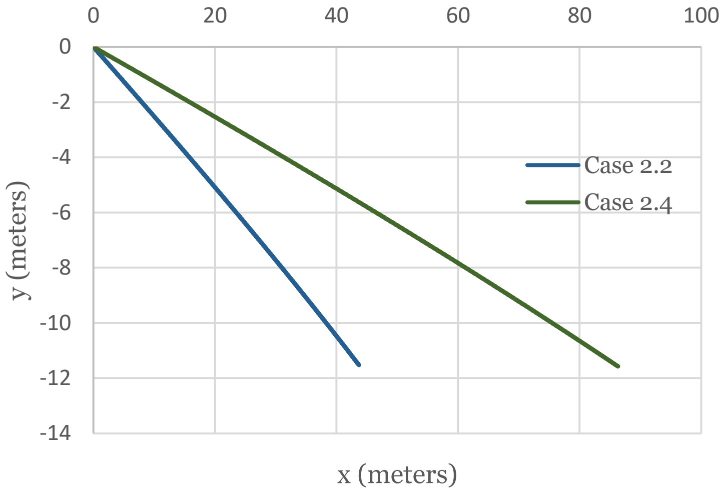

Figure 32 y(x) results for Configuration 3, from trajectory cases 2.2 and 2.4.

The first result to acknowledge is that the mean wind influence is only on x_g and y_g, while all other trajectory variables behave the same way, regardless the launching velocity, meaning that mean wind does not affect the projectile's attitude and stability. It can also be noticed that the effect of wind is the same, and that the difference in effect arises from the different trajectory times. For example, comparing Case 1.7 with Case 2.1 for the tube tail configuration (cases with the same launching height and launching velocity), the difference in x_g is around 11.98 m, which is the same as the mean wind velocity multiplied by the trajectory time and by the cosine of the direction, 0 º, and in Case 2.2 for the cone tail configuration, the final y_g is approximately -11.57 m, which is the same as the mean wind velocity multiplied by the trajectory time and by the sine of the wind direction, 90 º.

An interesting analysis to make is the influence on the trajectory if the dynamic coefficients are not considered. Figure 33 is the result for the trajectory case 1.7, for Configuration 3, with and without the consideration of the dynamic coefficients, and Figure 34 is the result for Case 1.9, also analyzed in this way:

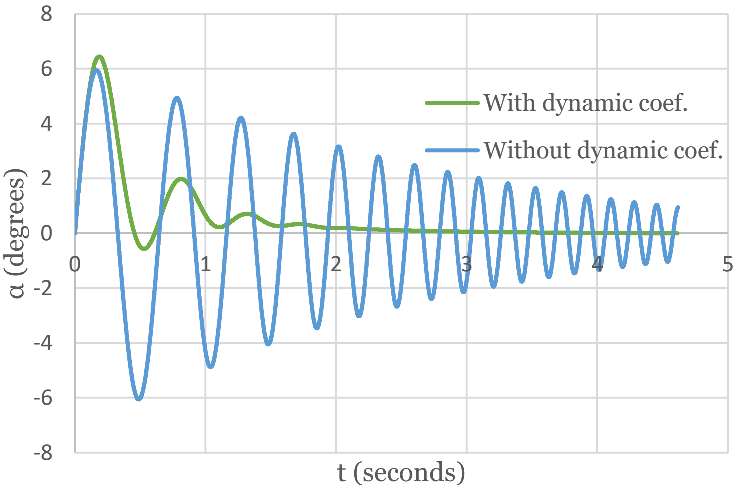

Figure 33 α(t) for Configuration 3, from trajectory case 1.7.

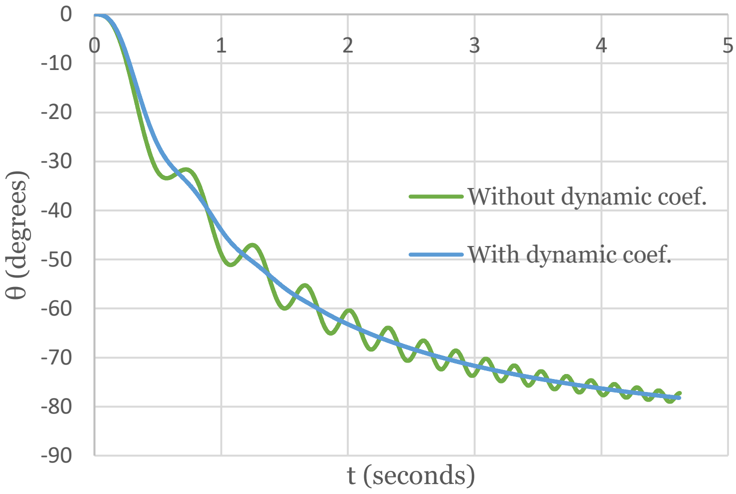

Figure 34 $\theta(t)$ results for Configuration 3, from trajectory case 1.7.

These results are the typical results for α(t) and θ(t) if no dynamic coefficients are considered. This is because C_{M_q} works to dampen the variation in the angle of attack and angle of pitch caused by C_M (in reality, the effect is actually caused by q, but q is in turn affected by C_M). In relation to the trajectory, no major differences were noticed: the differences in final x_g were on the order of centimeters, with a bigger difference in Case 1.9, and the difference s in velocities were negligible, the highest being in Case 1.7, about 0.03 m/s. Although it would be expected that a fluctuating value of the angle of attack would be met with a considerable increase in overall drag resistance throughout the trajectory (since higher angles of attack correspond to a higher drag coefficient), this might be due to the overall small angle of attack, even if no consideration of the dynamic coefficients is present, and since the drag coefficient does not change much in these lower angle of attack values, the difference is not very significant. Despite this, it is still important to consider them, to make sure the maximum amount of accuracy is possible. It is also relevant to recall that only a part of the dynamic coefficients is being considered in this model.

Another relevant study is the influence of wind turbulence in the trajectory. Cases 1.1, 1.3, 1.7, and 1.9 are analyzed, for Configuration 3, with the same pattern of wind turbulence considered. Figures 36 and 37 show some of these results, while Figure 35 presents the typical wind turbulence velocity pattern.

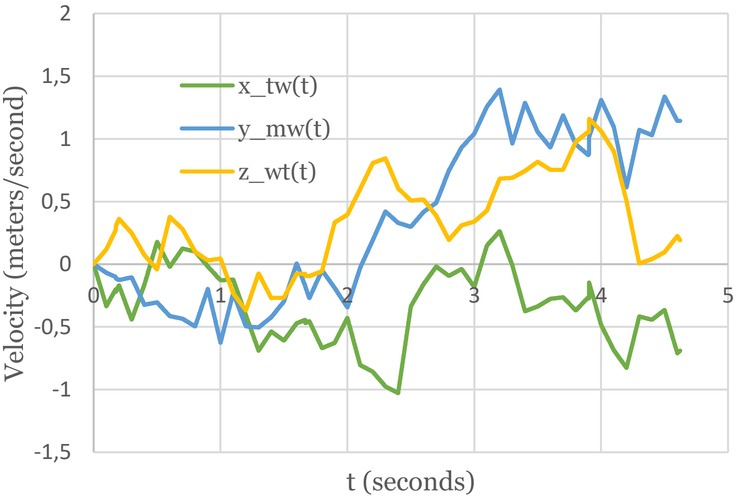

Figure 35 Typical wind turbulence velocity pattern. These values are in the projectile-fixed coordinate system.

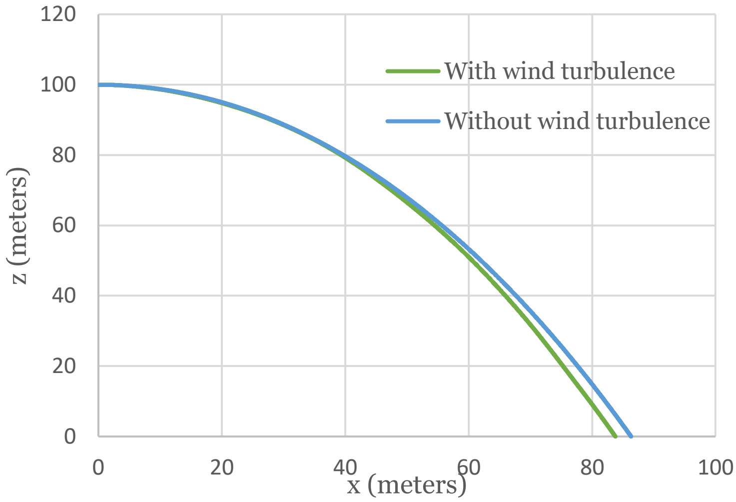

Figure 36 z(x) for Case 1.9, with and without wind turbulence, for Configuration 3.

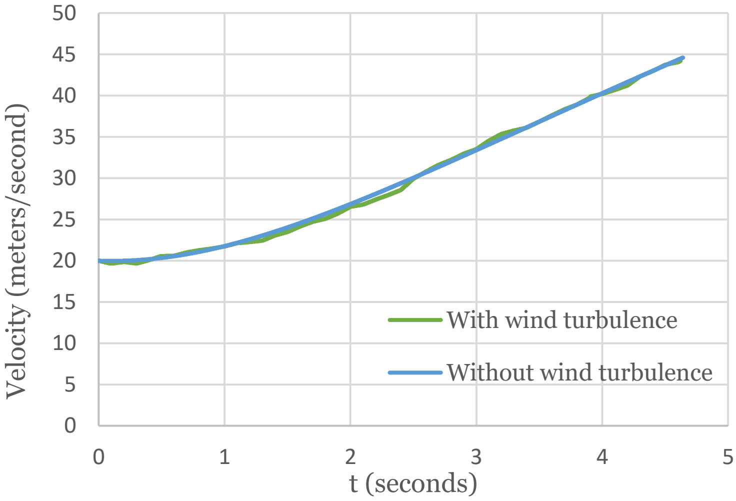

Figure 37 V(t) for Case 1.9, with and without wind turbulence, for Configuration 3.

The analysis makes it obvious that wind turbulence can have a considerable impact on the trajectory impact point. Between the tested cases, the minimum difference in x_g was 0.64 m, while the maximum was 2.18 m. The difference in the velocity throughout the trajectory can be seen in Figure 37, while the difference in the projectile's attitude and stability is negligible.

Another important analysis relates to the size of the fins. A different configuration was considered, based on Configuration 3, named Configuration 3.1, with double the area of the fins, while keeping the same total length, and the same diameter size, in order to assess what would be the impact on stability. This configuration has the inertial properties shown in Table 8, considering the same material properties for all other configurations, as well as the same fineness ratio:

Table 8 Inertial properties of Configuration 3.1.

x_{cg} (m)	Mass (kg)	I_x (kg.m²)	$I_y = I_z$ (kg.m²)	l (m)	d (m)	S (m²)
0.0938	0.570	0.000693	0.005783	0.440	0.110	0.00950332

The same analysis done previously to obtain the dynamic coefficients was carried. Using *XFLR5*, a_t was obtained, with the value 0,9568 rad^{-1}. Considering the position of the aerodynamic center, 18.18

%of the airfoil chord, which is at 32 mm, it follows that l_t=0.1972 m. With this, the values for the dynamic derivatives of Configuration 3.1 can be obtained, which are shown in Table 9:

Table 9 Dynamic coefficients for Configuration 3.1.

C_{Z_q}	C_{M_q}	C_{Y_r}	C_{N_r}
-6.9887	-12.5288	6.9887	-12.5288

Interestingly, even though the fin area doubled, a_t and l_t values lowered considerably, so the increase in S_t was not enough to increase the coefficients' values. The decrease in a_t is due to the aspect ratio of the tail halving (the tail aspect ratio is obtained by b^2/S_{tail}, with b being the tail span, and since b stays the same, while S_{tail} doubles, the aspect ratio halves), having therefore a considerably higher loss of lift and increase of drag due to tip vortexes [57], while the decrease in l_t arises from the aerodynamic center moving back and the advance in the gravity center.

The CFD results for this configuration are shown in Figures 38-40, and they are compared with the results for Configuration 3.

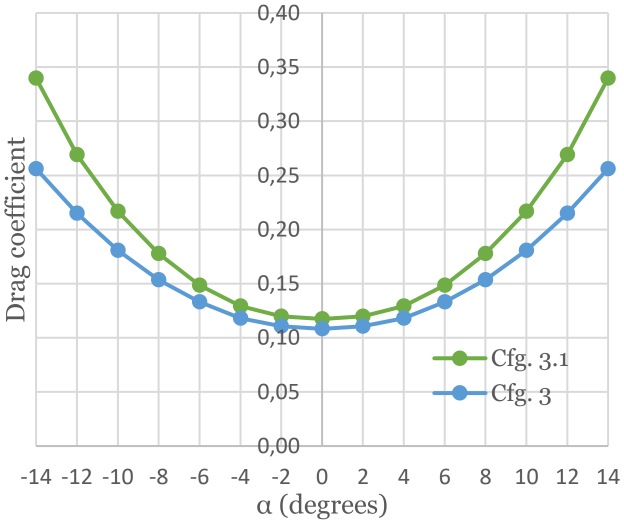

Figure 38 CFD results for drag coefficient for Configuration 3.1 and 3.

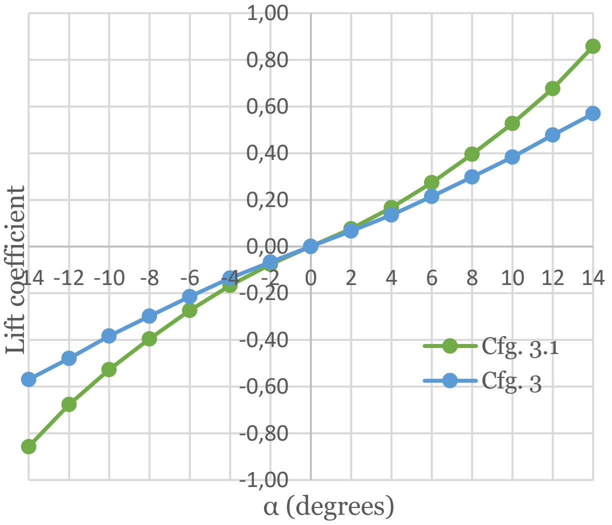

Figure 39 CFD results for lift coefficient for Configuration 3.1 and 3.

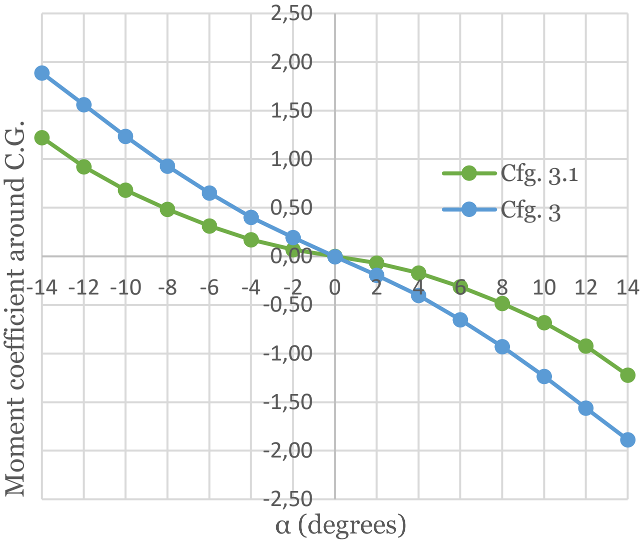

Figure 40 CFD results for moment coefficient around C.G. for Configuration 3.1 and 3.

As it can be observed, the drag coefficient increased overall, more significantly in higher angles of attack, as well as the lift coefficient. Interestingly, this increase in the lift coefficient did not translate into higher values for the moment coefficient around the center of gravity. This is because the distance between the center of gravity and the point where the resulting lifting force of the projectile is applied reduced significantly.

Cases 1.1, 1.3, 1.7 and 1.9 are evaluated and compared with the same results for Configuration 3, and Case 1.7 is evaluated with and without turbulence. Again, only some results are presented here, in Figures 41 throughout 43.

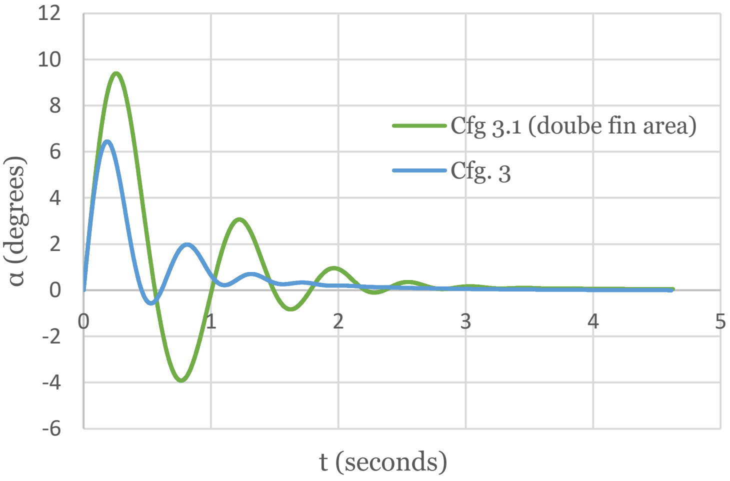

Figure 41 α(t) results for Configuration 3.1 and 3, from trajectory case 1.7.

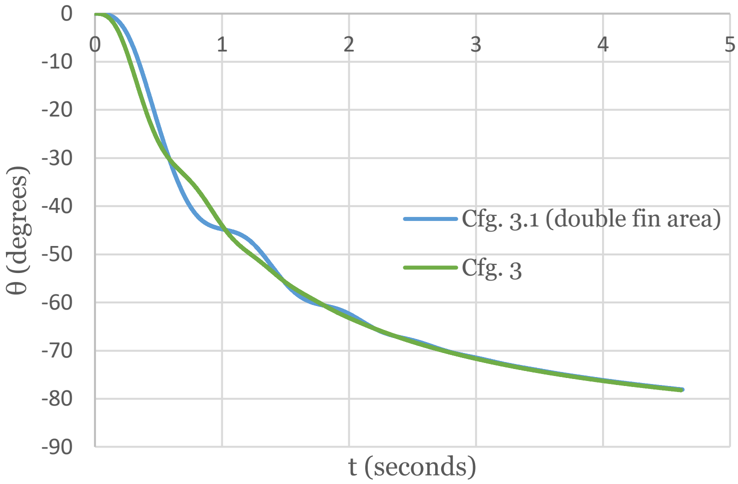

Figure 42 $\theta(t)$ results for Configuration 3.1 and 3, from trjactory case 1.7.

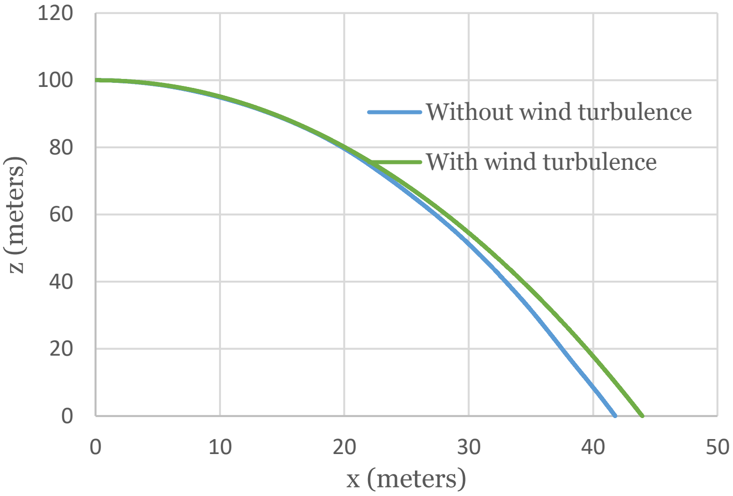

Figure 43 z(x) results for Configuration 3.1, from trajectory case 1.7, with and without wind turbulence.

As predicted, in terms of stability, since the values for the moment coefficient around the CG are smaller than Configuration 3, the maximum angle of attack is higher, and from the smaller absolute values for the dynamic coefficients, the configuration for the projectile with double the fin area is not as dynamically stable as the other configurations. As for the behavior of this configuration considering wind turbulence, the difference in performance is comparable, with an offset in the impact point of around 2 meters.

A question arises with the values for the dynamic coefficient values: what value would be the most appropriate for $\left(C_{M_{\dot{\alpha}}} + C_{M_q}\right)$, the dynamic coefficients related to the dynamic stability, for this range of launching velocities. From the simulations already performed, it can be seen that it probably needs to be lower than -23.8054. Configuration 3 is assumed for this analysis, and while it is understood that a change in this coefficient would probably translate to a change in some of the other characteristics, including the projectile's inertial properties and static coefficients, it can serve as a basis for a future study. Thus, the values -30, -50, -70, -90, and -120 are considered for $\left(C_{M_{\dot{\alpha}}} + C_{M_q}\right)$, while considering $\left(C_{Z_{\dot{\alpha}}} + C_{Z_q}\right)$=0. Case 1.8 is used for this evaluation, and a case with the same launching height and velocity while also considering an initial disturbance of q_1 =0.349 rad/s (approximately 20°/s) is considered. Figures 44-47 are the results for these analyses.

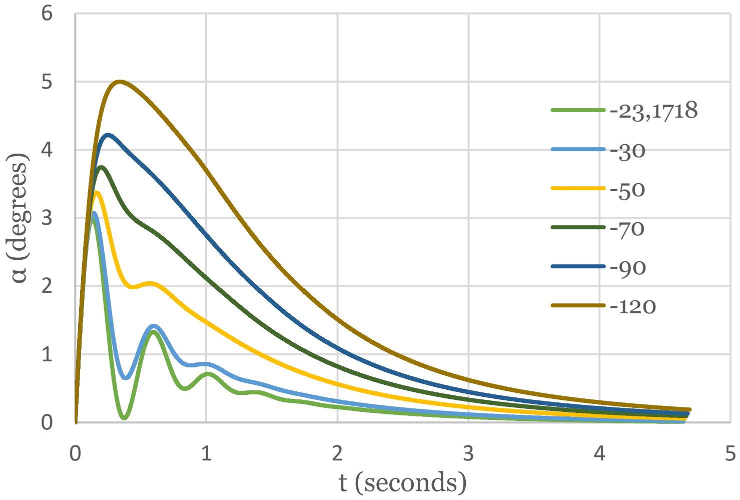

Figure 44 α(t) for different values of $\left(C_{M_{\dot{\alpha}}} + C_{M_q}\right)$*, from Case 1.8, considering the static coefficients and inertial properties of Configuration 3.*

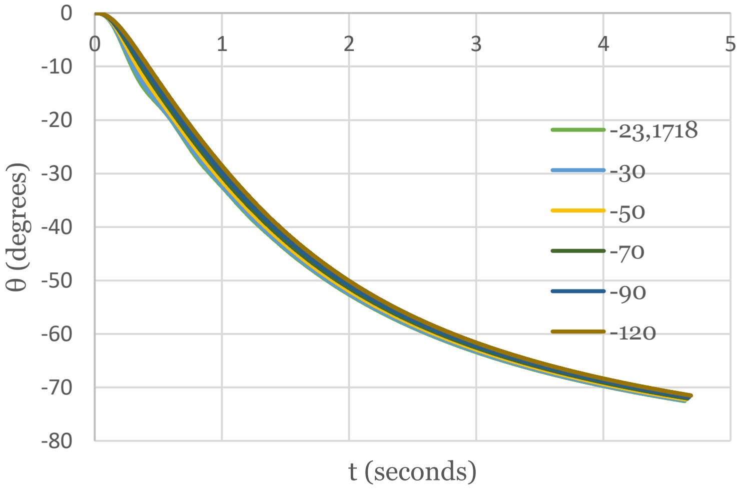

Figure 45 θ(t) for different values of $\left(C_{M_{\dot{\alpha}}} + C_{M_q}\right)$*, from Case 1.8, considering the static coefficients and inertial properties of Configuration 3.*

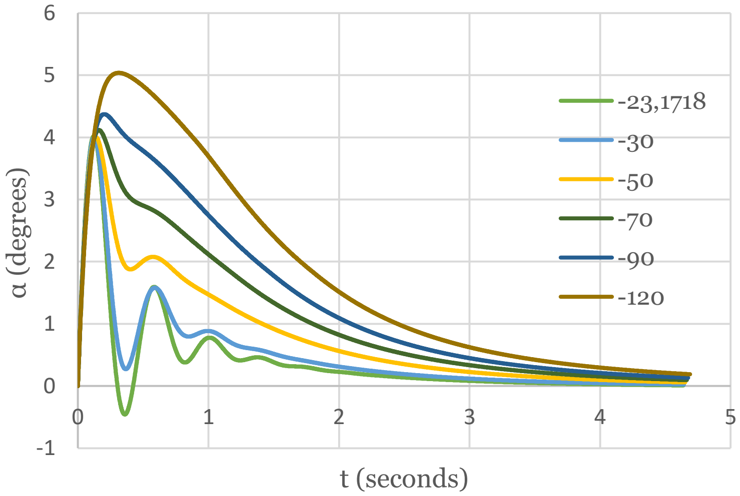

Figure 46 α(t) for different values of $\left(C_{M_{\dot{\alpha}}} + C_{M_q}\right)$*, from Case 1.8 considering an initial perturbation in q of 0.349 rad/s, considering the static coefficients and inertial properties of Configuration 3.*

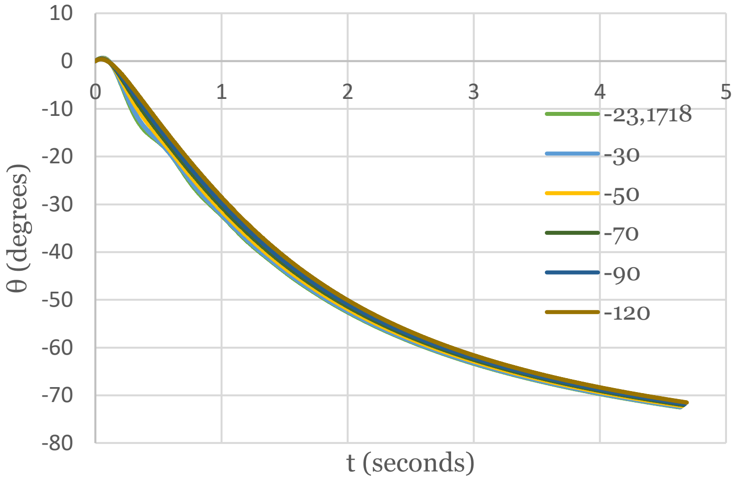

Figure 47 θ(t) for different values of $\left(C_{M_{\dot{\alpha}}} + C_{M_q}\right)$*, from Case 1.8 considering an initial perturbation in q of 0.349 rad/s, considering the static coefficients and inertial properties of Configuration 3.*

It can be observed that more negative values of $\left(C_{M_{\dot{\alpha}}} + C_{M_q}\right)$ allow for a quicker damping of the pitch and angle of attack values, while are also associated with a higher value of maximum α, which also occurs a bit later. From the simulated values for the dynamic coefficient, it seems that a value of -30 is desirable, since an under damped system remains stable and reactive, which is desirable.

In these trajectories, the coefficients are considered constant with Reynolds number, so it is relevant to assess if this consideration is affecting substantially their accuracy. Considering the study case 1.9, the terminal velocity is around 40 m/s for Configuration 2, 3, and 4. New coefficients were therefore obtained for that velocity, which, considering the same air properties, corresponds to a Reynolds number of around 301,000, around 2.7 times higher. These results are presented in Table 10.

Table 10 Percent difference for drag coefficient and lift coefficient between velocities 40 m/s and 15 m/s, for Configurations 2, 3, and 4.

	Configuration 2		Configuration 3		Configuration 4	
α (º)	Diff. C_D %	Diff. C_L %	Diff. C_D %	Diff. C_L %	Diff. C_D %	Diff. C_L %
0	-7.9	338.8	-13.5	-33.6	-13.9	-7.2
2	-15.8	45.9	-15.9	-3.5	-15.5	-2.4
4	-12.5	-15.6	-13.5	-0.5	-13.8	-0.6
6	-15.1	-10.5	-12.3	-0.2	-13.7	-0.7
8	-13.3	-1.0	-11.2	-0.2	-11.1	-0.1
10	-12.6	-4.0	-9.3	-1.2	-10.0	-0.8
12	-13.2	-1.6	-8.6	-0.1	-8.2	-0.1
14	-12.4	-0.3	-7.6	-0.1	-7.2	-0.4

In general, the increased Reynolds number translated to a decrease in both drag and lift coefficients. This decrease was more accentuated in the drag coefficient, and predominantly higher in Configuration 2, in both coefficients. This is because higher velocities in the flow around the leading sphere remains attached until a farther point, reducing the size of the wake and of the pressure drag. The high difference in the lift coefficient for angles of attack of 0 º and 2 º are not because of a very high difference in value, but because the values which they are compared to are very small, making the difference in percentage much more susceptible to differences in the coefficient value. On average, for this three configurations, increasing the Reynolds number of the flow to 2.7 times decreased the value of C_D around 12 % and the value of C_L around 4 %(without considering the two outliers in Configuration 2, for an angle of attack of 0 º and 2 º). This correlates to an increase in the flight velocity of the projectile, while changing the final x_g. This is more noticeable in cases with higher launching velocities and higher launching heights, since these are the cases that reach higher velocities and, therefore, higher Reynolds numbers.

7. Conclusions

The emerging situation regarding wildfires around the world was exposed, and the room for improvement regarding the first steps when tackling a wildfire, especially with the use of UAS, was laid out. Therefore, four projectile configurations which used a fire-extinguishing ball as a design basis were proposed and studied.

One of the considered configurations was just the FEB as it is. Its analysis was made resorting to papers and studies made on the aerodynamics of the sphere. As for the other configurations, which all had different tails and used empennages as mean of stabilization, their static aerodynamic coefficients were obtained through CFD, while the dynamic aerodynamic coefficients were obtained by simpler numerical methods. After their aerodynamic characterization was accomplished, a total of 17 trajectories were simulating resorting to an exterior ballistics model. These trajectories allowed for the comparison of the effect of different launching variables, the effect of mean wind and wind turbulence, size of the tail, and even the magnitude of the dynamic coefficients

It is possible to conclude that Configuration 1 and Configuration 2 both have an inherent difficulty in the predictability of their trajectory, for both have a transient behavior in the tested velocity range. Moreover, the 1st configuration, that is, the FEB as it is, might have a bad landing performance since the launching may resort to a fixed-wing UAV, which means that there will be a considerable translational speed. As for the cone tail and NACA tail configurations, their performance is very similar in the tested trajectories.

Regarding the studied trajectory cases, the consideration of the mean wind is of extreme importance, as it was expected, but the consideration of wind turbulence is also very important for the results, and a maximum difference in impact location of 2 meters was obtained, in trajectory case 1.7. Reynolds number might also have a considerable effect on the impact location, and considering its variation is relevant to obtain the greatest amount of accuracy possible.

The importance of the magnitude of the dynamic coefficients translates mostly to the stability and attitude characterization of the projectile.

Taking in consideration all the results, it can be concluded that the best suitable candidate for a fire-extinguishing projectile with an FEB as basis is Configuration 3, the tangential cone tail, since its behavior is easy to predict in the tested velocity range, and its construction is simple and able to be made resorting only to developable surfaces, which means it can be constructed with cheap, readily-available, and biodegradable materials, like cardboard. Moreover, this configuration would not need a drag reduction fairing, since it has a low drag in this velocity range.

The CFD methodology applied was extremely effective to obtain the results for the 3rd and 4th configurations, for their streamlined bodies. On the other hand, the results for the tube configuration have a transient behavior, with oscillatory values. Another problem related with this methodology application for Configuration 2 was the difficulty in replicating the results. However, the methodology allowed for an initial comparison between the different configurations for many different trajectories, without carrying a large computational cost. For the tube tail configuration, the best approach to obtain trajectory results with a much higher level of accuracy would be to obtain transient results or even implement an RBD/CFD coupled trajectory prediction method, although this carries great computational costs. Still in relation to the implemented CFD methodology, the use of double precision had a considerate positive impact in the precision of the results, as would be expected, but also had an important role in the convergence of these results, which the author did not predict according to their research.

7.1. Future work

The work present in this dissertation allowed for an initial analysis of the problem at question. However, it needs to be developed further, possibly tying together experimental results with the carried through theoretical and numerical analyses. Furthermore, some studies regarding the various aspects relating to this project need to be developed, such as the effectiveness of using FEB as means for fighting wildfires.

Undoubtedly, it is crucial to study the resistance of the FEB on impact. Since the outer material which comprises the ball is expanded polystyrene, it is possible it will not maintain its form on impact. It is relevant to assess if after impact, the FEB will work correctly.

After assessing the FEB’s resistance on impact, experimental launching of Configuration 3 should be carried out. If possible, the experimental results should be compared with the trajectories simulated in this work, or with new simulated trajectories.

Eventually, to apply the model of trajectory and impact prediction to a launching decision system, it will be necessary to obtain results for more Reynolds numbers, to guarantee the maximum accuracy possible.

It will also be relevant to implement an unsteady CFD methodology or other kind of techniques to find the value of $\left(C_{Z_{\dot{\alpha}}} + C_{Z_q}\right)$ and $\left(C_{M_{\dot{\alpha}}} + C_{M_q}\right)$ for the projectile. It was shown that a value around -30 is the most suitable for these launching velocities, and this result can be used to obtain the final configuration for the projectile.

References

[1] R. Fonte-Boa, "Análise de Balística Externa de um Projétil de Calibre 155 mm", Master's, IST - Universidade de Lisboa, 2014

[2] S. Marques et al., "Characterization of wildfires in Portugal", European Journal of Forest Research, vol. 130, no. 5, pp. 775-784, 2011

[3] A. Carvalho, M. Flannigan, K. Logan, L. Gowman, A. Miranda and C. Borrego, "The impact of spatial resolution on area burned and fire occurrence projections in Portugal under climate change", Climatic Change, vol. 98, no. 1-2, pp. 177-197, 2009

[4] L. Costa, K. Thonicke, B. Poulter and F. Badeck, "Sensitivity of Portuguese forest fires to climatic, human, and landscape variables: subnational differences between fire drivers in extreme fire years and decadal averages", Regional Environmental Change, vol. 11, no. 3, pp. 543-551, 2010

[5] A. Borunda, "How Fires In Europe Are Fueled By Climate Change", National Geographic, July 31, 2018. Accessed on: May 5, 2020. [Online]. Available: https://www.nationalgeographic.com/environment/2018/07/are-fires-in-europe-the-result-of-climate-change-/

[6] M. Green, "Australia's massive fires could become routine, climate scientists warn", Reuters, Jan. 14, 2020. Accessed on: May 5, 2020. [Online]. Available: https://www.reuters.com/article/us-climate-change-australia-report/australias-massive-fires-could-become-routine-climate-scientists-warn-idUSKBN1ZD06W

[7] "IPMA admite que é cada vez mais difícil prever risco de incêndio", PÚBLICO, Mar 27, 2019. Accessed on: May 5, 2020. [Online]. Available: https://www.publico.pt/2019/03/27/sociedade/noticia/chuva-calor-risco-incendio-imprevisivel-1866946

[8] Institute for Environment and Sustainability, "Recent forest fire related accidents in Europe", Publications Office of the European Union, Nov. 29, 2011

[9] D. Silva, "Why is Portugal so prone to wildfires?", Phys.org, July 24, 2019. Accessed on: May 5, 2020. [Online]. Available: https://phys.org/news/2019-07-portugal-prone-wildfires.html

[10] A. Ganteaume, A. Camia, M. Jappiot, J. San-Miguel-Ayanz, M. Long-Fournel and C. Lampin, "A Review of the Main Driving Factors of Forest Fire Ignition Over Europe", Environmental Management, vol. 51, no. 3, pp. 651-662, 2012

[11] F. Tedim, R. Remelgado, C. Borges, S. Carvalho and J. Martins, "Exploring the occurrence of mega-fires in Portugal", Forest Ecology and Management, vol. 294, pp. 86-96, 2013

[12] Departamento de Gestão de Áreas Públicas e de Proteção Florestal, "10.º Relatório provisório de incêionds florestais", Instituto da Conservação da Natureza e das Florestas, Oct. 11, 2017

[13] J. Phippen, "A Deadly Forest Fire in Portugal", The Atlantic, June 18, 2020. Accessed on: May 5, 2020. [Online]. Available: https://www.theatlantic.com/news/archive/2017/06/forest-fire-portugal/530745/

[14] A. Podlaha, S. Bowen, M. Lörinc, "Companion Volume to Weather, Climate & Catastrophe Insight: 2017 Annual Report", AON Plc, 2017

[15] "Incêndio em Monchique está ″dominado″. Arderam 27 mil hectares", Diário de Notícias, Aug. 10, 2018. Accessed on: May 5, 2020. [Online]. Available: https://www.dn.pt/pais/incendio-em-monchique-esta-dominado-arderam-27000-hectares-9702137.html

[16] California Department of Forestry and Fire Protection, "Top 20 Most Destructive California Wildfires", Mar. 14, 2019

[17] California Department of Forestry and Fire Protection, "Top 20 Largest California Wildfires", Mar. 14, 2019

[18] J. Burton, "'It was a line of fire coming at us': Firefighters return home", Busselton-Dunsborough Mail, Feb. 7, 2020. Accessed on: May 5, 2020. [Online]. Available: https://www.busseltonmail.com.au/story/6620313/it-was-a-line-of-fire-coming-at-us-firefighters-return-home/

[19] H. Lee, "Bushfires Release Over Half Australia's Annual Carbon Emissions", Time, Dec. 23, 2019. Accessed on: May 5, 2020. [Online]. Available: https://time.com/5754990/australia-carbon-emissions-fires/

[20] B. Butler, "Economic impact of Australia's bushfires set to exceed $4.4bn cost of Black Saturday", The Guardian, Jan. 7, 2020. Accessed on: May 5, 2020. [Online]. Available: https://www.theguardian.com/australia-news/2020/jan/08/economic-impact-of-australias-bushfires-set-to-exceed-44bn-cost-of-black-saturday

[21] C. Ferreira de Castro, G. Serra, J. Parola, J. Reis, L. Lourenço and S. Correia, Combate a incêndios florestais (vol. XIII), 2nd ed. Sintra: Escola Nacional de Bombeiros, 2003

[22] E. Zanenga, D. Leonello and C. Bottasso, "Feasibility Study of Rotorcraft Fire Fighting for High-Rise Buildings", Journal of Aerospace Engineering, vol. 23, no. 3, pp. 166-175, 2010

[23] T. Chen, P. Wu and Y. Chiou, "An early fire-detection method based on image processing", in International Conference on Image Processing, ICIP '04, 2004

[24] C. Yuan, Y. Zhang and Z. Liu, "A survey on technologies for automatic forest fire monitoring, detection, and fighting using unmanned aerial vehicles and remote sensing techniques", Canadian Journal of Forest Research, vol. 45, no. 7, pp. 783-792, 2015

[25] R. Graml and G. Wigley, "Bushfire Hotspot Detection Through Uninhabited Aerial Vehicles and Reconfigurable Computing", 2008 IEEE Aerospace Conference, 2008

[26] M. Avgeris, D. Spatharakis, D. Dechouniotis, N. Kalatzis, I. Roussaki and S. Papavassiliou, "Where There Is Fire There Is SMOKE: A Scalable Edge Computing Framework for Early Fire Detection", Sensors, vol. 19, no. 3, p. 639, 2019

[27] Z. Yahya Dewangga and S. Koesuma, "Development of forest fire early warning system based on the wireless sensor network in Lawu Mountain.", Journal of Physics: Conference Series, vol. 1153, p. 012025, 2019

[28] C. Yuan, Z. Liu and Y. Zhang, "Learning-Based Smoke Detection for Unmanned Aerial Vehicles Applied to Forest Fire Surveillance", Journal of Intelligent & Robotic Systems, vol. 93, no. 1-2, pp. 337-349, 2018

[29] M. Kumar, K. Cohen and B. HomChaudhuri, "Cooperative Control of Multiple Uninhabited Aerial Vehicles for Monitoring and Fighting Wildfires", Journal of Aerospace Computing, Information, and Communication, vol. 8, no. 1, pp. 1-16, 2011

[30] "Drones: Reporting for Work", Goldman Sachs. Accessed on: May 5, 2020. [Online]. Available: https://www.goldmansachs.com/insights/technology-driving-innovation/drones/

[31] J. Calado, "Projecto de um projéctil de caliber 155 mm para combate a incêndios florestais ", Master's, IST - Universidade de Lisboa, 2013

[32] "Firefighting Drones Infographic", Dronefly, 2018. Accessed on: May 21, 2020. [Online]. Available: https://www.dronefly.com/firefighting-drones-drones-in-the-field-infographic

[33] P. Schaft, "Firefighting Drones Aim to Fly Higher, Save More Lives", Robotics Business Review, July 25, 2018. Accessed on: May 21, 2020. [Online]. Available: https://www.roboticsbusinessreview.com/unmanned/firefighting-drones-aim-to-fly-higher-save-lives/

[34] E. Dias, "Desenvolvimento do conceito, fabrico e ensaio de um projéctil mecânico para combate a incêndios florestais: FIREND", Master's, IST - Universidade de Lisboa, 2007

[35] R. McCoy, Modern exterior ballistics. Atglen, Philadelphia: Schiffer Publishing, 1999

[36] M. Khalil, X. Rui and H. Hendy, "Discrete Time Transfer Matrix Method for Projectile Trajectory Prediction", Journal of Aerospace Engineering, vol. 28, no. 2, p. 04014057, 2015

[37] D. Marques, "Estudo de balística interna ", Master's, CET – Academia Militar, 2014

[38] D. Carlucci and S. Jacobson, Ballistics: Theory and design of guns and ammunition. Boca Raton, Florida: CRC Press, 2008

[39] V. Ravindra, Y. Bar-Shalom and P. Willett, "Impact point prediction and projectile identification", in Signal and Data Processing of Small Targets: Optical Engineering and Applications, San Diego, California, 2007

[40] J. Kokes, M. Costello and J. Sahu, "Generating an aerodynamic model for projectile flight simulation using unsteady time accurate computational fluid dynamic results", Computational Ballistics III, 2007

[41] C. Hutton, "Tartaglia", A Philosophical and Mathematical Dictionary, Vol. 2 of 2. 2020

[42] "Tartaglia, Niccolò", Encyclopædia Britannica. Horace Everett Hooper, 1910.

[43] L. Hainz and M. Costello, "Modified Projectile Linear Theory for Rapid Trajectory Prediction", Journal of Guidance, Control, and Dynamics, vol. 28, no. 5, pp. 1006-1014, 2005

[44] A. Elsaadany and Y. Wen-jun, "Accurate Trajectory Prediction for Typical Artillery Projectile", in Conference: Control Conference (CCC), Nanjing, China, 2014

[45] L. Barbosa, A. Blanco, D. Dutra, W. Santana and J. Abrunhosa, "A critical evaluation of three models of external ballistics", in International Congress of Mechanical Engineering, COBEM, Ouro Preto, Minas Gerais, 2005

[46] V. Ivchenko, "On projectile motion with quadratic drag force", European Journal of Physics, vol. 39, no. 4, p. 045004, Apr. 30 2018

[47] "X. The aerodynamics of a spinning shell", Philosophical Transactions of the Royal Society of London. Series A, Containing Papers of a Mathematical or Physical Character, vol. 221, no. 582-593, pp. 295-387, 1921

[48] L. Baranowski, "Feasibility analysis of the modified point mass trajectory model for the need of ground artillery fire control systems", Journal of Theoretical and Applied Mechanics, vol. 51, no. 3, pp. 511-522, 2013

[49] U. S. Army Materiel Command, Ballistic Research Laboratories, "Equations of motion for a Modified Point Mass trajectory", Maryland, 1966

[50] O. Nordgren, "Development and Evaluation of a Modified Point-Mass Trajectory Model using Firing Data", Master's, KTH Royal Institute of Technology, 2014

[51] L. Baranowski, B. Gadomski, P. Majewski and J. Szymonik, "Explicit “ballistic M-model”: a refinement of the implicit “modified point mass trajectory model”", Bulletin of the Polish Academy of Sciences Technical Sciences, vol. 64, no. 1, pp. 81-89, 2016

[52] G. Cooper and M. Costello, "Flight Dynamic Response of Spinning Projectiles to Lateral Impulsive Loads", Journal of Dynamic Systems, Measurement, and Control, vol. 126, no. 3, pp. 605-613, 2004

[53] G. Cooper, F. Fresconi and M. Costello, "Flight Stability of an Asymmetric Projectile with Activating Canars", Journal of Spacecraft and Rockets, vol. 49, no. 1, pp. 130-135, 2012

[54] G. Kowaleczko and A. Żyluk, "Influence of Atmospheric turbulence on bomb release", Journal of Theoretical and Applied Mechanics, vol. 47, no. 1, pp. 69-90, 2009

[55] J. Sahu, "Time-Accurate Numerical Prediction of Free-Flight Aerodynamics of a Finned Projectile", Journal of Spacecraft and Rockets, vol. 45, no. 5, pp. 946-954, 2008

[56] A. Attallah, "Modeling and Simulation for Free Fall Bomb Dynamics in Windy Environment", in 16th International Conference on AEROSPACE SCIENCES & AVIATION TECHNOLOGY, ASAT - 16, 2015

[57] D. Raymer, Aircraft design, 2nd ed. AIAA, 1992

[58] H. Lyon, "The effect of turbulence on the drag of airship models", Master's, Massachusetts Institute of Technology, 1932

[59] S. Hoerner, Fluid-dynamic Drag. Bakersfield, Californa, 1992

[60] M. Karim, M. Rahman and M. Alim, "Computation of Axisymmetric Turbulent Viscous Flow Around Sphere", Journal of Scientific Research, vol. 1, no. 2, pp. 209-219, 2009

[61] P. Weinacht, "Projectile Performance, Stability, and Free-Flight Motion Prediction Using Computational Fluid Dynamics", Journal of Spacecraft and Rockets, vol. 41, no. 2, pp. 257-263, 2004

[62] M. Karim, M. Rahman and M. Alim, "Comparative study between flows around sphere and pod using finite volume method", Journal of Naval Architecture and Marine Engineering, vol. 8, no. 1, pp. 49-58, 2011

[63] D. Durston, "LinAir: A multi-element discret vortex Weissinger aerodynamic prediction method", NASA, 1993

[64] “Projectile", Merriam-Webster.com Dictionary

[65] A. Godfrey, An Account of the New Method of Extinguishing Fires by Explosion and Suffocation, London, 1724

[66] K. Kohlstedt, "Stop, Drop & Roll (or Throw): Fighting Fires with Fire Grenades - 99% Invisible", 99% Invisible, June 13, 2018. Accessed on: May 24, 2019. [Online]. Available: https://99percentinvisible.org/article/stop-drop-roll-throw-fighting-fires-fire-grenades/

[67] "BBC - A History of the World - Object : Harden Star Fire Grenades", Bbc.co.uk, 2014. Accessed on: May 5, 2019. [Online]. Available: http://www.bbc.co.uk/ahistoryoftheworld/objects/HqIKMBwbSM2Hxf2EXPCBRA.

[68] R. Chisholm, "Fire-extinguishing gun", United States Patent 798355, 1905

[69] R. Roberts, “Aerial device for fire extinguishing, etc.”, United States Patent2306321A, 1942

[70] D. Mackay, “Means for fighting forest fires”, United States Patent 2359573A, 1944

[71] J. Pearson, J. Rall, “Projectile fire extinguishing device”, United States Patent 30657984, 1962

[72] A. Briddon, “Large fires extinguished from safe distance by projectile - containing extinguishing agent spread by explosive or pressurised gas”, Germany Patent 2518918A1, 1976

[73] A. Moreau, “Air borne device for fighting forest fires”, European Patent 0320554A1, 1989

[74] D. Fiorelli, “Projectile for spraying fire-resistant substances over burning areas”, International Patent 1992012763A1, 1992

[75] S. Ishida, “Mountain fire-extinguishing rocket shell”, Japan Patent H0951957A, 1997

[76] J. O’Dwyer, “Projectile launching apparatus”, United States Patent 20050022657A1, 2005

[77] C. Daegun, “A bomb for forest fire extinguishing and installing the fire prevention”, South Korea Patent 20020042394A, 2002

[78] R. Woodall, F. Garcia, C. Doyle, “Fire retardant bio-friendly practice munition”, United States Patent 6470805B1, 2002

[79] W. Cleary, M. Rhohrlick, “Firefighting bomblets and a precision aerial firefighting method utilizing the same”, United States Patent 20060011355A1, 2006

[80] V. Korenkov, et. al, “Method and Device for Controlling and/or Putting Out Fires”, United States Patent 20080271900A1, 2008

[81] M. Shangkai, “Fire-extinguishing bomb”, China Patent 1935295A, 2007

[82] H. Wang, “Mortar bomb for extinguishing forest fire”, China Patent 201123970Y, 2008

[83] C. Li, “Fire-fighting bomb for forest”, China Patent 101485924A, 2009

[84] R. Pavesi, “Silent responder fire fighting systems”, United States Patent 20120061109A1, 2012

[85] J. Fernadez, “Firefighting apparatus”, United States Patent 9119981B2, 2011

[86] B. Zhang, “Firefighting bomb”, China Patent 103471471A, 2013

[87] T. Erickson, et. al., “Fire-retarding artillery shell”, United States Patent 20160216091A1, 2016

[88] B. Aydin and E. Selvi, J. Tao and M. Starek, "Use of Fire-Extinguishing Balls for a Conceptual System of Drone-Assisted Wildfire Fighting", Drones, vol. 3, no. 1, p. 17, 2019

[89] L. Almeida, “Stress analysis and design of a 155 mm projectile shell to be used in firefighting”, Master’s, IST – Universidade de Lisboa, 2016

[90] V. Korenkov, "ASP - 500 Fire-extinguishing Air System", Revue Militaire Suisse, vol. 149, no. 9, pp. 32-33, 2004

[91] Kilburn Fire Extinguisher Bomb (KFEB), 2015. Accessed on: July 11, 2019. [Online]. Available: http://www.kilburnfeb1.com/

[92] Elidefire - Portugal - Bola extintora. Accessed on: May 5, 2019. [Online]. Available: https://www.elidefire.pt/

[93] Automatic Fire Extinguisher Ball Manufacturer and Supplier in India. Accessed on: May 5, 2019. [Online]. Available: https://www.afofireballs.com/

[94] V. Sherstjuk, M. Zharikova and I. Sokol, "Forest Fire Fighting Using Heterogeneous Ensemble of Unmanned Aerial Vehicles," 2019 IEEE 5th International Conference Actual Problems of Unmanned Aerial Vehicles Developments (APUAVD), Kiev, Ukraine, 2019, pp. 218-223

[95] W. Marchant and S. Tosunoglu, "Rethinking Wildfire Suppression With Swarm Robotics", in 22th Florida Conference on Recent Advances in Robotics, FCRAR 2016, Miami, Florida, 2016, pp. 186-191

[96] C. Beltran, M. Freitas and A. Moribe, "Unmanned Aerial Vehicle with fire Extinguishing Grenade Release and Inspection System", Florida International University, November 2013

[97] "Fire Terminology", Fs.fed.us. Accessed on: May 8, 2020 [Online]. Available: https://www.fs.fed.us/nwacfire/home/terminology.html

[98] “Unidade de Emergência de Proteção e Socorro”, GNR. Accessed on: May 8, 2020. [Online]. Availabe: https://www.gnr.pt/atrib_GIPS.aspx

[99] “Somejumpers: 80 Years of Wildland Firefighting”, Smokejumpers, March 18, 2020. Accessed on: May 8 2020. [Online]. Availabe: https://storymaps.arcgis.com/stories/381fcd4a36584aa28f9d836247d9a939

[100] “Russian Smokejumpers”, National Geographic. Accessed on: May 8 2020. [Online]. Availabe: https://www.nationalgeographic.com/environment/natural-disasters/russian-smokejumpers

[101] Castanheira and C. Marques, “Fabrico e ensaio balístico em condições reais de conceito melhorado de um projétil de detonação mecânica”, Master’s, CET – Academia Militar, Oct. 2012

[102] L. Vočadlo, Class Lecture, Topic:"Global Geophysics"GEOL0012, University College of London, London

[103] G. Larose and A. D’Auteuil, "On the Reynolds number sensitivity of the aerodynamics of bluff bodies with sharp edges", Journal of Wind Engineering and Industrial Aerodynamics, vol. 94, no. 5, pp. 365-376, 2006

[104] V. Brederode, Fundamentos de Aerodinâmica Incompressível, 1st ed. IDMEC Instituto Superior Técnico, 1997

[105] S. Hoerner and H. Borst, Fluid-dynamic Lift, 2nd ed. Albuquerque, New Mexico, 1992

[106] “Coriolis force”, Encyclopædia Britannica. Accessed on: June 18, 2019. [Online]. Available: https://www.britannica.com/science/Coriolis-force

[107] "Coriolis Effect", National Geographic. Accessed on: June 18, 2019. [Online]. Available: https://www.nationalgeographic.org/encyclopedia/coriolis-effect/

[108] Cornell Aeronautical Laboratory, "Background Information and User Guide for Mil-F-8785B (ASG), 'Military Specification-Flying Qualities of Piloted Airplanes'", Buffalo, New York, 1969

[109] P. Zipfel, Modeling and Simulation of Aerospace Vehicle Dynamics, 2nd ed. AIAA, 2007

[110] M. Shinozuka, "Simulation of Multivariate and Multidimensional Random Processes", The Journal of the Acoustical Society of America, vol. 49, no. 1, pp. 357-368, 1971

[111] T. de Karman and L. Howarth, "On the Statistical Theory of Isotropic Turbulence", Proceedings of the Royal Society of London. Series A - Mathematical and Physical Sciences, vol. 164, no. 917, pp. 192-215, 1938

[112] H. Dryden, “A review of the statistical theory of turbulence”, in Turbulence: Classical Papers on Statistical Theory, 1942, ch. 5, pp. 115-132

[113] MATLAB Simulink. Mathworks Inc., 2015

[114] “Generate continuous wind turbulence with Dryden velocity spectra – Simulink”, MathWorks. Accessed on: Dec 16. 2019. [Online]. Available: https://www.mathworks.com/help/aeroblks/drydenwindturbulencemodelcontinuous.html

[115] B. Etkin and L. Reid, Dynamics of flight: stability and control, 3rd ed. 1996

[116] ANSYS. Ansys Inc., 2018

[117] ANSYS Fluent User’s Guide, Release 18.2, ANSYS, Inc. 2017

[118] D. Jones and D. Clarke, "Simulation of Flow Past a Sphere using the Fluent Code", Defence Science and Technology Organisation - Maritime Platforms Division, Victoria, Australia, 2008

[119] CATIA V6, Dassault Systemes SolidWorks Corporation, 2011

[120] “Standard Atmosphere”, International Organization for Standardization, ISO 2533:1975, 1975

[121] F. Menter, "Two-equation eddy-viscosity turbulence models for engineering applications", AIAA Journal, vol. 32, no. 8, pp. 1598-1605, 1994

[122] J. Hart, "Comparison of Turbulence Modeling Approaches to the Simulation of a Dimpled Sphere", Procedia Engineering, vol. 147, pp. 68-73, 2016

[123] F. Menter, M. Kuntz and R. Langstry, “Ten Years of Industrial Experience with the SST Turbulence Model”, Turbulence, Heat and Mass Transfer 4, 2003

[124] C. Zhang, C. Bounds, L. Foster and M. Uddin, "Turbulence Modeling Effects on the CFD Predictions of Flow over a Detailed Full-Scale Sedan Vehicle", Fluids, vol. 4, no. 3, p. 148, 2019

[125] V. Bhagwandin and J. Sahu, "Numerical Prediction of Pitch Damping Derivatives for a Finned Projectile at Angles of Attack", 50th AIAA Aerospace Sciences Meeting including the New Horizons Forum and Aerospace Exposition, 2012

[126] V. Bhagwandin and J. Sahu, "Numerical Prediction of Pitch Damping Stability Derivatives for Finned Projectiles", Journal of Spacecraft and Rockets, vol. 51, no. 5, pp. 1603-1618, 2014

[127] J. Sahu and K. Heavey, "Time-Accurate Computations for Rapid Generation of Missile Aerodynamics", AIAA Atmospheric Flight Mechanics Conference, 2010

[128] J. Danberg and P. Weinacht, "An Approximate Method for Pitch-Damping Prediction", U.S. Army Research Laboratory, 2003

[129] P. Weinacht and J. Danberg, "Prediction of the Pitch-Damping Coefficients Using Sacks's Relations", Journal of Spacecraft and Rockets, vol. 42, no. 5, pp. 865-872, 2005

[130] C. Grillo and F. Montano, "An Extended Kalman Filter-Based Technique for On-Line Identification of Unmanned Aerial System Parameters", Journal of Aerospace Technology and Management, vol. 7, no. 3, pp. 323-333, 2015

[131] XFLR5, Open-source software, 2019

[132] B. Hunt, "Asymmetric vortex forces and wakes on slender bodies", in 9th Atmospheric Flight Mechanics Conference, San Diego, California, 1982

[133] D. Degani, "Effect of splitter plate on unsteady flows around a body of revolution at incidence", Physics of Fluids A: Fluid Dynamics, vol. 3, no. 9, pp. 2122-2131, 1991

[134] V. de Briey, I. Ndindabahizi, B. Marinus and M. Pirlot, "Aerodynamical CFD Study of a Non-Lethal 12-Gauge Fin-Stabilized Projectile", Human Factors and Mechanical Engineering for Defense and Safety, vol. 3, no. 1, 2019

[135] "Aerospaceweb.org | Ask Us - Missile Control Systems", Aerospaceweb.org. Accessed on: May 10, 2020. [Online]. Available: http://www.aerospaceweb.org/question/weapons/q0158.shtml

[136] Naval Ordnance Laboratory, “Static and Dynamic stability studies on several Lazy Dog configurations at subsonic and transonic speeds”, May 18, 1964

[137] Center for International Stabilization and Recovery, “Iraq Ordnance Identification Guide – Bombs”, James Madison University

[138] S. Callens and A. Zadpoor, "From flat sheets to curved geometries: Origami and kirigami approaches", Materials Today, vol. 21, no. 3, pp. 241-264, 2018

[139] J. Southard, Class Lecture, Topic: “Introduction to Fluid Motions, Sediment Transport, and Current-Generated Sedimentary Structures” 12.090, Massachusetts Institute of Technology, Cambridge, 2006

[140] G. Constantinescu and K. Squires, "Numerical investigations of flow over a sphere in the subcritical and supercritical regimes", Physics of Fluids, vol. 16, no. 5, pp. 1449-1466, 2004

[141] H. Sakamoto and H. Haniu, "A Study on Vortex Shedding From Spheres in a Uniform Flow", Journal of Fluids Engineering, vol. 112, no. 4, pp. 386-392, 1990

[142] Y. Wang, P. Jackson and J. Ackerman, "Numerical investigations of flow over a sphere using LES and the Spalart-Allmaras turbulence model", in Thirteenth annual conference of the Computation Fluid Dynamics Society of Canada (CFD 2005), Newfoundland, Canada, 2005

[143] A. Norman and B. McKeon, "Unsteady force measurements in sphere flow from subcritical to supercritical Reynolds numbers", Experiments in Fluids, vol. 51, no. 5, pp. 1439-1453, 2011

[144] E. Achenbach, "Experiments on the flow past spheres at very high Reynolds numbers", Journal of Fluid Mechanics, vol. 54, no. 3, pp. 565-575, 1972

[145] R. Deshpande, A. Desai, V. Kanti and S. Mittal, "Experimental investigation of boundary layer transition in flow past a bluff body", Journal of Physics: Conference Series, vol. 822, no. 1, p. 012003, 2017

[146] S. Hoerner, "Tests of Spheres with Reference to Reynolds Number, Turbulence, and Surface Roughness", National Advisory Committee for Aerodynamics, Washington, Oct. 1, 1935

[147] D. Bacon and E. Reid, "The resistance of spheres in wind tunnels and in air", National Advisory Committee for Aeronautics, Langley Aeronautical Laboratory, Washington, Jan. 1, 1967

[148] J. Seifert, "A review of the Magnus effect in aeronautics", Progress in Aerospace Sciences, vol. 55, pp. 17-45, 2012

[149] V. de Briey, B. Marinus and M. Pirlot, "Aerodynamic Characterization of a Non-Lethal Finned Projectile at Low Subsonic Velocity", in AIAA Aviation 2019 Forum, Dallas, Texas, 2019

[150] “Density of Selected Solids”, Engineering Toolbox. Accessed on: May 8, 2020. [Online]. Available: https://www.engineeringtoolbox.com/density-solids-d_1265.html

Annexes

Annex 1 – Nondimensionalized coordinates of the fins’ airfoil

x/c	y/c	x/c	y/c	x/c	y/c	x/c	y/c
1	0	0.087358	0.028409	0.000812	-0.00674	0.9375	-0,02841
0.999188	0.006742	0.075568	0.028409	0.001623	-0.00947	0.948864	-0,02841
0.998377	0.009466	0.063778	0.028409	0.002435	-0.01151	0.960227	-0,02841
0.997565	0.011508	0.051989	0.028409	0.003247	-0.01319	0.971591	-0,02841
0.996753	0.013188	0.040199	0.028409	0.004058	-0.01463	0.972403	-0,0284
0.995942	0.014633	0.028409	0.028409	0.00487	-0.01591	0.973214	-0,02836
0.99513	0.015906	0.027597	0.028397	0.005682	-0.01705	0.974026	-0,0283
0.994318	0.017045	0.026786	0.028363	0.006494	-0.01808	0.974838	-0,02822
0.993506	0.018077	0.025974	0.028305	0.007305	-0.01902	0.975649	-0,02812
0.992695	0.019018	0.025162	0.028223	0.008117	-0.01988	0.976461	-0,02799
0.991883	0.019882	0.024351	0.028118	0.008929	-0.02068	0.977273	-0,02784
0.991071	0.020678	0.023539	0.027989	0.00974	-0.02141	0.978084	-0,02766
0.99026	0.021414	0.022727	0.027835	0.010552	-0.0221	0.978896	-0,02745
0.989448	0.022095	0.021916	0.027657	0.011364	-0.02273	0.979708	-0,02722
0.988636	0.022727	0.021104	0.027454	0.012175	-0.02331	0.980519	-0,02697
0.987825	0.023314	0.020292	0.027225	0.012987	-0.02386	0.981331	-0,02669
0.987013	0.023859	0.019481	0.02697	0.013799	-0.02436	0.982143	-0,02638
0.986201	0.024364	0.018669	0.026687	0.01461	-0.02483	0.982955	-0,02604
0.98539	0.024833	0.017857	0.026377	0.015422	-0.02527	0.983766	-0,02567
0.984578	0.025267	0.017045	0.026037	0.016234	-0.02567	0.984578	-0,02527
0.983766	0.025668	0.016234	0.025668	0.017045	-0.02604	0.98539	-0,02483
0.982955	0.026037	0.015422	0.025267	0.017857	-0.02638	0.986201	-0,02436
0.982143	0.026377	0.01461	0.024833	0.018669	-0.02669	0.987013	-0,02386
0.981331	0.026687	0.013799	0.024364	0.019481	-0.02697	0.987825	-0,02331
0.980519	0.02697	0.012987	0.023859	0.020292	-0.02722	0.988636	-0,02273
0.979708	0.027225	0.012175	0.023314	0.021104	-0.02745	0.989448	-0,0221
0.978896	0.027454	0.011364	0.022727	0.021916	-0.02766	0.99026	-0,02141
0.978084	0.027657	0.010552	0.022095	0.022727	-0.02784	0.991071	-0,02068
0.977273	0.027835	0.00974	0.021414	0.023539	-0.02799	0.991883	-0,01988
0.976461	0.027989	0.008929	0.020678	0.024351	-0.02812	0.992695	-0,01902
0.975649	0.028118	0.008117	0.019882	0.025162	-0.02822	0.993506	-0,01808
0.974838	0.028223	0.007305	0.019018	0.025974	-0.0283	0.994318	-0,01705
0.974026	0.028305	0.006494	0.018077	0.026786	-0.02836	0.99513	-0,01591
0.973214	0.028363	0.005682	0.017045	0.027597	-0.0284	0.995942	-0,01463
0.972403	0.028397	0.00487	0.015906	0.028409	-0.02841	0.996753	-0,01319
0.971591	0.028409	0.004058	0.014633	0.040199	-0.02841	0.997565	-0,01151
0.960227	0.028409	0.003247	0.013188	0.051989	-0.02841	0.998377	-0,00947
0.948864	0.028409	0.002435	0.011508	0.063778	-0.02841	0.999188	-0,00674
0.9375	0.028409	0.001623	0.009466	0.075568	-0.02841	1	0
0.926136	0.028409	0.000812	0.006742	0.087358	-0.02841		
0.914773	0.028409	0	0	0.926136	-0,02841		

Annex 2 – Three-view drawing of Configuration 2

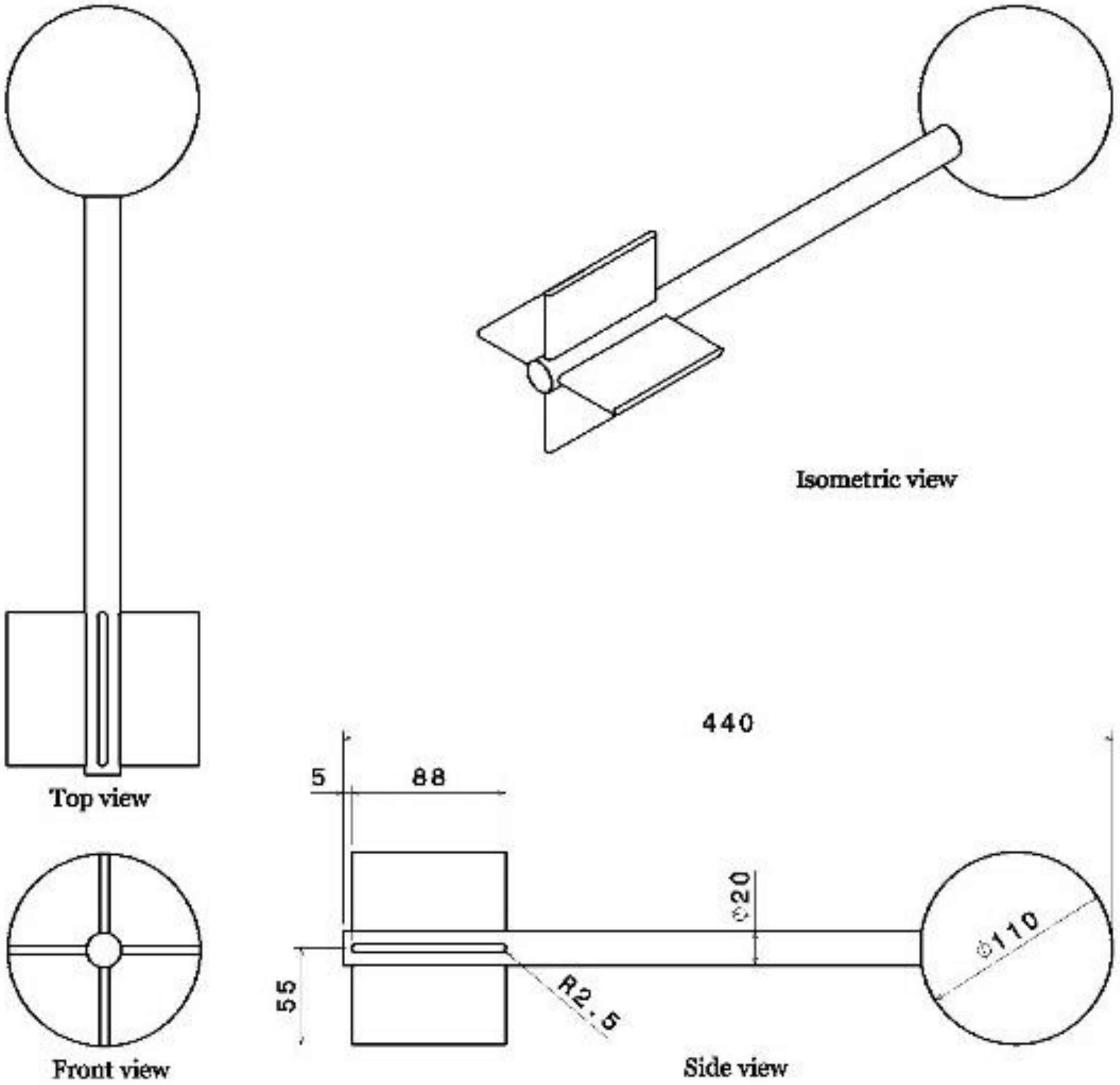

Figure 48 Three-view drawing of Configuration 2.

Annex 3 – Three-view drawing of Configuration 3

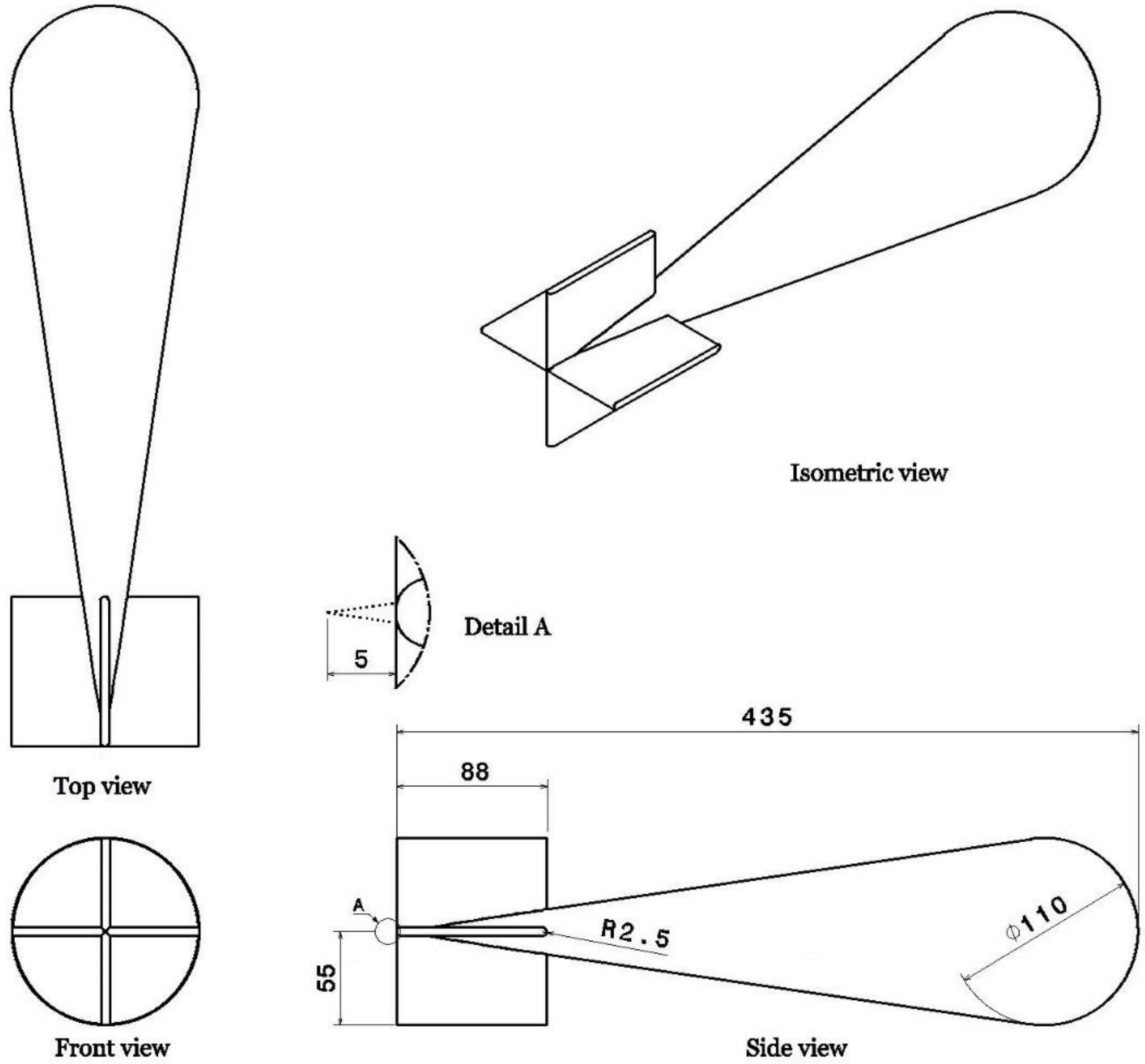

Figure 49 Three-view drawing of Configuration 3.

Annex 4 – Three-view drawing of Configuration 4

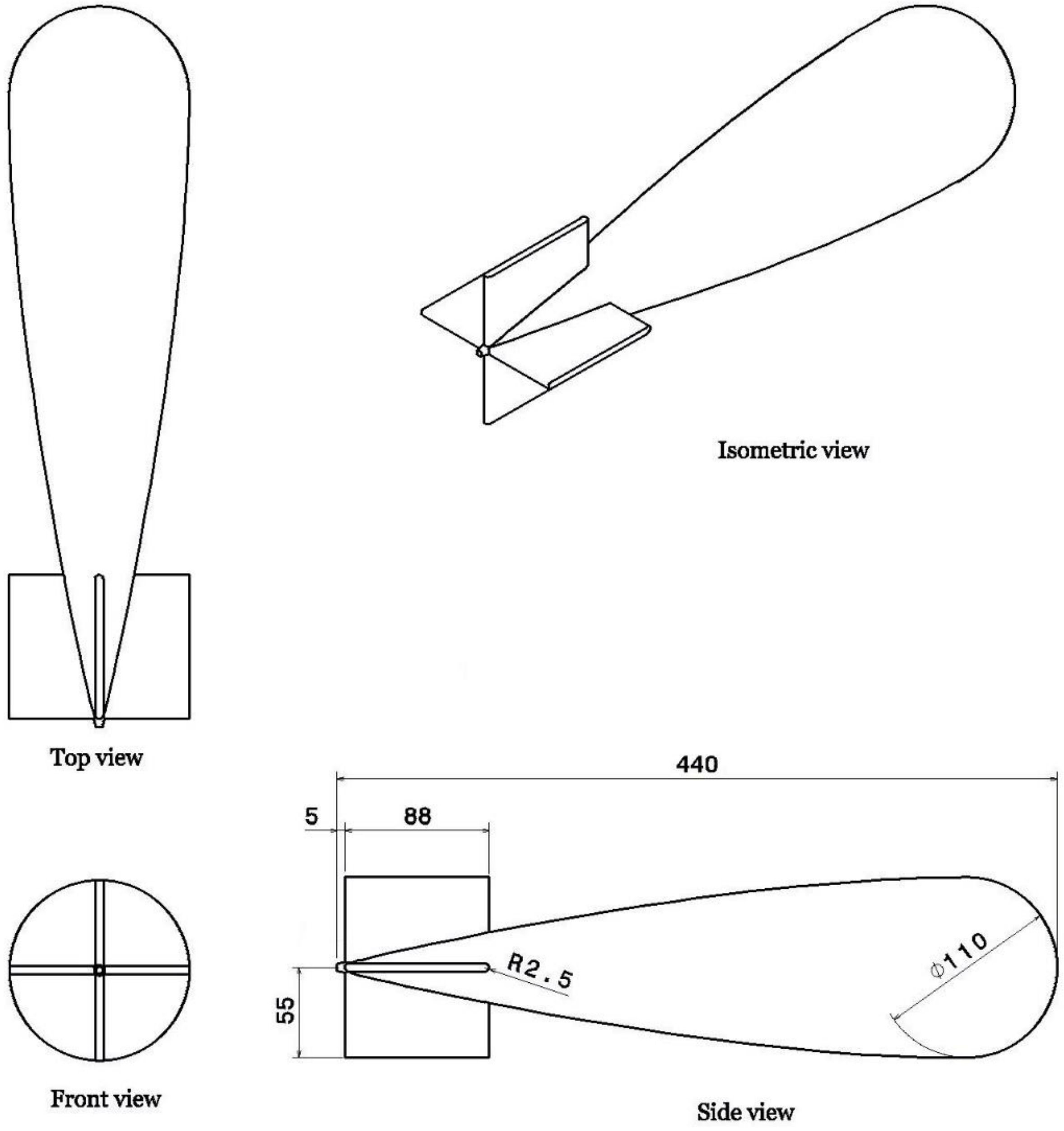
Isometric view

Top view

Front view

Side view

Figure 50 Three-view drawing of Configuration 4.

Annex 5 – Results for CFD validation

Table 11 Results for CFD validation for the Non-Lethal 12-Gauge Fin-stabilized projectile. The percent errors are in relation to the results from [149].

α (º)	C_D	C_L	E_{Drag} (%)	E_{Lift} (%)
0	0.141	0.0002	7.1	69.2
2	0.1434	0.0469	7.2	1.3
4	0.1499	0.0973	6.8	0.8
6	0.1602	0.1578	13.2	1.7
8	0.3162	0.2018	2.8	7.1
10	0.3845	0.2356	6.6	2.4
12	0.4352	0.2322	6.1	6.3
14	0.4773	0.2217	6.5	3.4
16	0.5195	0.2354	6.7	3.7
18	0.5607	0.2535	6.2	3.9
20	0.6018	0.2693	4.3	1.7

Annex 6 – Results for Grid independence study

Table 12 Results for Grid independence study, for Configuration 3.

Nº of Elements	C_D
495,4941	0.1247
7,506,355	0.1046
15,220,376	0.1080
22,711,992	0.1081
30,400,655	0.1077
41,026,695	0.1078
49,309,001	0.1076
60,914,428	0.1071

Annex 7 – CFD static pressure results for the fins at α=14º, in Configuration 3

Figures 51 and 52 show the static pressure distribution for the fins at 14 º of angle of attack, in Configuration 3, at 15 m/s.

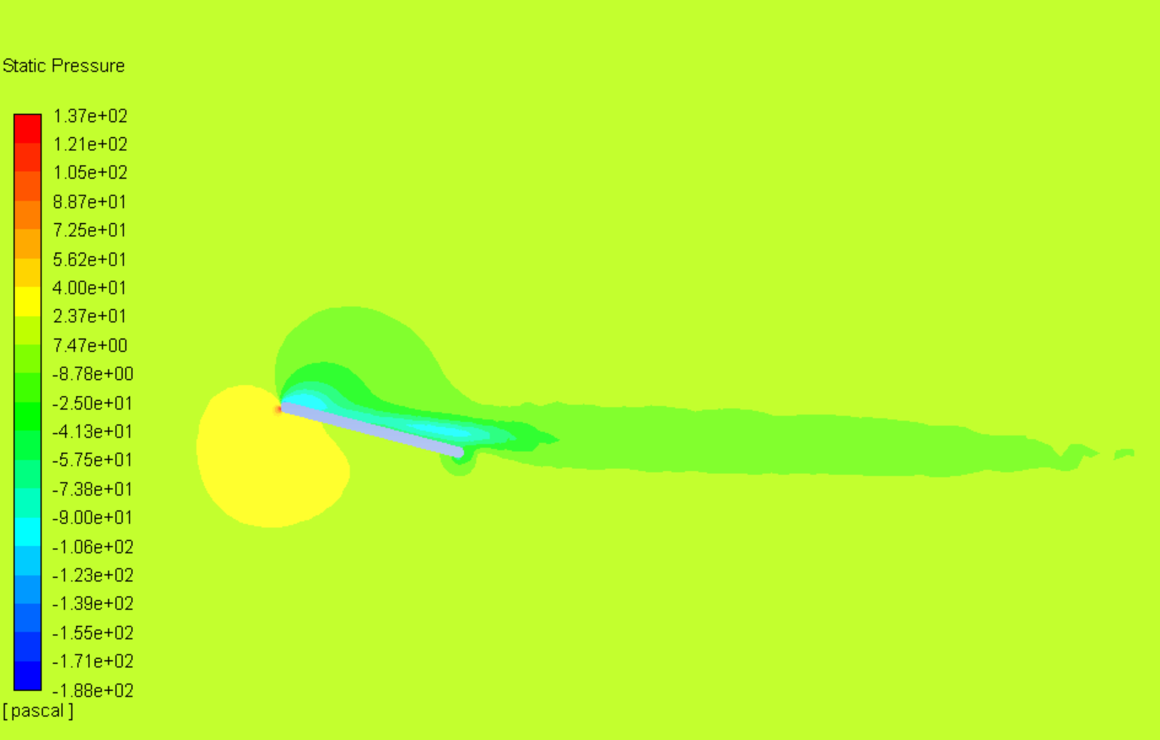

Figure 51 CFD static pressure results for the fins at 14º of angle of attack, in Configuration 3, viewed from plane xy.

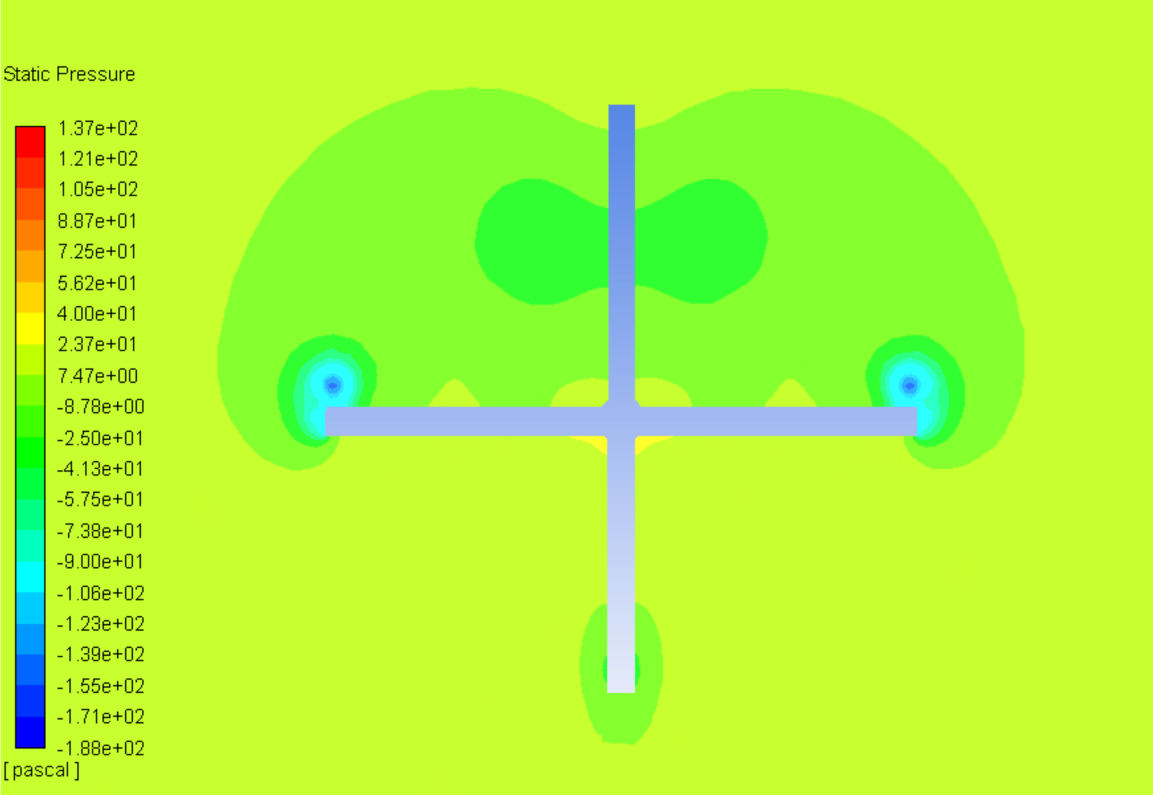

Figure 52 CFD static pressure results for the fins at 14º of angle of attack, in Configuration 3, viewed from the plane perpendicular to the fins, located at the Aerodynamic Center (18.18% of the chord):

Annex 8 – CFD aerodynamic results for Configuration 2

Table 13 CFD aerodynamic results for the static aerodynamic coefficients, for Configuration 2, at 15 m/s.

α (º)	C_D	C_L	C_M
0	0.2908	0.0018	-0.0031
2	0.2964	0.0324	-0.2667
4	0.3107	0.0664	-0.4325
6	0.3331	0.1446	-0.5548
8	0.3530	0.2084	-0.7176
10	0.3778	0.2824	-0.8706
12	0.4066	0.3578	-1.0291
14	0.4414	0.4283	-1.1888

Table 14 CFD aerodynamic results for the static aerodynamic coefficients, for Configuration 2, at 40 m/s.

α(º)	C_D	C_L
0	0.2678	0.0081
2	0.2495	0.0473
4	0.2719	0.0561
6	0.2829	0.1295
8	0.3060	0.2063
10	0.3302	0.2711
12	0.3528	0.3521
14	0.3867	0.4269

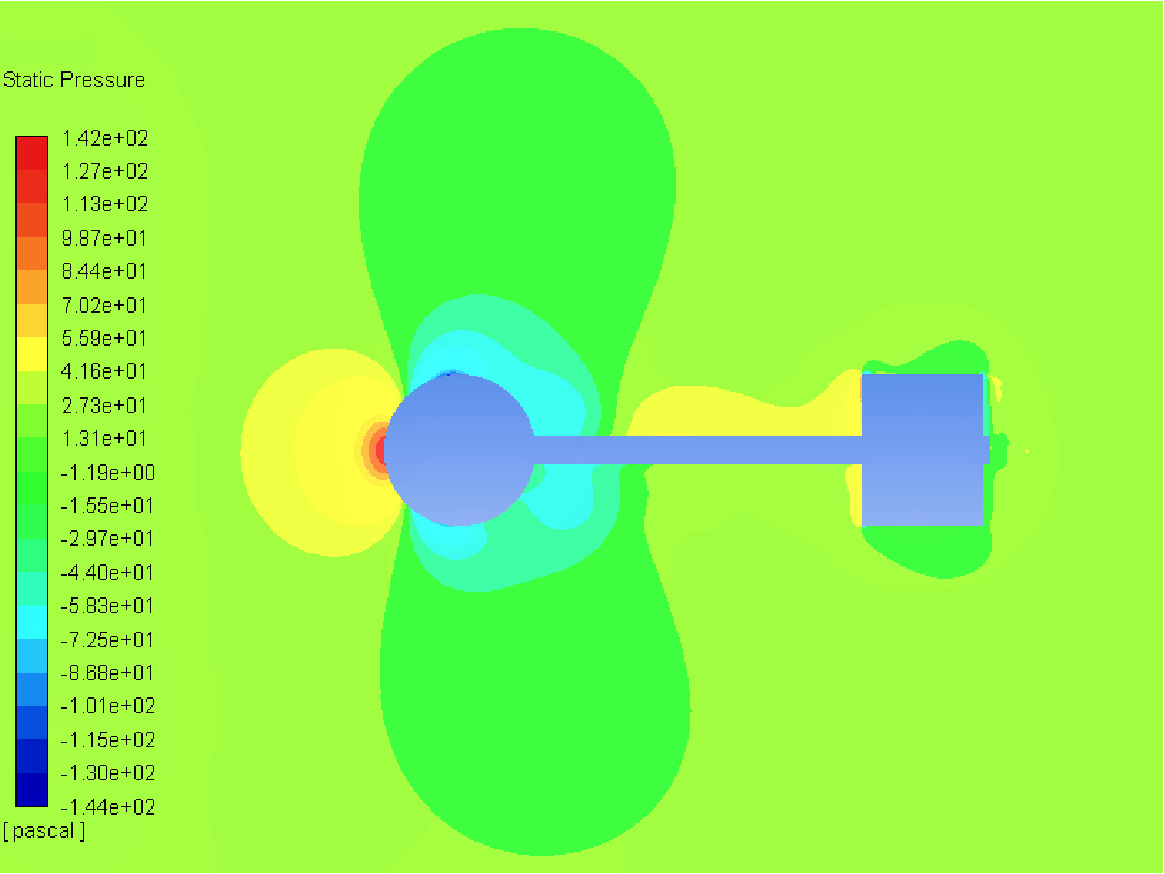

Figure 53 CFD static pressure results for Configuration 2 at 0º of angle of attack, viewed from plane xy

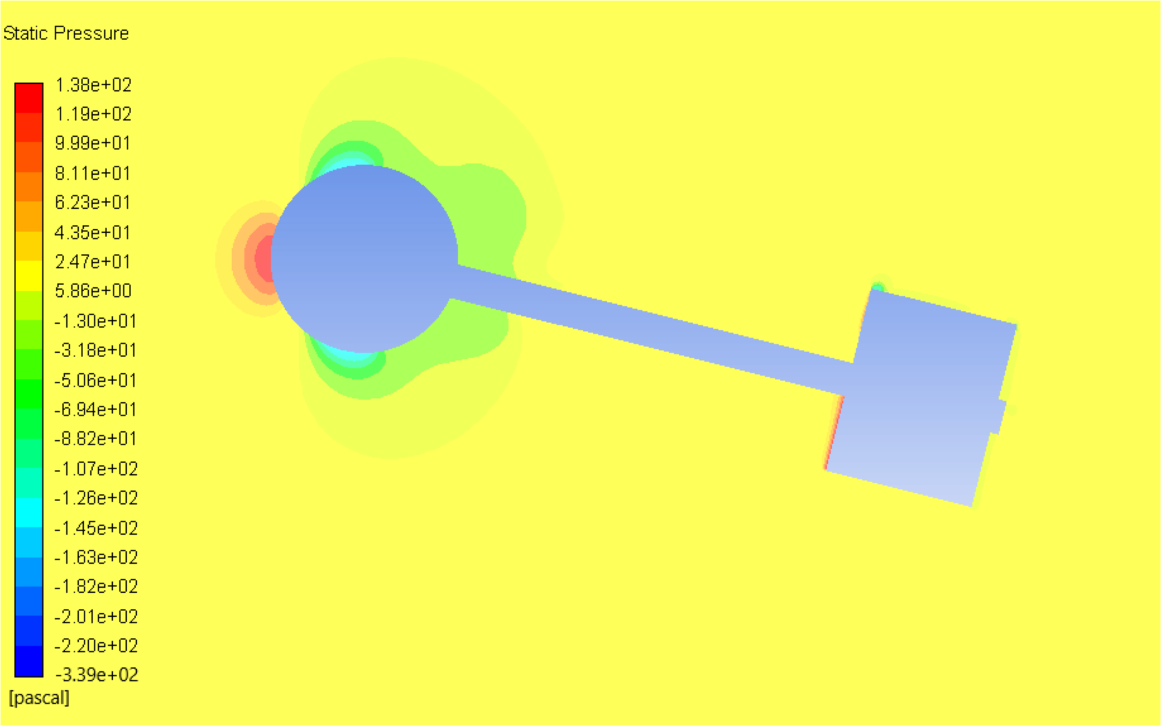

Figure 54 CFD static pressure results for Configuration 2 at 14º of angle of attack, viewed from plane xy

Annex 9 – CFD aerodynamic results for Configuration 3

Table 15 CFD aerodynamic results for the static aerodynamic coefficients, for Configuration 3, at 15 m/s.

α(º)	C_D	C_L	C_M
0	0.1082	0.0006	-0.0030
2	0.1105	0.0666	-0.1951
4	0.1181	0.1355	-0.4008
6	0.1331	0.2139	-0.6525
8	0.1536	0.2976	-0.9298
10	0.1807	0.3829	-1.2340
12	0.2151	0.4785	-1.5601
14	0.2562	0.5694	-1.8868

Table 16 CFD aerodynamic results for the static aerodynamic coefficients, for Configuration 3, at 40 m/s.

α(º)	C_D	C_L
0	0.0936	0.0004
2	0.0929	0.0643
4	0.1022	0.1348
6	0.1167	0.2134
8	0.1365	0.2971
10	0.1639	0.3875
12	0.1967	0.4790
14	0.2367	0.5702

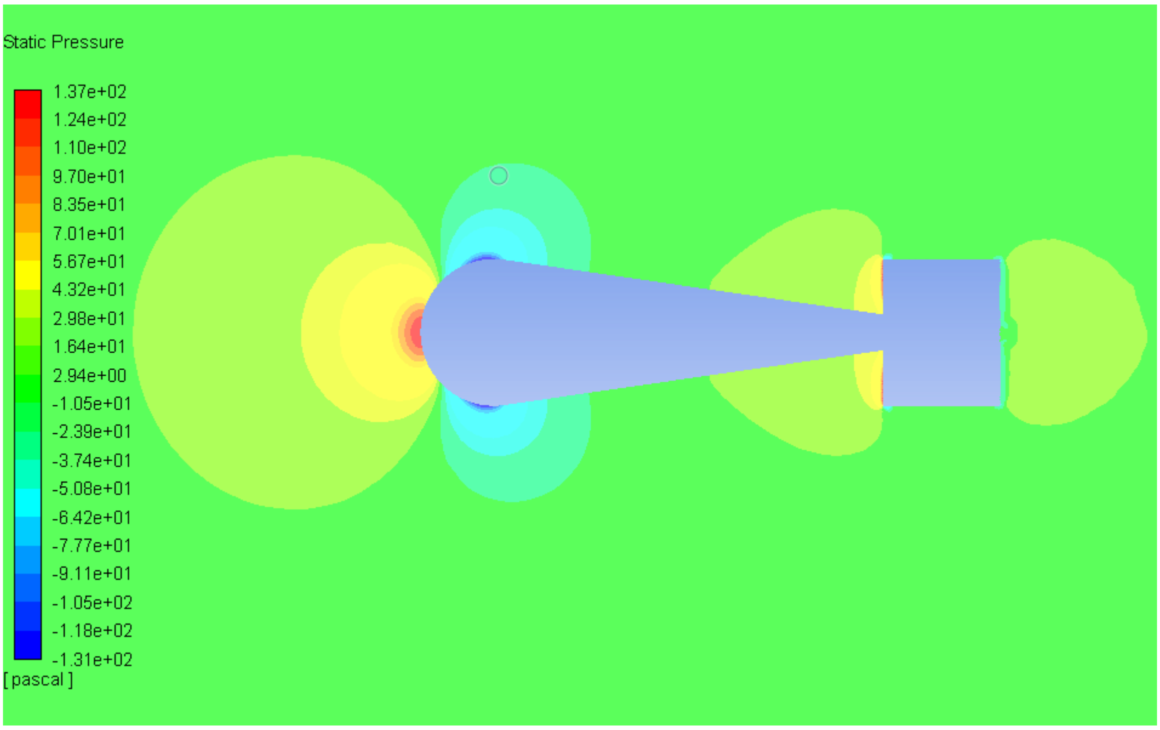

Figure 55 CFD static pressure results for Configuration 3 at 0º of angle of attack, viewed from plane xy

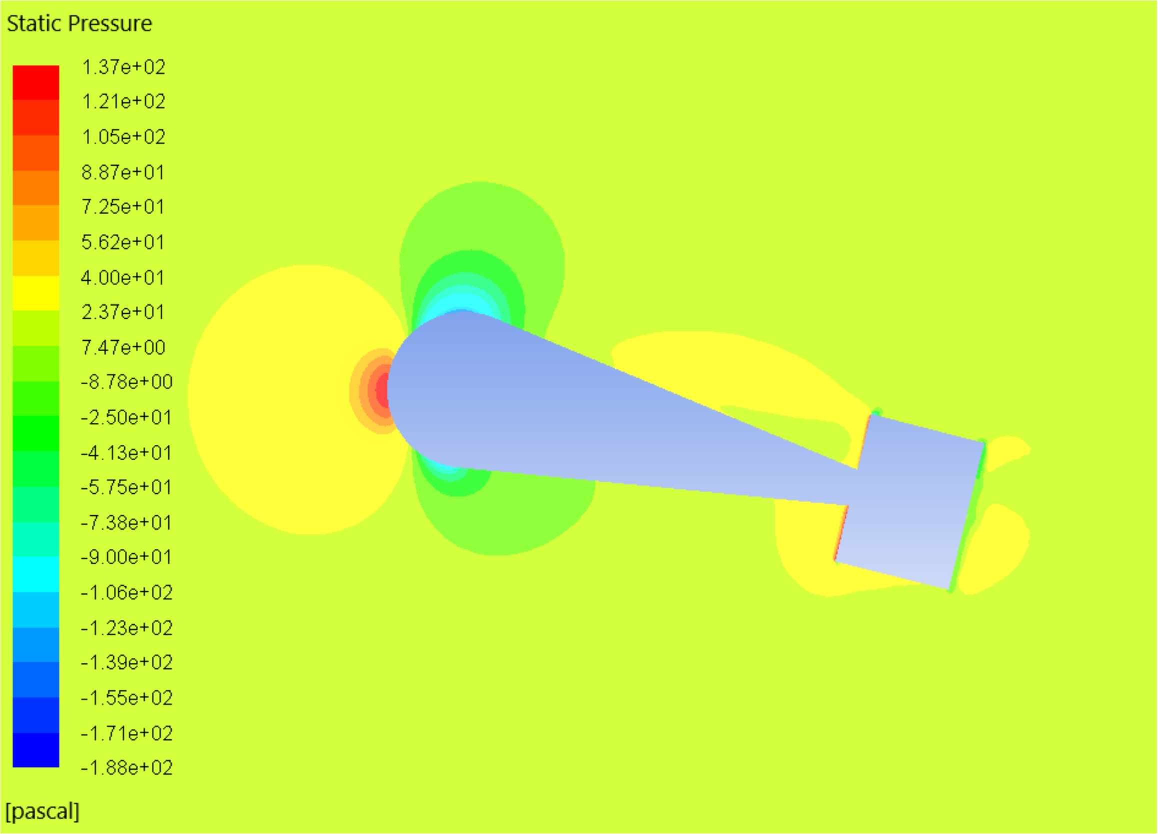

Figure 56 CFD static pressure results for Configuration 3 at 14º of angle of attack, viewed from plane xy

Annex 10 – CFD aerodynamic results for Configuration 4

Table 17 CFD aerodynamic results for the static aerodynamic coefficients, for Configuration 4, at 15 m/s.

α(º)	C_D	C_L	C_M
0	0.1103	0.0019	-0.0088
2	0.1129	0.0651	-0.1282
4	0.1205	0.1365	-0.2865
6	0.1348	0.2134	-0.4719
8	0.1555	0.3004	-0.7082
10	0.1833	0.3913	-0.9661
12	0.2201	0.4907	-1.2723
14	0.2652	0.6000	-1.6253

Table 18 CFD aerodynamic results for the static aerodynamic coefficients, for Configuration 4, at 40 m/s.

α(º)	C_D	C_L
0	0.0949	0.0018
2	0.0953	0.0636
4	0.1038	0.1357
6	0.1163	0.2119
8	0.1382	0.3001
10	0.1649	0.3881
12	0.2020	0.4900
14	0.2460	0.5979

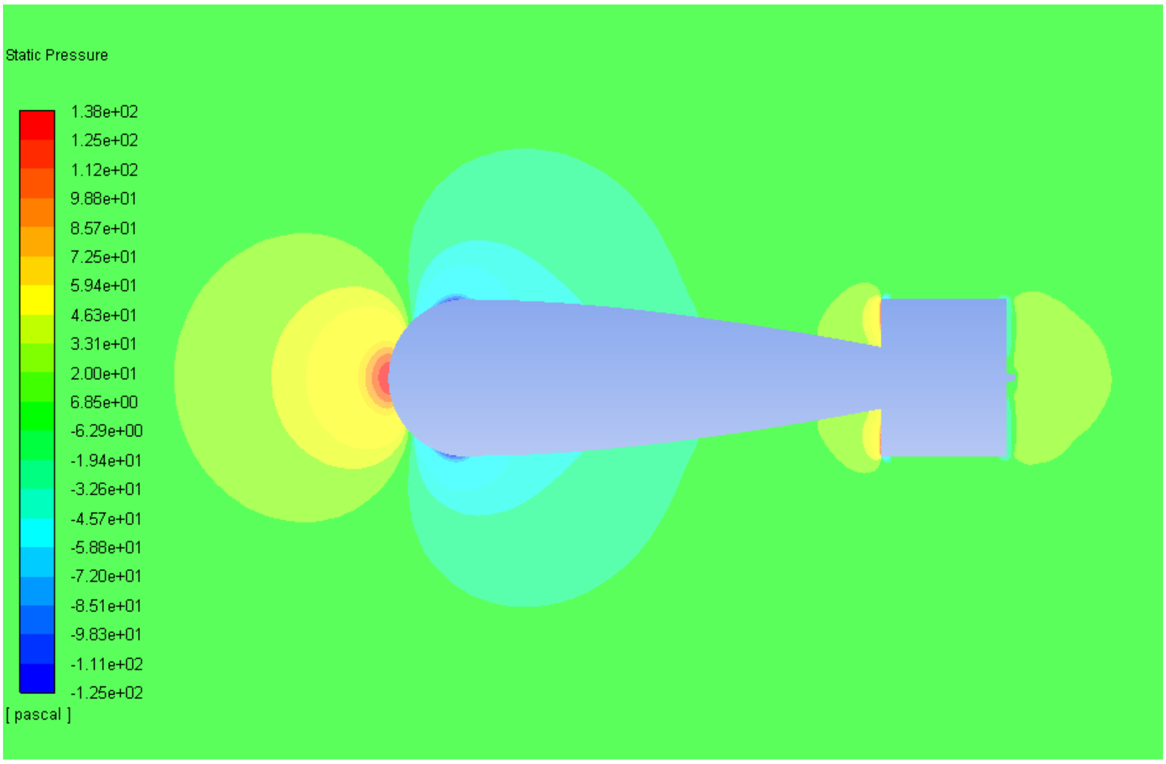

Figure 57 CFD static pressure results for Configuration 4 at 0º of angle of attack, viewed from plane xy

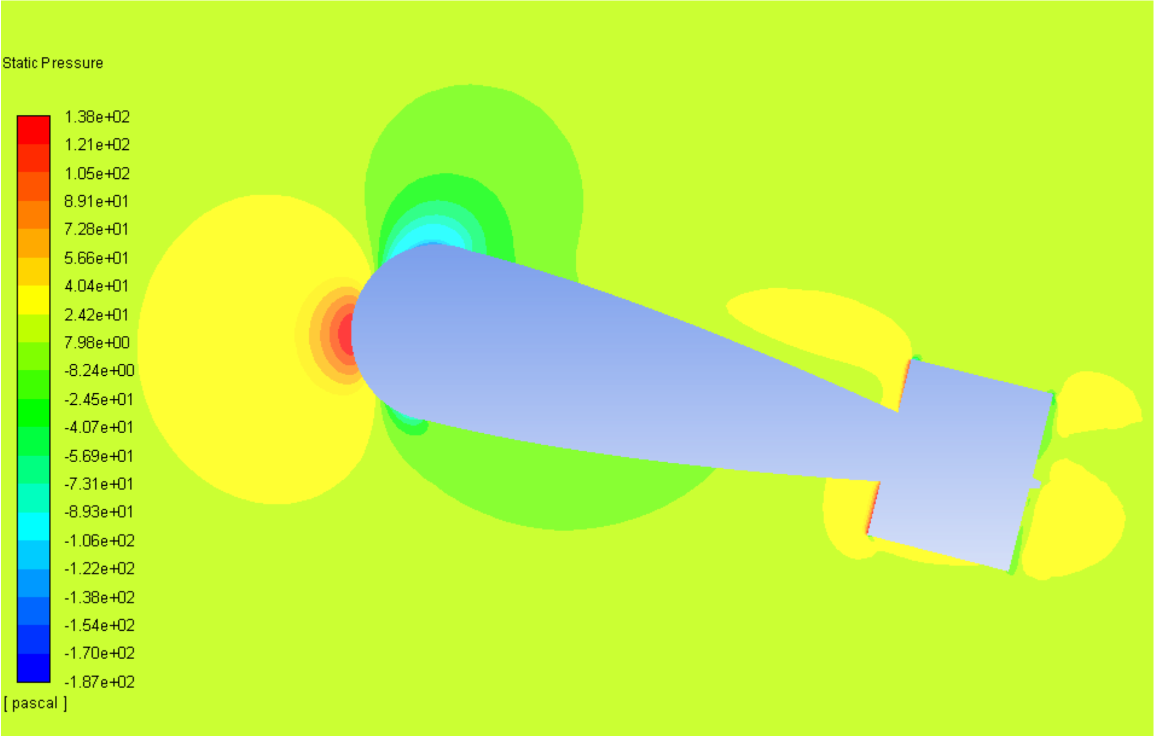

Figure 58 CFD static pressure results for Configuration 4 at 14º of angle of attack, viewed from plane xy

Annex 11 – Trajectory results for Configuration 2

Figures 59-75 present the results for Configuration 2. Figures 59-61 are from Cases 1.1, 1.2, and 1.3, Figures 62-64 are from Cases 1.4, 1.5, and 1.6, Figures 65-67 are from Cases 1.7, 1.8, and 1.9, Figures 68 and 69 are from Cases 2.1 and 2.2, Figures 70 and 71 are from Cases 2.3 and 2.4, Figures 72 and 73 are from Cases 2.5 and 2.6, and Figures 74 and 75 are from Cases 2.7 and 2.8. Tables 19 and 20 present some of the impact variables results for Group 1 and Group 2, respectively. It is important to notice that the $\alpha(t)$ and $V(t)$ results for the cases 2.1, 2.2, 2.5, and 2.6 are the same as Case 1.7, while the $\alpha(t)$ and $V(t)$ results for the cases 2.3, 2.4, 2.7, and 2.8 are the same as Case 1.9.

Table 19 Results of some impact variables for the trajectory results in Group 1, for Configuration 2.

	Case 1.1	Case 1.2	Case 1.3	Case 1.4	Case 1.5	Case 1.6	Case 1.7	Case 1.8	Case 1.9
α_{max} (º)	6.4	2.6	1.4	6.4	2.6	1.4	6.4	2.6	1.4
θ_{impact} (º)	-69.2	-60.8	-53.9	-74.2	-67.5	-61.7	-79.7	-75.2	-71.2
${x_g}_{impact}$ (m)	23.79	35.30	46.54	30.26	44.81	58.92	41.40	61.11	80.04
V_{impact} (m/s)	24.56	26.14	28.03	29.85	30.90	32.18	38.27	38.74	39.31
t_{flight} (s)	2.52	2.53	2.54	3.30	3.31	3.33	4.79	4.81	4.84

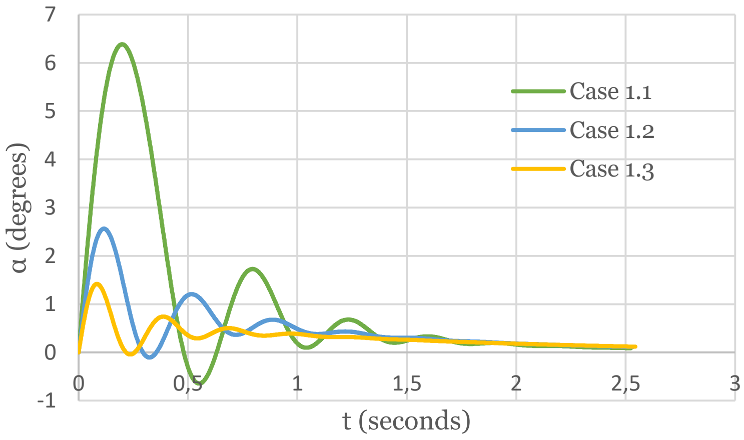

Figure 59 α(t) results for Configuration 2, from trajectory cases 1.1, 1.2, and 1.3.

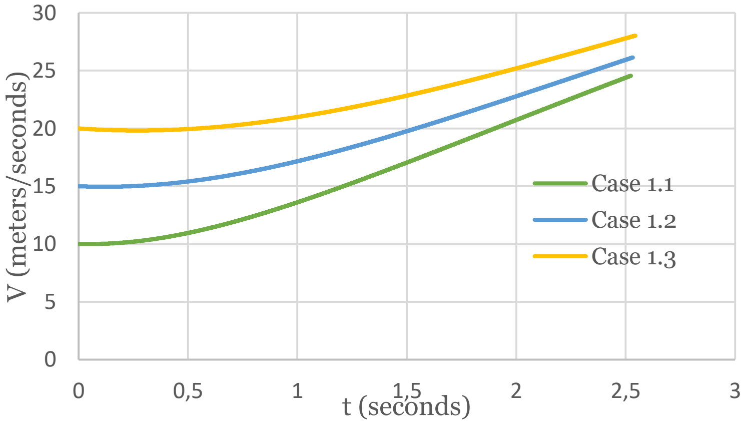

Figure 60 V(t) results for Configuration 2, from trajectory cases 1.1, 1.2, and 1.3.

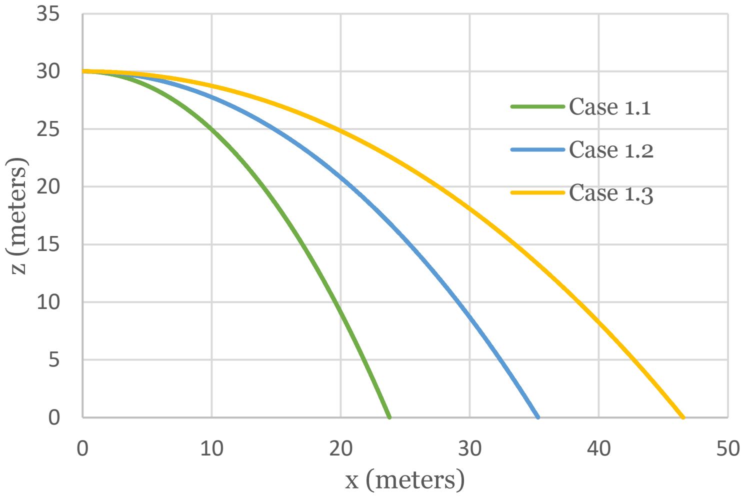

Figure 61 z(x) results for Configuration 2, from trajectory cases 1.1, 1.2, and 1.3.

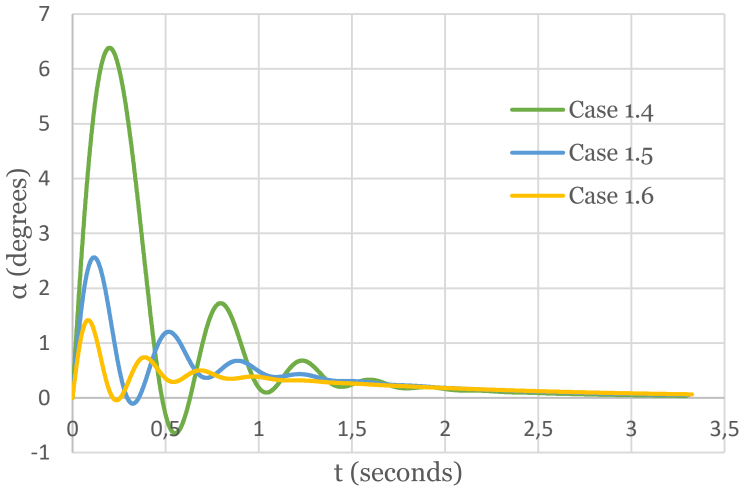

Figure 62 α(t) results for Configuration 2, from trajectory cases 1.4, 1.5, and 1.6.

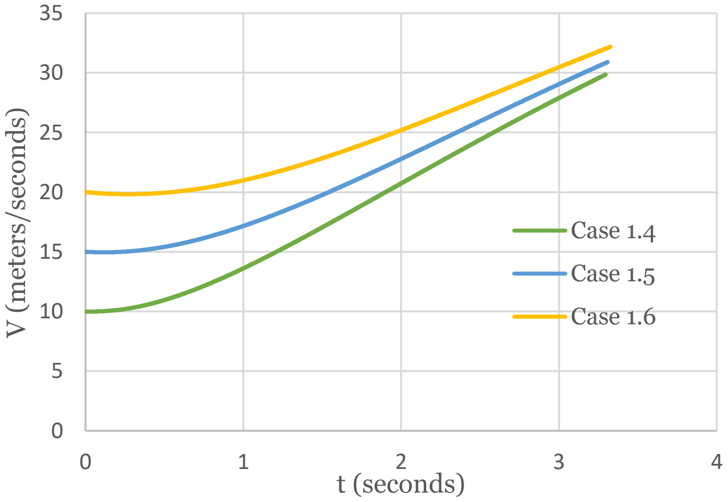

Figure 63 V(t) results for Configuration 2, from trajectory cases 1.4, 1.5, and 1.6.

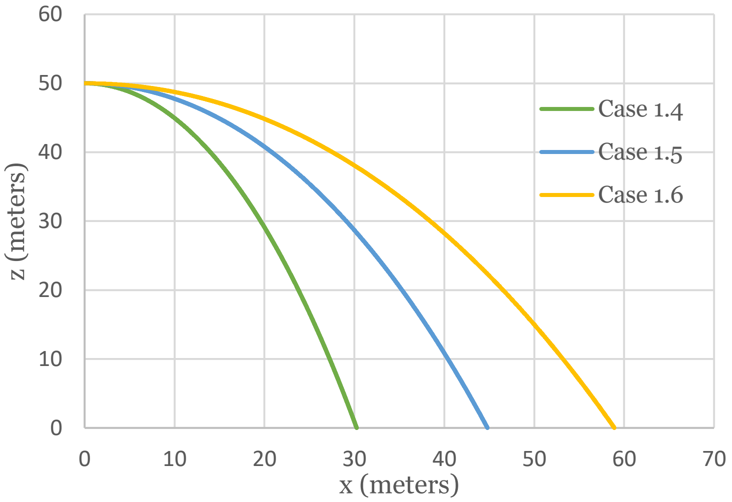

Figure 64 z(x) results for Configuration 2, from trajectory cases 1.4, 1.5, and 1.6.

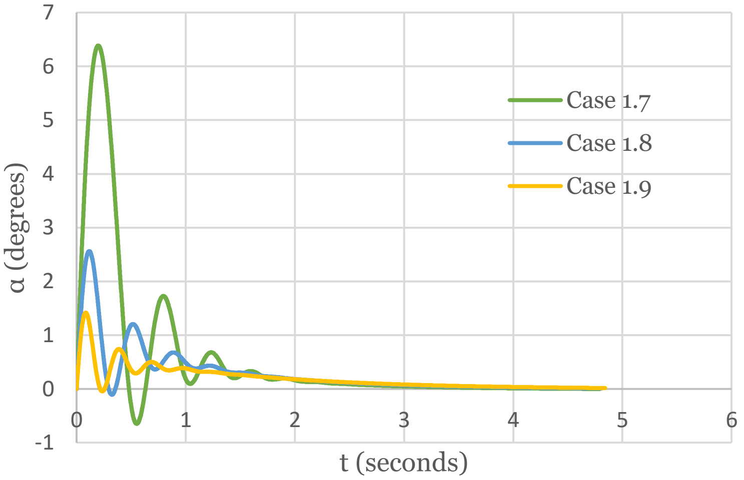

Figure 65 α(t) results for Configuration 2, from trajectory cases 1.7, 1.8, and 1.9.

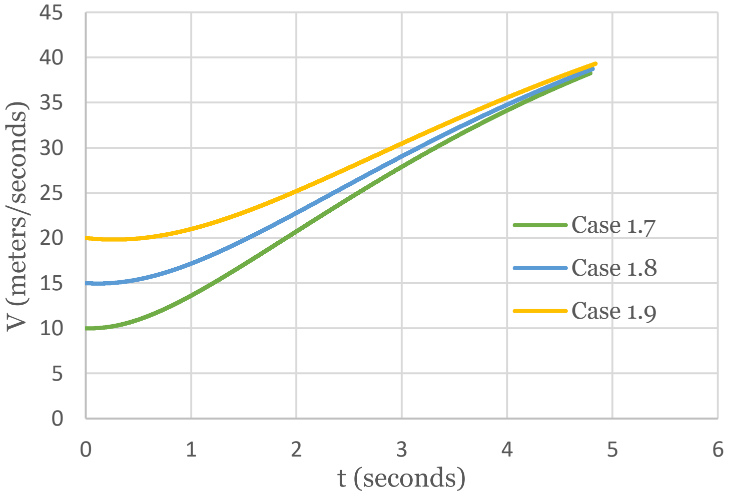

Figure 66 V(t) results for Configuration 2, from trajectory cases 1.7, 1.8, and 1.9.

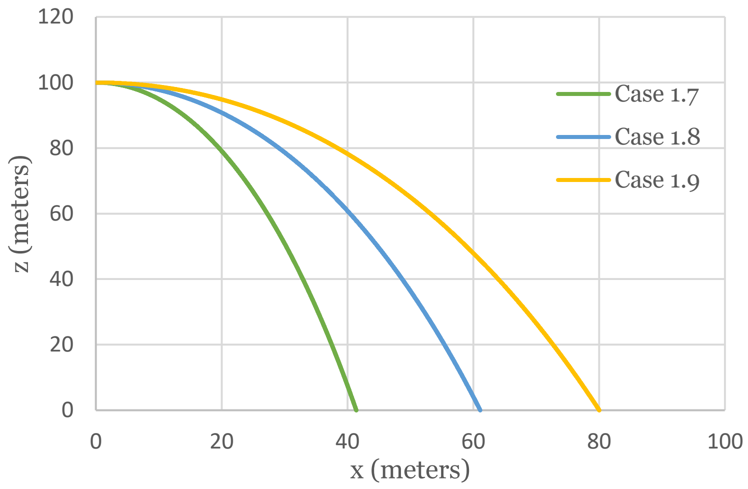

Figure 67 z(x) results for Configuration 2, from trajectory cases 1.7, 1.8, and 1.9.

Table 20 Results of some impact variables for the trajectory results in Group 2, for Configuration 2.

	Case 2.1	Case 2.2	Case 2.3	Case 2.4	Case 2.5	Case 2.6	Case 2.7	Case 2.8
α_{max} (º)	6.4	6.4	1.4	1.4	6.4	6.4	1.4	1.4
θ_{impact} (º)	-79.7	-79.7	-71.2	-71.2	-79.7	-79.7	-71.2	-71.2
$x_{g\,impact}$ (m)	29.42	41.40	67.94	80.04	17.44	41.40	55.84	80.04
$y_{g\,impact}$ (m)	-0.07	-12.04	-0.10	-12.21	-0.07	-24.02	-0.10	-24.31
V_{impact} (m/s)	38.27	38.27	39.31	39.31	38.27	38.27	39.31	39.31
t_{flight} (s)	4.79	4.79	4.84	4.84	4.79	4.79	4.84	4.84

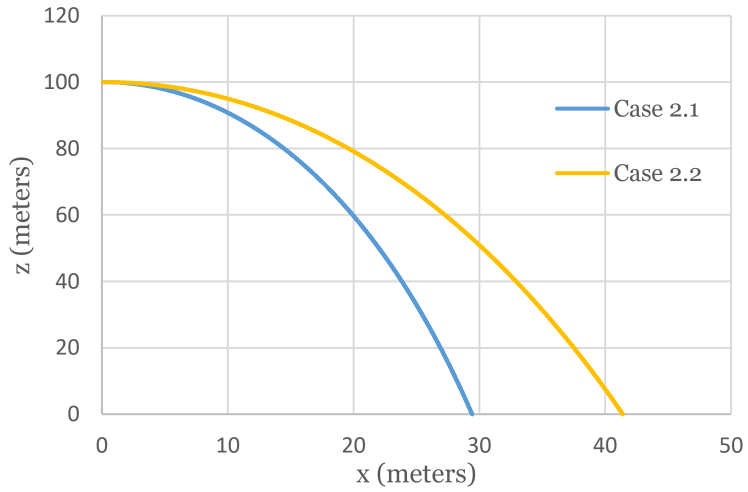

Figure 68 z(x) results for Configuration 2, from trajectory cases 2.1, and 2.2.

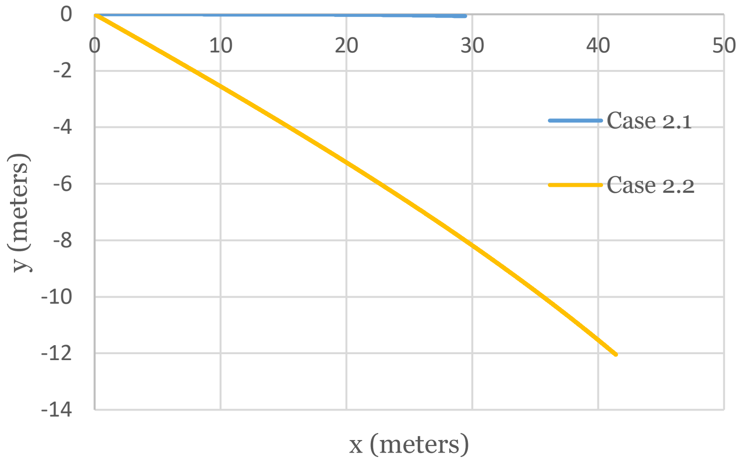

Figure 69 y(x) results for Configuration 2, from trajectory cases 2.1, and 2.2.

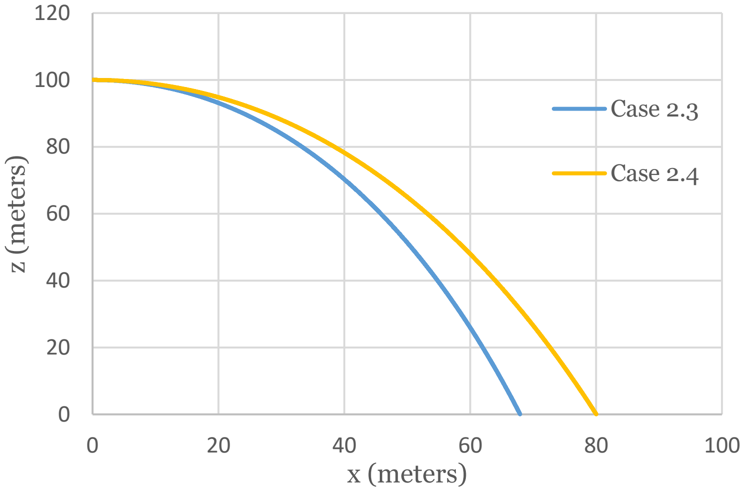

Figure 70 z(x) results for Configuration 2, from trajectory cases 2.3, and 2.4.

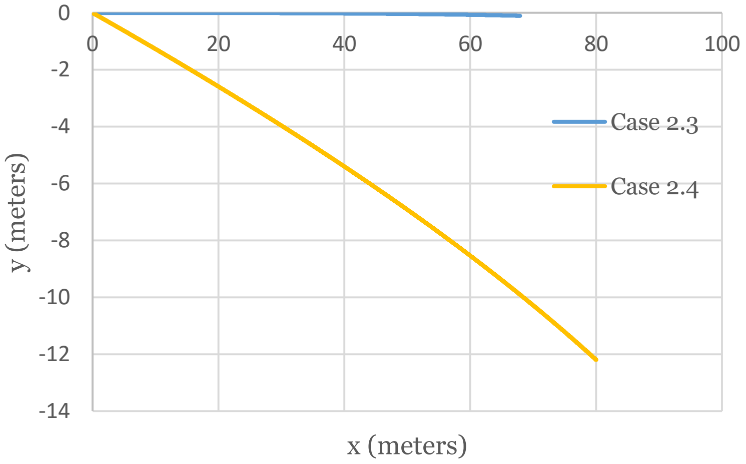

Figure 71 y(x) results for Configuration 2, from trajectory cases 2.3, and 2.4.

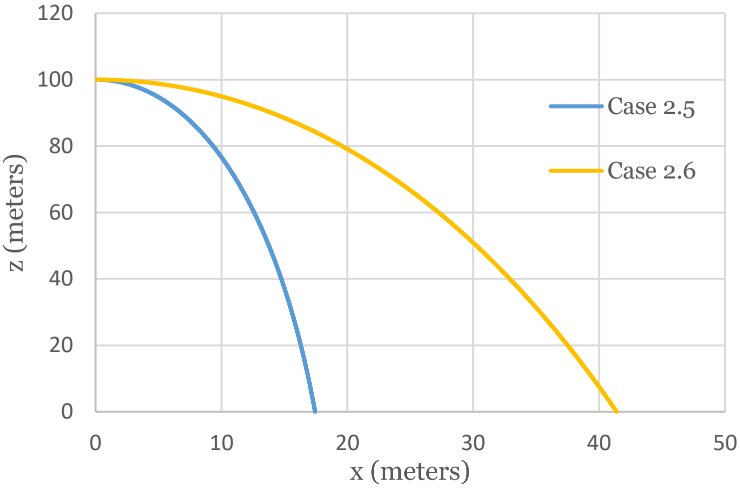

Figure 72 z(x) results for Configuration 2, from trajectory cases 2.5, and 2.6.

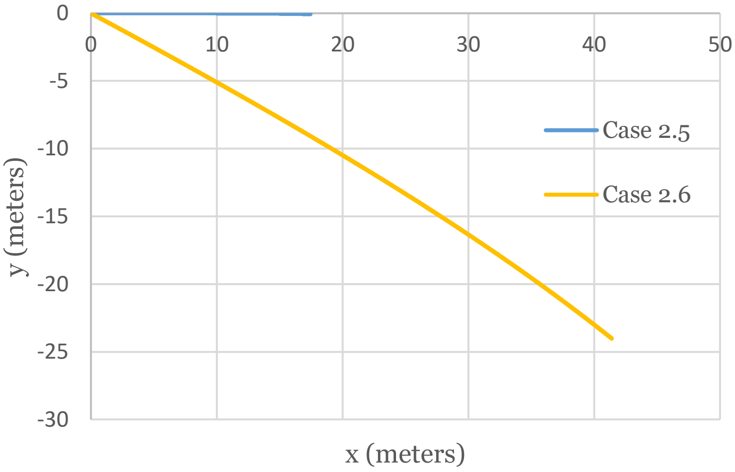

Figure 73 y(x) results for Configuration 2, from trajectory cases 2.5, and 2.6.

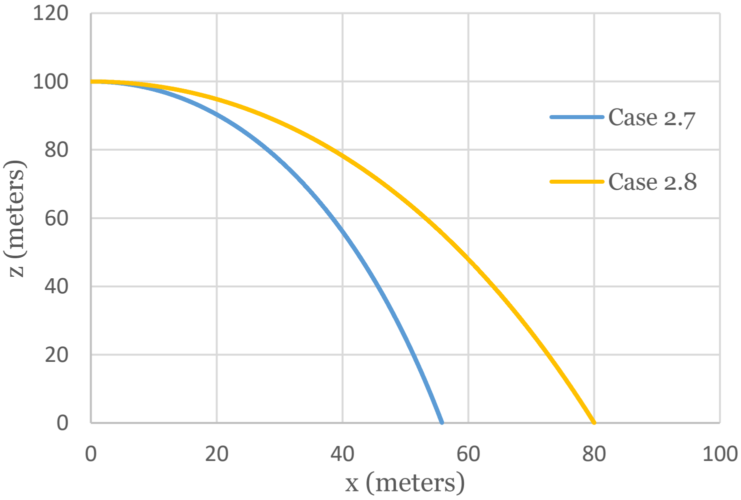

Figure 74 z(x) results for Configuration 2, from trajectory cases 2.7, and 2.8.

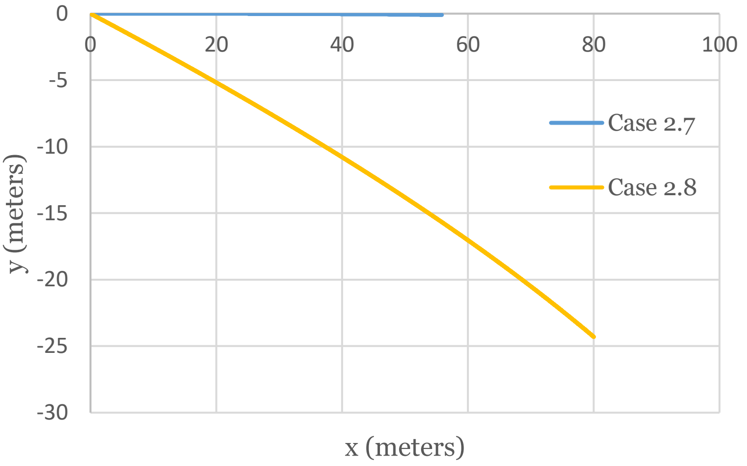

Figure 75 y(x) results for Configuration 2, from trajectory cases 2.7, and 2.8.

Annex 12 – Trajectory results for Configuration 3

Figures 76-92 present the results for Configuration 3. Figures 76-78 are from Cases 1.1, 1.2, and 1.3, Figures 79-81 are from Cases 1.4, 1.5, and 1.6, Figures 82-84 are from Cases 1.7, 1.8, and 1.9, Figures 85 and 86 are from Cases 2.1 and 2.2, Figures 87 and 88 are from Cases 2.3 and 2.4, Figures 89 and 90 are from Cases 2.5 and 2.6, and Figures 91 and 92 are from Cases 2.7 and 2.8. Tables 21 and 22 present some of the impact variables results for Group 1 and Group 2, respectively. It is important to notice that the $\alpha(t)$ and $V(t)$ results for the cases 2.1, 2.2, 2.5, and 2.6 are the same as Case 1.7, while the $\alpha(t)$ and $V(t)$ results for the cases 2.3, 2.4, 2.7, and 2.8 are the same as Case 1.9.

Table 21 Results of some impact variables for the trajectory results in Group 1, for Configuration 3.

	Case 1.1	Case 1.2	Case 1.3	Case 1.4	Case 1.5	Case 1.6	Case 1.7	Case 1.8	Case 1.9
α_{max} (º)	6.4	3.0	1.7	6.4	3.0	1.7	6.4	3.0	1.7
θ_{impact} (º)	-68.1	-59.1	-51.6	-73.0	-65.5	-59.0	-78.2	-72.7	-67.7
$x_{g_{impact}}$ (m)	24.41	36.49	48.45	31.34	33.26	62.10	43.79	65.34	86.54
V_{impact} (m/s)	25.62	27.62	30.13	31.74	46.82	35.20	42.63	43.58	44.81
t_{flight} (s)	2.49	2.50	2.50	3.23	3.24	3.24	4.61	4.62	4.63

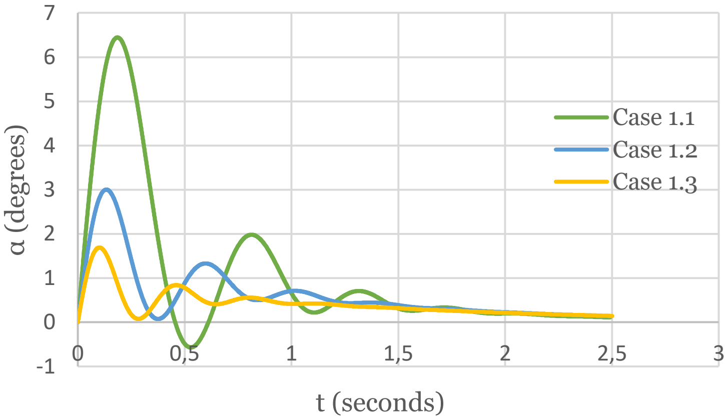

Figure 76 α(t) results for Configuration 3, from trajectory cases 1.1, 1.2, and 1.3.

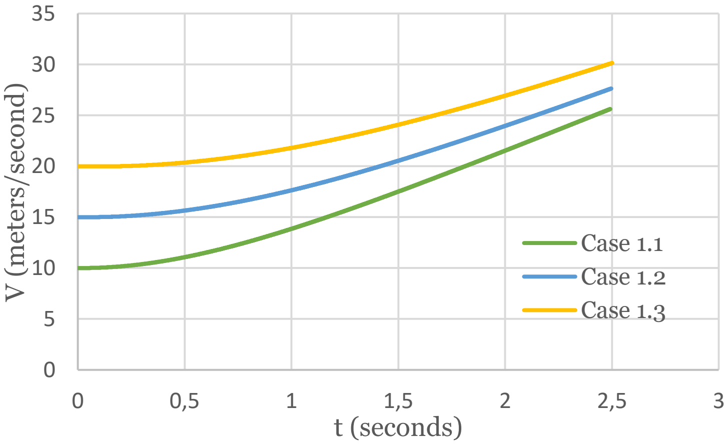

Figure 77 V(t) results for Configuration 3, from trajectory cases 1.1, 1.2, and 1.3.

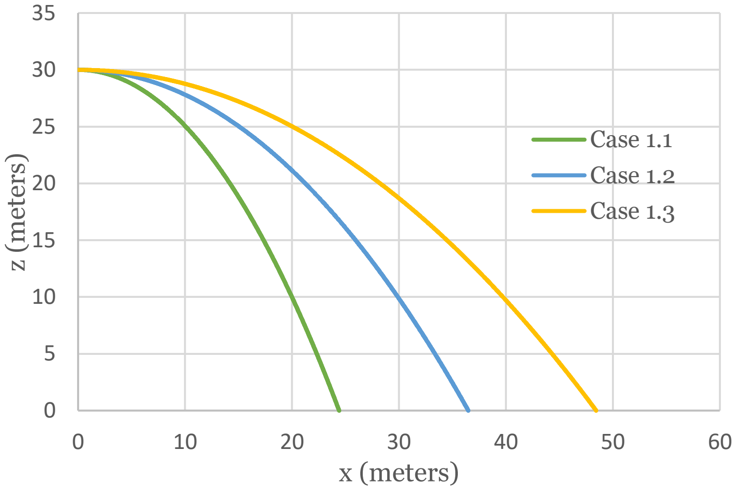

Figure 78 z(x) results for Configuration 3, from trajectory cases 1.1, 1.2, and 1.3.

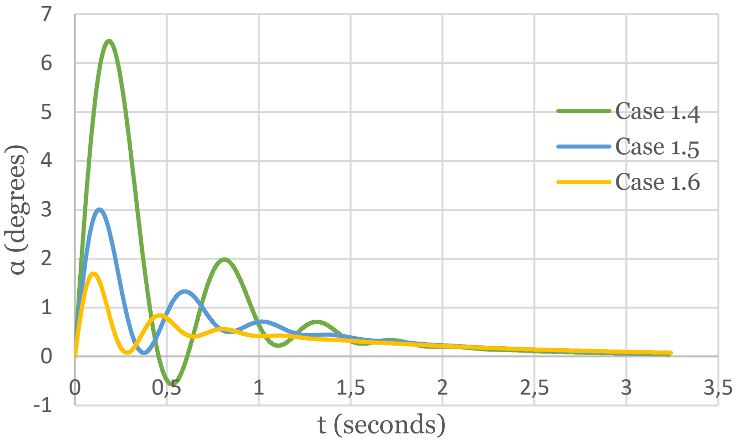

Figure 79 α(t) results for Configuration 3, from trajectory cases 1.4, 1.5, and 1.6.

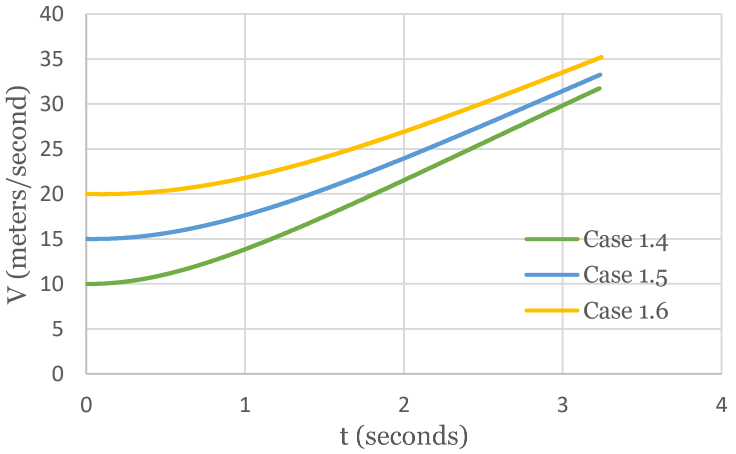

Figure 80 V(t) results for Configuration 3, from trajectory cases 1.4, 1.5, and 1.6.

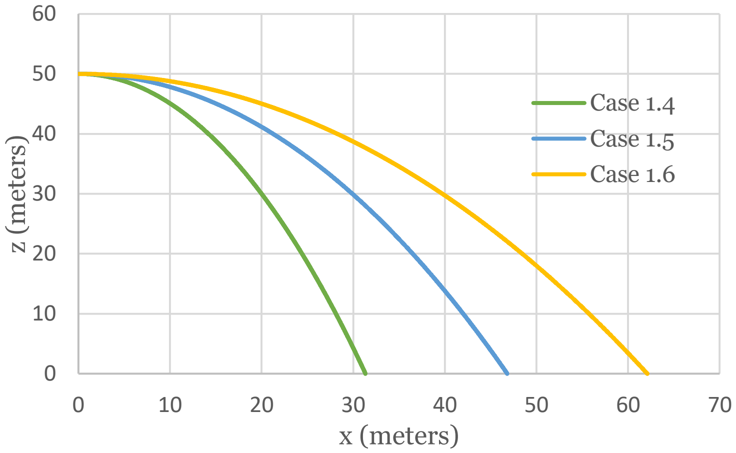

Figure 81 z(x) results for Configuration 3, from trajectory cases 1.4, 1.5, and 1.6.

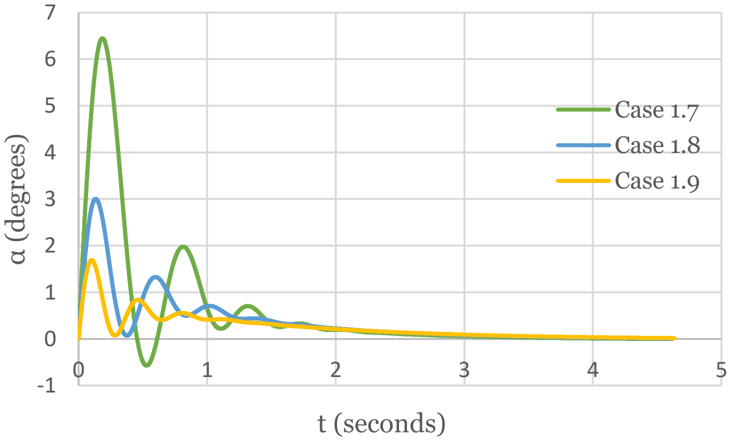

Figure 82 α(t) results for Configuration 3, from trajectory cases 1.7, 1.8, and 1.9.

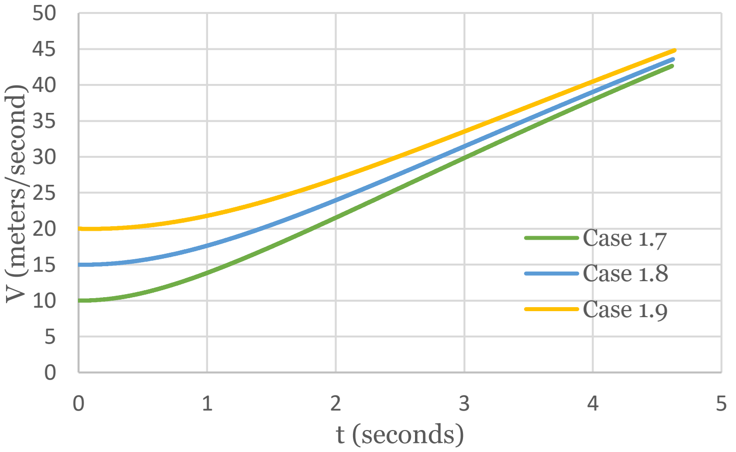

Figure 83 V(t) results for Configuration 3, from trajectory cases 1.7, 1.8, and 1.9.

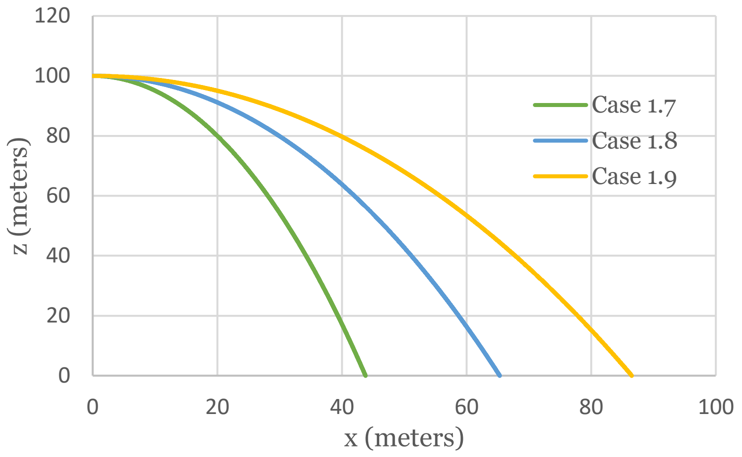

Figure 84 z(x) results for Configuration 3, from trajectory cases 1.7, 1.8, and 1.9.

Table 22 Results of some impact variables for the trajectory results in Group 2, for Configuration 3.

	Case 2.1	Case 2.2	Case 2.3	Case 2.4	Case 2.5	Case 2.6	Case 2.7	Case 2.8
α_{max} (°)	6.4	6.4	1.7	1.7	6.4	6.4	1.7	1.7
θ_{impact} (°)	-78.2	-78.2	-67.7	-67.7	-78.2	-78.2	-67.7	-67.7
$x_{g_{impact}}$ (m)	32.25	43.79	74.95	86.54	20.72	43.79	63.36	86.54
$y_{g_{impact}}$ (m)	0.02	-11.52	0.03	-11.56	0.02	-23.05	0.03	-23.14
V_{impact} (m/s)	42.63	42.63	44.81	44.81	42.63	42.63	44.81	44.81
t_{flight} (s)	4.61	4.61	4.63	4.63	4.61	4.61	4.63	4.63

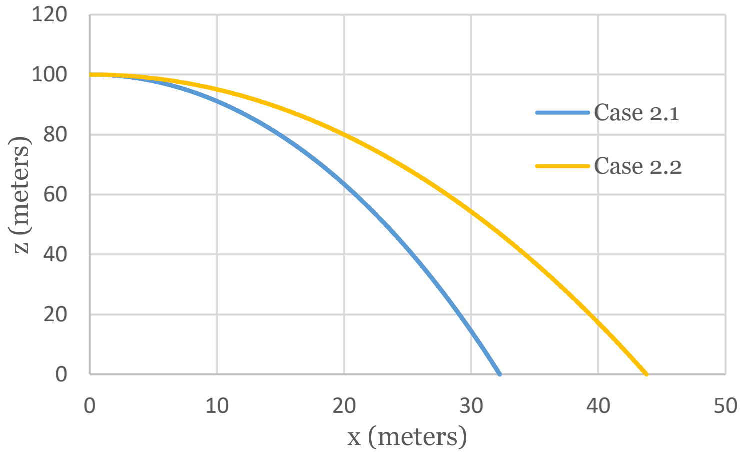

Figure 85 z(x) results for Configuration 3, from trajectory cases 2.1, and 2.2.

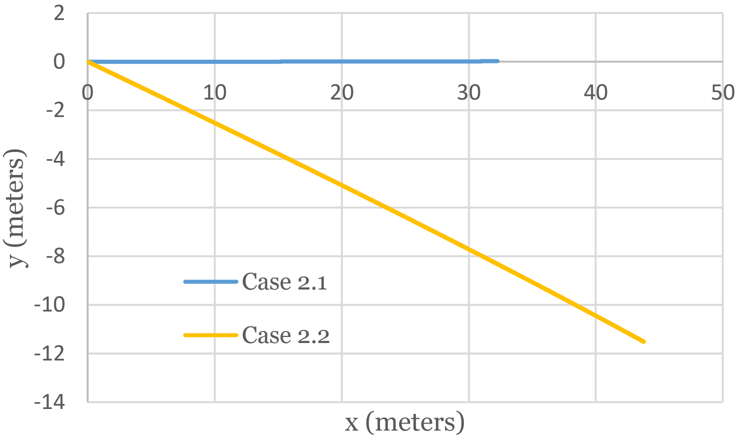

Figure 86 y(x) results for Configuration 3, from trajectory cases 2.1, and 2.2.

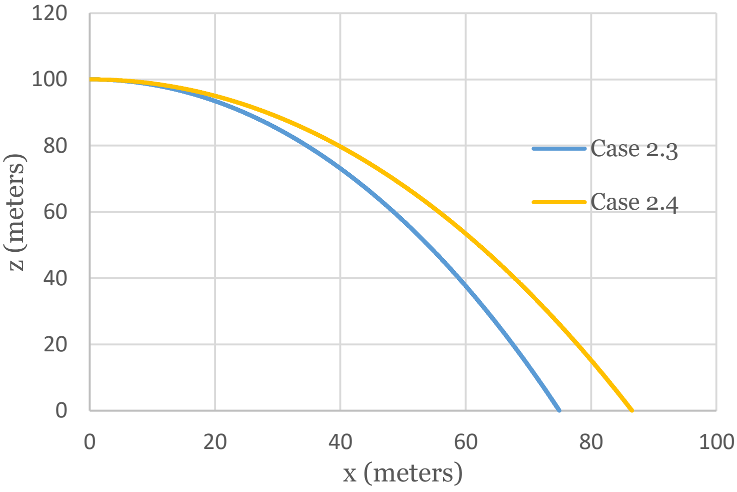

Figure 87 z(x) results for Configuration 3, from trajectory cases 2.3, and 2.4.

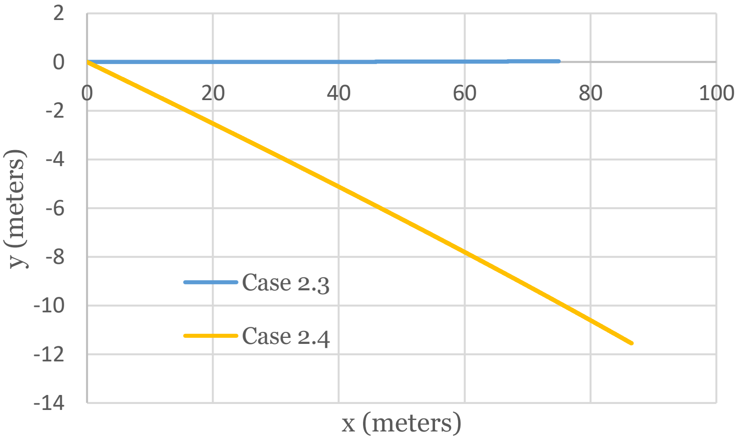

Figure 88 y(x) results for Configuration 3, from trajectory cases 2.3, and 2.4.

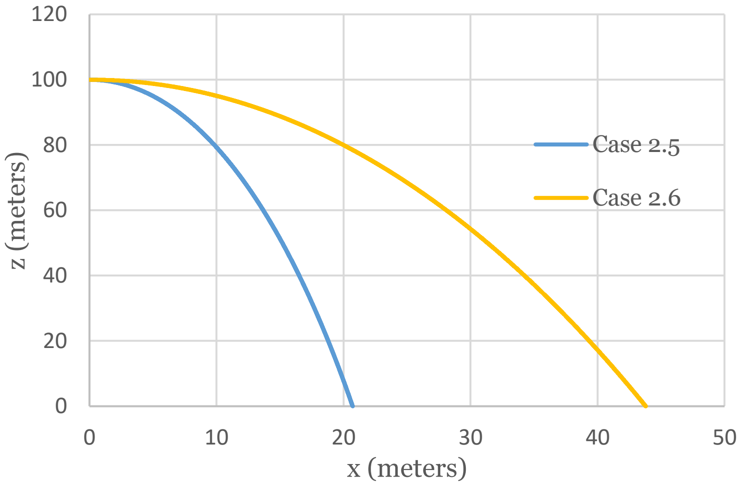

Figure 89 z(x) results for Configuration 3, from trajectory cases 2.5, and 2.6.

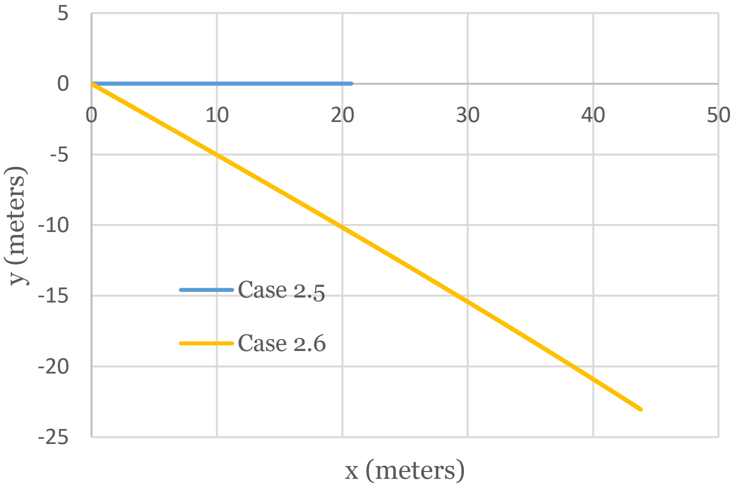

Figure 90 y(x) results for Configuration 3, from trajectory cases 2.5, and 2.6.

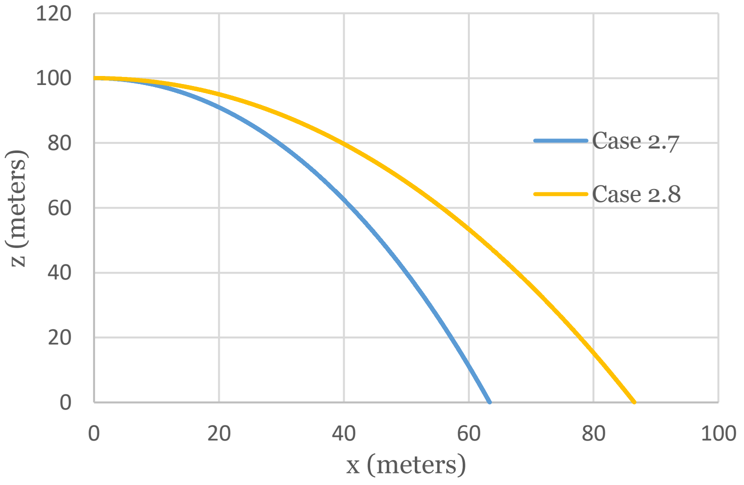

Figure 91 z(x) results for Configuration 3, from trajectory cases 2.7, and 2.8.

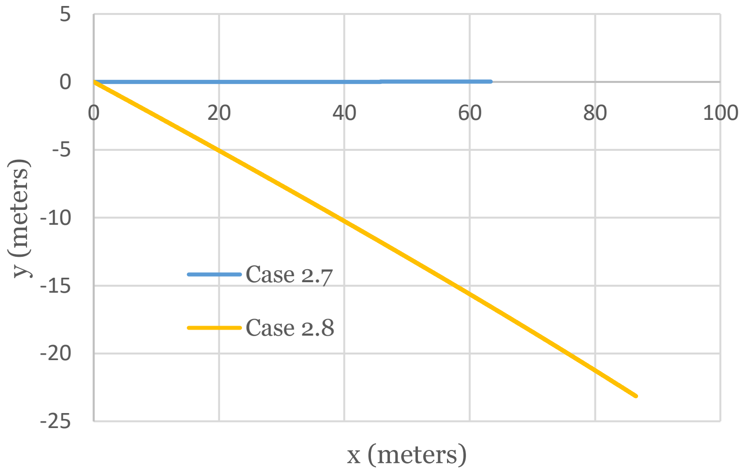

Figure 92 y(x) results for Configuration 3, from trajectory cases 2.7, and 2.8.

Annex 13 – Trajectory results for Configuration 4

Figures 93-109 present the results for Configuration 4. Figures 93-95 are from Cases 1.1, 1.2, and 1.3, Figures 96-98 are from Cases 1.4, 1.5, and 1.6, Figures 99-101 are from Cases 1.7, 1.8, and 1.9, Figures 102 and 103 are from Cases 2.1 and 2.2, Figures 104 and 105 are from Cases 2.3 and 2.4, Figures 106 and 107 are from Cases 2.5 and 2.6, and Figures 108 and 109 are from Cases 2.7 and 2.8. Tables 23 and 24 present some of the impact variables results for Group 1 and Group 2, respectively. It is important to notice that the $\alpha(t)$ and $V(t)$ results for the cases 2.1, 2.2, 2.5, and 2.6 are the same as Case 1.7, while the $\alpha(t)$ and $V(t)$ results for the cases 2.3, 2.4, 2.7, and 2.8 are the same as Case 1.9.

Table 23 Results of some impact variables for the trajectory results in Group 1, for Configuration 4.

	Case 1.1	Case 1.2	Case 1.3	Case 1.4	Case 1.5	Case 1.6	Case 1.7	Case 1.8	Case 1.9
α_{max} (º)	8.3	4.1	2.3	8.3	4.1	2.3	8.3	4.1	2.3
θ_{impact} (º)	-68	-59	-51.6	-73.0	-65.4	-58.9	-78.2	-72.7	-67.7
$x_{g_{impact}}$ (m)	24.47	36.61	48.61	31.43	46.99	62.34	43.92	65.61	86.93
V_{impact} (m/s)	25.67	27.69	30.23	31.83	33.37	35.35	42.83	43.81	45.09
t_{flight} (s)	2.5	2.5	2.5	3.23	3.24	3.24	4.61	4.62	4.63

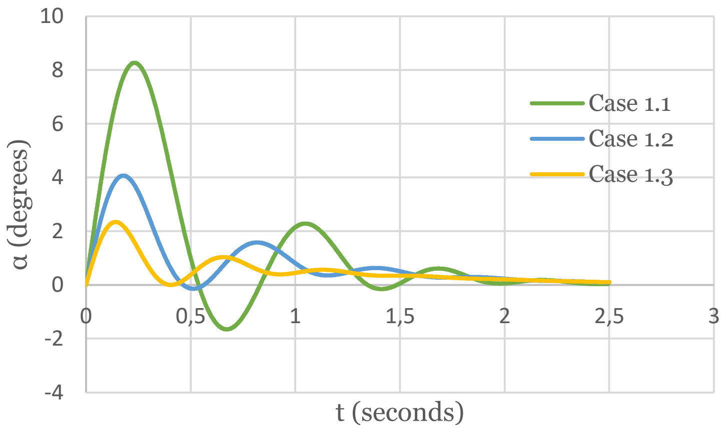

Figure 93 α(t) results for Configuration 4, from trajectory cases 1.1, 1.2, and 1.3.

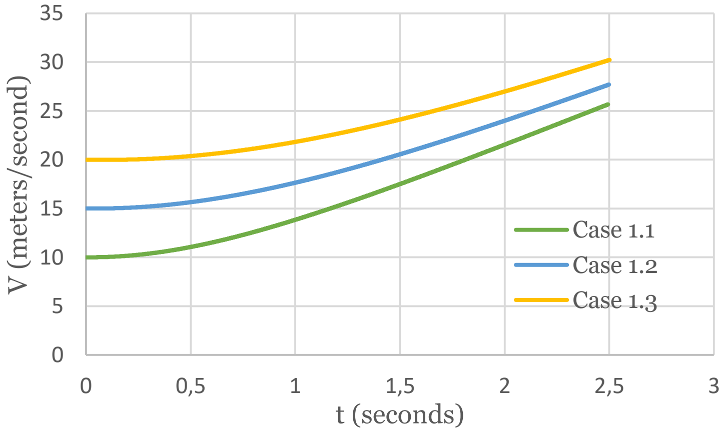

Figure 94 V(t) results for Configuration 4, from trajectory cases 1.1, 1.2, and 1.3.

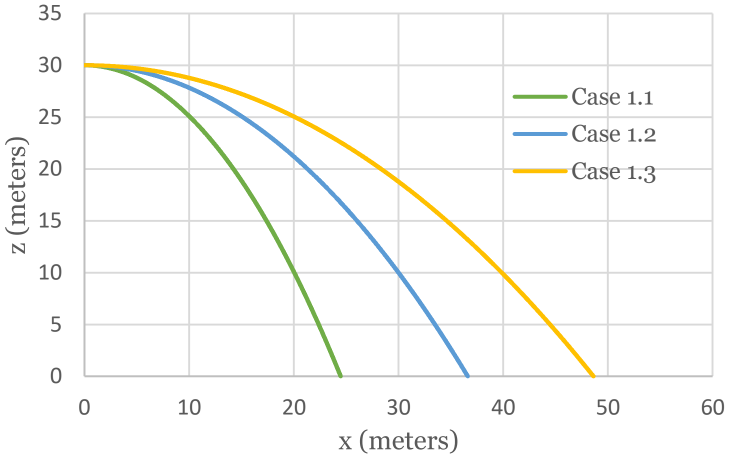

Figure 95 z(x) results for Configuration 4, from trajectory cases 1.1, 1.2, and 1.3.

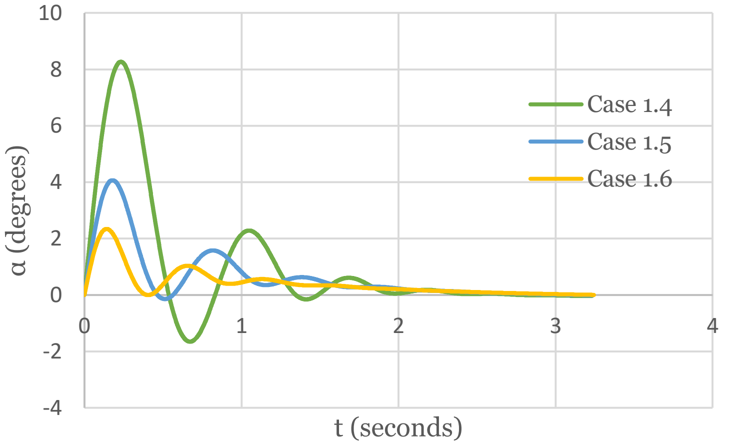

Figure 96 α(t) results for Configuration 4, from trajectory cases 1.4, 1.5, and 1.6.

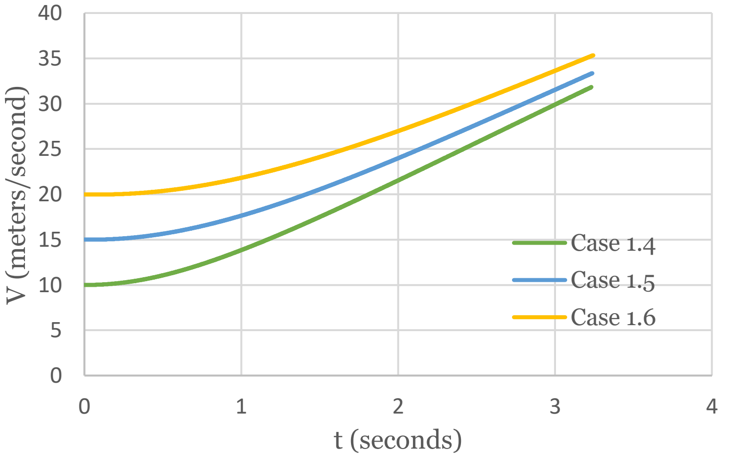

Figure 97 V(t) results for Configuration 4, from trajectory cases 1.4, 1.5, and 1.6.

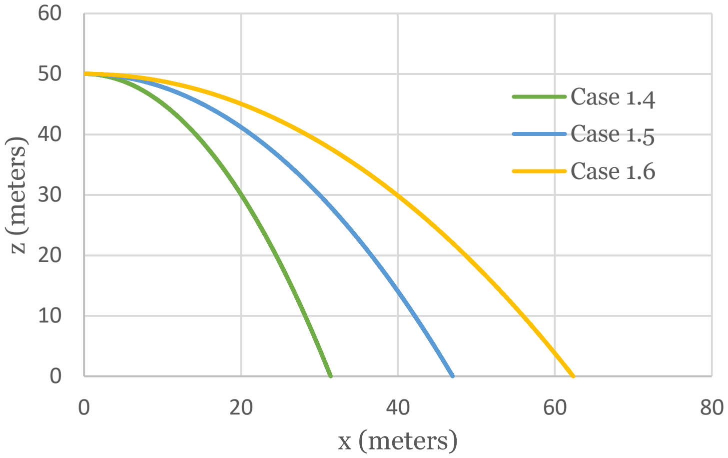

Figure 98 z(x) results for Configuration 4, from trajectory cases 1.4, 1.5, and 1.6.

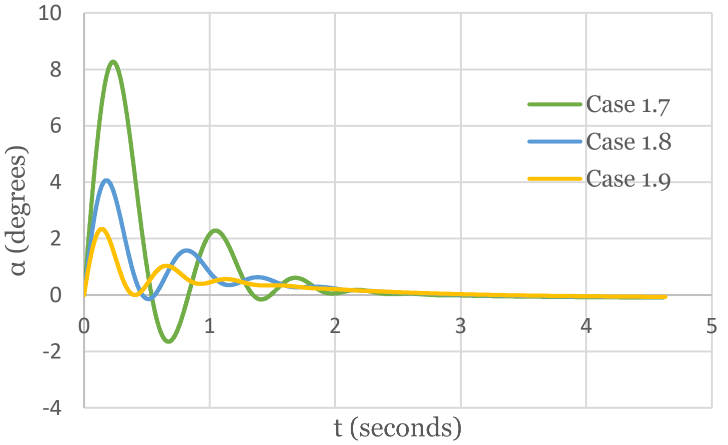

Figure 99 α(t) results for Configuration 4, from trajectory cases 1.7, 1.8, and 1.9.

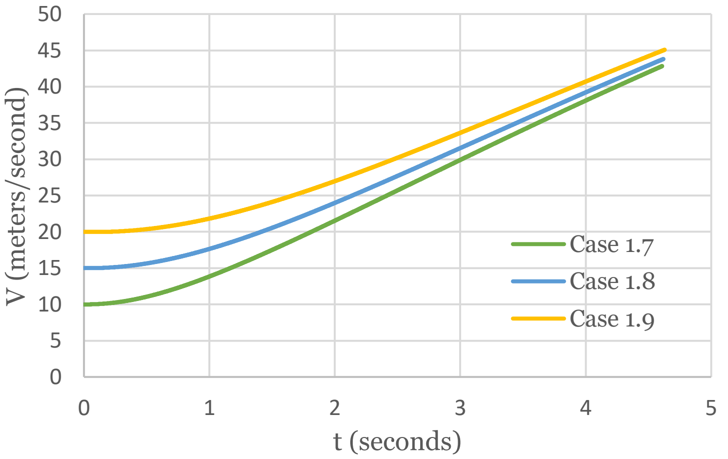

Figure 100 V(t) results for Configuration 4, from trajectory cases 1.7, 1.8, and 1.9.

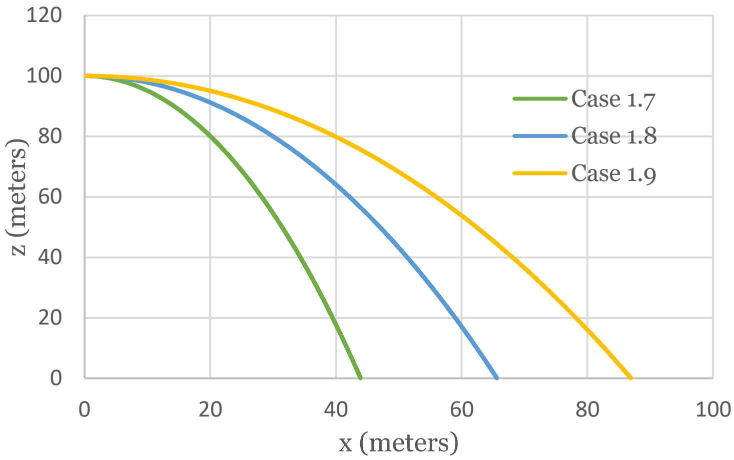

Figure 101 z(x) results for Configuration 4, from trajectory cases 1.7, 1.8, and 1.9.

Table 24 Results of some impact variables for the trajectory results in Group 2, for Configuration 4.

	Case 2.1	Case 2.2	Case 2.3	Case 2.4	Case 2.5	Case 2.6	Case 2.7	Case 2.8
α_{max} (°)	8.3	8.3	2.3	2.3	8.3	8.3	2.3	2.3
θ_{impact} (°)	-78.2	-78.2	-67.7	-67.7	-78.2	-78.2	-67.7	-67.7
$x_{g_{impact}}$ (m)	32.40	43.92	75.36	86.93	20.87	43.92	63.78	86.93
$y_{g_{impact}}$ (m)	0.09	-11.43	0.16	-11.41	0.09	-22.96	0.16	-22.99
V_{impact} (m/s)	42.83	42.83	45.09	45.09	42.83	42.83	45.09	45.09
t_{flight} (s)	4.61	4.61	4.63	4.63	4.61	4.61	4.63	4.63

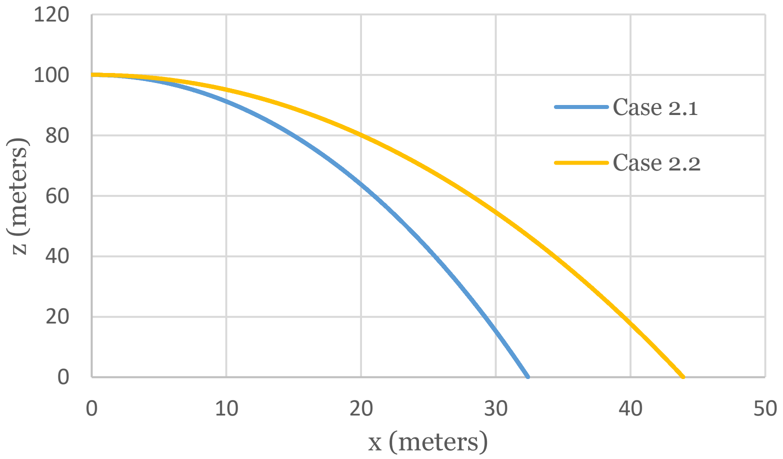

Figure 102 z(x) results for Configuration 4, from trajectory cases 2.1, and 2.2.

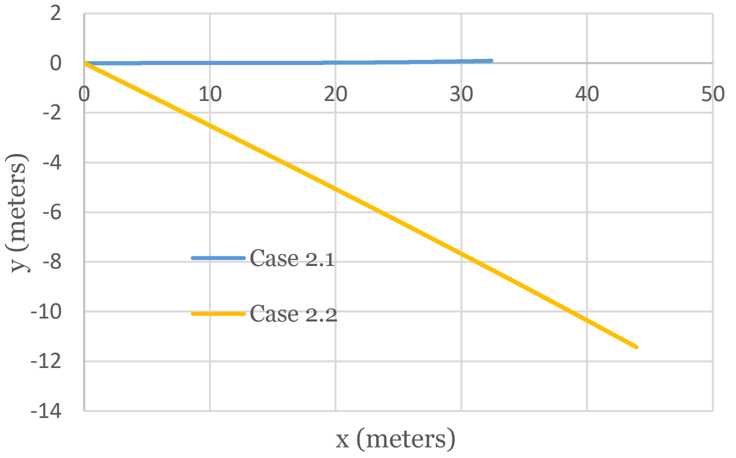

Figure 103 y(x) results for Configuration 4, from trajectory cases 2.1, and 2.2.

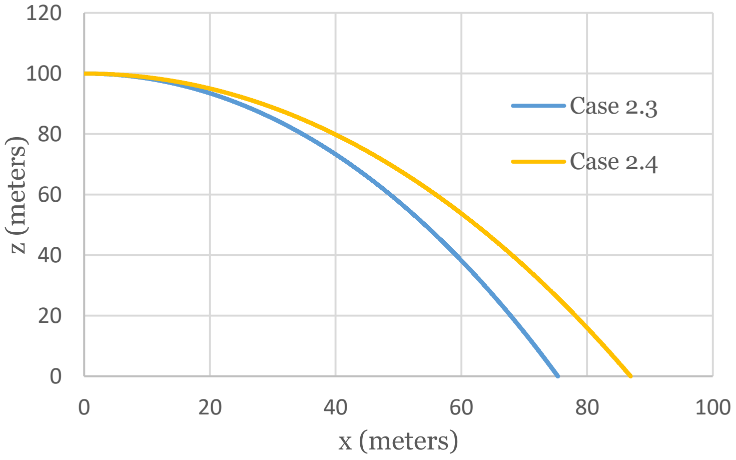

Figure 104 z(x) results for Configuration 4, from trajectory cases 2.3, and 2.4.

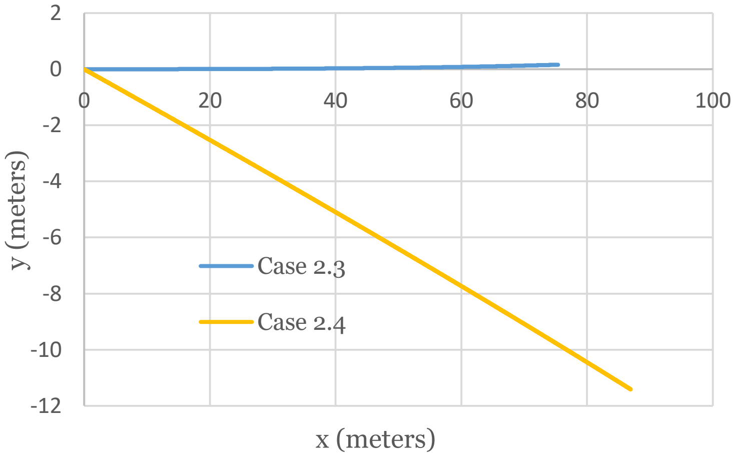

Figure 105 y(x) results for Configuration 4, from trajectory cases 2.3, and 2.4.

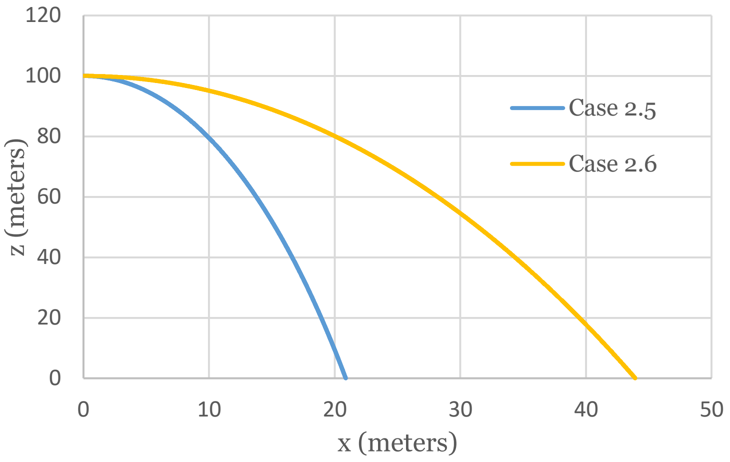

Figure 106 z(x) results for Configuration 4, from trajectory cases 2.5, and 2.6.

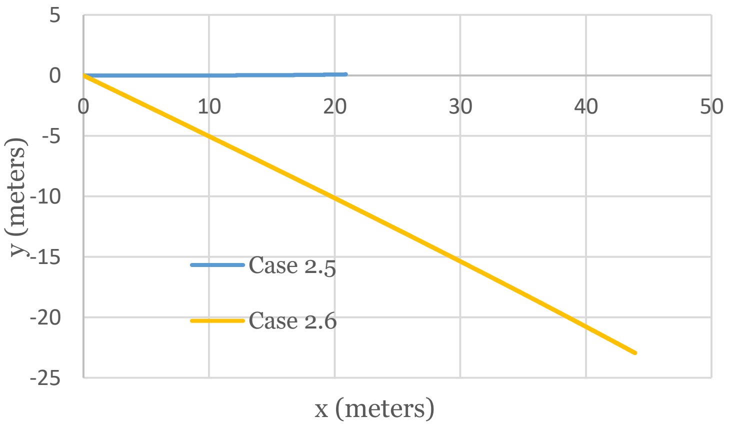

Figure 107 y(x) results for Configuration 4, from trajectory cases 2.5, and 2.6.

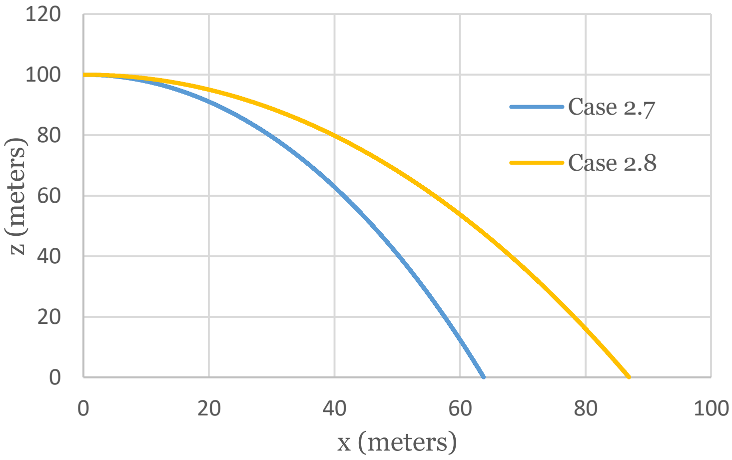

Figure 108 z(x) results for Configuration 4, from trajectory cases 2.7, and 2.8.

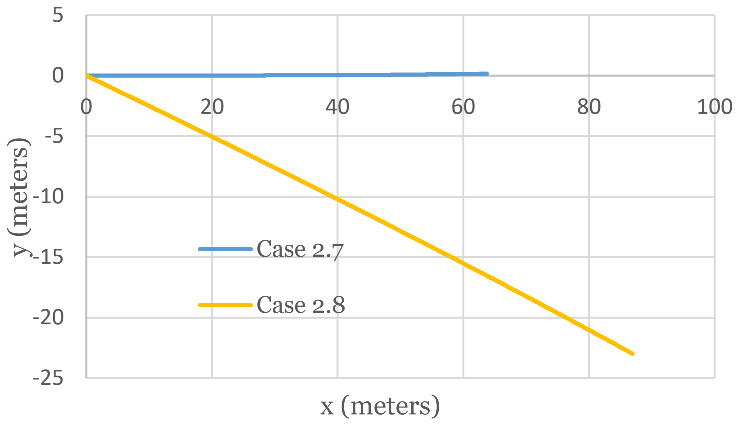

Figure 109 y(x) results for Configuration 4, from trajectory cases 2.7, and 2.8.

Annex 14 – Static coefficient results for Configuration 3.1

Table 25 CFD aerodynamic results for the static aerodynamic coefficients for Configuration 3.1, at 15 m/s.

α (º)	C_D	C_L	C_M
0	0,1174	0,0002	0,0000
2	0,1199	0,0756	-0,0679
4	0,1294	0,1661	-0,1709
6	0,1486	0,2741	-0,3131
8	0,1778	0,3949	-0,4838
10	0,2169	0,5267	-0,6813
12	0,2690	0,6760	-0,9211
14	0,3397	0,8571	-1,2231

Annex 15 – Additional trajectory results

The following figures are trajectory results which were not presented in the main text. Figures 110-112 are from Case 1.1, Figures 113-115 from Case 1.3, Figures 116-118 from Case 1.7, and Figures 119-121 from Case 1.9, all for Configuration 3, while Figures 122-124 are from Cases 1.1 and 1.3, and Figures 125-127 are from Cases 1.7 and 1.9, for Configuration 3.1.

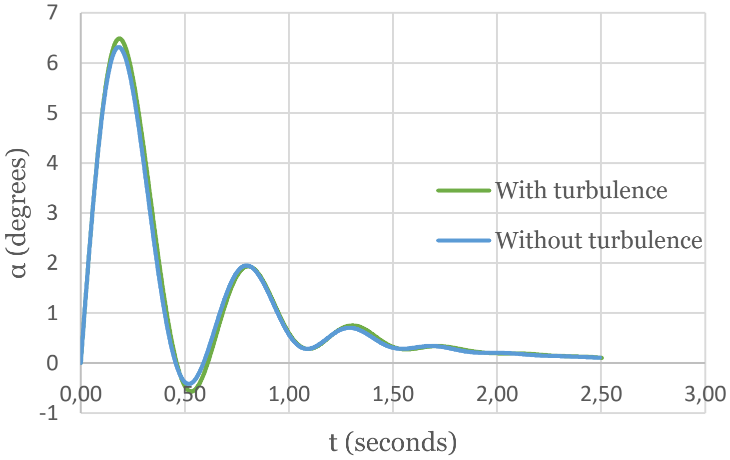

Figure 110 α(t) results for Configuration 3, from trajectory case 1.1, with and without considering wind turbulence.

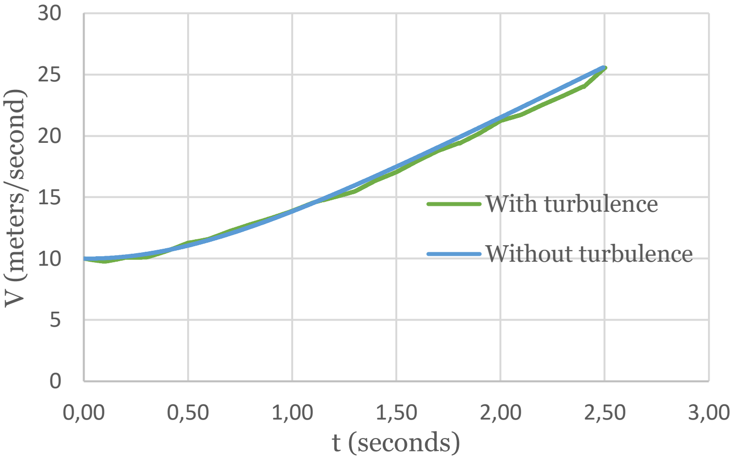

Figure 111 V(t) results for Configuration 3, from trajectory case 1.1, with and without considering wind turbulence.

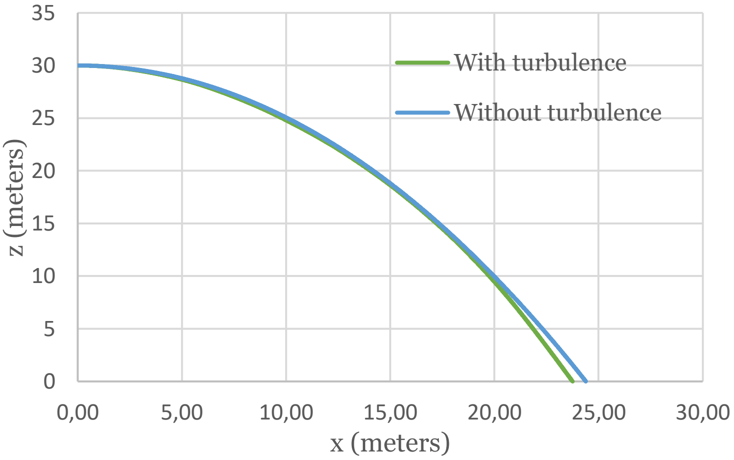

Figure 112 z(x) results for Configuration 3, from trajectory case 1.1, with and without considering wind turbulence.

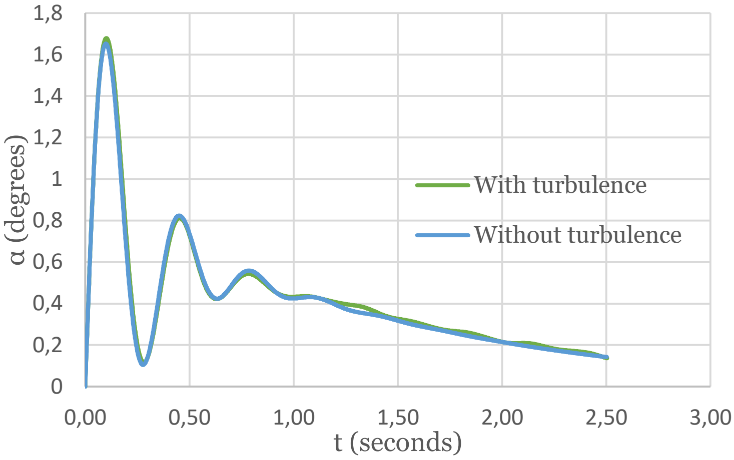

Figure 113 α(t) results for Configuration 3, from trajectory case 1.3, with and without considering wind turbulence.

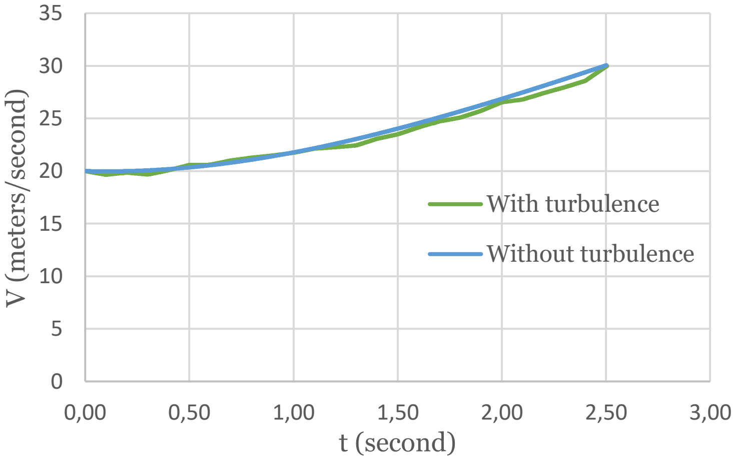

Figure 114 V(t) results for Configuration 3, from trajectory case 1.3, with and without considering wind turbulence.

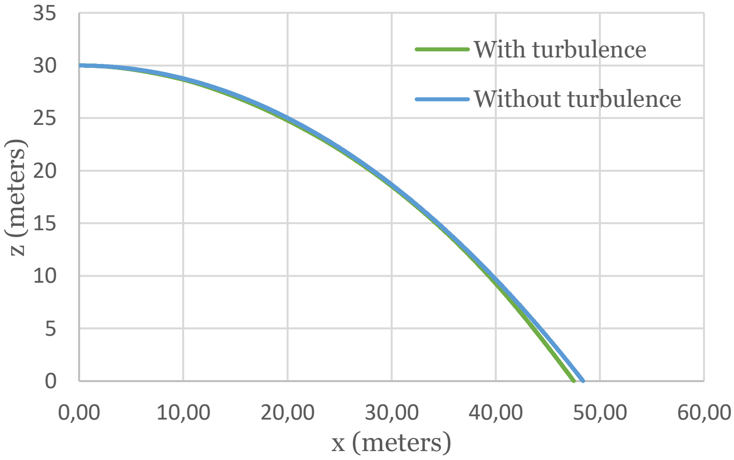

Figure 115 z(x) results for Configuration 3, from trajectory case 1.3, with and without considering wind turbulence.

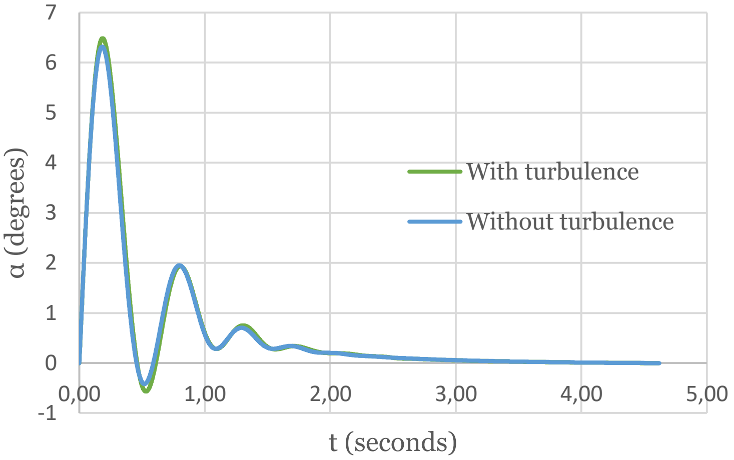

Figure 116 α(t) results for Configuration 3, from trajectory case 1.7, with and without considering wind turbulence.

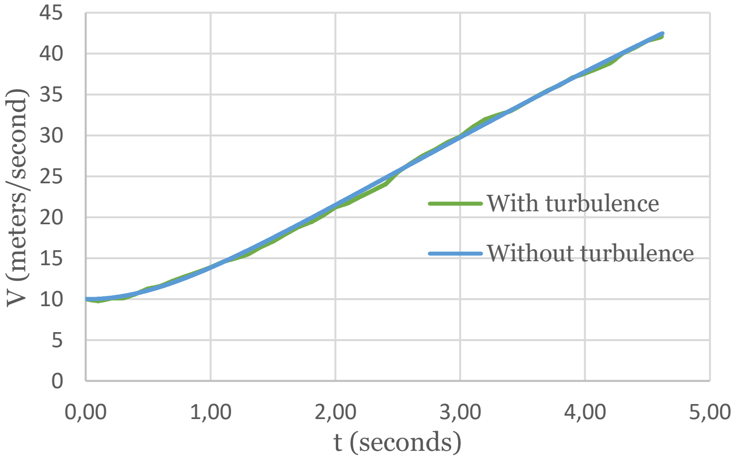

Figure 117 V(t) results for Configuration 3, from trajectory case 1.7, with and without considering wind turbulence.

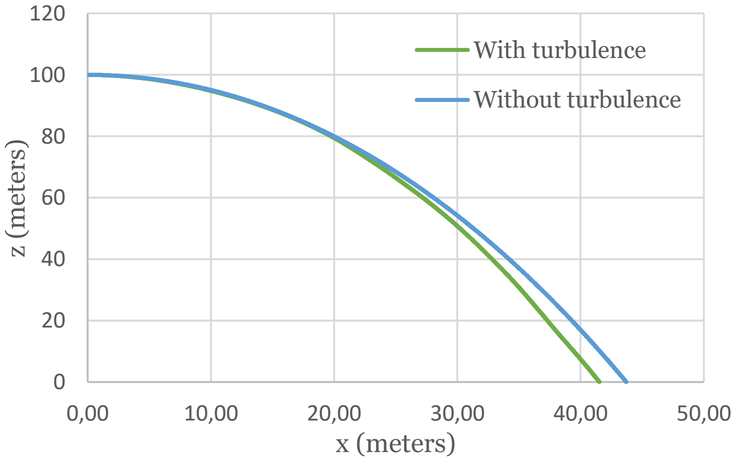

Figure 118 z(x) results for Configuration 3, from trajectory case 1.7, with and without considering wind turbulence.

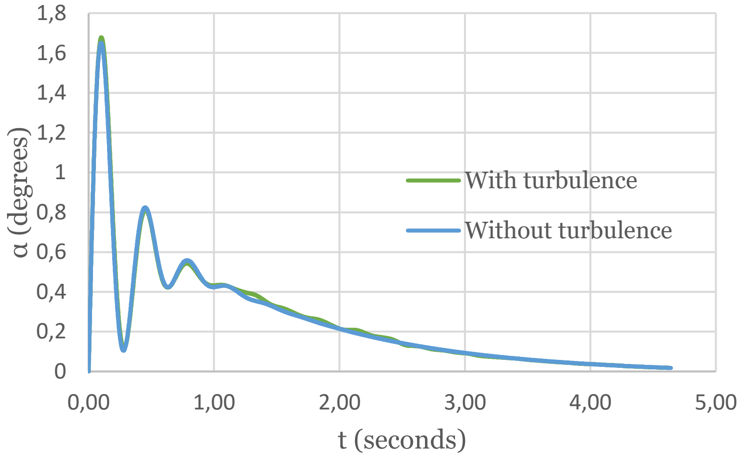

Figure 119 α(t) results for Configuration 3, from trajectory case 1.9, with and without considering wind turbulence.

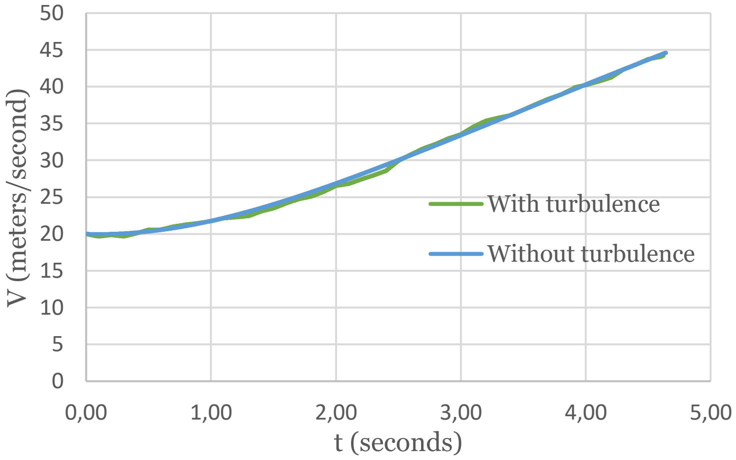

Figure 120 V(t) results for Configuration 3, from trajectory case 1.9, with and without considering wind turbulence.

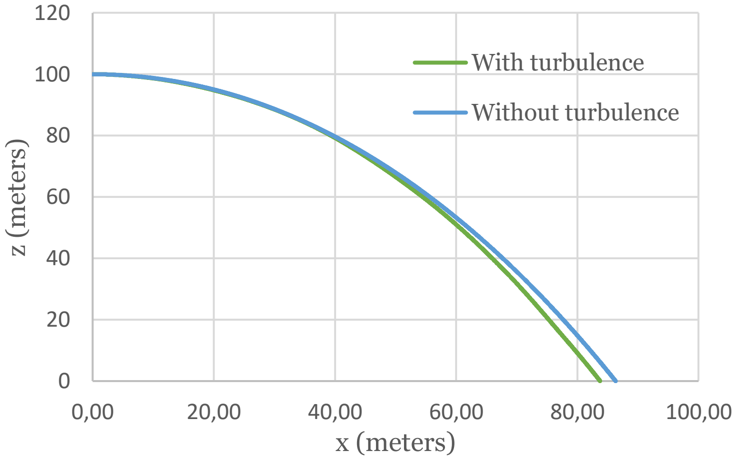

Figure 121 z(x) results for Configuration 3, from trajectory case 1.9, with and without considering wind turbulence.

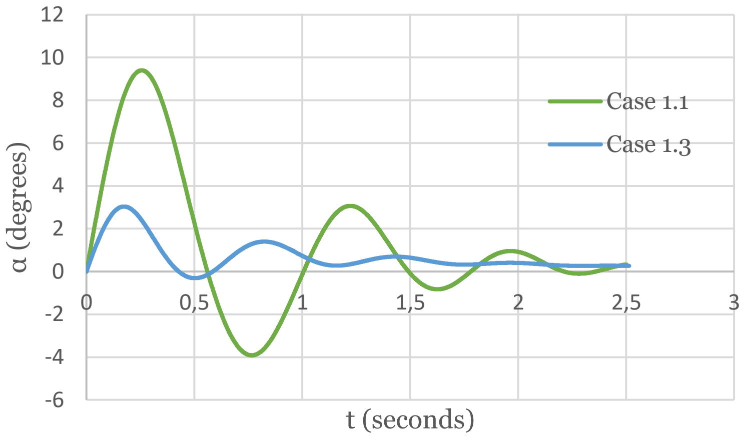

Figure 122 α(t) results for Configuration 3.1, from trajectory cases 1.1 and 1.3.

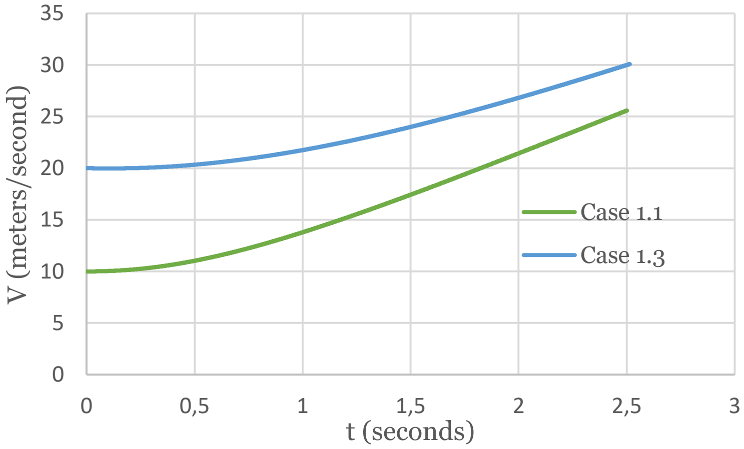

Figure 123 V(t) results for Configuration 3.1, from trajectory cases 1.1 and 1.3.

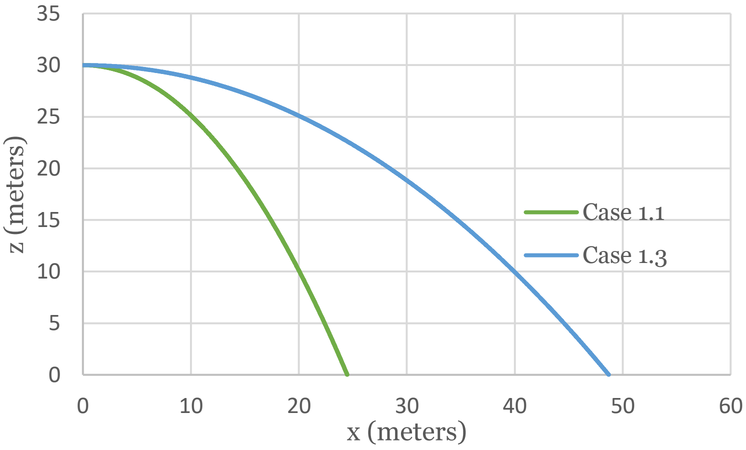

Figure 124 z(x) results for Configuration 3.1, from trajectory cases 1.1 and 1.3.

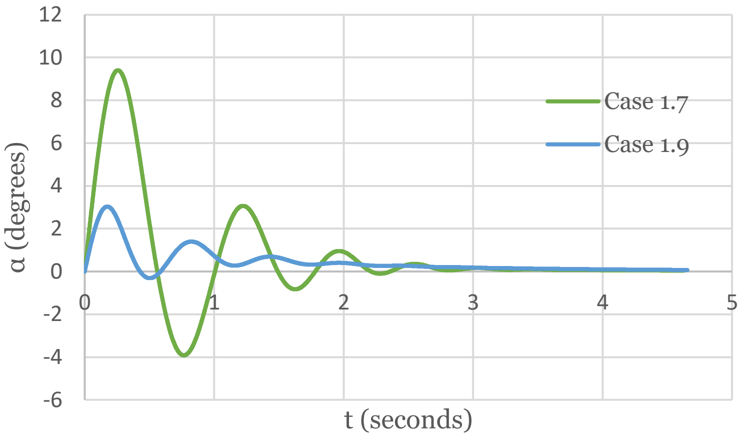

Figure 125 α(t) results for Configuration 3.1, from trajectory cases 1.7 and 1.9.

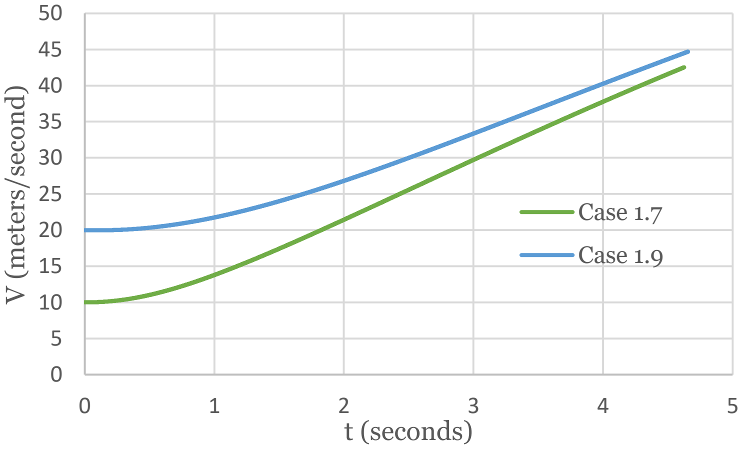

Figure 126 V(t) results for Configuration 3.1, from trajectory cases 1.7 and 1.9.

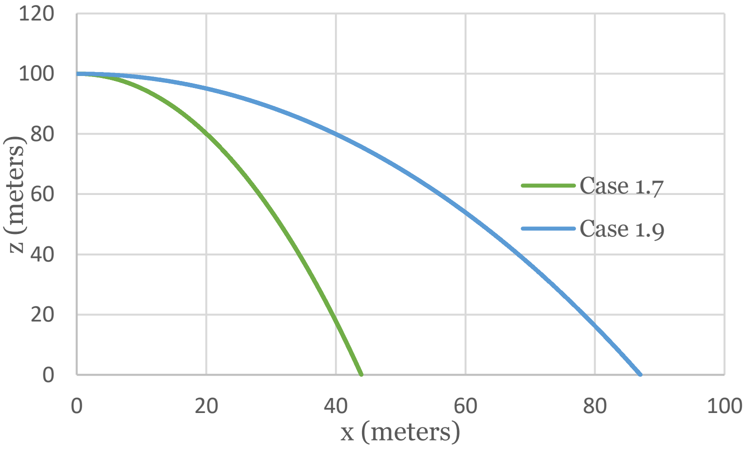

Figure 127 z(x) results for Configuration 3.1, from trajectory cases 1.7 and 1.9.

Annex 16 – Article of the dissertation

In the next pages an article of the present dissertation is laid out.

UBI – AERONAUTICAL ENGINEERING – MASTERS DISSERTATION ARTICLE, June 2020

Design and analysis of air launched fire-extinguishing projectiles

Rocha H.

Abstract

Wildfires are a source of human and environmental loss, and the available means to combat them in their early stages can be improved. With the aid of unmanned aircraft systems and FEB (fire-extinguishing balls), wildfires' early stages might be suppressed while keeping human lives risk-free. Considering the use of a fixed wing unmanned air vehicle to launch the fire-extinguishing projectile, launching the FEB without any modification does not seem to be the best option, with problems ranging from difficulty in predicting its trajectory to the possible bad impact performance. Therefore, three other configurations for the projectile with FEB as its basis were studied, all of them utilizing fins for the means of stability. These configurations differed in terms of tail design attached to the FEB: one is a tube, the other a tangential cone, and the other a symmetrical NACA airfoil revolved around its axis. Their static coefficients were obtained through CFD (computational fluid dynamics), while the dynamic ones were obtained through numerical methods. Using an implemented 6-DOF (degrees of freedom) model, 17 trajectories were studied for each of these configurations. Other analyses were carried out, like the influence of wind turbulence, consideration of a fourth configuration with double the area of the fins, and asserting the importance of the consideration of the dynamic coefficients while testing different values for some of these coefficients. Regarding the projectile configurations, CFD results suggest that the tube configuration has a transient behavior in the tested speeds, and that the tangential cone is a very suitable way of streamlining the FEB in these range of speeds, with no considerable difference to the NACA tail configuration. Trajectory results highlight the importance of considering the mean wind speed and direction, the importance of obtaining an appropriate estimate of the wind turbulence, and the importance of the dynamic coefficients for the stability and attitude results. Ultimately, between the tested configurations, the best candidate is the cone tail configuration, for its simplicity in construction and performance in the trajectories.

Keywords: Fire-extinguishing; ball; UAS; wildfires; trajectory; ballistics; 6-DOF; CFD; aerodynamics

Nomenclature

CFD: Computational Fluid Dynamics
CG: Center of gravity
DOF: Degrees of freedom
FEB: Fire-extinguishing ball/balls
UAS: Unmanned aerial systems
UAV: Unmanned aerial vehicle
a_t: Slope of the $C_L(\alpha)$ curve of the tail
C_D: Drag coefficient
C_L: Lift coefficient
C_M: Pitching/overturning moment coefficient
C_{M_q}: Pitch damping moment coefficient proportional to q
$C_{M\_\dot{\alpha}}$: Pitch damping moment coefficient proportional to $\dot{\alpha}$
C_{N_r}: Yaw damping moment coefficient proportional to r
$C_{N_{\dot{\beta}}}$: Yaw damping moment coefficient proportional to $\dot{\beta}$
C_X: Axial force coefficient
C_Y: Side force coefficient
C_{Y_r}: Yaw damping force coefficient proportional to r
$C_{Y_{\dot{\beta}}}$: Yaw damping force coefficient proportional to $\dot{\beta}$
C_Z: Normal force coefficient
C_{Z_q}: Pitch damping force coefficient proportional to q
$C_{Z_{\dot{\alpha}}}$: Pitch damping force coefficient proportional to $\dot{\alpha}$
d: Diameter of the projectile
D: Drag force
g: Gravitational acceleration
I_x, I_y, I_z: Moments of inertia
I_{xy}, I_{yx}, I_{yz}, I_{zy}, I_{xz}, I_{zx}: Products of inertia
l: Length of the projectile
L: Lift force
l_t: Distance between the projectile's CG and the tail aerodynamic center
m: Mass of the projectile
$MW_{direction}$: Mean wind direction
$MW_{velocity}$: Mean wind velocity
$Oxyz$: Projectile-fixed reference coordinate system
$Ox_ay_az_a$: Air-trajectory reference coordinate system
$Ox_gy_gz_g$: Earth-fixed reference coordinate system
p: Rolling velocity
PDF: Pitch damping force
PDM: Pitch damping moment
PM: Pitching/overturning moment
q: Pitching velocity
Q_∞: Dynamic pressure
r: Yawing velocity
R: Range of flight, in trajectory model validation
Re: Reynolds number
S: Reference area (projectile's frontal area)
S_{tail}: Reference area of the horizontal tail (area projected on the xz plane)
t: Time variable during trajectory
T_{flight}: Time of flight, in trajectory model validation
u: Projectile velocity in x axis
u_{WT}: Wind turbulence velocity in x axis
v: Projectile velocity in y axis
V: Total projectile air velocity
V_H: Horizontal tail volume coefficient
v_{WT}: Wind turbulence velocity in y axis
w: Projectile velocity in z axis
W: Weight force
w_{WT}: Wind turbulence velocity in z axis
x_{cg}: Position of the projectile's center of gravity, measured from the most forward point
YDF: Yaw damping force
YDM: Yaw damping moment
YM: Yawing moment
α: Angle of attack
$\dot{\alpha}$: Rate of change of angle of attack
β: Sideslip/yaw angle
$\dot{\beta}$: Rate of change of angle of sideslip
θ: Pitch angle
ρ: Density of the airflow
ϕ: Bank angle
ψ: Yaw angle

1. Introduction

During the last decade, Portugal has seen an increase of wildfires severity and number of occurrences. The current climate change scenario is an important factor, which will worsen the situation as average temperatures rise and atmospheric precipitation decreases, leading to more prolonged dry seasons [1]-[6], all while the unpredictability of occurrence of forest fires is at an all-time high [7]. Some of the other contributing factors are: an increased Urban-Wildlife Interface from the great number of secondary housings in rural areas[8]; advanced age population in the countryside, which are unable to correctly clean their plots [9]; slash-and-burn agriculture [10]; bad planning and managing of the country's forest, especially the planting of highly flammable arboreal species [9], [11].

Wildfires are a source of economic, social, and environmental cost. In 2017, Portugal was marked by having an increase of 428% in burnt area, comparing to the annual average until that date, with a burnt area of more than 4,420 km^2, distinguishing it as the year with most burnt area since 2007 [12]. Pedrogão Grande's forest fire stands out, killing 66 people [13], affecting more than 1000 structures, and costing about 500 million euros [14]. In 2018, the state of California in the U.S.A. suffered both its deadliest forest fire, with 85 dead [15], and the biggest in terms of burnt area, with a single forest fire burning more than 459,000 hectares [16]. The 2019/2020 bushfires in Australia ravaged more than 18 million hectares of land, destroyed more than 2,000 homes, killed 34 people and about one billion animals [17], while releasing an estimate of 306 million tons of carbon dioxide [18], and costing more than 4.4 billion Australian dollars [19].

By focusing efforts on forest fires prevention and a quick and efficient attack on its origin, the costs associated with firefighting could be reduced drastically, especially since putting out a fire in its initial stages, with a small hotspot, is easier than fighting a fully developed forest fire [20]. Unmanned Aircraft Systems (UAS) can fulfill various activities related to this, such as surveillance and direct freighting, reducing the necessary human resources, and decreasing their risk of injury or death. They can also act on circumstances when resorting to conventional firefighting means is difficult or even impossible, such as fires on terrains of difficult access, on top of buildings, in oil rigs, or in inadequate meteorological or visibility conditions that prevent the use of the currently available firefighting aerial resources [21]-[25].

SpaceWay proposed the concept of suppressing the very first stages of a forest fire by launching a projectile from an UAV, which upon impact with the ground or near impact would explode and release a fire suppressant or retardant chemical. It is also proposed for a fire-extinguishing ball to be the projectile design basis. This UAS would act as an initial attack, mobilized immediately after the detection and actuating precisely on the area where the fire is starting, before it spreads to the fuel surrounding it, preventing therefore a full-blown forest fire. In this work four possible configurations for the projectile will be studied and evaluated, analyzing their aerodynamics and their resulting trajectory in different cases.

Exterior Ballistics are the sub-field of Ballistics which studies the movement of the projectile along its atmospheric trajectory, including the forces, moments, and other variables that affect it, such as air properties or the projectile's geometry [26].

Different Exterior Ballistics trajectory models consider different sets of forces and considerations. 6-DOF (degrees of freedom) models originated in 1920 [27], and in this model the projectile is considered a rigid body, i.e., the body is undeformable, and their dynamics are described by the application of either Newton's second law or Lagrangian mechanics, and by the laws of kinematics. Three rotational and three translational degrees of freedom make this model the most accurate to date, adequately describing most physics along the projectile's trajectory, as well as its complete movement [26], [28]-[30].

The accuracy of the trajectory prediction is also tied in with the accuracy the projectile aerodynamics characteristics are obtained, while different trajectory models require different data input and theoretical or mathematical considerations and their different usage might depend on the developing stage of projectile or even the importance or type of the project itself. The aerodynamic characteristics necessary for the implementation of an Exterior Ballistics model cannot be obtained through a general method, therefore, depending on the available information, available resources, and the problem itself, different techniques are employed [31].

To predict a projectile configuration trajectory utilizing a 6DOF model, usually four sets of techniques are used to obtain the necessary aerodynamics: CFD (computational fluid dynamics) simulations, wind tunnel testing, flight testing, or using some aerodynamic coefficient prediction software package. It is important to notice that the correct estimation of the projectile aerodynamic behavior is especially important in new configurations, in order to correctly assess its trajectory prior to flight tests, therefore reducing development costs [32]-[34].

In CFD simulations, the fluid flow is modeled by equations, which are then numerically solved for a specific configuration. These equations are based on the Navier-Stokes equations, which fully describe the flow, and different sets of equations have different levels of simplification, since it is not feasible to fully solve the Navier-Stokes equations by use of Direct Numerical Simulation in a time-adequate manner [35]. Recent advances in computing and CFD technologies allow for less costly design developments and deeper insight into the aerodynamic phenomena. Moreover, presently it is possible to correctly predict projectile dynamics during its flight based only on CFD simulations, with the principal advantage being the ease of changing almost any definition of the simulation [32]-[34], [36]-[38]. The major problem with CFD is that it requires substantial knowledge and experience on the subject to correctly setup the calculations. The choice of the correct turbulence model for the case in study, as well as its boundary resolution, and the implementation of a good grid generation which can correctly predict the important aspects of the flow are three of the major considerations for a good CFD implementation [36], [38].

Regarding firefighting projectiles, the earliest record for this kind of devices dates to 1723 [39], while the first air launched firefighting projectile dates to 1939 [40]. Multiple firefighting concepts, projectiles and their respective delivery systems have been patented or studied since then, for example [41]-[46]. The developed projectiles usually differ in ways the fire-extinguishing or suppressant payload is delivered, or the way the projectile is deployed, most of them requiring a “firearm-like” device to launch it.

In Portugal there is a project being developed since 2005 called FIREND. This firefighting projectile concept was presented in 2005 by Lieutenant-Colonel Marquês Sousa, Pedro Vilaça da Silva, and Francisco Lima [41]. Since then, several changes have been made, like shell design and detonation method, accompanied by several Internal and External Ballistics studies.

The project which encompasses this work plans to use a fire-extinguishing ball (FEB). There are two main manufacturers of this kind of fire extinguishing device, Elide Fire [47] and AFO [48]. The one this project intends to use is the AFO Ball, which will be the base part of all projectile configurations studied in this dissertation. It comprises of a polystyrene shell, which encloses a dry fire extinguishing agent, Mono Ammonium Phosphate. The outer case encompasses a fuse, which after a few seconds detonates a charge present on the center of the ball, blasting the case and spreading the fire extinguishing powder.

As for projects and researches much similar to this one, that is, using fire-extinguishing balls, some studies were made quite recently. One very important study is the one by Aydin et.al [42], in which the effectiveness of FEB to combat wildfires is assessed, and the results show that there is a good possibility of using this technology for this effect. Another interesting study [46] analyzed three different UAV (unmanned aerial vehicle) configurations to launch/release a FEB to prevent or extinguish various types of fires, including. However, no study was found on the trajectory of the FEB after release.

The objective of this work is to evaluate the aerodynamics and trajectory performance of possible configurations for a fire-extinguishing projectile which uses a fire-extinguishing ball as a design basis. Firstly, the trajectory prediction model is defined, followed by the explanation of the used methods for obtaining the aerodynamic coefficients. After this, the projectile design follows, defining the projectile and mission requirements, the preliminary design choices, and presenting the proposed configurations. Subsequently, the results are presented, including the aerodynamic coefficient results and the trajectory prediction results. Finally, the conclusions of the work are presented.

2. Models

2.1. Projectile 6-DOF model

The different forces a projectile undergoes during its aerodynamic flight depend mostly on the projectile’s method of stabilization, while some forces are common to any type of projectile. McCoy [26] presents a detailed overview of the complete force-moment system of projectiles, which will be followed to some degree in this chapter. Since the proposed projectile configurations will employ a fin-stabilization method, only the forces and moments relevant to the trajectory prediction of this type of projectiles are presented. One important thing to notice is the individual consideration of both pitching and yawing moment. Another relevant note is that the gravitational acceleration will be considered constant and the Coriolis effect will not be considered, since the trajectory’s distance is small. Therefore, the considered forces and moments for the 6DOF trajectory model are the following:

$$\text{Weight: } W = mg \tag{1}$$

$$\text{Drag: } D = \frac{1}{2}\rho V^2 S C_D = Q_\infty S C_D \tag{2}$$

$$\text{Lift: } L = Q_\infty S C_L \tag{3}$$

$$\text{Pitching moment: } M = Q_\infty S d C_M \tag{4}$$

$$\text{Yawing moment: } N = Q_\infty S d C_N \tag{5}$$

$$\text{Pitch damping force: } PDF = Q_\infty S \left(\frac{qd}{V}\right)\left(C_{z_q} + C_{z_{\dot{\alpha}}}\right) \tag{6}$$

$$\text{Yaw damping force: } YDF = Q_\infty S \left(\frac{rd}{V}\right)\left(C_{Y_r} + C_{Y_{\dot{\beta}}}\right) \tag{7}$$

$$\text{Pitch damping moment: } PDM = Q_\infty S d \left(\frac{qd}{V}\right)\left(C_{M_q} + C_{M_{\dot{\alpha}}}\right) \tag{8}$$

$$\text{Yaw damping moment: } YDM = Q_\infty S d \left(\frac{rd}{V}\right)\left(C_{N_r} + C_{N_{\dot{\beta}}}\right) \tag{9}$$

There are three sets of coordinate systems: $Oxyz$, the projectile-fixed reference coordinate system; $Ox_ay_az_a$, the air-trajectory reference coordinate system; and $Ox_gy_gz_g$, the Earth-fixed reference coordinate system.

The projectile-fixed system $Oxyz$ relates to the Earth-fixed reference system $Ox_gy_gz_g$ by means of the Euler angles (ϕ, θ, ψ, which are the roll, pitch, and yaw angles, respectively), by the following equation, using a transformation matrix:

$$\begin{bmatrix} x_g \\ y_g \\ z_g \end{bmatrix} = \begin{bmatrix} \cos\theta\cos\psi & \sin\phi\sin\theta\cos\psi - \cos\phi\sin\psi & \cos\phi\sin\theta\cos\psi + \sin\phi\sin\psi \\ \cos\theta\sin\psi & \sin\phi\sin\theta\sin\psi + \cos\phi\cos\psi & \cos\phi\sin\theta\sin\psi + \sin\phi\cos\psi \\ -\sin\theta & \sin\phi\cos\theta & \cos\phi\cos\theta \end{bmatrix} \begin{bmatrix} x \\ y \\ b \end{bmatrix} \tag{10}$$

The projectile-fixed system $Ox_by_bz_b$ and the air-trajectory system $Ox_ay_az_a$ are related by the angle of attack α and the sideslip angle β as follows:

$$\begin{bmatrix} x_a \\ y_a \\ z_a \end{bmatrix} = \begin{bmatrix} \cos\alpha\cos\beta & \sin\beta & \sin\alpha\cos\beta \\ -\cos\alpha\sin\beta & \cos\beta & -\sin\alpha\sin\beta \\ -\sin\alpha & 0 & \cos\alpha \end{bmatrix} \begin{bmatrix} x \\ y \\ b \end{bmatrix} \tag{11}$$

The relation between the projectile-fixed system and the Earth-fixed one defined in (10) can be visually represented by Figure 1.

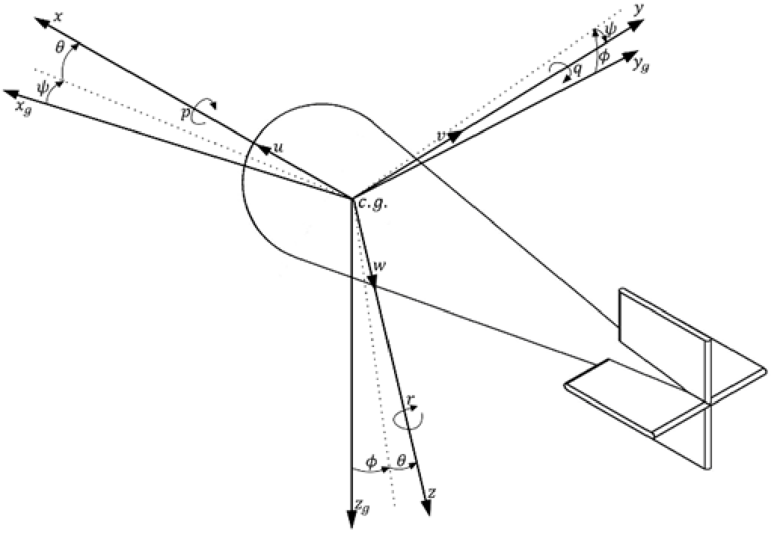

Figure 1 Geometry between $Ox_by_bz_b$ and $Ox_gy_gz_g$

On the other hand, the relationship in (11) can be visually represented by Figure 2.

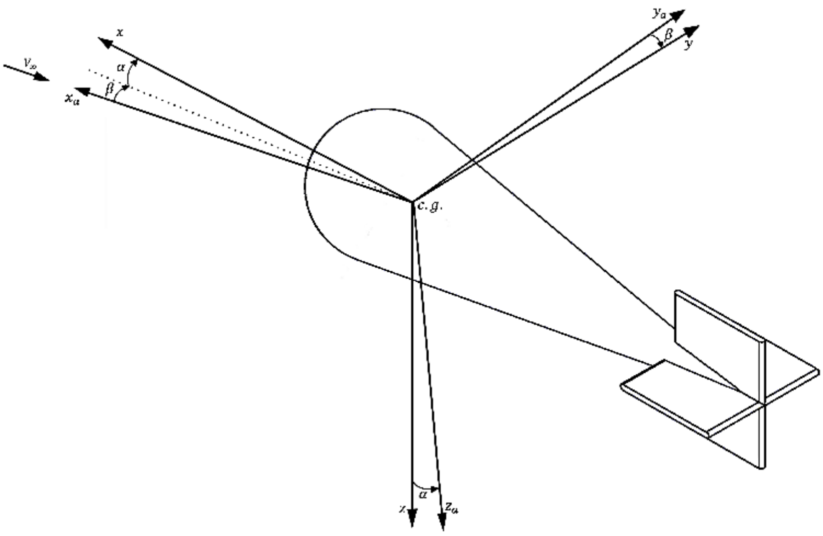

Figure 2 Geometry between $Ox_by_bz_b$ and $Ox_ay_az_a$

In order to construct this 6-DOF model, a number of assumptions have been made:

1 – the projectile is considered a rigid body, with a constant mass, moment of inertia, and position of center of mass;

2 – the projectile has two planes of symmetry, xy and xz, and the stabilizing surfaces are all equal, fixed, arranged symmetrically in a cross. This means the products of inertia I_{xy}, I_{yx}, I_{yz}, I_{zy}, I_{xz} and I_{zx} are equal to zero and that I_y=I_z;

3 – the Earth is considered flat and non-rotating, with a constant gravity acceleration, and the azimuth angle during the trajectory remains constant.

The trajectory model is developed from Newton’s second law of motion. [31] and [34] present the development of similar models. Some simplifications were made to the general 6-DOF model: since the projectile will be fin-stabilized and no rotation caused by the wind will be considered, p can be initially set to zero. Both these considerations will be substantiated later. Additionally, as no moment will act on the roll axis, $\dot{p}$ will be always zero, and therefore we can assume that p will also always be nonexistent. Consequently, ϕ will be zero throughout the flight. Considering these simplifications, the previously established assumptions, and the considered forces and moments, the equations defining the trajectory model are:

$$\begin{bmatrix} \dot{\phi} \\ \dot{\theta} \\ \dot{\psi} \end{bmatrix} = \begin{bmatrix} r \tan\theta \\ q \\ \frac{r}{\cos\theta} \end{bmatrix} \tag{12}$$

$$\begin{bmatrix} \dot{x}_g \\ \dot{y}_g \\ \dot{z}_g \end{bmatrix} = \begin{bmatrix} u\cos\theta\cos\psi - v\sin\psi + w\sin\theta\cos\psi \\ u\cos\theta\sin\psi + v\cos\psi + w\sin\theta\sin\psi \\ -u\sin\theta + w\cos\theta \end{bmatrix} \tag{13}$$

$$\begin{bmatrix} \dot{u} \\ \dot{v} \\ \dot{w} \end{bmatrix} = \begin{bmatrix} \frac{-mg\sin\theta + Q_\infty S C_X}{m} + rv - qw \\ \frac{mg\sin\phi\cos\theta + Q_\infty S\left(C_Y + \left(C_{Y_r} + C_{Y_{\dot{\beta}}}\right)\frac{rd}{V}\right)}{m} - ru \\ \frac{mg\cos\phi\cos\theta + Q_\infty S\left(C_Z + \left(C_{Z_q} + C_{Z_{\dot{\alpha}}}\right)\frac{qd}{V}\right)}{m} + qu \end{bmatrix} \tag{14}$$

$$\begin{bmatrix} \dot{p} \\ \dot{q} \\ \dot{r} \end{bmatrix} = \begin{bmatrix} 0 \\ \frac{1}{I_y} Q_\infty Sd\left(C_M + \left(C_{M_q} + C_{M_{\dot{\alpha}}}\right)\frac{qd}{V}\right) \\ \frac{1}{I_z} Q_\infty Sd\left(C_N + \left(C_{N_r} + C_{N_{\dot{\beta}}}\right)\frac{rd}{V}\right) \end{bmatrix} \tag{15}$$

These differential equations will be solved forward in time with the 4th order Runge-Kutta numerical integration method.

2.1.1. Trajectory model validation

In order to correctly implement the trajectory prediction model, it is fundamental to carry out a validation procedure. In this work, this was done by implementing the properties of a 120mm mortar, from [26], since it is also a fin stabilized projectile, using the validation cases from the same reference. The aerodynamic coefficients were obtained by linear interpolation, and the step-size used in the numeric integration method was 10^{-5} seconds. The launch variables in the validation cases as well as the results are made explicit in Table 1. It is observable that the percent error in time of flight, range and maximum height is below 1% for almost all values in relation to [26]. Therefore, it can be concluded the accuracy of the model is suited for this first stage in the project, allowing for the comparison between the projectile configurations.

Table 1 Validation case variables for the different validation cases and their respective results.

Case	$M.V.$ (m/s)	$Q.E.$ (degrees)	q_1 (rad/s)	Ψ_1 (degrees)	$E_{T_{flight}}$(%)	E_R(%)	$E_{M.H.}$(%)
1	102	45	0,913	8	0.00	0.89	0.00
2	102	65	0,913	8	0.00	1.43	0.95
3	102	85	0,913	8	0.00	1.21	0.00
4	318	45	1,795	3	0.24	0.23	0.10
5	318	65	1,795	3	0.19	0.16	0.15
6	318	85	1,795	3	0.17	0.24	0.62

2.2. Wind model

In order to understand the influence of various parameters on the projectile's trajectory and consequently on its precision, the influence of wind will be considered. Wind is described in [49] as "a continuous vector random process that varies in three space dimensions and also in time" and, according to [50], it can be divided in two parts: the large-scale horizontal winds, with a certain direction and mean magnitude, and the localized turbulence. This wind turbulence has inherent stochastic behavior, which is caused by pressure instabilities and variations of temperature, which change in space and time.

Comparing the characteristic dimensions of wind gusts and the dimension of the projectiles in study, a uniform effect in the objects can be assumed, and no rotations caused by them will be considered. Thus, only the translational speed variations will be taken into consideration, which in turn affect the angle of attack and sideslip of the projectile [31].

The horizontal mean wind speed and direction can be obtained through weather databases or weather forecasts. MATLAB's Simulink [51] will be used to obtain the wind turbulence, by using the Dryden Continuous Wind Model for a series of speeds, and the values will be interpolated for the current projectile speed. The model's defining expressions can be found in detail in [52], along their respective original references, which are military handbooks.

With this, a slight modification is needed in the trajectory model, in order to account for the mean wind and wind turbulence. Considering that the obtained wind turbulence velocity components are in the projectile body-fixed system [50], equations (13) and (14) are now substituted by equations (16) and (17), respectively:

$$\begin{bmatrix} \dot{x_g} \\ \dot{y_g} \\ \dot{z_g} \end{bmatrix} = \begin{bmatrix} (u+u_{WT})\cos\theta\cos\psi - (v+v_{WT})\sin\psi + (w+w_{WT})\sin\theta\cos\psi - MW_{vel}\times\cos\ MW_{dir} \\ (u+u_{WT})\cos\theta\sin\psi + (v+v_{WT})\cos\psi + (w+w_{WT})\sin\psi\sin\psi - MW_{vel}\times\sin\ MW_{dir} \\ -(u+u_{WT})\sin\theta + (w+w_{WT})\cos\theta \end{bmatrix} \tag{16}$$

$$\begin{bmatrix} \dot{u} \\ \dot{v} \\ \dot{w} \end{bmatrix} = \begin{bmatrix} \frac{-mg\sin\theta + QSC_X}{m} + r(v+v_{WT}) - q(w+w_{WT}) \\ \frac{mg\sin\phi\cos\theta + QS\left(C_Y + \left(C_{Y_r} + C_{Y_{\dot{\beta}}}\right)\frac{rd}{V}\right)}{m} - r(u+u_{WT}) \\ \frac{mg\cos\phi\cos\theta + QS\left(C_Z + \left(C_{Z_q} + C_{Z_{\dot{\alpha}}}\right)\frac{qd}{V}\right)}{m} + q(u+u_{WT}) \end{bmatrix} \tag{17}$$

2.3. Static aerodynamic coefficients and CFD methodology

In this work, the static aerodynamic coefficients were obtained through CFD analysis and the dynamic derivative coefficients will be estimated using the analytical methods present in [53]. These methods were chosen taking in consideration the available resources, including time available, and the current early stage of the project.

The axial force coefficient C_X and the normal force coefficient C_Z will be calculated based on the drag coefficient C_D and lift coefficient C_L, which will be obtained with the software *ANSYS Fluent* [54], along with the pitch damping moment C_M. Since the projectile has both xy and xz as planes of symmetry, the existence of dynamic symmetry between these planes can be considered. Therefore, the side force C_Y derivative with respect to the angle of sideslip β will be considered equal to the C_Z derivative with respect to the angle of attack α, and the yaw damping moment C_N derivative with respect to β will be considered equal to the C_M derivative with respect to α. It is important to refer, again, that this definition is not unheard of (for example, [34], takes this approach), and it is valid for the cases in study since there will not be a considerable β in the launching cases of study. If that would be the case, C_X, C_Y, C_Z and the moment derivatives would have to be considered as a function of both α and β.

The work carried out utilizes the CFD software package *ANSYS Fluent*. The used method works by solving the governing integral equations of conservation of momentum, mass, energy, turbulence, and other fluid variables using a finite volume discretization process to solve the Reynolds-averaged Navier-Stokes equations [55].

Before the numerical analysis itself, the geometry of the object in study is defined, as well the surrounding fluid domain. Secondly, the meshing process is carried out. The boundary conditions are defined, the method for Pressure-Velocity Coupling is chosen, and the turbulence model is defined, which is needed to simulate the small scale and high frequency fluctuations of a turbulent flow [56].

The domain is radially extended 10 projectile lengths in front of the body and 20 projectile lengths downstream of the body. The fluid domain has a finer mesh subdivision, in order to more accurately resolve the wake behind the projectile and to guarantee the correct orientation of the streamlines in front of the projectile. This subdivision is radially extended 1,5 body lengths in front of the projectile and 3 lengths aft of the body. An unstructured mainly tetrahedral mesh is used, since it is appropriate for different complex configurations, allowing for a consistent meshing methodology. A velocity inlet boundary condition was considered for the upstream boundary and a pressure outlet for the downstream boundary. Both were set with the atmospheric conditions at sea level, according to the International Standard Atmosphere [57]. Regarding the projectile wall, an adiabatic no slip boundary was defined. No compressibility effects were taken into consideration, since the Mach number which will be tested is around 0.04. Figure 3 is a representation of the computational domain.

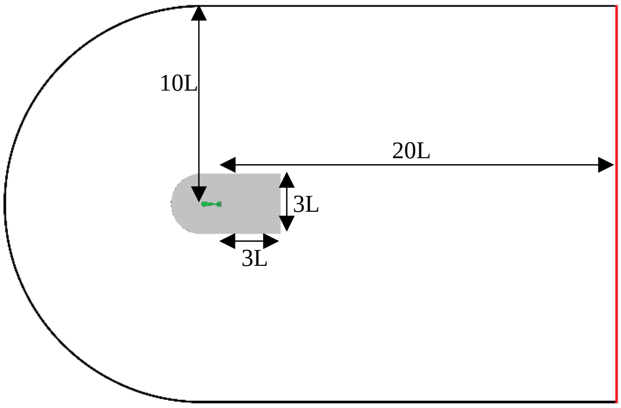

Figure 3 CFD Domain. The projectile's adiabatic no slip wall is in green, the pressure outlet in red, and the velocity inlet in black. The area in grey is the finer subdivision of the mesh. The dimensions are all in relation to the projectile's length

The model used is the k-ω SST [58], which is a two-equation eddy-viscosity model. This model was chosen for its large use in aeronautics, and because it is considered a good model for flows withstanding separation, which might be a relevant aspect in some of the flow around the proposed configurations [58], [59]. Since the model solves the flow up to the viscous sub-layer every mesh is ensured to have a $y^+ \leq 1$ in order to properly resolve the boundary layer, while keeping the minimum orthogonal quality above 0.01 will ensure better results [35], [38], [59]. As for the coupling between the pressure and velocity fields, the Coupled scheme was selected.

2.3.1 CFD methodology validation and Grid independence

To ensure a correct CFD methodology, it is imperative to validate it, by comparing the aerodynamic results of the used method with available results. This was carried out by comparing the results of a Non-Lethal 12-Gauge Fin-Stabilized projectile, with the ones present in [60]. This projectile and test case were chosen for the similar flow characteristics, which are low speed and uncompressible flow, and since it also employed fin-stabilization. Figure 4 presents the results for the CFD methodology validation.

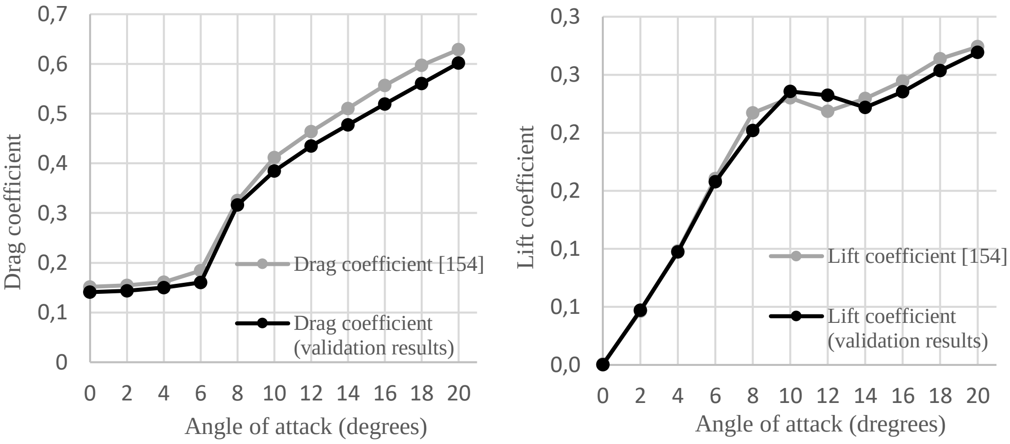

Figure 4 CFD Validation results for drag (left) and lift (right) coefficients.

A maximum difference of 13.2 % for the drag coefficient for α=6° and 7.1 % for the lift coefficient for α=8° are observed in these results, while most results for drag are below 7.2 % and below 7.1% for lift. Moreover, the drag and lift curves are correctly predicted, which indicates a correct prediction of the aerodynamic effects around the body, such as stall. Therefore, the CFD model is considered correctly validated. It is important to refer that the maximum percentual difference for the lift coefficient is actually 69% at 0 degrees of angle of attack, but the difference in the value is just 0.004, not being therefore a considerable difference in the coefficient value.

Another relevant aspect to study in CFD methodologies is grid independence. Grid independence studies are used to have an estimate if the number of elements used is enough to obtain an accurate result while taking in consideration the time of calculation. In this dissertation, the grid independence study was carried out using the 2nd Configuration, by varying the density of the mesh in its finer subsection, by varying the Element Size in the Body of Influence meshing method. The difference between 30 million elements and 61 million is approximately 0.58%, and since after 30 million elements the simulation time cost gets quite large, 30 million elements is considered a good value for the number of elements in the mesh. Therefore, all CFD simulations are run with meshes with an element number around this value.

2.4. Dynamic aerodynamic coefficients

Etkin [53] presents a quite accurate way to calculate the dynamic derivative coefficients based on analytical expressions, which is the method used in this work to do so. Analogous to before, $\left(C_{Y_r} + C_{Y_{\dot\beta}}\right)$ will be considered equal to $\left(C_{Z_q} + C_{Z_{\dot\alpha}}\right)$ and $\left(C_{N_r} + C_{N_{\dot\beta}}\right)$ will be considered equal to $\left(C_{M_q} + C_{M_{\dot\alpha}}\right)$ because of the dynamic symmetry between xy and xz.

The dynamic coefficients that will be obtained can be divided into two groups, q derivatives and $\dot\alpha$ derivatives. The first ones arise from the aerodynamic effects on the tail when the projectile rotates around its y axis, while the angle of attack remains zero. The latter ones emerge from the delayed adjustment of the pressure distribution on the tail after a quick change in angle of attack.

Etkin defines $C_{Z_{\dot\alpha}}$ and $C_{M_{\dot\alpha}}$ based on the lag of the downwash present on the tail, which is primarly caused by the trailing vortices of a wing. Since the projectile does not have wing, $C_{Z_{\dot\alpha}}$ and $C_{M_{\dot\alpha}}$ will be considered both zero. Even though this consideration might give rise to some attitude prediction errors in relation to reality, it will be considered a suitable approximation for this primary stage of the project, and it is in line with many other works that only consider the q derivatives [61].

The equations for C_{Z_q} and C_{M_q} are the following:

$$C_{Z_q} = -\frac{2V}{d}\frac{\partial C_L}{\partial q} = -\frac{2V}{d} a_t \frac{S_t l_t}{SV} = -2a_t V_H \tag{18}$$

$$C_{M_q} = -\frac{2V}{d}\frac{\partial \Delta C_M}{\partial q} = -2a_t \frac{l_t}{d} V_H \tag{19}$$

The detailed explanation of the equations is presented in [53].

3. Projectile design

3.1. Projectile and mission requirements

Before analyzing all the design choices, as well as their theorical and practical justifications, it is important to define the projectile and mission requirements. One of the requirements of the projectile is that during the phase of transportation of the mission the additional drag must be low, since it will be transported outside the UAV, and a low impact on its performance is desired. Another evident requirement is the precision of the projectile. This objective is fundamental to all projectile missions, but with the inherent emergency of a firefighting mission this objective becomes even more critical. The importance of precision is evidenced in the way the FEB works: a great offset from the fire source will prevent the fuse from being ignited and, therefore, will not spread the fire-extinguishing agent, and the objective will not be met. An additional requirement is good characteristics of both static and dynamic stability. A further requirement is to obtain a quick Minimum Viable Product. The project is a proposition from *SpaceWay*, and the company requires a viable product as quickly as possible, facing the emergent situation of increased wildfires. Thus, some decisions will be made having this in consideration.

3.2. Preliminary design choices

There are various ways to control the attitude of a projectile, and their respective use depends on several factors [62]. In this project, the projectiles may not be retrievable, and therefore the use of an active control system would increase the general cost of the projectile production. Therefore, the choice was to implement an unguided projectile configuration. In this type of configuration, attitude stability is achieved by two ways: imposed rotation around the symmetry axis of the projectile, or by using tail fins [1]. The tail fins were chosen since the method of launching would be simpler, at first analysis.

This irretrievability also influences the choice of materials for the tail and fins, which will consequently gravitate towards low price and environmentally safe. Some good contenders, depending on the configuration geometry, are some type of biodegradable wood derivative -like cardboard or paper-, bamboo hardwood or other cheap wood, and cork.

In relation to length of the projectile, the length/diameter ratio l/d, also called fineness ratio, was set at 4, by comparing its value from some fin-stabilized free-flight projectiles [63], [64].

The area of the fins was chosen similarly to the projectile length, taking in consideration the values of some fin-stabilized free-flight projectiles [63], [64]. When nondimensionalized by d^2, the value of the total area chosen for the fins was 0.4. The span of the fins was set at the value of the FEB radius, 1/2 d. Therefore, from the area value and this value, it comes that the fin span would be 4/5 d.

For the fin airfoil, the most important consideration was that it should be a developable surface, that is, it can be constructed by “bending a planar surface, without requiring extensional deformations” [65]. This is important to maintain a simple construction and also allows the use of paper or cardboard for their materials, which are both cheap, recyclable, and somewhat biodegradable. Influenced by the fins in the non-lethal 12-gauge fin-stabilized projectile studied by [66], the fin design can be observed in Figure 5, in the following section, which presents the side view of the proposed projectile configurations.

3.3. Proposed configurations

Configuration 1 – Sphere: The simplest implementation of the projectile would be to not make any modification to the FEB, and simply launching it as it is. The external ballistics performance of this configuration will be evaluated resorting to the various studies carried out throughout the years, consisting of CFD analysis, wind-tunnel testing and even free-flight testing. Some of these studies, and references containing these studies are [56], [67]-[72]. A drag reducing fairing can be used to transport the FEB during the transport phase.

Configuration 2 – Sphere, tubular boom, and fins: One of the other possible configurations according to the requirements and preliminary design choices is to attach a tubular boom to the aft part of the sphere, with the fins located at the other end of it. This way the possible problems with landing performance and the Magnus effect from the 1st configuration can be minimized or even eliminated. If necessary, a fairing can accommodate this configuration in the transport phase, reducing the possible considerable drag and its impact on the UAV performance. The implementation of this configuration can be simple, since it only uses developable surfaces.

Configuration 3 – Sphere, tangential cone, and fins: This configuration is a really simple way to streamline the fire-extinguishing sphere, considerably reducing the separation that occurs in the aft part of the sphere. The lengthened afterbody will maintain the flow attached to the surface for longer, reducing the pressure drag, while probably increasing the skin friction drag [56]. This might be good for the transportation-phase and can even mitigate the need for a fairing. Its construction will still be simple, since the tail can be made with just developable surfaces, as the previous configuration. It is important to notice that the actual full length of this configuration 435 mm since the last 5 mm of the cone are cut (as can be seen in detail A of the drawing), so the actual l/d of this configuration is, approximately, 3.954 and not 4. This has two justifications: firstly, this would be hard to construct in certain materials, because of the sharp vertex, and the replicability of the configuration is of great importance; secondly, this very small section is of complex representation in the CFD mesh, and it might have created calculation problems. This will not be considered a problem in the comparison of the configurations, but it is appropriate to refer.

Configuration 4 – Sphere, NACA tail, and fins: A streamlined afterbody with an intrinsically curved surface is also proposed to be studied. For this work, it was decided to rotate a symmetrical NACA 0020 airfoil around its chord line, and cutting the leading edge at the maximum thickness, accommodating the sphere in front. The idea behind this configuration design is the same as in the sphere-cone configuration, i.e., a reduction in pressure drag by the lengthening the afterbody, but it would be interesting to understand if significant difference between these two configurations arise at the tested Reynolds number. The construction of this configuration might be more complex, and probably more difficult to guarantee its construction in biodegradable materials, because of the intrinsic curvature of the tail. Some possible materials for the tail could be cork or wood.

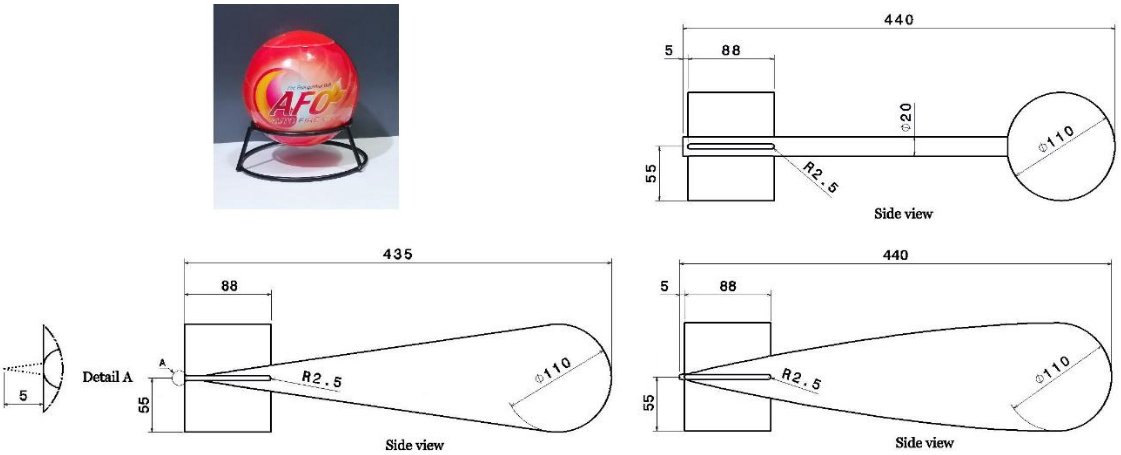

Figure 5 Design of the proposed configurations: the AFO ball (FEB) as it is (top left), Configuration 2 (top right), Configuration 3 (bottom left), and Configuration 4 (bottom right).

4. Results

4.1. Configuration 1

As mentioned before, the analysis of this configuration will be done in a theoretical sense, using various papers and studies to analyze the possible performance of launching. the FEB by itself.

The flow around the sphere, the resulting wake, and their characteristics are somewhat complex and very unstable [69]. For the case in study, there is no interest in characterizing the flow at very low Reynolds numbers, since it would translate, in this case, to very small speeds. In fact, as it will be appointed later, the launching velocity of the simulations will be between 10 m/s and 20 m/s, which, considering air properties at sea level in ISA atmosphere and the FEB diameter as the reference length, corresponds to a Reynolds number range between 0.75×10^5 and 1.5×10^5.

Thus, according to Achenbach [70], starting from Reynolds numbers in the order of 10^4 it is possible to divide the flow regime around a sphere in four characteristic regimes. A first one, denominated subcritical regime, in which there is an almost independency between the drag coefficient and Reynolds number, thus the drag coefficient in this regime is considered constant, with a generally considered value of 0.5 [56]. The second phase is called critical regime, and it is characterized by a brisk decrease on the drag coefficient. This phenomenon, also called drag crisis, was first recognized by Eiffel and Prandtl [67], and it is due to boundary layer transition from laminar to turbulent. Since a turbulent boundary layer has more kinetic energy than a laminar one, it endures the positive pressure gradient along the rearward surface of the sphere more effectively. This makes it remain attached further rearward, narrowing the wake and reducing the pressure drag [26], [67], and consequently the drag coefficient reaches a minimum of 0.08 at the critical Reynolds number $Re=3.8\times10^5$ [70], [71]. After this, the supercritical regime is entered, where an increase in Re number is met with an increase in C_D. By further increasing the *Re* number, the transcritical regime is reached, and here C_D also increases with Re number [70], [71].

As explained, the flow around a sphere is unstable and difficult to predict, while also being affected by the inherent unpredictability of the boundary layer transition, as this phenomenon is affected by a great number of flow and body characteristics [67]. Furthermore, other aspects impact the correct prediction of the real trajectory of a falling sphere. One, for example, is surface imperfections, which cause unpredictability of the boundary layer transition, and can cause an erratic behavior on the boundary layer [72]. In fact, spheres without a smooth surface (by patching, for example) can twist and “corkscrew” when falling [69]. This might present a problem in the present case, since the used fire-extinguishing sphere has a protruding fuse, preventing an almost perfect roundness. Another consideration to the unpredictability of the sphere path is the fluctuating lateral forces caused by vortex shedding, especially in the subcritical regime [71]. Furthermore, one more physical phenomenon that can highly impact the correct estimation of the sphere trajectory is the Magnus effect. If rotation on the FEB arises while launching, a deflection in the direction of the rotation results, caused by the Magnus force [72]. Both these facts can add a layer of complexity to the prediction of the aerodynamic coefficients of the flow around the sphere, or to the model used. Figure 6 presents typical experimental results for the drag coefficient of the sphere in the critical regime.

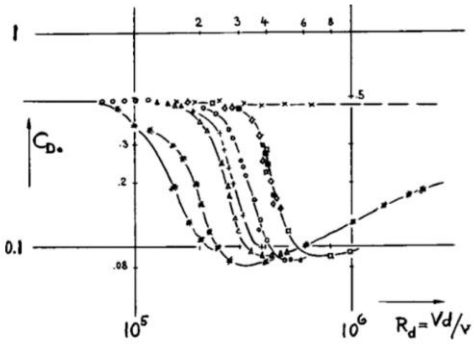

Figure 6 Experimental results for the drag coefficient of spheres in the critical regime [67].

The referred difficulty in predicting the necessary aerodynamics is shown here. Moreover, as referred in the beginning of this section, the Reynolds number at launch will range between 0.75×10^5 and 1.5×10^5. This means the velocity of the FEB throughout the trajectory would be mostly in this critical regime.

One remark can be made about the landing quality. There is a possibility of the sphere rolling away from the target when landing, nullifying completely the value of the launch. This is especially relevant since the UAV that will be used to carry the projectile will probably be a fixed wing one, and, therefore, the launching phase will have considerable translational speed.

Taking all previous aspects into account, launching just the FEB is not considered a good option. Therefore, this configuration will not be considered a viable option, and will not be further discussed.

In this section the inertial properties for Configuration 2, 3, and 4 are presented. The inertial properties of these configurations were obtained through CATIA. The FEB was considered a solid sphere, with its mass uniformly distributed. Since the mass of the FEB is 0.470 kg, and its diameter is 0.11 m, the resulting density is 674 kg/m3. The tail components were considered made of cardboard with a density of 700 kg/m^3 (value obtained from [73]) and 1 mm of thickness. The inertial properties of the configurations are presented in Table 2. x_{cg} is the position of the center of gravity, measured from the most forward point, in front of the FEB. It is important to mention that even though cardboard could not be used for the construction of configuration 4, the material will be considered in theory, in order to properly compare the results with the other configurations.

Table 2 Inertial properties for Configurations 2,3, and 4.

	x_{cg} (m)	m (kg)	I_x (kg.m²)	$I_y = I_z$ (kg.m²)	l (m)	d (m)	S (m²)
Configuration 2	0.0794	0.5120	0.0006	0.004273	0.440	0.110	0.0095
Configuration 3	0.0832	0.5426	0.000663	0.004489	0.440	0.110	0.0095
Configuration 4	0.0952	0.6004	0.000797	0.005945	0.440	0.110	0.0095

4.3. Static aerodynamic coefficients

The CFD aerodynamic results were obtained for angles of attack ranging from 0º to 14º, every 2º, for a velocity of 15 m/s (the average launching velocity), which, considering the reference length 0.11 m, an air density of 1.225 kg/m^3, and a dynamic viscosity of 1.7894×10^{-5} kg/(m.s), corresponds to a Reynolds number of around 113,000. Dynamic symmetry was considered, as explained before, in order to obtain the results from -14º to -2º. The CFD methodology explained before was applied. The global sizing method was set to Fine, and the finest mesh subsection was defined using a Body of Influence method, with an element size of11 mm. A Face Sizing method was used to mesh the projectile wall, with an element size of 0.9 mm, and an Inflation method was applied to the projectile wall, with 20 layers and a first layer height of 0.015 mm, guaranteeing a $y^+ \leq 1$. As for the turbulence model and other definitions, the ones defined previously were used. Figure 7 presents the results for the tested configurations:

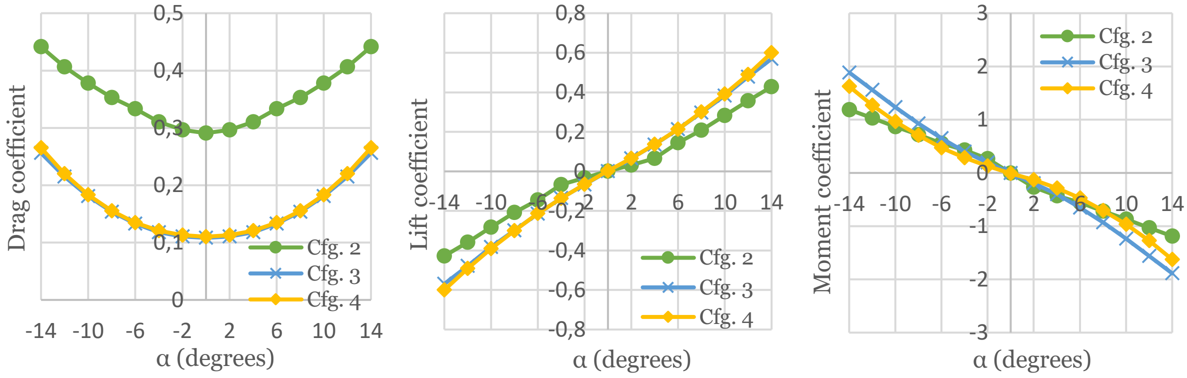

Figure 7 CFD results for the static aerodynamic coefficients for Configurations 2, 3, and 4. On the left is the drag coefficient, in the center the lift coefficient, and on the left the moment coefficient.

Firstly, by the moment coefficient results, it can be noted that all configurations are statically stable since the moment coefficient with respect to α curves have a negative slope, as it was expected for this kind of fin stabilized configurations. It can also be observed that in terms of C_D and C_L the results for the 3rd and 4th configurations are very similar, and the difference between them in the moment coefficient arises from the different center of gravity position. As for Configuration 2, a much greater amount of drag coefficient, more than 2 times of the other configurations, can be observed. This is due to the larger pressure drag arising from the wake behind the FEB, in the areas where the tail is not connected, which are areas of detached flow. This can be observed in Figure 8.

As for the other configurations, for this range of α, the flow seems to be mostly attached to the body, especially in the lower values of α. This is mostly because of their streamlined bodies which do not have any geometric discontinuities. This can be observed in Figures 9 and 10.

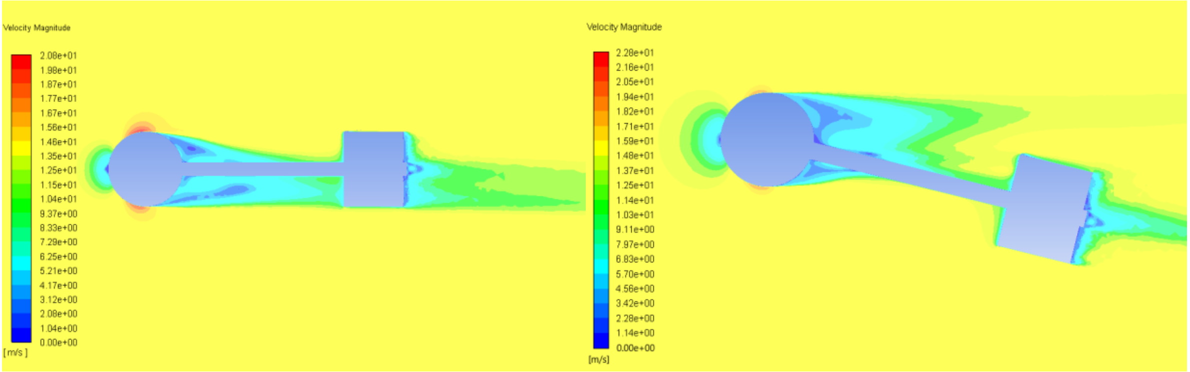

Figure 8 Velocity profile in the plane xy of Configuration 2, at 15 m/s, at 0º of angle of attack (left) and 14º of angle of attack (right).

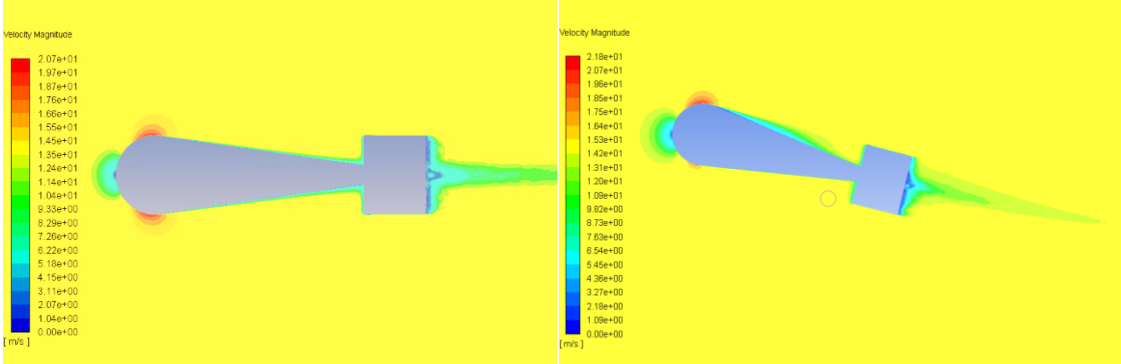

Figure 9 Velocity profile in the plane xy of Configuration 3, at 15 m/s, at 0º of angle of attack (left) and 14º of angle of attack (right).

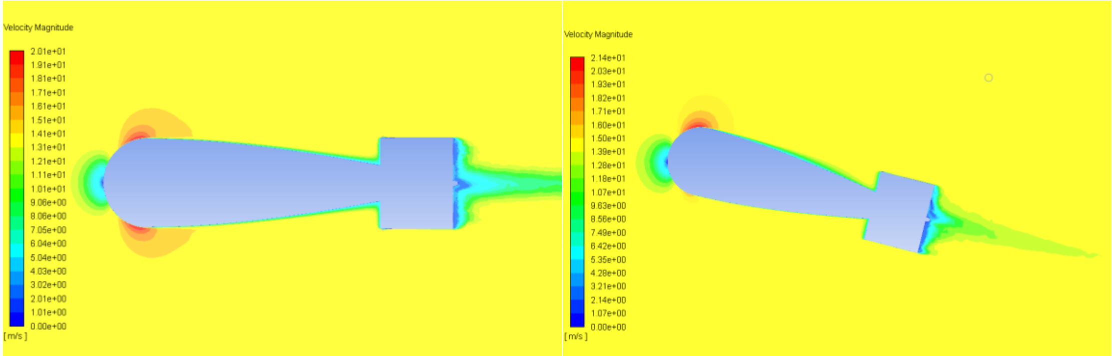

Figure 10 Velocity profile in the plane xy of Configuration 4, at 15 m/s, at 0º of angle of attack (left) and 14º of angle of attack (right).

As for the fins, it seems that a certain amount of detachment is always present, at least at the trailing edge, and a considerable amount at the upper surface as α reaches its higher values of the range, which can be observed in Figure 11. All these assessments could be better evaluated by analyzing the axial wall shear stress and the pressure coefficient, but it will not be considered a relevant analysis for this work.

As for the adequacy of the applied CFD methodology, it was very efficient to obtain the results for the cone and NACA tail configurations. On the other hand, Configuration 2 was noted to have a transient behavior, indicated by its results having oscillatory patterns. Therefore, for Configuration 2, the static aerodynamic results which were considered were the ones with minimum residual values, while for the other configurations the converged values were considered, which also coincided with the lowest residual values. Also, double precision was used for the calculations, which had a notable positive impact on the precision of the results, and also accelerated the convergence of the results. Another limitation regarding the CFD results for Configuration 2 was that different runs of the CFD calculations gave slightly different results, sometimes with more than 15% difference.

Even though some limitations arise with this methodology, the results still allow for an early comparison between the projectile configurations, while giving important insight on the configurations' aerodynamic behavior, which can affect the predictability of the configurations' trajectory.

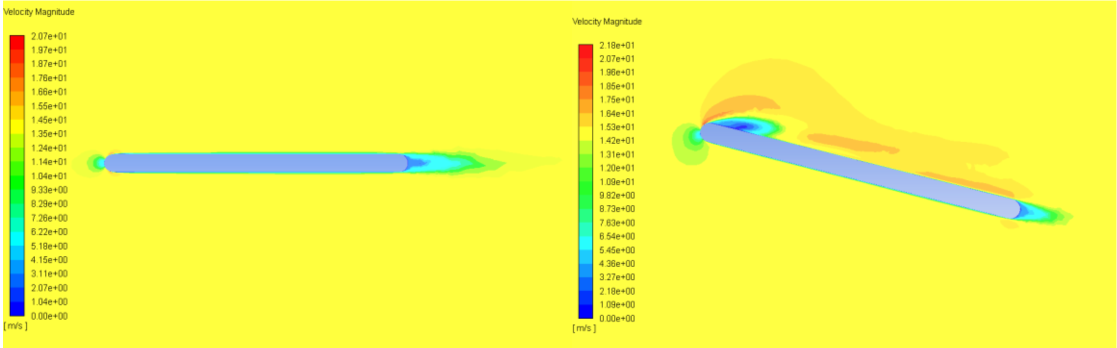

Figure 11 Velocity profile in the plane xy of the fins, in Configuration 3, at 15 m/s, at 0º of angle of attack (left) and 14º of angle of attack (right).

4.3. Dynamic aerodynamic coefficients

To obtain the dynamic coefficients of the fins, it is necessary to determine l_t and a_t, which was done using *XFLR5*. l_t is the distance between the projectile center of gravity and the fins' aerodynamic center, and a_t is the slope of the $C_L(\alpha)$ curve. From the linear regression of the $C_L(\alpha)$ curve obtained through *XFLR5*, it can be determined that $a_t = 1.758\ rad^{-1}$. In order to obtain the aerodynamic center, an iterative method was used, by plotting the $C_M(\alpha)$ curve in various locations, until the point in which the slope is 0, i.e., the C_M is constant, is found. That point is the aerodynamic center. With this approach, it was found that the aerodynamic center is located at, approximately, 18.18 % of the chord, at 0.016 m from the leading edge. Therefore, with the center of gravity of the different configurations specified in the "Inertial properties" section, the l_t for the different configurations can be obtained, as shown in Table 3, accompanied by the resulting dynamic coefficients for the configurations, obtained through equations (17) and (18), while $C_{Y_r} = -C_{Z_q}$ and $C_{N_r} = C_{M_q}$, since geometric and dynamic symmetry is considered.

Table 3 l_t and dynamic coefficient results for Configurations 2,3, and 4

	Configuration 2	Configuration 3	Configuration 4
l_t (m)	0.2836	0.2798	0.2678
C_{Z_q}	-9.2334	-9.1097	-8.7190
C_{M_q}	-23.8054	-23.1718	-21.2268
C_{Y_r}	9.2334	9.1097	8.7190
C_{N_r}	-23.8054	-23.1718	-21.2268

4.5. Trajectory predictions

A total of 11 trajectory cases have been chosen, with the variables being height of launch h_{launch}, velocity of launch V_{launch}, mean wind speed MW_{vel}, and mean wind direction MW_{dir}. These were divided in two groups: Group 1, which evaluates the different results for different launching heights and different launch velocities while considering inexistent mean wind speed; and Group 2, which assesses the influence of the mean wind on the trajectory and projectile's behavior, varying its speed and direction for two launching velocities while maintaining the height of launch. Table 4 presents the cases for Group 1 and their launch variables, and Table 5 the ones for Group 2:

Table 4 Trajectory launching case for Group 1.

	Group 1						
	Case 1.1	Case 1.2	Case 1.3	Case 1.4	Case 1.5	Case 1.6	Case 1.7
h_{launch} (m)	30	30	30	50	100	100	100
V_{launch} (m/s)	10	15	20	15	10	15	20

Table 5 Trajectory launching case for Group 2.

	Group 2			
	Case 2.1	Case 2.2	Case 2.3	Case 2.4
h_{launch} (m)	100	100	100	100
V_{launch} (m/s)	10	10	20	20
MW_{dir}(°)	0	90	90	0
MW_{vel} (m/s)	2.5	2.5	2.5	5

It is relevant to refer that, whenever necessary, some results will be suppressed, in order to not clutter the following pages with extremely similar result images, or ones that will not allow for and relevant analyses. Nonetheless, all relevant results will be discussed, and whenever similar or equal results arise, they will be mentioned.

Firstly, the results for $\alpha(t)$, $\theta(t)$, $V(t)$, and $z(x)$ for all three configurations from Case 1.2 are shown in Figures 12 and 13.

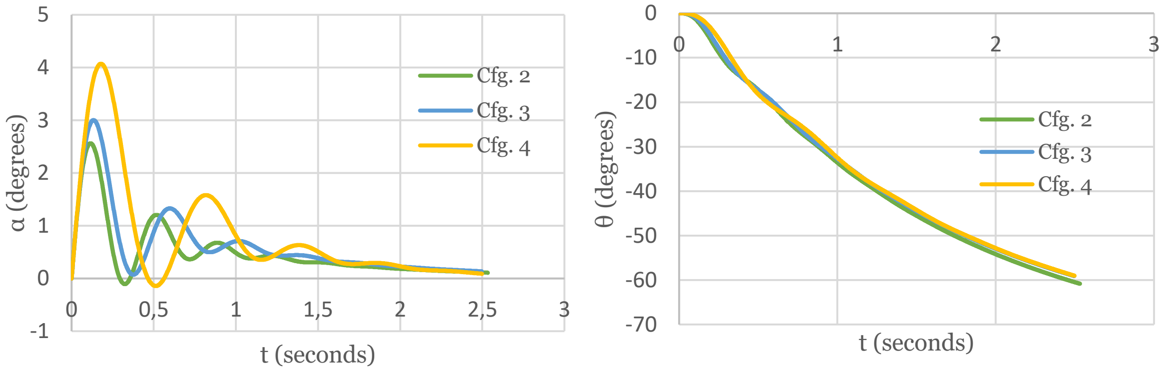

Figure 12 $\alpha(t)$ (left) and $\theta(t)$ results for Configurations 2, 3, and 4, from the trajectory case 1.2.

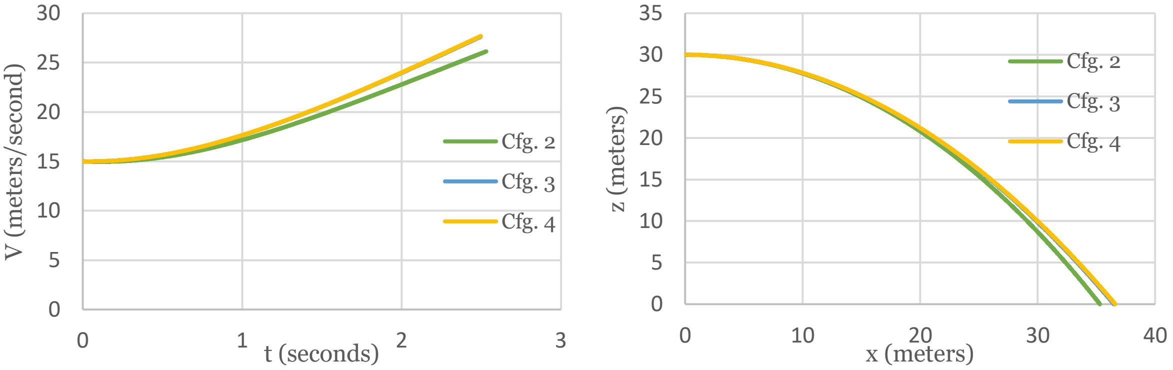

Figure 13 $V(t)$ (left) and $z(x)$ results for Configurations 2, 3, and 4, from the trajectory case 1.2.

From figure 12 it can be confirmed that all configurations have positive dynamic and static stability, which, considering the results for the previously obtained coefficients, was already expected and referred. All configurations have a dynamically damped behavior, decreasing the oscillation amplitude of the angle of attack and pitch angle throughout the trajectory, and eventually asymptotically approaching 0 ° and 90 °, respectively. It can also be observed that the 2nd and 3rd configurations seem to have a slightly better dynamically stable behavior than the NACA tail configuration, since they dampen the oscillations quicker than the other configuration, which is a result from slightly higher absolute values for the dynamic coefficients and l_t, and a lower value of I_y and I_z, which seem to be more adequate for these trajectory cases.

It can also be observed by Figure 13 that the 2nd configuration has a final velocity lower than the others, which was expected from the higher C_D value, which also translates to a lower final x position.

The results shown in Figures 17 and 18 represent the baseline results from the trajectory cases in Group 1, for the three configurations, and all the other results are very similar. The results from this group allow to draw the conclusion that, in terms of impact velocity and location, configurations 3 and 4 are very similar. Even the final θ in all cases are extremely close, differing 0.1° at most. The impact θ can be relevant, because if the angle between the projectile and ground during landing is low then the projectile might slide. Considering that α is small on impact, this angle of impact is practically equal to θ.

Subsequently, Cases 1.1, 1.2, and 1.3 are evaluated for Configuration 3, with the relevant results being presented in Figure 14.

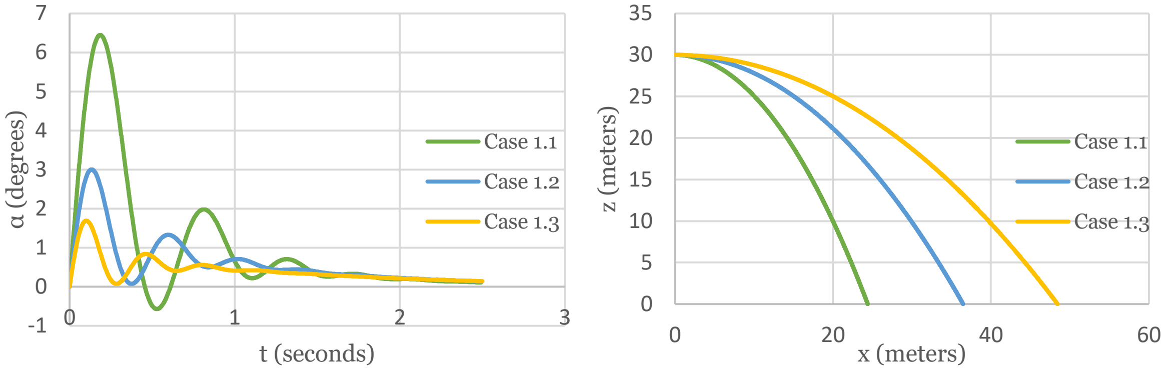

Figure 14 $\alpha(t)$ *(left) and* $z(x)$ *results for Configurations 3, from the trajectory cases 1.1, 1.2, and 1.3.*

The trajectory cases 1.2, 1.4, and 1.6 are also considered, although their results are not shown since they are all very similar. From the results in Figure 14 and from these last mentioned trajectory cases, it can be assessed that, in relation to the launching variables, the factor that influences the maximum angle of attack in the trajectory is the launching velocity, and a higher launching velocity reduces the maximum angle of attack the projectile endures during flight. It can also be determined that the impact θ is affected by two launching variables: launching height and launching speed. A slower launching speed and a higher launching height correlate to a higher θ on impact. Also, on the right side of Figure 14 it can be seen observed that the launching velocity highly affects the impact location, which was already expected.

Now, results for Group 2 are presented. Figure 15 shows a result for Case 2.1 and Case 2.4 are compared with Cases 1.5 and 1.7, for Configuration 3, and a result for Cases 2.2 and 2.3.

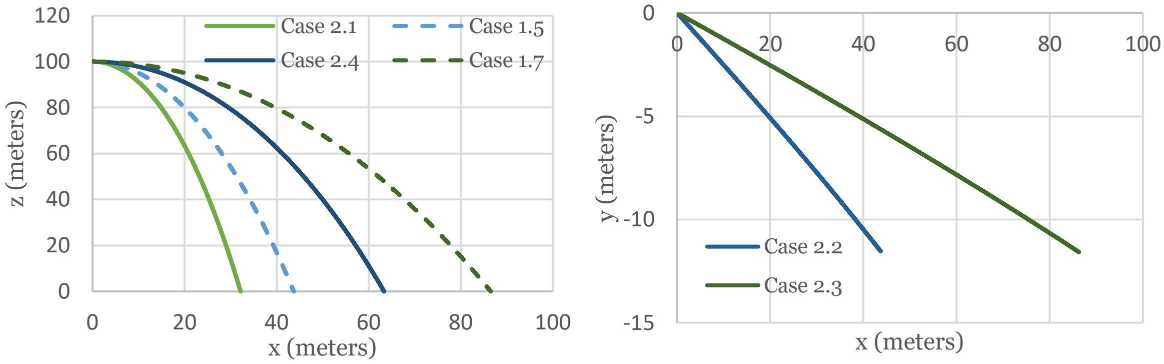

Figure 15 On the right, the z(x) results for Case 2.1 and 2.4 (full lines) are compared with the results for Cases 1.5 and 1.7 (dashed lines). On the left, the y(x) results for Cases 2.2 and 2.3 are presented. All these trajectory results are for Configuration 3.

The first result to acknowledge is that the mean wind influence is only on x_g and y_g, while all other trajectory variables behave the same way, meaning that mean wind does not affect the projectile's attitude and stability. It can also be noticed that the effect of wind is the same, regardless the launching velocity, and that the difference in effect arises from the different trajectory times: comparing Case 1.5 with Case 2.1 (cases with the same launching height and launching velocity), the difference in x_g is around 11.55 m, which is the same as the mean wind velocity multiplied by the trajectory time and by the cosine of the direction, 0 °, and in Case 2.2, the final y_g is approximately -11.57 m, which is the same as the mean wind velocity multiplied by the trajectory time and by the sine of the wind direction, 90 °.

Another relevant study is the influence of wind turbulence in the trajectory. Cases 1.1, 1.3, 1.5, and 1.7 are analyzed, for Configuration 3, with and without turbulence. Figure 17 shows these results for Case 1.7, while Figure 16 presents the typical wind turbulence velocity pattern.

The analysis makes it obvious that wind turbulence can have a considerable impact on the trajectory impact point. Between the tested cases, the minimum difference in x_g was 0.64 m, while the maximum was 2.18 m. This can be observed in Figure 17, on the left. The difference in the velocity throughout the trajectory is not considerable, which can be seen in on the right of Figure 17, while the difference in the projectile's attitude and stability is negligible.

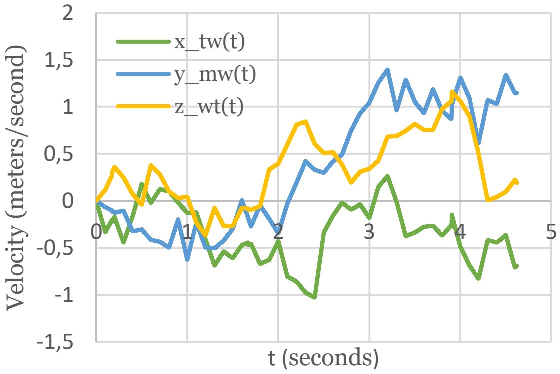

Figure 16 Typical wind turbulence velocity pattern. These values are in the projectile-fixed coordinate system.

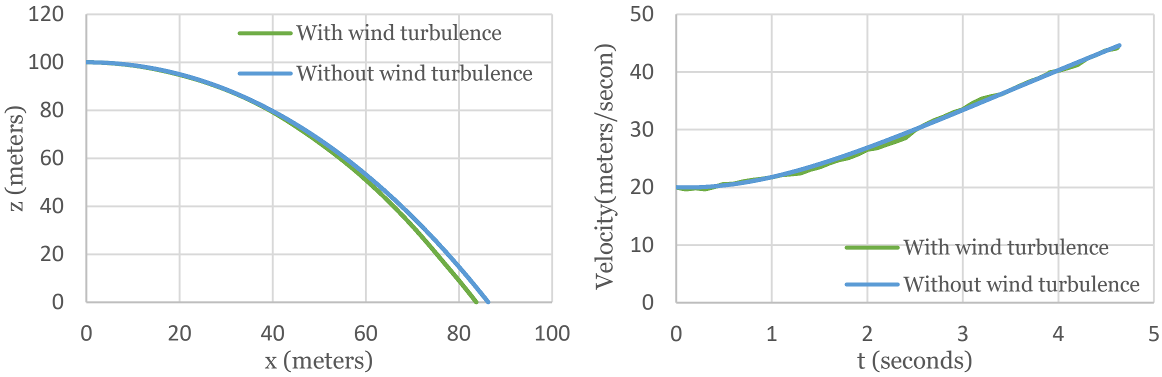

Figure 17 z(x) (on the left) and V(t) (on the right) for Case 1.7, with and without wind turbulence, for Configuration 3.

Another important analysis relates to the size of the fins. A different configuration was considered, based on Configuration 3, with double the area of the fins, which will be named Configuration 3.1, in order to assess what would be the impact on stability. This configuration's inertial properties are obtained considering the same material properties for all other configurations, as well as the same fineness ratio. The same analysis done previously to obtain the dynamic coefficients was carried. Using *XFLR5*, a_t was obtained, with the value 0,9568 rad^{-1}. Considering the position of the aerodynamic center, 18.18 %of the airfoil chord, which is at 32 mm, it follows that l_t=0.1972 m. With this, the values for the dynamic derivatives of Configuration 3.1 can be obtained, which are shown in Table 6, while Table 7 shows the configuration's inertial properties.

Table 6 Inertial properties of Configuration 3.1.

x_{cg} (m)	Mass (kg)	I_x (kg.m²)	$I_y = I_z$ (kg.m²)	l (m)	d (m)	S (m²)
0.0938	0.570	0.000693	0.005783	0.440	0.110	0.00950332

Table 7 Dynamic coefficients for Configuration 3.1.

C_{Z_q}	C_{M_q}	C_{Y_r}	C_{N_r}
-6.9887	-12.5288	6.9887	-12.5288

Interestingly, even though the fin area doubled, a_t and l_t values lowered considerably, so the increase in S_t was not enough to increase the coefficients' values. The decrease in a_t is due to the aspect ratio of the tail halving (the tail aspect ratio is obtained by b^2/S_{tail}, with b being the tail span, and since b stays the same, while S_{tail} doubles, the aspect ratio halves), having therefore a considerably higher loss of lift and increase of drag due to tip vortexes [57], while the decrease in l_t arises from the aerodynamic center moving back and the advance in the gravity center.

The CFD results for this configuration are shown in Figure 18, and they are compared with the results for Configuration 3.

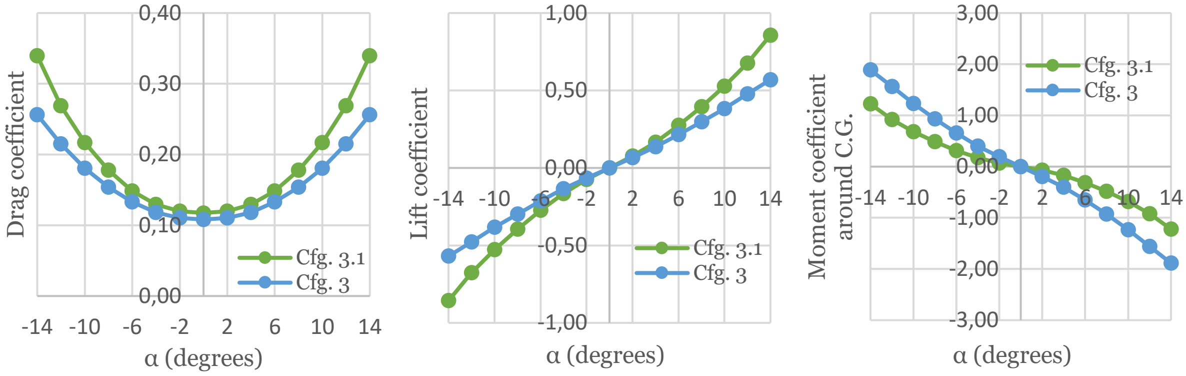

Figure 18 CFD results for drag coefficient (left), lift coefficient (middle), and moment coefficient around C.G. (right) for Configuration 3.1 and 3.

As it can be observed, the drag coefficient increased overall, more significantly in higher angles of attack, as well as the lift coefficient. Interestingly, this increase in the lift coefficient did not translate into higher values for the moment coefficient around the center of gravity. This is because the distance between the center of gravity and the point where the resulting lifting force of the projectile is applied reduced significantly.

The trajectory case 1.5 will be evaluated and compared with the same results for Configuration 3. The case will also be evaluated with and without turbulence. Again, only some results are presented here, in Figure 19.

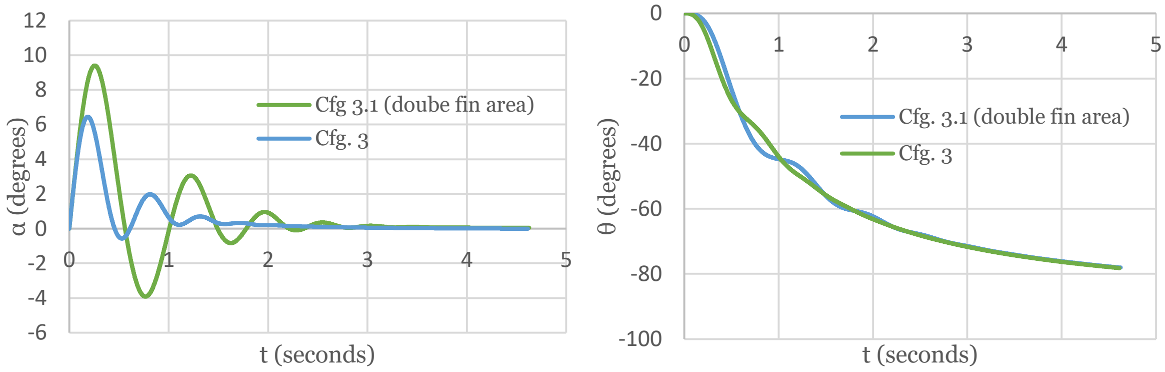

Figure 19 $\alpha(t)$(left) and $\theta(t)$ results for Configuration 3.1 and 3, from trajectory case 1.5.

As predicted, in terms of stability, since the values for the moment coefficient around the CG are smaller than Configuration 3, the maximum angle of attack is higher, and from the smaller absolute values for the dynamic coefficients, the configuration for the projectile with double the fin area is not as dynamically stable as the other configurations. As for the behavior of this configuration considering wind turbulence, the difference in performance is comparable, with an offset in the impact point of around 2 meters.

A question arises with the values for the dynamic coefficient values: what value would be the most appropriate for $\left(C_{M_{\dot{\alpha}}} + C_{M_q}\right)$, the dynamic coefficients related to the dynamic stability, for this range of launching velocities. From the simulations already performed, it can be seen that it probably needs to be lower than -23.8054. Configuration 3 will be assumed for this analysis, and while it is understood that a change in this coefficient would probably translate to a change in some of the other characteristics, including the projectile's inertial properties and static coefficients, it can serve as a basis for a future study. Thus, the values -30, -50, -70, -90, and -120 are considered for $\left(C_{M_{\dot{\alpha}}} + C_{M_q}\right)$, while considering $\left(C_{Z_{\dot{\alpha}}} + C_{Z_q}\right)$=0. Case 1.6 will be used for this evaluation, and a case with the same launching height and velocity while also considering an initial disturbance of q_1=0.349 rad/s (approximately 20 °/s) will be considered. Figures 20 and 21 are the results for these analyses.

It can be observed that more negative values of $\left(\mathrm{C}_{\mathrm{M}_{\dot{\alpha}}} + \mathrm{C}_{\mathrm{M}_{\mathrm{q}}}\right)$ allow for a quicker damping of the pitch and angle of attack values, while are also associated with a higher value of maximum α, which also occurs a bit later. From the simulated values for the dynamic coefficient, it seems that a value of -30 is desirable, since an under damped system will remain stable and reactive, which is desirable.

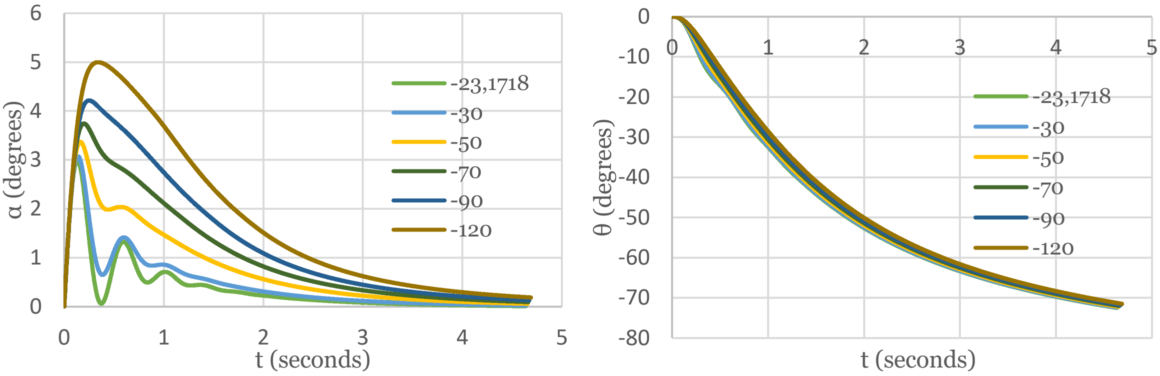

Figure 20 $\alpha(t)$ *(left) and* $\theta(t)$ *(right) for different values of* $\left(C_{M_{\dot\alpha}} + C_{M_q}\right)$*, from Case 1.6, considering the static coefficients and inertial properties of Configuration 3.*

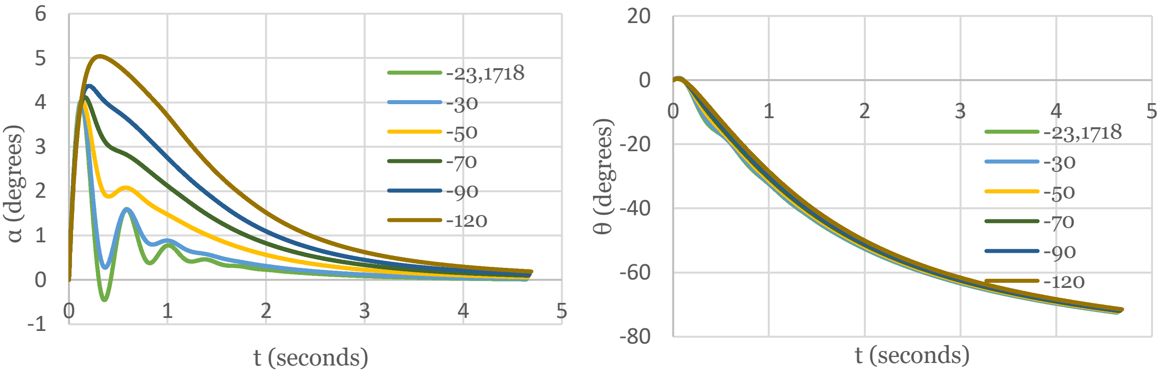

Figure 21 $\alpha(t)$ *(left) and* $\theta(t)$ *(right) for different values of* $\left(C_{M_{\dot\alpha}} + C_{M_q}\right)$*, from Case 1.8 considering an initial perturbation in q of 0.349 rad/s, considering the static coefficients and inertial properties of Configuration 3.*

In these trajectories, the coefficients are considered constant with Reynolds number, so it is relevant to assess if this consideration is affecting substantially their accuracy. Considering the study case 1.7, the terminal velocity is around 40 m/s for Configuration 2, 3, and 4. New coefficients were obtained for that velocity, which, considering the same air properties, corresponds to a Reynolds number of around 301,000, around 2.7 times higher. In general, the increased Reynolds number translated to a decrease in both drag and lift coefficients. This decrease was more accentuated in the drag coefficient, and predominantly higher in Configuration 2, in both coefficients. This is because higher velocities in the flow around the leading sphere attach at a farther point, reducing the size of the wake and of the pressure drag. On average, for these three configurations, increasing the Reynolds number of the flow to 2.7 times decreased the value of C_D around 12 % and the value of C_L around 4 %. This correlates to an increase in the flight velocity of the projectile, while changing the final x_g. This is more noticeable in cases with higher launching velocities and higher launching heights, since these are the cases that reach higher velocities and, therefore, higher Reynolds numbers.

5. Conclusions

The emerging situation regarding wildfires around the world was exposed, and the room for improvement regarding the first steps when tackling a wildfire, especially with the use of UAS, was laid out. Therefore, four projectile configurations which used a fire-extinguishing ball as a design basis were proposed and studied.

One of the considered configurations was just the FEB as it is. Its analysis was made resorting to papers and studies made on the aerodynamics of the sphere. As for the other configurations, which all had different tails and used empennages as mean of stabilization, their static aerodynamic coefficients were obtained through CFD, while the dynamic aerodynamic coefficients were obtained by simpler numerical methods. After their aerodynamic characterization was accomplished, a total of 17 trajectories were simulating resorting to an exterior ballistics model. These trajectories allowed for the comparison of the effect of different launching variables, the effect of mean wind and wind turbulence, size of the tail, and even the magnitude of the dynamic coefficients

It is possible to conclude that Configuration 1 and Configuration 2 both have an inherent difficulty in the predictability of their trajectory, for both have a transient behavior in the tested velocity range. Moreover, the

1st configuration, that is, the FEB as it is, might have a bad landing performance since the launching may resort to a fixed-wing UAV, which means that there will be a considerable translational speed. As for the cone tail and NACA tail configurations, their performance is very similar in the tested trajectories.

Regarding the studied trajectory cases, the consideration of the mean wind is of extreme importance, as it was expected, but the consideration of wind turbulence is also very important for the results, and a maximum difference in impact location of 2 meters was obtained. Reynolds number might also have a considerable effect on the impact location, and considering its variation is relevant to obtain the greatest amount of accuracy possible.

The importance of the magnitude of the dynamic coefficients translates mostly to the stability and attitude characterization of the projectile, although their disregard can eventually affect the final target result of the trajectory.

Taking in consideration all the results, it can be concluded that the best suitable candidate for a fire-extinguishing projectile with an FEB as basis is Configuration 3, the tangential cone tail, since its behavior is easy to predict in the tested velocity range, and its construction is simple and able to be made resorting only to developable surfaces, which means it can be constructed with cheap, readily-available, and biodegradable materials, like cardboard. Moreover, this configuration would not need a drag reduction fairing, since it has a low drag in this velocity range.

The CFD methodology applied was extremely effective to obtain the results for the 3rd and 4th configurations, for their streamlined bodies. On the other hand, the results for the tube configuration have a transient behavior, with oscillatory values. Another problem related with this methodology application for Configuration 2 was the difficulty in replicating the results. However, the methodology allowed for an initial comparison between the different configurations for many different trajectories, without carrying a large computational cost. For the tube tail configuration, the best approach to obtain trajectory results with a much higher level of accuracy would be to obtain transient results or even implement an RBD/CFD coupled trajectory prediction method, although this carries great computational costs. Still in relation to the implemented CFD methodology, the use of double precision had a considerate positive impact in the precision of the results, as would be expected, but also had an important role in the convergence of these results, which the author did not predict according to their research.

Acknowledgements

This work was achieved with the help and guidance of Professor Pedro Gamboa, from UBI’s Aeronautical Engineering Department. The results needed for the CFD validation were facilitated by Véronique deBriey, from Brussels’ Royal Military Academy’s Department of Mechanics. The use of the HPC was made possible by UBI’s Aeronautical Engineering Department Professor Francisco Brójo.

References

[1] R. Fonte-Boa, "Análise de Balística Externa de um Projétil de Calibre 155 mm", Master’s, IST - Universidade de Lisboa, 2014

[2] S. Marques et al., "Characterization of wildfires in Portugal", European Journal of Forest Research, vol. 130, no. 5, pp. 775-784, 2011

[3] A. Carvalho, M. Flannigan, K. Logan, L. Gowman, A. Miranda and C. Borrego, "The impact of spatial resolution on area burned and fire occurrence projections in Portugal under climate change", Climatic Change, vol. 98, no. 1-2, pp. 177-197, 2009

[4] L. Costa, K. Thonicke, B. Poulter and F. Badeck, "Sensitivity of Portuguese forest fires to climatic, human, and landscape variables: subnational differences between fire drivers in extreme fire years and decadal averages", Regional Environmental Change, vol. 11, no. 3, pp. 543-551, 2010

[5] A. Borunda, "How Fires In Europe Are Fueled By Climate Change", National Geographic, July 31, 2018. Accessed on: May 5, 2020. [Online]. Available: https://www.nationalgeographic.com/environment/2018/07/are-fires-in-europe-the-result-of-climate-change-/

[6] M. Green, "Australia's massive fires could become routine, climate scientists warn", Reuters, Jan. 14, 2020. Accessed on: May 5, 2020. [Online]. Available: https://www.reuters.com/article/us-climate-change-australia-report/australias-massive-fires-could-become-routine-climate-scientists-warn-idUSKBN1ZD06W

[7] “IPMA admite que é cada vez mais difícil prever risco de incêndio", PÚBLICO, Mar 27, 2019. Accessed on: May 5, 2020. [Online]. Available: https://www.publico.pt/2019/03/27/sociedade/noticia/chuva-calor-risco-incendio-imprevisivel-1866946

[8] Institute for Environment and Sustainability, "Recent forest fire related accidents in Europe", Publications Office of the European Union, Nov. 29, 2011

[9] D. Silva, "Why is Portugal so prone to wildfires?", Phys.org, July 24, 2019. Accessed on: May 5, 2020. [Online]. Available: https://phys.org/news/2019-07-portugal-prone-wildfires.html

[10] A. Ganteaume, A. Camia, M. Jappiot, J. San-Miguel-Ayanz, M. Long-Fournel and C. Lampin, "A Review of the Main Driving Factors of Forest Fire Ignition Over Europe", Environmental Management, vol. 51, no. 3, pp. 651-662, 2012

[11] F. Tedim, R. Remelgado, C. Borges, S. Carvalho and J. Martins, "Exploring the occurrence of mega-fires in Portugal", Forest Ecology and Management, vol. 294, pp. 86-96, 2013

[12] Departamento de Gestão de Áreas Públicas e de Proteção Florestal, "10.º Relatório provisório de incêionds florestais", Instituto da Conservação da Natureza e das Florestas, Oct. 11, 2017

[13] J. Phippen, "A Deadly Forest Fire in Portugal", The Atlantic, June 18, 2020. Accessed on: May 5, 2020. [Online]. Available: https://www.theatlantic.com/news/archive/2017/06/forest-fire-portugal/530745/

[14] A. Podlaha, S. Bowen, M. Lörinc, “Companion Volume to Weather, Climate & Catastrophe Insight: 2017 Annual Report”, AON Plc, 2017

[15] California Department of Forestry and Fire Protection, "Top 20 Most Destructive California Wildfires", Mar. 14, 2019

[16] California Department of Forestry and Fire Protection, "Top 20 Largest California Wildfires", Mar. 14, 2019

[17] J. Burton, "'It was a line of fire coming at us': Firefighters return home", Busselton-Dunsborough Mail, Feb. 7, 2020. Accessed on: May 5, 2020. [Online]. Available: https://www.busseltonmail.com.au/story/6620313/it-was-a-line-of-fire-coming-at-us-firefighters-return-home/

[18] H. Lee, "Bushfires Release Over Half Australia’s Annual Carbon Emissions", Time, Dec. 23, 2019. Accessed on: May 5, 2020. [Online]. Available: https://time.com/5754990/australia-carbon-emissions-fires

[19] B. Butler, "Economic impact of Australia's bushfires set to exceed $4.4bn cost of Black Saturday", The Guardian, Jan. 7, 2020. Accessed on: May 5, 2020. [Online]. Available: https://www.theguardian.com/australia-news/2020/jan/08/economic-impact-of-australias-bushfires-set-to-exceed-44bn-cost-of-black-saturday

[20] C. Ferreira de Castro, G. Serra, J. Parola, J. Reis, L. Lourenço and S. Correia, Combate a incêndios florestais (vol. XIII), 2nd ed. Sintra: Escola Nacional de Bombeiros, 2003

[21] E. Zanenga, D. Leonello and C. Bottasso, "Feasibility Study of Rotorcraft Fire Fighting for High-Rise Buildings", Journal of Aerospace Engineering, vol. 23, no. 3, pp. 166-175, 2010

[22] M. Kumar, K. Cohen and B. HomChaudhuri, "Cooperative Control of Multiple Uninhabited Aerial Vehicles for Monitoring and Fighting Wildfires", Journal of Aerospace Computing, Information, and Communication, vol. 8, no. 1, pp. 1-16, 2011

[23] J. Calado, "Projecto de um projéctil de caliber 155 mm para combate a incêndios florestais ", Master’s, IST - Universidade de Lisboa, 2013

[24] “Firefighting Drones Infographic", Dronefly, 2018. Accessed on: May 21, 2020. [Online]. Available: https://www.dronefly.com/firefighting-drones-drones-in-the-field-infographic

[25] P. Schaft, "Firefighting Drones Aim to Fly Higher, Save More Lives", Robotics Business Review, July 25, 2018. Accessed on: May 21, 2020. [Online]. Available: https://www.roboticsbusinessreview.com/unmanned/firefighting-drones-aim-to-fly-higher-save-lives/

[26] R. McCoy, Modern exterior ballistics. Atglen, Philadelphia: Schiffer Publishing, 1999

[27] “X. The aerodynamics of a spinning shell", Philosophical Transactions of the Royal Society of London. Series A, Containing Papers of a Mathematical or Physical Character, vol. 221, no. 582-593, pp. 295-387, 1921

[28] M. Khalil, X. Rui and H. Hendy, "Discrete Time Transfer Matrix Method for Projectile Trajectory Prediction", Journal of Aerospace Engineering, vol. 28, no. 2, p. 04014057, 2015

[29] D. Carlucci and S. Jacobson, Ballistics: Theory and design of guns and ammunition. Boca Raton, Florida: CRC Press, 2008

[30] L. Baranowski, "Feasibility analysis of the modified point mass trajectory model for the need of ground artillery fire control systems", Journal of Theoretical and Applied Mechanics, vol. 51, no. 3, pp. 511-522, 2013

[31] G. Kowaleczko and A. Żyluk, "Influence of Atmospheric turbulence on bomb release", Journal of Theoretical and Applied Mechanics, vol. 47, no. 1, pp. 69-90, 2009

[32] J. Kokes, M. Costello and J. Sahu, "Generating an aerodynamic model for projectile flight simulation using unsteady time accurate computational fluid dynamic results", Computational Ballistics III, 2007

[33] J. Sahu, "Time-Accurate Numerical Prediction of Free-Flight Aerodynamics of a Finned Projectile", Journal of Spacecraft and Rockets, vol. 45, no. 5, pp. 946-954, 2008

[34] A. Attallah, "Modeling and Simulation for Free Fall Bomb Dynamics in Windy Environment", in 16th International Conference on AEROSPACE SCIENCES & AVIATION TECHNOLOGY, ASAT - 16, 2015

[35] M. Karim, M. Rahman and M. Alim, "Computation of Axisymmetric Turbulent Viscous Flow Around Sphere", Journal of Scientific Research, vol. 1, no. 2, pp. 209-219, 2009

[36] D. Raymer, Aircraft design, 2nd ed. AIAA, 1992
[37] P. Weinacht, "Projectile Performance, Stability, and Free-Flight Motion Prediction Using Computational Fluid Dynamics", Journal of Spacecraft and Rockets, vol. 41, no. 2, pp. 257-263, 2004
[38] M. Karim, M. Rahman and M. Alim, "Comparative study between flows around sphere and pod using finite volume method", Journal of Naval Architecture and Marine Engineering, vol. 8, no. 1, pp. 49-58, 2011
[39] A. Godfrey, An Account of the New Method of Extinguishing Fires by Explosion and Suffocation, London, 1724
[40] R. Roberts, “Aerial device for fire extinguishing, etc.”, United States Patent2306321A, 1942
[41] E. Dias, "Desenvolvimento do conceito, fabrico e ensaio de um projéctil mecânico para combate a incêndios florestais: FIREND", Master’s, IST - Universidade de Lisboa, 2007
[42] L. Almeida, “Stress analysis and design of a 155 mm projectile shell to be used in firefighting”, Master’s, IST – Universidade de Lisboa, 2016
[43] A. Moreau, “Air borne device for fighting forest fires”, European Patent 0320554A1, 1989
[44] J. O’Dwyer, “Projectile launching apparatus”, United States Patent 20050022657A1, 2005
[45] R. Woodall, F. Garcia, C. Doyle, “Fire retardant bio-friendly practice munition”, United States Patent 6470805B1, 2002
[46] C. Beltran, M. Freitas and A. Moribe, "Unmanned Aerial Vehicle with fire Extinguishing Grenade Release and Inspection System", Florida International University, November 2013
[47] Elidefire - Portugal - Bola extintora. Accessed on: May 5, 2019. [Online]. Available: https://www.elidefire.pt/
[48] Automatic Fire Extinguisher Ball Manufacturer and Supplier in India. Accessed on: May 5, 2019. [Online]. Available: https://www.afofireballs.com/
[49] Cornell Aeronautical Laboratory, "Background Information and User Guide for Mil-F-8785B (ASG), 'Military Specification-Flying Qualities of Piloted Airplanes'", Buffalo, New York, 1969
[50] P. Zipfel, Modeling and Simulation of Aerospace Vehicle Dynamics, 2nd ed. AIAA, 2007
[51] MATLAB Simulink. Mathworks Inc., 2015
[52] “Generate continuous wind turbulence with Dryden velocity spectra – Simulink”, MathWorks. Accessed on: Dec 16. 2019. [Online]. Available: https://www.mathworks.com/help/aeroblks/drydenwindturbulencemodelcontinuous.html
[53] B. Etkin and L. Reid, Dynamics of flight: stability and control, 3rd ed. 1996
[54] ANSYS. Ansys Inc., 2018
[55] ANSYS Fluent User’s Guide, Release 18.2, ANSYS, Inc. 2017
[56] D. Jones and D. Clarke, "Simulation of Flow Past a Sphere using the Fluent Code", Defence Science and Technology Organisation - Maritime Platforms Division, Victoria, Australia, 2008
[57] “Standard Atmosphere”, International Organization for Standardization, ISO 2533:1975, 1975
[58] F. Menter, "Two-equation eddy-viscosity turbulence models for engineering applications", AIAA Journal, vol. 32, no. 8, pp. 1598-1605, 1994
[59] J. Hart, "Comparison of Turbulence Modeling Approaches to the Simulation of a Dimpled Sphere", Procedia Engineering, vol. 147, pp. 68-73, 2016
[60] V. de Briey, B. Marinus and M. Pirlot, "Aerodynamic Characterization of a Non-Lethal Finned Projectile at Low Subsonic Velocity", in AIAA Aviation 2019 Forum, Dallas, Texas, 2019
[61] C. Grillo and F. Montano, "An Extended Kalman Filter-Based Technique for On-Line Identification of Unmanned Aerial System Parameters", Journal of Aerospace Technology and Management, vol. 7, no. 3, pp. 323-333, 2015
[62] “Aerospaceweb.org | Ask Us - Missile Control Systems", Aerospaceweb.org. Accessed on: May 10, 2020. [Online]. Available: http://www.aerospaceweb.org/question/weapons/q0158.shtml
[63] Naval Ordnance Laboratory, “Static and Dynamic stability studies on several Lazy Dog configurations at subsonic and transonic speeds”, May 18, 1964
[64] Center for International Stabilization and Recovery, “Iraq Ordnance Identification Guide – Bombs”, James Madison University
[65] S. Callens and A. Zadpoor, "From flat sheets to curved geometries: Origami and kirigami approaches", Materials Today, vol. 21, no. 3, pp. 241-264, 2018
[66] V. de Briey, I. Ndindabahizi, B. Marinus and M. Pirlot, "Aerodynamical CFD Study of a Non-Lethal 12-Gauge Fin-Stabilized Projectile", Human Factors and Mechanical Engineering for Defense and Safety, vol. 3, no. 1, 2019
[67] S. Hoerner, Fluid-dynamic Drag. Bakersfield, Californa, 1992
[68] J. Southard, Class Lecture, Topic: “Introduction to Fluid Motions, Sediment Transport, and Current-Generated Sedimentary Structures” 12.090, Massachusetts Institute of Technology, Cambridge, 2006
[69] D. Bacon and E. Reid, "The resistance of spheres in wind tunnels and in air", National Advisory Committee for Aeronautics, Langley Aeronautical Laboratory, Washington, Jan. 1, 1967

[70] E. Achenbach, "Experiments on the flow past spheres at very high Reynolds numbers", Journal of Fluid Mechanics, vol. 54, no. 3, pp. 565-575, 1972

[71] R. Deshpande, A. Desai, V. Kanti and S. Mittal, "Experimental investigation of boundary layer transition in flow past a bluff body", Journal of Physics: Conference Series, vol. 822, no. 1, p. 012003, 2017

[72] S. Hoerner, "Tests of Spheres with Reference to Reynolds Number, Turbulence, and Surface Roughness", National Advisory Committee for Aerodynamics, Washington, Oct. 1, 1935

[73] J. Seifert, "A review of the Magnus effect in aeronautics", Progress in Aerospace Sciences, vol. 55, pp. 17-45, 2012

[74] “Density of Selected Solids”, Engineering Toolbox. Accessed on: May 8, 2020. [Online]. Available: https://www.engineeringtoolbox.com/density-solids-d_1265.html